Hot spots in Ammonium Nitrate

Nicholas Taylor

Department of Physics

Churchill College, University of Cambridge

This dissertation is submitted for the degree of

Doctor of Philosophy

April 2011

Acknowledgements

This research would not have been possible without the assistance of others. Corporately, Orica Mining Services and the Atomic Weapons Establishment envisioned and funded the project.

From Orica, Ian Kirby, Jim Chan, John Cooper and Richard Goodridge all provided useful support, insight and questions. Caroline Handley and Hugh James fulfilled a similar role on behalf of AWE, while Geoff Wanstall, Jane Didham and Maurice Marshall did so for the Defence Science and Technology Laboratory. Dr. Marshall is particularly to be thanked for providing a sample of Nitram prills; high-purity ammonium nitrate fertilizer prills are understandably difficult to obtain from garden centres.

Without Ray Flaxman and Bob Marrah of the Cavendish workshops, and Saevar Sigurdsson of the electronics workshop, it's doubtful any of the apparatus used in this research would have worked well enough, or for long enough, to produce the results presented here. While David Powell and Nigel Palfrey of the student workshop didn't manage to turn me into a competent machinist, thanks to their efforts I can now see that state on a clear day. Perhaps more impressively, they also managed to prevent my suffering any serious injury in the process.

Trevor Fairhead of the Cavendish operated the ESEM used in this research. Peter Laity of Earth Sciences operated the X-ray tomography machine. Stewart Palmer of the SMF group provided invaluable assistance in the operation of the Instron.

David Williamson supervised the end of this research, having taken over adroitly when my original supervisor, Bill Proud, left the Cavendish. John Field provided many useful discussions. I am indebted to

all three. David Chapman, David Bell, Adam Collins, Martin Greenaway, Tacye Phillipson, Chris Braithwaite, Stephen Walley and Mike Morley, all of the SMF group, provided helpful comments and discussion.

Last and by no means least, I wish to thank my long-suffering wife Michelle. Without her support it's unlikely this research would have been completed.

Declaration

This dissertation is the result of my own work and includes nothing which is the outcome of work done in collaboration except where indicated in the text. No part of this dissertation has been submitted for any other degree at any institution. The length of this dissertation does not exceed the sixty thousand words permitted by the Physics and Chemistry Degree Committee.

Nicholas Taylor
March 2011

Abstract

Ammonium nitrate (AN) is commonly used as an explosive and as a fertilizer. In both roles it is provided as prills or pellets, approximately spherical and a few millimetres in diameter. The microstructures of several commercially-available AN compositions were investigated using environmental scanning electron microscopy (ESEM) and X-ray microtomography. Those intended for explosive use were found to be more porous than those intended for fertilizer use. The pores in explosive prills were also found to form a connected network. The elemental composition of pellets of mixed AN and dolomite was investigated using energy-dispersive X-ray spectroscopy (EDX); the dolomite additive was found to take the form of grains roughly $50\,\mu$m in size.

The compaction behaviour of confined cylindrical beds of these prills and pellets was studied at strain rates between $4 \times 10^{-4}\,\mathrm{s}^{-1}$ and $200\,\mathrm{s}^{-1}$. Quasi-static experiments were performed using a screw-driven instrumented press, while higher-rate experiments used a drop weight, instrumented with a line laser and load cell. The resistance of a bed to compaction was found to depend on the microstructure of its prills in most cases. Denser prills offered greater resistance to compaction. The exception to this rule was a pellet, rather than prill, formulation. Beds were also found to offer more resistance to compaction at higher strain rates. The Kawakita compaction model was found to agree well with the experimental data.

A commercial fertilizer, not containing any AN, was assessed for use as an inert mock for AN prills and pellets. Prills of a suitable size for this purpose were found using EDX to consist of P_2O_5, with a coating of unknown composition. They were supplied mixed with smaller

K_2CO_3 and urea prills. The mixture was found to have comparable compaction behaviour to AN compositions, indicating that it was useful as a mock for those compositions. In a plate impact experiment on a single layer of P_2O_5 prills, very little light was observed. This indicated that these prills were sufficiently inert for these purposes.

The light produced by shocked granular ammonium nitrate beds and single prill layers was investigated using high-speed framing photography, photodiodes and gated visible-light spectroscopy. Framing photography of prill layers suggested that reaction in prill beds was dominated by effects internal to prills. This was further supported by the similarity between photodiode recordings of prill beds and beds of inert prills containing a single reactive prills. Framing photography of drop weight experiments searching for a mechanism for initiation of reaction by interaction between prills found nothing.

Decay of the light output of the beds suggested that in both granular and prill beds this light output was due to small regions heated to thousands of kelvin, which then cooled. Spectroscopic study confirmed this. These regions were found to reach a peak temperature of $6660 \pm 20\,\mathrm{K}$, well in excess of the approximately 2000 K predicted by a simple chemical model. Investigation of spectral lines observed during this study indicated that the exothermic reaction that led to heating of these emitting regions involved NO.

Contents

List of Figures

List of Symbols

Roman Symbols

A	Area
A, B	Some constants
A_1, A_2	Resistances of axial strain gauges in Wheatstone bridge load cell
$\boldsymbol{a}$	Parameters of a model
c	The speed of light in a vacuum, approx. $2.998 \times 10^8\,\mathrm{m\,s^{-1}}$
c_0	Empirically determined parameter of Hugoniot curve
c_b	Wave speed along a bar
c_l	Longitudinal sound speed
$\boldsymbol{D}$	Hessian matrix of χ^2 at point $\boldsymbol{p}$, see equation (2.33)
$\boldsymbol{d}$	Value of $\boldsymbol{\nabla}\chi^2$ at point $\boldsymbol{p}$, see equation (2.33)
D	Detonation velocity
d	Diameter
E	Energy
e	Engineering strain, $\frac{\Delta l}{l}$
F	Force

G	Gauge factor of a resistive strain gauge
h	Planck's constant, approx. $6.626 \times 10^{-34}\,\mathrm{J\,s}$
i	Index of a single data point
$I(\lambda)$	Spectrum
J	Impulse
K	Bulk modulus, in chapter 4
k	Position along linear detector
k_B	Boltzmann's constant, approx. $1.381 \times 10^{-23}\,\mathrm{J\,K^{-1}}$
k, l	Indices of a single parameter
l	Length
M	Number of parameters in a model; equivalently, length of $\boldsymbol{a}$
m	Mass
N	Some integer
P	Pressure
$P_\theta(k)$	X-ray absorption
P_1, P_2	Resistances of circumferential strain gauges in Wheatstone bridge load cell
$P(\boldsymbol{a})$	Probability of data given parameters $\boldsymbol{a}$, see equation (2.30)
$\boldsymbol{p}$	Point in parameter space about which χ^2 is Taylor-expanded, see equation (2.33)
p	Momentum
Q	Heat energy

R	Resistance
s	Displacement
s	Empirically determined parameter of Hugoniot curve, in chapter 5
$S(\lambda)$	Wavelength-dependent sensitivity of a spectroscope
T	Temperature
t	Time
u	Velocity
V	Voltage
v	Specific volume, $\frac{1}{\rho}$
$\dot{W}$	Power
x_i	Value of independent variable for i^{th} data point
Y	Young's modulus
y_i	Value of dependent variable for i^{th} data point
$y(x_i; \boldsymbol{a})$	Value of dependent variable of model for an independent variable x_i and parameters $\boldsymbol{a}$
Z	Atomic number

Greek Symbols

α	Attenuation coefficient
$\boldsymbol{\alpha}'$	Modified Hessian matrix, see equation (2.44)
$\boldsymbol{\alpha}$	Matrix defined for convenience in model fitting; $-\frac{1}{2}\boldsymbol{D}$
$\boldsymbol{\beta}$	Vector defined for convenience in model fitting; $-\frac{1}{2}\boldsymbol{d}$
γ	Fracture surface energy, in chapter 4

γ	Value of χ^2 at point $\boldsymbol{p}$, see equation (2.33)
$\boldsymbol{\delta a}$	Iteration step in model-fitting techniques
ε	Emissivity, in chapter 5
ε	Strain
$\dot{\varepsilon}$	Strain rate
ζ	Parameter of heat conduction model: $\zeta = \dfrac{2K}{C_p\rho}$
θ	Angle
κ	Factor by which ξ is multiplied or divided
λ	Wavelength
ν	Poisson's ratio, in chapter 2
ν	Vibrational energy quantum number, in chapter 6
ξ	Switching factor in Levenberg-Marquardt algorithm
σ	Stress
σ_B	Stefan-Boltzmann constant, approx. $5.670 \times 10^{-8}\,\mathrm{W\,m^{-2}\,K^{-4}}$
σ_i	Uncertainty in y_i
ϕ	Azimuthal angle, in chapter 5
χ^2	Weighted sum of squared deviations between a model and data, see equation (2.29)
ω	Angular frequency

Acronyms

AN	Ammonium nitrate
ANFO	Ammonium nitrate/fuel oil explosive

boPET	Biaxially orientated poly(ethylene terephthalate), a transparent plastic film. Also known as Mylar.
CJ	Chapman-Jouguet, a theory of detonation
EDX	Energy-dispersive X-ray spectroscopy
ESEM	Environmental scanning electron microscopy
MCP	Microchannel plate
NPL	National Physical Laboratory
P20	A particular scintillator material, used as the phosphor screen in some image tubes.
PIN	p-type, intrinsic, n-type semiconductor junction
PMMA	Poly(methyl methacrylate), a transparent plastic. Also known as Perspex or Plexiglas.
PN	p-type, n-type semiconductor junction
POM	Poly(oxymethylene), a plastic. Also known as acetal or Delrin.
PVDF	Poly(vinylidene difluoride), a piezoelectric polymer
S25	A particular material of low work function, used as the photocathode in some image tubes.
SEM	Scanning electron microscopy
SHPB	Split Hopkinson pressure bar
TATB	Tri-amino-tri-nitro-benzene, an explosive
TMD	Theoretical maximum density
TTL	Transistor-Transistor Logic; a TTL pulse is a +5 V electrical signal.
ZND	Zeldovich-von Neumann-Döring, a theory of detonation

Chapter 1

Introduction and literature review

Ammonium nitrate is a widely used agricultural fertilizer. As a component of ammonium nitrate/fuel oil (ANFO) and emulsion explosives, it is a very popular commercial explosive. Mechanisms by which it can be initiated are therefore of interest both for safety of handling and for development of explosive formulations.

Hot spots are widely held to be the means by which a mechanical shock or impact can cause detonation of a heterogeneous explosive. As such, they are an interesting and useful field of study. Many potential hot spot mechanisms have been proposed, but determining which are relevant in a particular situation remains challenging.

1.1 Ammonium nitrate

Ammonium nitrate is a colourless, highly hygroscopic crystal. When crystallized from aqueous solution, it tends to form needles. By careful choice of solvents and the use of chelating agents, this can be modified (Doxsee and Francis, 2000). When commercially produced for use in fertilizer and ANFO, it is usually in the form of prills. These are pellets, roughly 5 mm long, and generally with some coating. The prills are usually produced by spraying molten ammonium nitrate from a "shower head" at the top of a tower. An upwards draught of air

keeps these pellets aloft and cools them (Kjaergaard, 2000). This cooling tends to leave prills with a void in the centre, as the outside solidifies first and the inside contracts as it cools (Kwok et al., 2003). The coating is added afterwards, to inhibit the ammonium nitrate's absorption of moisture. For laboratory use, ammonium nitrate is available as granules, produced by milling pure AN crystals or prills.

1.1.1 Phases of ammonium nitrate

Ammonium nitrate has five stable phases at atmospheric pressure. They are summarized in table 1.1. Details of their structures are given in appendix A. The existence of a low-temperature phase VII has been suggested (Volfkovich et al., 1954) but subsequently rejected (Ahtee et al., 1983b; Choi and Prask, 1983).

With the exception of those involving phase III, the phase transitions are unremarkable. They all involve a loss of order as temperature rises, accompanied by slight modifications of the unit cell (Brown and McLaren, 1962). The IV $\rightleftharpoons$ III transition, however, merits special consideration. It involves a density change (from $1.72\,\mathrm{g\,cm^{-3}}$ for phase IV to $1.66\,\mathrm{g\,cm^{-3}}$ for phase III). As a result, it tends to break crystals and loosen polycrystalline mixtures. The resulting fragments cause the material to cake, making handling more difficult (Oommen and Jain, 1999).

The IV $\rightleftharpoons$ III transition requires water, and appears to proceed by dissolution of phase IV and recrystallization of phase III in a thin layer of water (Brown and McLaren, 1962; Davey et al., 1991). As the phase transition temperature is approached from below, phase IV becomes more soluble in water than phase III.

The phase change front moves at $100\,\mu\mathrm{m\,s^{-1}}$ at its fastest (Davey et al., 1991). This is substantially slower than the other phase transitions, so phase III may be bypassed altogether on sufficiently rapid heating or cooling, or in the absence of water (Ingman et al., 1982). There has also been extensive work on suppressing this phase transition. A variety of chemical additives have been found to stabilize one or another phase of ammonium nitrate, preventing the awkward IV $\rightleftharpoons$ III transition in a wide range around room temperature (Choi et al., 1980; Highsmith et al., 1994; Mishra, 1985).

Phase	**Symmetry, space group**	**Lattice constants/Å, *Z***	**Ordered?**	**References**
I	Cubic	$a = 4.3655(2)$	No	a, b
	$Pm\bar{3}m$	$Z = 1$		
		398 K		
II	Tetragonal	$a = 5.7193(1)$	No	c, d
	$P\bar{4}2_1m$	$c = 4.9326(1)$		
	(at 355 K)	$Z = 2$		
		356 K		
III	Orthorhombic	$a = 7.7184(3)$	No	e, f
	$Pnma$	$b = 5.8447(1)$		
	(at 318 K)	$c = 7.1624(2)$		
		$Z = 4$		
		305 K		
IV	Orthorhombic	$a = 5.7574(1)$	Yes	g, d
	$Pmmn$	$b = 5.4394(1)$		
	(at 300 K)	$c = 4.9298(1)$		
		$Z = 2$		
		257 K		
V	Orthorhombic	$a = 7.9804(1)$	Yes	h
	$Pccn$	$b = 8.0027(1)$		
	(at 233 K)	$c = 9.8099(1)$		
		$Z = 8$		

Table 1.1: The phases of ammonium nitrate. References: (a) Shinnaka (1959), (b) Ahtee et al. (1979), (c) Shinnaka (1956), (d) Lucas et al. (1979), (e) Goodwin and Whetstone (1947), (f) Lucas et al. (1980), (g) Choi et al. (1972), (h) Ahtee et al. (1983a).

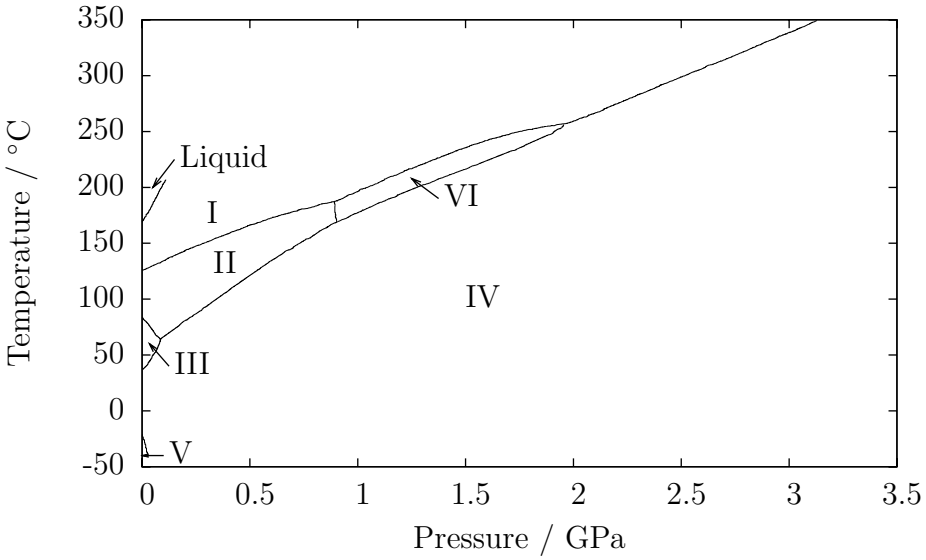

Figure 1.1: Ammonium nitrate pressure-temperature phase diagram, from Rapoport and Pistorius (1966).

The pressure-temperature phase diagram of ammonium nitrate is shown in figure 1.1. The structure of the high-pressure phase VI is poorly studied. Another phase, labelled VIII, is accessible only by shear loading and is not shown on the phase diagram (Adams and Sharma, 1976).

1.1.2 Thermal decomposition of ammonium nitrate

The mechanism and products of this decomposition change with heating rate and pressure. When ammonium nitrate is heated slowly ($\sim 50\,^{\circ}\mathrm{C}$/hour) to between $180\,^{\circ}\mathrm{C}$ and $300\,^{\circ}\mathrm{C}$, it decomposes exothermically. The overall reaction (Friedman and Bigeleisen, 1950; Saunders, 1922) is

$$\mathrm{NH_4NO_3} \longrightarrow \mathrm{N_2O} + 2\,\mathrm{H_2O}\ . \tag{1.1}$$

This reaction requires trace amounts of water. Dry ammonium nitrate will not decompose up to $300\,^{\circ}\mathrm{C}$. A small amount of water vapour allows it to decompose at $180\,^{\circ}\mathrm{C}$. Using isotope tracing shows this water is not incorporated in the $\mathrm{N_2O}$

	Reaction	**Times/s**	**ΔH/kcal**
A	$4[NH_4NO_3(\ell) \rightarrow HNO_3(g) + NH_3(g)$ $\rightarrow NH_4NO_3(\textit{solid aerosol})]$	1–7	4(44)
B	$3[5NH_4NO_3(\ell) \rightarrow 2HNO_3 + 4N_2 + 9H_2O]$	1–3	3(−35)
C	$5[NH_4NO_3(\ell) \rightarrow N_2O + 2H_2O]$	2–7	5(−13)
D	$4NH_4NO_3(\ell) \rightarrow$ $2NH_3 + 3NO_2 + NO + N_2 + 5H_2O$	2–7	81

Table 1.2: Proposed reaction scheme for decomposition of ammonium nitrate under rapid heating at atmospheric pressure. ΔH for reaction A only includes the dissociation step. From Brill et al. (1993).

produced (Friedman and Bigeleisen, 1950). It seems likely that the mechanism is

$$NH_4^+ + NO_3^- \longrightarrow H_2N{-}NO_2 + H_2O \ , \tag{1.2}$$

$$H_2N{-}NO_2 \rightleftharpoons HN{=}NO_2^- + H^+ \rightleftharpoons HN{=}N\begin{matrix}=O\\ \diagdown OH\end{matrix} \ , \tag{1.3}$$

$$HN{=}N\begin{matrix}=O\\ \diagdown OH\end{matrix} \xrightarrow[\text{or acid catalysis}]{\text{Basic}} N_2O + H_2O \ . \tag{1.4}$$

Other oxides of nitrogen are also produced, along with nitrogen gas.

At higher rates of heating, the reaction changes. On heating to ∼ 400 °C at ∼ 2000 °C/s in argon at atmospheric pressure, Fourier transform infrared spectroscopy suggests the system of reactions in table 1.2. These reactions are endothermic overall. This is consistent with pure ammonium nitrate's inability to burn at atmospheric pressure. At higher pressures, the NH_3 and NO_2 produced are confined, and can react exothermically:

$$2\,NH_3 + 2\,NO_2 \longrightarrow N_2O + N_2 + 3\,H_2O \qquad (\Delta H \approx -148\,\text{kcal}) \ . \tag{1.5}$$

However, the overall reaction remains slightly endothermic up to at least 33 atmospheres (Brill et al., 1993).

1.1.2.1 Kinetics

Vyazovkin et al. (2001) studied the isothermal decomposition of AN using a thermogravimetric technique. They determined that this decomposition was due to the reaction

$$\mathrm{NH_4NO_3(s)} \longleftrightarrow \mathrm{NH_3(g)} + \mathrm{HNO_3(g)} \ , \tag{1.6}$$

and that this had an activation energy of approximately $90\,\mathrm{kJ\,mol^{-1}}$ for both solid and liquid AN. They also reviewed existing work on the topic and found a wide range of activation energies quoted for this process. This may be due to flawed kinetic models, or to the complexity of the sequence of reactions involved in AN decomposition.

1.2 Hot spots

Hot spots are regions of a material which become much hotter than the bulk during shock or impact. They are generally thought to cause the onset of reaction in shocked or impacted energetic materials. If a hot spot is large enough, and remains hot for long enough, the heat produced by reaction of the material can exceed that lost to conduction. Such a hot spot is called 'critical', and reaction can grow from one throughout the material.

The minimum temperature of a critical hot spot will depend on the explosive. It can be measured by adding grits to an explosive. If the melting point of the grit exceeds the ignition temperature of the explosive, the grit's addition sensitizes the explosive to frictional loading. Otherwise, the grit has little effect. For most secondary explosives, the minimum temperature for a critical hot spot is in the region of 700 K (Bowden and Gurton, 1948, 1949).

The minimum size of a critical hot spot can be calculated using a heat-balance argument. This depends on the thermal conductivity, density, heat capacity, and heat of reaction of the explosive, and on the temperature of the hot spot. For most secondary explosives, any hot spot smaller than about $1\,\mu$m must be implausibly hot to be critical (Bowden and Yoffe, 1952).

There are several proposed mechanisms by which the mechanical energy of the shock is concentrated and converted to heat. They include the collapse of

pores in the material, friction between grains or at surfaces produced by fracture, the formation of shear bands, and the growth of cracks. These mechanisms do not compete: their effects are additive.

1.2.1 Crack growth

Explosives are relatively weak, and therefore release relatively little energy in fracture. A theoretical treatment shows that the energy released in the growth of a single crack is insufficient to initiate a secondary explosive. It may, however, be able to cause partial reaction (Holmes et al., 1999). Experimentally, even primary explosives are not initiated by fracture (Chaudhri, 1989). Fracture can, however, cause partial reaction (Fox and Soria-Ruiz, 1970).

A crack creates free surfaces, which may rub against each other. Together with the products of partial reaction, this may sensitize the explosive to subsequent stimuli. Also, while explosives are weak, the plastics used to bind polymer-bonded explosives are stronger. A crack passing through such a material close to a grain of explosive could conceivably ignite it.

1.2.2 Cavity collapse

There are several mechanisms by which the collapse of a cavity may generate heat. In the collapse, the surrounding material must undergo plastic deformation, which will raise its temperature. Any gas contained in the cavity will be adiabatically compressed by the shock, reaching a high temperature. The shock may evaporate explosive from the upstream wall of the cavity; this could cross the void, and stagnate against the downstream wall, again reaching a high temperature. A shock can also cause a jet to form from the upstream wall of the cavity, which would strike the downstream wall with great force.

1.2.2.1 Plastic deformation

The plastic work around a symmetrically collapsing spherical void has been analytically treated. The heat produced could cause a critical hot spot in a strong shock (Khasainov et al., 1981). However, weaker shocks have been seen to cause

cavity collapse, leading to initiation.

1.2.2.2 Adiabatic compression

From study of bubbles in water near single crystals of primary explosives, it seems adiabatic compression is the main mechanism by which cavity collapse causes initiation in shocks of a few hundred megapascals (Chaudhri, 1989; Chaudhri and Field, 1974). A collapsing bubble rebounds after the shock has passed, generating an expansion shock. By holding the bubble close to the crystal, but not in thermal contact with it, the expansion shock was eliminated as an initiation mechanism. This also removed the possibility that radiation produced in the compression was important. Using a two-dimensional bubble, the jet was visible. The explosive crystal did not detonate when the jet struck it, but when the bubble had been compressed significantly (Chaudhri and Field, 1974).

1.2.2.3 Evaporation and stagnation

Using streak photography, the evaporation and stagnation effect can be studied. Two crystals of PETN were separated by vacuum, and the first detonated. The detonation products were not visible while traversing the space between the crystals. A bright flash of light was seen at the face of the second crystal, at a time when the detonation products might reasonably have reached the second crystal (Blackburn and Seely, 1965). Atomistic simulations show that a similar effect can be seen when the incident shock is inert (Holian et al., 2002).

1.2.2.4 Jets

Though jets were shown not to be able to initiate primary explosives in weak shocks (Chaudhri and Field, 1974), they are more important in strong shocks of around a gigapascal (Bourne and Field, 1991; Chaudhri, 1989). Under these circumstances, the jet reaches a speed of a few kilometres a second (Bourne and Milne, 2003; Field, 1994). Fast framing photography shows that there is some heating of gas trapped by the jet tip as it strikes the downstream wall of the cavity. There is far more heating as the toroid cavity remaining around the jet is compressed. When a cavity in ammonium nitrate solution was investigated,

though, reaction broke out at the point of the jet impact, and not around the torus. It is possible that the increase of the number and energy of inter-molecular collisions by the jet, or hydrodynamic loading of the downstream wall by the jet, is more important than the heating (Hatano, 2004).

1.2.3 Friction

The rubbing of grains converts mechanical energy to heat. Most secondary explosives, including ammonium nitrate, melt below their ignition temperature, and therefore cannot be initiated by friction between the grains. In primary explosives, this is not the case.

If a flat-tipped needle is dropped into a granular bed of explosive, grains adhere to it and rub against grains in the bed (Chaudhri, 1989). Under these circumstances, initiation is predictable from the coefficient of friction and the ignition temperature (Chaudhri, 1976). The coefficient of friction can be measured, even when growing a large crystal is difficult (Amuzu et al., 1976).

1.2.4 Shear bands

When a material undergoes plastic deformation, heat is generated in the deforming region. Many materials become softer as their temperature is raised. In impact loading, this effect can be stronger than the work-hardening of the deforming region. This results in strain localization: the easiest region to deform is one that has already deformed to some degree. This results in narrow bands of material experiencing intense strain; these regions are referred to as shear bands. The localized heating associated with this deformation is capable of initiating some explosives (Winter and Field, 1975). It has been speculated that the high density of dislocations may allow multi-phonon excitation in such a band (Coffey, 1991)

1.2.5 Vibrational up pumping

Heating excites the phonon modes of a material, but it is the excitation of the internal vibrational modes which causes chemistry (Dlott and Fayer, 1990). The

rate at which energy can be transferred between these modes is therefore an important factor in the response of a material to a hot spot.

For rapid transfer between phonons and internal vibrations, the modes cannot be purely harmonic. Anharmonicity permits multiple phonons to couple to an internal vibration. This is necessary, as the lowest-energy internal vibration is usually more energetic than the highest-energy phonon.

One possible mechanism for energy transfer involves so-called 'doorway modes'. This model only applies to crystals in which the energy levels have certain properties. The lowest-frequency internal vibration must have less than twice the energy of the highest frequency phonon. In addition, the energy difference between any internal vibration and the next most energetic internal vibration must not exceed the energy of the most energetic phonon mode. Most large organic molecular crystals meet these criteria. Under these circumstances, only three-mode interactions are needed to excite all the internal vibrational modes. The doorway modes are those internal vibrations which can be excited by two phonons. The rate at which they are excited can be calculated from relaxation times at low temperatures.

The model is that both phonon and internal vibrational modes rapidly reach thermal equilibrium among themselves, but energy transfer between these two sets of modes is restricted by excitation of the doorway modes. Each set of modes is assigned a quasi-temperature which describes its internal energy distribution, and the problem of energy transfer to the internal modes is treated as one of thermal conduction.

This mechanism provides an interesting new hot spot mechanism. Some defects enhance the anharmonicity of vibrational modes in the region around the defect. In such a region energy from the phonons would flow into the internal vibrations more rapidly than it would in the bulk. The internal vibrational quasi-temperature in that region would then overshoot the equilibrium temperature, possibly allowing a reaction to start (Dlott and Fayer, 1990; Tokmakoff et al., 1993).

An alternative model for vibrational up pumping involves direct excitation of vibrational modes by many phonons. In this model, the phonon modes are treated separately, rather than as a sea of uniform mode density. Resonance

between overtones of the phonon modes and the internal vibrational modes becomes important, and is used in the model. An interaction between the N^{th} overtone of some phonon mode and an internal vibrational mode is equivalent to an interaction between N phonons belonging to that mode, and the internal vibrational mode. This model was used to find the energy transfer in the first ten femtoseconds after impact. This quantity correlated well with the energy to ignition of various energetic materials (McNesby and Coffey, 1997).

1.2.6 Sensitization centres

Sub-critical hot spots may allow partial reaction to take place. Many organic secondary explosives begin to react by the molecules breaking into more reactive fragments. In a critical hot spot, these would then go on to complete reaction. In a sub-critical hot spot they remain unreacted. These reactive fragments provide a point at which reaction can start more readily under subsequent stimulus than in the bulk. Such sensitization centres have been seen in TATB (Sharma et al., 1987).

1.2.7 Hot spots in ammonium nitrate

Most work on hot spots in ammonium nitrate has used flat granular beds under projectile impact (8210X, 2003; Proud, 2002; Proud et al., 2003). The design of the cell is shown in figure 1.2. The projectile was fired from a gas gun at speeds between 400 and 700 $\mathrm{m\,s^{-1}}$. The response of the bed was studied using framing photography, a photodiode, and a spectrometer.

1.2.7.1 Framing photography

Figure 1.3 shows photographs of the impact process on 2 mm beds at various flyer speeds. The bright ring which develops is due to the copper front plate being driven into the glass back plate. The edges of the projectile produce intense shear in the front plate at this point. This heats it, producing light.

The light output clearly depends strongly on the flyer speed. However, evacuating the test chamber appears to have little effect on the light output. The

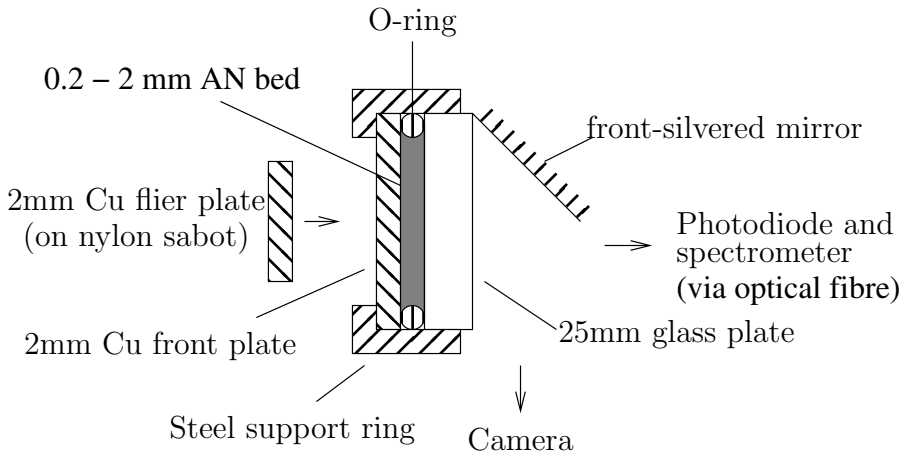

Figure 1.2: Layout of cell for impact on granular ammonium nitrate bed used in Proud (2002), 8210X (2003), and Proud et al. (2003).

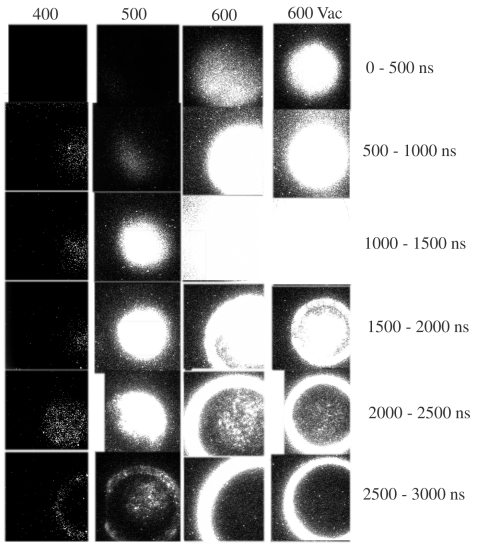

Figure 1.3: Framing photography on 2 mm AN beds from Proud et al. (2003). Each column contains frames from a single experiment, and is labelled with the impact velocity for that experiment in $\mathrm{m\,s^{-1}}$. The suffix "Vac" indicates that the experiment took place under a rough vacuum of 1 mbar. The row labels give the times after impact over which the frames were exposed.

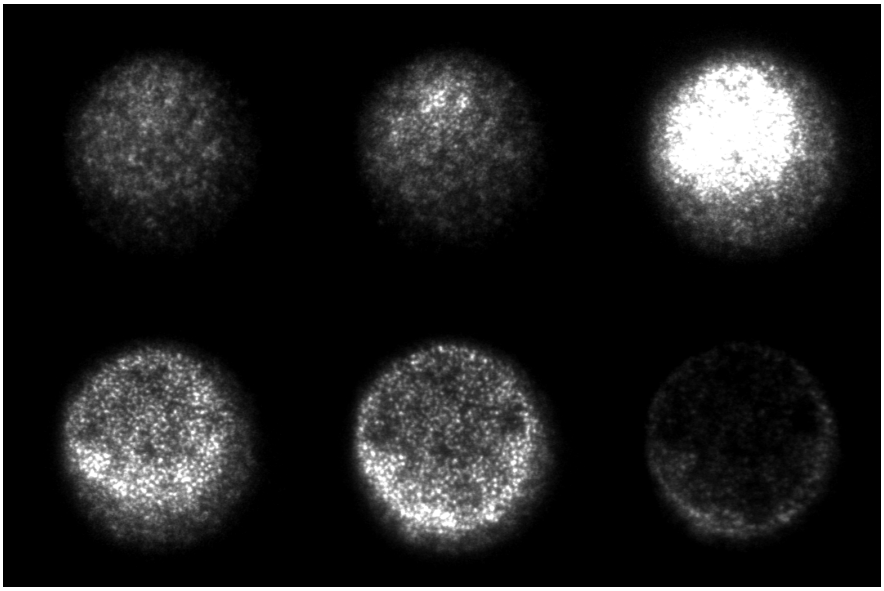

Figure 1.4: Framing photography on a 0.4 mm bed, from Proud et al. (2003). Grain size 150–210 μm. Exposure time of each frame 30 ns. Flyer velocity 700 m s^{-1}. Frames are in order left to right, top to bottom. Reaction region viewed approx. 8 mm diameter.

sequence labelled "600" was taken at atmospheric pressure, while that labelled "600 Vac" was taken at 1 mbar. The only difference is due to the magnification. This suggests that gas trapped in the pores before the experiment is unimportant to the process.

The 2 mm bed was too thick to resolve individual hot spots. Any light relating to a hot spot was scattered or absorbed. To avoid this, an 0.4 mm bed was used for framing photography. Figure 1.4 shows the sequence thus obtained. The growth of critical hot spots and the quenching of sub-critical hot spots are visible between the first two frames.

1.2.7.2 Light output

The photodiode gave a more quantitative measure of total light output than the camera. The total light output in the experiment is a useful indicator of the density of critical hot spots. Ammonium nitrate reacts quite slowly, so only a certain volume of material surrounding each hot spot will have time to react

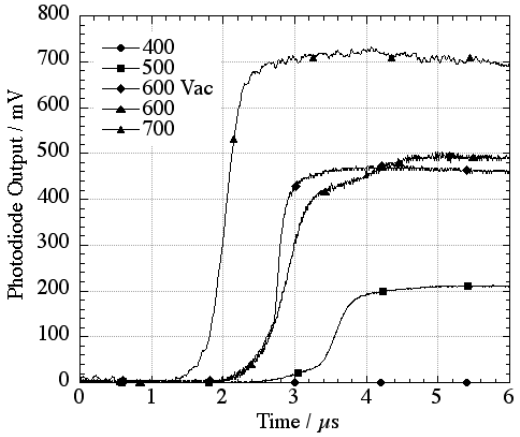

Figure 1.5: Light outputs of 2 mm ammonium nitrate beds, under impact from flyers of a range of velocities, from Proud et al. (2003). The legend gives the flyer velocity that gave rise to each trace in $\mathrm{m\,s^{-1}}$. The suffix "Vac" indicates that the experiment took place under a rough vacuum of 1 mbar.

over the course of the experiment. Figure 1.5 shows the photodiode outputs corresponding to the high-speed sequences in figure 1.3.

Figure 1.6 shows the normalized outputs. The output has been scaled so that all the traces have the same maximum value. The time has been scaled to account for the different shock travel times at different flyer velocities. The similarity of the traces suggests that the kinetics of the situation are unchanged by the flyer velocity.

Figure 1.7 shows the effect of the bed's porosity on the light output. The ammonium nitrate was pressed before putting it in the cell, to control its porosity. Reducing the porosity will favour fracture as a hot spot mechanism. The lower pore fraction naturally reduces the importance of cavity collapse. The decreased scope for grain movement will also reduce the importance of friction. The marked decrease in light output as the packing density increases suggests that fracture is of little importance as a hot spot mechanism.

Figure 1.8 shows the effect of adding chalk to the bed. Chalk is commonly added to ammonium nitrate to reduce caking and improve safety. It seems from the traces that it acts as a heat sink, absorbing energy from critical hot spots and thereby rendering them sub-critical. However, as the hot spot density rises,

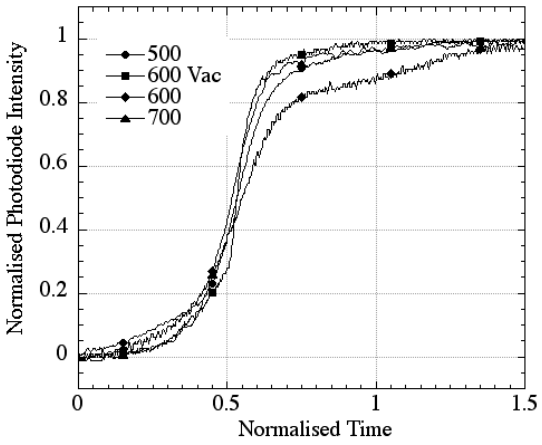

Figure 1.6: Normalized light outputs of 2 mm ammonium nitrate beds, under impact from flyers of a range of velocities, from Proud et al. (2003). The legend gives the flyer velocity that gave rise to each trace in $\mathrm{m\,s^{-1}}$. The suffix "Vac" indicates that the experiment took place under a rough vacuum of 1 mbar. Corresponding non-normalized light output shown in figure 1.5.

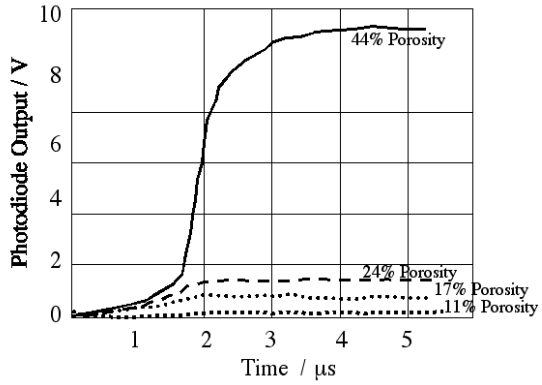

Figure 1.7: Light output of 2 mm ammonium nitrate beds of varying density, under impact from a flyer at $700\,\mathrm{m\,s^{-1}}$, from Proud et al. (2003).

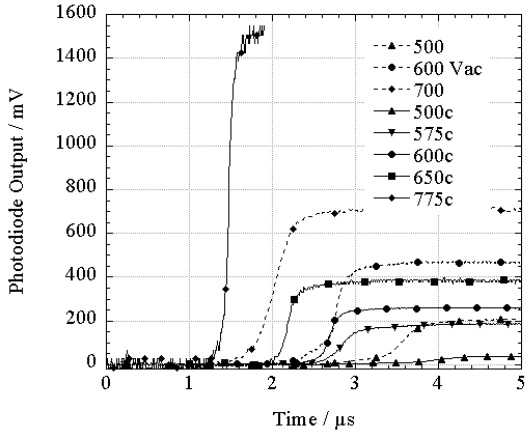

Figure 1.8: Light output of 2 mm ammonium nitrate beds under flyer impact of variable velocity, from Proud et al. (2003). Legend indicates the flyer velocity that gave rise to each trace, in $\mathrm{m\,s^{-1}}$. The suffix "Vac" indicates that the experiment was performed under a rough vacuum of 1 mbar. The suffix "c" indicates that the ammonium nitrate bed also contained 10 % chalk by weight.

its finite heat capacity makes it less effective at preventing reaction.

1.2.7.3 Spectroscopy

Figures 1.9, 1.10 and 1.11 show the spectra recorded during an impact. Their intensities have been normalized: the intensities of their peaks were originally in the ratio 1:55:1000. Figure 1.9 shows peaks consistent with NO. This could be some early partial reaction. The gas thus produced could fill the cavities in the material, allowing adiabatic compression. In figure 1.10, the spectrum is broadening, consistent with the sample warming up. In figure 1.11, the spectrum has become that of a black body at $\sim 6000\,\mathrm{K}$.

1.3 Detonation

A detonation is a reactive shock. The shock causes chemical reaction in the material through which it propagates. This reaction, in turn, sustains the shock wave. Only one-dimensional, steady state detonation is analytically tractable. Detonations normally deviate from this. The front often has some three-dimensional

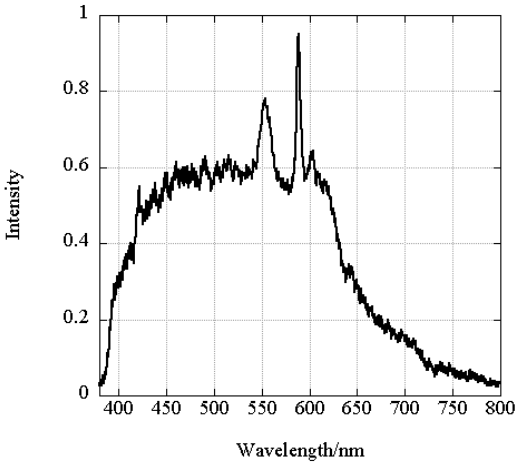

Figure 1.9: Spectrum of 2 mm ammonium nitrate bed under flyer impact, from Proud et al. (2003). Impact velocity not reported. Spectrum was gathered between 60 ns and 560 ns after impact.

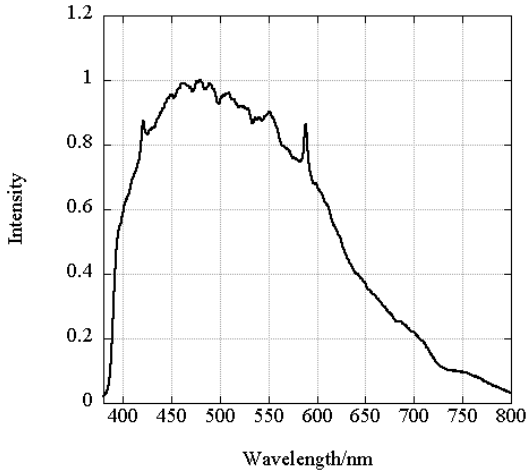

Figure 1.10: Spectrum of 2 mm ammonium nitrate bed under flyer impact, from Proud et al. (2003). Impact velocity not reported. Spectrum was gathered between 1 μs and 1.5 μs.

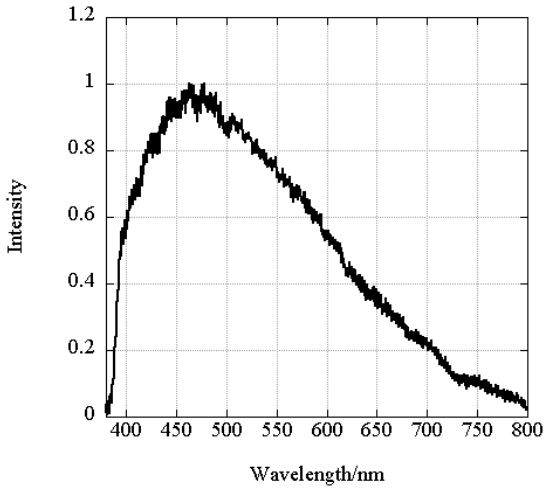

Figure 1.11: Spectrum of 2 mm ammonium nitrate bed under flyer impact, from Proud et al. (2003). Impact velocity not reported. Spectrum was gathered between 2 μs and 2.5 μs.

structure. The test charge is also of finite diameter. This introduces rarefaction waves from the walls of the charge, which modify the process somewhat. Nonetheless, the models are still useful for a qualitative understanding of detonation.

1.3.1 Chapman-Jouguet detonation theory

Chapman-Jouguet (CJ) theory (Ficket and Davis, 1979) was the first analytical treatment of detonation, by two independent workers. It assumes a one-dimensional steady detonation, an instantaneous reaction taking place at the shock front, and that the material the shock front reaches is entirely unreacted. It also assumes mass, momentum and energy are conserved across the shock. Under these assumptions, the behaviour is entirely determined by the material's equation of state and the rear boundary conditions. The latter is treated as a piston following the shock with constant velocity u_p.

1.3.1.1 Conservation relations

Conservation of mass and momentum give the Rayleigh line (Ficket and Davis, 1979). Any single shock is constrained by the relation

$$\frac{D^2}{v_0^2} = \frac{P - P_0}{v_0 - v} \ , \tag{1.7}$$

where D is the speed of the detonation front, P is the pressure after the shock, P_0 is the pressure before the shock, v is the specific volume or reciprocal density after the shock, and v_0 is the specific volume before the shock.

The Rayleigh line is a straight line in P–v co-ordinates. Its gradient is $-\left(\frac{v_0}{D^2}\right)$, which must always be negative.

Conservation of energy gives the Hugoniot curve. To conserve energy the shock must satisfy

$$E_0 - E = \tfrac{1}{2}(P_0 + P)(v - v_0) \ , \tag{1.8}$$

where E is the internal energy in the shocked, reacted material and E_0 is the internal energy in the unshocked material.

In an inert shock, the Rayleigh line is a chord to the Hugoniot. It joins the unshocked conditions to the shocked conditions, and its slope determines the shock speed. In a detonation, the reaction moves the Hugoniot for the reacted material. The Rayleigh line goes from P_0 and v_0 on the unreacted Hugoniot, and touches the reacted Hugoniot at a tangent. The point of contact between the Rayleigh line and the reacted Hugoniot is called the Chapman-Jouguet point. The slope of the Rayleigh line is the Chapman-Jouguet detonation velocity, D_{CJ}. In the frame of reference of a detonation travelling at D_{CJ}, the shocked material retreats from it at the speed of sound in the material.

1.3.1.2 The rear boundary conditions

If $u_p < D_{CJ}$, the detonation will travel at D_{CJ}. It will be followed by a rarefaction fan which takes the particle velocity down to u_p. If $u_p > D_{CJ}$, the detonation is over-driven. All the material behind the detonation will travel at u_p, and the detonation velocity will be increased.

Over-driven detonation is not sustainable without the rear piston. In the

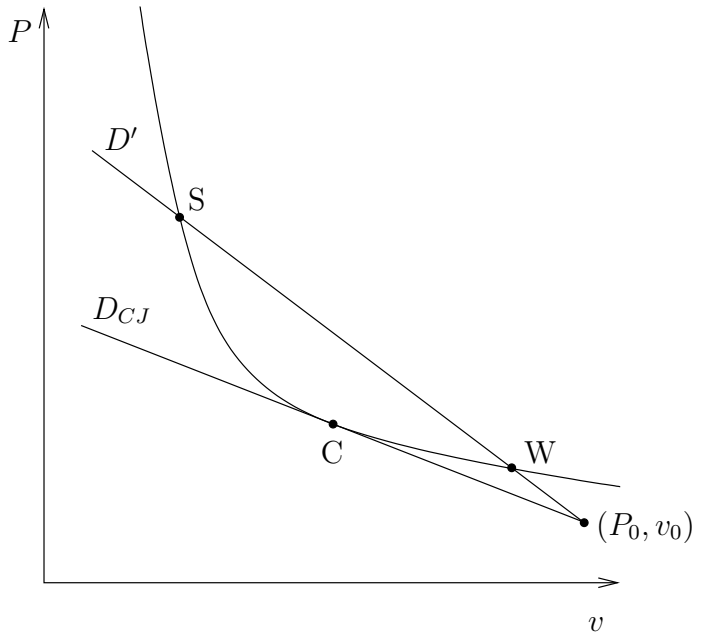

Figure 1.12: Intersection of Rayleigh lines with the reacted Hugoniot. C is the Chapman-Jouguet point. S and W are the strong and weak points, respectively.

frame of an over-driven detonation, the shocked material is receding at less than the sound speed. This means rarefaction waves can catch up with the detonation, and reduce its velocity to D_{CJ}.

As figure 1.12 shows, the Rayleigh line crosses the reacted Hugoniot twice when the detonation is over-driven. The high- and low-pressure points are called the strong and weak points, respectively. An over-driven detonation will assume the state corresponding to the strong point. At the weak point, the shocked material retreats from the detonation faster than the sound speed.

1.3.2 Zeldovich-von Neumann-Döring detonation theory

This is an extension of CJ theory (Ficket and Davis, 1979). It no longer assumes an instantaneous reaction. It does, however, assume that the reaction is a single, irreversible reaction. In Zeldovich-von Neumann-Döring (ZND) theory, the reaction takes place over a reaction zone behind the detonation front. The reaction zone moves with the detonation. The state in which the reaction is completed is equivalent to the CJ point. This means that ZND theory and CJ theory both

predict the same detonation velocities.

The structure of the front is changed from that expected under CJ theory. The products of the explosive reaction are usually more compressible than the initial explosive. As the detonation is now compressing unreacted material, the front now reaches a higher pressure than in CJ theory. This pressure drops over the reaction zone, as more compressible products are formed. The high-pressure region is referred to as a 'von Neumann spike'.

Under ZND theory, the weak point becomes unattainable.

1.3.3 Non-ideal detonation

In the frame of the unshocked material, the shocked material is accelerated by the detonation and moves in the same direction as it, but more slowly. As the material gets further from the shock, it decelerates. In the detonation's frame of reference, the shocked material is moving backwards from it, and gets faster as it becomes more distant. In the reaction zone, this motion is sub-sonic. Energy released in the reaction zone can therefore reach the detonation and reinforce it. At the CJ point, the material moves at the speed of sound; beyond that point, the material's retreat is supersonic. Material beyond the CJ point cannot, therefore, contribute energy to the detonation.

In an ideal detonation, all the energy of the material is liberated before the CJ point. A non-ideal detonation is one in which that is not the case (King and Bauer, 1980; Luebcke, 1995). This could be caused by the slow reaction of the explosive, by large explosive grains, or by rarefaction waves from the walls of the charge.

Some energetic materials (including AN) give off relatively little energy on reaction. This reduces the rate of reaction. Because reaction spreads only slowly through such a material, the density of critical hot spots is very important to its detonation characteristics.

Heat conduction from hot reaction products into grains of explosive is not sufficiently fast that the entire grain will react simultaneously. Instead, the grain burns in layers (Eyring et al., 1949). An explosive composed of larger grains will present less surface area per unit volume for burning. It will, therefore, react

more slowly. This may cause the detonation to become non-ideal.

The rarefaction waves from the walls of a finite charge will, some time after the detonation, reach the reaction zone. The reduction in pressure when they arrive will reduce the reaction rate there. This effect will be more important in smaller charges, as the rarefaction waves have less distance to travel. This can change an ideal detonation to a non-ideal one. It can also prevent detonation altogether. This leads to the concept of a critical diameter for an explosive, below which detonation is impossible.

1.3.4 Detonation of ammonium nitrate

There has been little work on detonation of pure ammonium nitrate. King and Bauer (1980) studied the detonation of prilled and molten ammonium nitrate. They found the critical diameter for prilled ammonium nitrate was about one metre. The detonation characteristics depend on the prill type. The porosity of prills varies between manufacturers (Kwok et al., 2003). This will affect the hot spot density. 11–68 % of the prills failed to react in the reaction zone.

Molten ammonium nitrate forms bubbles from thermal decomposition. Above 220 °C these bubbles sensitize it enough that detonation is possible. The bubbles also reduce the bulk energy density of the material, reducing the detonation velocity.

Hollow glass spheres were used to introduce artificial bubbles to molten ammonium nitrate at 190 °C. Enough spheres were added to reduce the density to that of ammonium nitrate at 260 °C. This ammonium nitrate was found to have very similar detonation characteristics to ammonium nitrate at 260 °C. This suggests that gas cavities were the primary hot spot mechanism in molten ammonium nitrate.

ANFO explosives based on agricultural ammonium nitrate fertilizer are popular terrorist weapons. Considerable effort has therefore been expended on modifying ammonium nitrate fertilizer to render it less effective as a component of ANFO (EC2003; Porter, 1965). The most common approach involves the addition of an inert material, which absorbs energy from hot spots without reacting exothermically. This should reduce the density of critical hot spots, and thereby

render the explosive less sensitive. However, large-scale trials have found that the additives have negligible effect on the performance of ANFO made with adulterated ammonium nitrate (Reza and McCarthy, 1999). This suggests that these additives merely increase the critical diameter, so that the small-scale trials used in testing them fail to detonate.

1.4 Compaction

Compaction is the process by which a porous material loses porosity in response to load. Since several hot spot mechanisms involve the collapse of pores in a material, compaction may be relevant to the study of initiation.

Compaction is used as a manufacturing process for pharmaceuticals, and for metal and ceramic parts. It is also relevant for understanding of soils and some geological processes. It has therefore been widely studied and repeatedly reviewed (Cunningham et al., 2004; Denny, 2002; Kremer and Hancock, 2006; Sinka, 2007).

1.4.1 Experimental studies

The usual way in which compaction is studied is using a triaxial system, as described in Sinka and Cocks (2007) and Pavier and Doremus (1999). This consists of a uniaxial press whose working surfaces are mounted inside a hydrostatic cell. The powder to be studied is placed into an elastic sleeve of negligible strength, and the packaged powder is then placed between the working surfaces of the press. The length and diameter of this package are then monitored as it is subjected to superimposed hydrostatic and axial loads.

While this technique allows a wide range of stress states in the powder to be explored, it is restricted to slow compaction of the powder. The uniaxial press cannot exceed $1\,\mathrm{mm\,s^{-1}}$, while industrial compaction processes may reach $10\,\mathrm{m\,s^{-1}}$. Many experiments therefore use a simple confined piston arrangement (Adams et al., 1994; Doremus et al., 2010). Greenaway (2005) used a modified split Hopkinson pressure bar apparatus to achieve even higher compaction rates. Borg et al. (2005) used plate impact to probe compaction response under shock

loading.

1.4.2 Compaction models

A wide range of models are used in an attempt to understand compaction processes. Given the wide range of materials and phenomena covered by the term "powder compaction", this is unsurprising. For compaction at low porosities, soil models have proven popular (Drucker and Prager, 1952; Schofield and Wroth, 1968). Fleck (1995) modelled the compacting bed as a random array of identical rigid-plastic spheres with some success. However, this model was unable to use a single state variable for the compacting bed: it required the full stress history. Cocks and Sinka (2007) observed that the stress history of the bed was of a simple form, and that plastic work (rather than density, as is usual) could be used as a single state variable for the model.

Two models, though, have proven especially popular. These are the Heckel and Kawakita models, and are covered in more detail.

1.4.2.1 Heckel model

The Heckel model (Heckel, 1961a,b) is based on the differential equation

$$\frac{\mathrm{d}\phi}{\mathrm{d}P} = -\alpha\phi \ , \tag{1.9}$$

where ϕ is the void fraction in the material, P is the applied pressure, and α is a constant. Integrating gives

$$\ln\frac{1}{\phi} = \ln\frac{1}{\phi_0} + \alpha P \ , \tag{1.10}$$

where ϕ_0 is the void fraction of the bed at zero applied pressure. A plot of $\ln\frac{1}{\phi}$ against P is therefore expected to give a straight line of slope α and intercept $\ln\frac{1}{\phi_0}$. However, in most materials this plot shows some curvature at low pressure (Denny, 2002). This is usually interpreted as the material deforming by some means other than plastic deformation. The straight line region of such a graph does not, therefore, agree with the initially observed ϕ_0.

Heckel (1961b) observed that the parameter α could be related to the yield stress σ_0 of the bed material by

$$\alpha = \frac{1}{3\sigma_0} \ . \tag{1.11}$$

However, Sonnergaard (1999) finds this interpretation to be, at best, highly prone to error.

1.4.2.2 Kawakita equation

Kawakita and Lüdde (1970) present the powder-compression relationship

$$e = \frac{V_0 - V}{V_0} = \frac{ABP}{1 + BP} \ , \tag{1.12}$$

where V_0 is the initial volume of the powder, V is its volume at applied pressure P, and A and B are constants. For a uniaxial confined experiment, e is the engineering strain $\frac{\Delta l}{l}$ of the sample. Equation 1.12 may be rearranged to give

$$\frac{P}{e} = \frac{1}{AB} + \frac{P}{A} \ . \tag{1.13}$$

$\frac{P}{e}$ may then be plotted against P to give a straight line of slope A^{-1} and intercept $(AB)^{-1}$, in a fashion very similar to that of the Heckel equation. In confined uniaxial compaction work on powder agglomerates, B^{-1} has been found to be proportional to the failure stress of the agglomerated particles (Adams and McKeown, 1996; Adams et al., 1994). The constant of proportionality was found to be very close to unity when friction within the testing apparatus was taken into account.

References

Candidate 8210X. Hot spot ignition of granular ammonium nitrate through high velocity impact. Part III project report, University of Cambridge, 2003.

D. M. Adams and S. K. Sharma. Spectroscopy at very high pressure, part 8: an infrared study of shear-stress-induced transitions in ammonium and sodium nitrates. *Journal of the Chemical Society, Faraday Transactions 2*, 72:2069–2074, 1976.

M. J. Adams and R. McKeown. Micromechanical analyses of the pressure-volume relationships for powders under confined uniaxial compression. *Powder Technology*, 88:155–163, 1996.

M. J. Adams, M. A. Mullier, and J. P. K. Seville. Agglomerate strength measurement using a uniaxial confined compression test. *Powder Technology*, 78: 5–13, 1994.

M. Ahtee, K. Kurki-Suonio, B. W. Lucas, and A. W. Hewat. Determination of molecular orientations in cubic ND_4NO_3. *Acta Crystallographica A*, 35:591–597, 1979.

M. Ahtee, K. J. Smolander, B. W. Lucas, and A. W. Hewat. The structure of the low-temperature phase V of ammonium nitrate, ND_4NO_3. *Acta Crystallographica C*, 39(6):651–655, 1983a.

M. Ahtee, K. J. Smolander, B. W. Lucas, and A. W. Hewat. Low-temperature behaviour of ammonium nitrate by neutron diffraction. *Acta Crystallographica B*, 39:685–687, 1983b.

J. K. A. Amuzu, B. J. Briscoe, and M. M. Chaudhri. Frictional properties of explosives. *Journal of Physics D*, 9:133–143, 1976.

J. H. Blackburn and L. B. Seely. Detonation light in granular explosives. *Transactions of the Faraday Society*, 61:537–545, 1965.

J. P. Borg, D. J. Chapman, K. Tsembelis, W. G. Proud, and J. R. Cogar. Dynamic compaction of porous silica powder. *Journal of Applied Physics*, 98: 073509, 2005.

N. K. Bourne and J. E Field. Bubble collapse and the initiation of explosion. *Proceedings of the Royal Society of London, Series A*, 435:423–435, 1991.

REFERENCES

N. K. Bourne and A. M. Milne. The temperature of a shock-collapsed cavity. *Proceedings of the Royal Society of London, Series A*, 459:1851–1861, 2003.

F. P. Bowden and O. A. Gurton. Initiation of explosions by grit particles. *Nature*, 162:654–655, 1948. doi: 10.1038/162654a0.

F. P. Bowden and O. A. Gurton. Initiation of solid explosives by impact and friction: the influence of grit. *Proceedings of the Royal Society of London, Series A*, 198(1054):337–349, 1949.

F. P. Bowden and A. D. Yoffe. *Initiation and Growth of Explosions in Liquids and Solids*. Cambridge University Press, Cambridge, 1952.

T. B. Brill, P. J. Brush, and D. G. Patil. Thermal decomposition of energetic materials 58. Chemistry of ammonium nitrate and ammonium dinitramides near the burning surface temperature. *Combustion and Flame*, 92:178–186, 1993.

R. N. Brown and A. C. McLaren. On the mechanism of the thermal transformations in solid ammonium nitrate. *Proceedings of the Royal Society of London, Series A*, 266:329–343, 1962.

M. M. Chaudhri. Stab initiation of explosions. *Nature*, 263:121–122, 1976.

M. M. Chaudhri. The initiation of fast decomposition in solid explosives by fracture, plastic flow, friction, and collapsing voids. In *Proceedings of the Ninth International Symposium on Detonation*, OCNR 113291-7, pages 857–867, 1989.

M. M. Chaudhri and J. E. Field. The role of rapidly compressed gas pockets in the initiation of condensed explosives. *Proceedings of the Royal Society of London, Series A*, 340(1620):113–128, 1974.

C. S. Choi and H. J. Prask. The structure of ND_4NO_3 phase V by neutron powder diffraction. *Acta Crystallographica B*, B39:414–420, 1983.

C. S. Choi, J. E. Mapes, and E. Prince. The structure of ammonium nitrate (IV). *Acta Crystallographica B*, 28:1357–1361, 1972.

C. S. Choi, H. J. Prask, and E. Prince. Phase transitions in ammonium nitrate. *Journal of Applied Crystallography*, 13:403–409, 1980.

A. C. F. Cocks and I. C. Sinka. Constitutive modelling of powder compaction – I. Theoretical concepts. *Mechanics of Materials*, 39:392–403, 2007.

C. S. Coffey. The localization of energy and plastic deformation in crystalline solids during shock or impact. *Journal of Applied Physics*, 70(8):4248–4254, 1991.

J. C. Cunningham, I. C. Sinka, and A. Zavaliangos. Analysis of tablet compaction. I. Characterization of mechanical behavior of powder and powder/tooling friction. *Journal of Pharmaceutical Sciences*, 93:2022–2039, 2004.

R. J. Davey, A. J. Ruddick, P. D. Guy, B. Mitchell, S. J. Maginn, and L. A. Polywka. The IV–III polymorphic phase transition in ammonium nitrate: a unique example of solvent mediattion. *Journal of Physics D*, 24:176–185, 1991.

P. J. Denny. Compaction equations: a comparison of the Heckel and Kawakita equations. *Powder Technology*, 127:162–172, 2002.

D. D. Dlott and M. D. Fayer. Shocked molecular solids: Vibrational up pumping, defect hot spot formation, and the onset of chemistry. *Journal of Chemical Physics*, 92:3798–3612, 1990.

P. Doremus, Y. le Guennec, D. Imbault, and G. Puente. High-velocity compaction and conventional compaction of metallic powders; comparison of process parameters and green compact properties. *Proceedings of the Institution of Mechanical Engineers, Part E: Journal of Process Mechanical Engineering*, 224: 177–184, 2010.

K. M. Doxsee and P. E. Francis, Jr. Crystallization of ammonium nitrate from nonaqueous solvents. *Industrial and Engineering Chemistry Research*, 39:3493–3498, 2000.

D. C. Drucker and W. Prager. Soil mechanics and plastic analysis or limit design. *Quarterly of Applied Mathematics*, 10:157–175, 1952.

REFERENCES

EC2003. Regulation (EC) No. 2003/2003 of the European Parliament and of the Council, 13 October 2003.

H. Eyring, R. E. Powell, G. E. Duffey, and R. B. Parlin. The stability of detonation. *Chemical Reviews*, 45:69, 1949.

W. Ficket and W. C. Davis. *Detonation*. University of California Press, Berkeley, 1979.

J. E. Field. Experimental studies of bubble collapse. In J. R. Blake et al., editors, *Bubble Dynamics and Interface Phenomena*, pages 17–31. Kluwer Academic Publishers, 1994.

N. A. Fleck. On the cold compaction of powders. *Journal of the Mechanics and Physics of Solids*, 43:1409–1431, 1995.

P. G. Fox and J. Soria-Ruiz. Fracture-induced thermal decomposition in brittle crystalline solids. *Proceedings of the Royal Society of London, Series A*, 317 (1528):79–90, 1970.

L. Friedman and J. Bigeleisen. Oxygen and nitrogen isotope effects in the decomposition of ammonium nitrate. *Journal of Chemical Physics*, 18(10):1325–1331, 1950.

T. H. Goodwin and J. Whetstone. The crystal structure of ammonium nitrate III, and atomic scattering factors in ionic crystals. *Journal of the Chemical Society*, pages 1455–1461, 1947.

M. W. Greenaway. Measurement of intergranular stress and porosity during dynamic compaction of porous beds of cyclotetramethylene tetranitramine. *Journal of Applied Physics*, 97:093521, 2005.

T. Hatano. Spatiotemporal behavior of void collapse in shocked solids. *Physical Review Letters*, 92(1):015503, 2004.

R. W. Heckel. Density-pressure relationships in powder compaction. *Transactions of the Metallurgical Society of AIME*, 221:671–675, 1961a.

R. W. Heckel. An analysis of powder compaction phenomena. *Transactions of the Metallurgical Society of AIME*, 221:1001–1008, 1961b.

T. K. Highsmith, C. J. Hinshaw, and R. B. Wardle. Phase-stabilized ammonium nitrate and method of making same. US Patent No. 5,292,387, 1994.

B. L. Holian, T. C. Germann, J.-B. Maillet, and C. T. White. Atomistic mechanism for hot spot initiation. *Physical Review Letters*, 89(28):285501, 2002. Erratum: Holian et al. (2003).

B. L. Holian, T. C. Germann, J.-B. Maillet, and C. T. White. Erratum: Atomistic mechanism for hot spot initiation (Holian et al., 2002). *Physical Review Letters*, 90(6):069902(E), 2003.

W. Holmes, R. S. Francis, and M. D. Fayer. Crack propagation induced heating in crystalline energetic materials. *Journal of Chemical Physics*, 110(7):3576–3583, 1999.

J. S. Ingman, G. J. Kearley, and S. F. A. Kettle. Optical and thermal studies of transitions between phases II, III and IV of ammonium nitrate. *Journal of the Chemical Society – Faraday Transactions 1*, 78:1817–1826, 1982.

K. Kawakita and K.-H. Lüdde. Some considerations on powder compression equations. *Powder Technology*, 4:61–68, 1970.

B. A. Khasainov, A. A. Borisov, B. S. Ermolaev, and A. I. Korotkov. Two phase visco-plastic model of shock initiation of detonation in high density press explosives. In J. M. Short, editor, *Proceedings of the Seventh International Symposium on Detonation*, NSWC MP 82-334, pages 435–447, Naval Surface Weapons Center, White Oak, Silver Spring, MD, 1981.

A. W. King and A. Bauer. Shock initiation characteristics of ammonium nitrate. Summary report, Department of Mining Engineering, Queen's University, Kingston, Ontario, May 1980.

O. G. Kjaergaard. Prilling – multiple core encapsulation. http://www.niroinc.com/html/chemical/cprilling.html, 2000.

REFERENCES

D. M. Kremer and B. C. Hancock. Process simulation in the pharmaceutical industry: a review of some basic physical models. *Journal of Pharmaceutical Sciences*, 95:517–529, 2006.

Q. S. M. Kwok, D. E. G. Jones, and P. Kruus. Investigation of the wettability of ammonium nitrate prills. In J. Vágenknecht, editor, *Proceedings of the sixth seminar on new trends in research of energetic materials*, pages 183–197, Pardubice, Czech Republic, 2003. University of Pardubice.

B. W. Lucas, M. Ahtee, and A. W. Hewat. The crystal structure of phase II ammonium nitrate. *Acta Crystallographica B*, 35:1038–1041, 1979.

B. W. Lucas, M. Ahtee, and A. W. Hewat. The structure of phase III ammonium nitrate. *Acta Crystallographica B*, 36:2005–2008, 1980.

P. E. Luebcke. *The deflagration-to-detonation transition in granular secondary explosives*. PhD thesis, University of Cambridge, 1995.

K. L. McNesby and C. S. Coffey. Spectroscopic determination of impact sensitivities of explosives. *Journal of Physical Chemistry*, 101:3097–3104, 1997.

I. B. Mishra. Potassium fluoride stabilized ammonium nitrate. US Patent No. 4,552,736, 1985.

C. Oommen and S. R. Jain. Ammonium nitrate: a promising rocket propellant oxidizer. *Journal of Hazardous Materials A*, 67:253–281, 1999.

E. Pavier and P. Doremus. Triaxial characterisation of iron powder behaviour. *Powder Metallurgy*, 42(4):345–352, 1999.

S. J. Porter. Method of desensitizing fertilizer grade ammonium nitrate and the product obtained. US Patent 3,366,468, 1965.

W. G. Proud. The measurement of hot-spots in granulated ammonium nitrate. In M. D. Furnish, N. N. Thadhani, and Y. Horie, editors, *Shock Compression of Condensed Matter – 2001*, volume 620 of *AIP Conference Proceedings*, pages 1081–1084, Atlanta, Georgia, June 2002. American Physical Society.

W. G. Proud, E. J. W. Crossland, and J. E. Field. High-speed photography and spectroscopy in determining the nature, number and evolution of hot-spots in energetic materials. In C. Cavailler, G. P. Haddleton, and M. Hugenschmidt, editors, *25th International Congress on High-Speed Photography and Photonics*, volume 4948 of *SPIE*, pages 510–518, Physics and Chemistry of Solids Group, Cavendish Laboratory, University of Cambridge, 2003. SPIE.

E. Rapoport and C. W. F. T. Pistorius. Polymorphism and melting of ammonium, thallous, and silver nitrates to 45 kbar. *Journal of Chemical Physics*, 44: 1514–1519, 1966.

A. Reza and R. L. McCarthy. Measurements to determine the effect of selected additives on the detonability of ANFO mixtures. In *Proceedings of the twenty-fifth annual conference on explosives and blasting technique*, pages 249–261, Nashville, Tennessee USA, February 1999. International Society of Explosives Engineers, International Society of Explosives Engineers, 29100 Aurora Road, Cleveland, Ohio, USA, 44139-1800.

H. L. Saunders. The decomposition of ammonium nitrate by heat. *Journal of the Chemical Society*, 121:698–711, 1922. doi: 10.1039/CT9222100698.

A. N. Schofield and C. P. Wroth. *Critical State Solid Mechanics*. McGraw-Hill, New York, 1968.

J. Sharma, J. W. Forbes, C. S. Coffey, and T. P. Liffiard. The physical and chemical nature of sensitization centres left from hot spots caused in triaminotrinitrobenzene by shock or impact. *Journal of Physical Chemistry*, 91:5139–5144, 1987.

Y. Shinnaka. On the metastable transition and the crystal structure of ammonium nitrate (tetragonal modification). *Journal of the Physical Society of Japan*, 11:393–396, 1956.

Y. Shinnaka. X-ray study on the molecular rotation in cubic ammonium nitrate. *Journal of the Physical Society of Japan*, 14(8):1073–1083, 1959.

I. C. Sinka. Modelling powder compaction. *KONA*, 25:4–22, 2007.

REFERENCES

I. C. Sinka and A. C. F. Cocks. Constitutive modelling of powder compaction – II. Evaluation of material data. *Mechanics of Materials*, 39:404–416, 2007.

J. M. Sonnergaard. A critical evaluation of the Heckel equation. *International Journal of Pharmaceutics*, 193:63–71, 1999.

A. Tokmakoff, M. D. Fayer, and Dana D. Dlott. Chemical reaction initiation and hot-spot formation in shocked energetic molecular materials. *Journal of Physical Chemistry*, 97(9):1901 – 1913, 1993.

S. I. Volfkovich, S. M. Rubinchik, and V. M. Kozhin. *Bulletin of the Academy of Sciences of the USSR, Division of Chemical Science*, 209:167–174, 1954.

S. Vyazovkin, J. S. Clawson, and C. A. Wight. Thermal dissociation kinetics of solid and liquid ammonium nitrate. *Chemistry of Materials*, 13:960–966, 2001.

R. E. Winter and J. E. Field. The role of localized plastic flow in the impact initiation of explosives. *Proceedings of the Royal Society of London, Series A*, 343:399–413, 1975.

Chapter 2

Experimental techniques

This chapter provides a description of the established experimental techniques used in this research. It also details the capabilities of the equipment used. All this information is available from other sources. However, collecting this information was not trivial, and therefore it is provided here for convenience.

2.1 Environmental scanning electron microscopy

Environmental scanning electron microscopy (ESEM) is a technique for examining the surface of a material at a resolution of up to a few nanometres, at up to atmospheric pressure. Its chief advantages over conventional scanning electron microscopy are that it can image uncoated, insulating specimens, and that it does not require the specimen to be held in a vacuum (Danilatos, 1988). This research used an FEG XL30 microscope, manufactured by FEI.

In ESEM, an electron beam is generated using an electron gun, typically of either tungsten filament or field-emission design with an accelerating voltage in the tens of kilovolts. This beam is then focused using magnetic lenses to generate a small spot on the sample. The size of this spot will limit the resolution of the microscope. This spot is deflected by electric fields to scan it across the sample in a controlled fashion.

The high electric fields involved in these processes require that these stages be performed in a high vacuum. To achieve this, while allowing the sample chamber

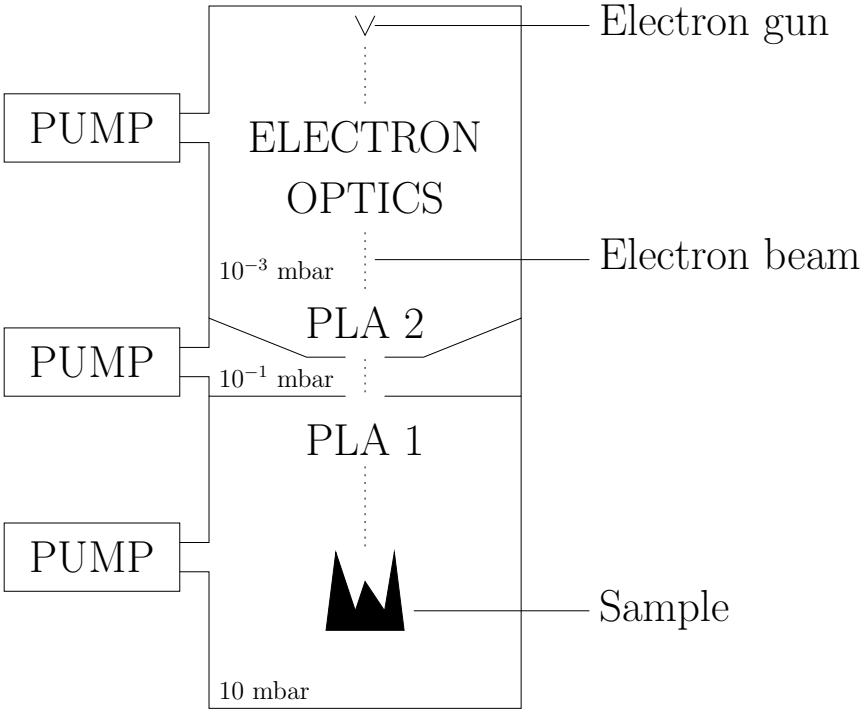

Figure 2.1: Diagram of an ESEM. "PLA" indicates a pressure-limiting aperture. Pressures given are typical pressures in each section of the ESEM. Not to scale.

to be held at a much higher pressure, the beam passes through a series of pressure-limiting apertures. These are essentially small holes, which restrict the rate of gas flow through them but provide no obstacle to the electron beam. Each pressure-reducing stage is connected to a separate vacuum pump, and consequently the pressure is reduced dramatically over a few such stages. See figure 2.1 for a simple arrangement involving two pressure-limiting apertures.

When an electron from the beam interacts with an atom in the sample, it excites an electron, causing it to be ejected from the atom. These secondary electrons form the basis for imaging in ESEM. Secondary electrons which are captured by other atoms within the sample will not be detected, and the probability that they will be captured before escaping the sample depends strongly on the distance they must travel. As the electron beam penetrates some finite distance into the sample before provoking secondary electron emission, this distance, and hence the intensity of the secondary-electron signal recorded, will depend on

the angle between the sample surface and the beam. Surfaces normal to the beam will produce the weakest signal, while those at a sharp angle to it will produce a stronger signal.

Typically the secondary electron signal from a given point on the sample is displayed as a single greyscale pixel, with higher signals assigned paler shades of grey. An image is built up by scanning the electron beam across the sample, and the eye usefully interprets this as an image of the sample surface.

2.1.1 Secondary electron detection

Secondary electrons are detected using avalanche multiplication (Danilatos, 1990). An electric field is set up in the sample chamber, with the sample at the cathode. Secondary electrons escaping from the sample are accelerated by the field until they have sufficient energy that, on interaction with an atom in the gas, they ionize it. This releases another electron which undergoes the same process, amplifying the current due to the electrons emitted by the sample. This current is recorded, and forms the secondary electron signal. Effectively the secondary electrons from the sample cause a Townsend discharge between the sample and the detector.

The ionized gas thus formed also neutralizes any build-up of charge on the sample, eliminating the need to give a conductive coating to insulating samples as in vacuum SEM.

2.1.2 Beam damage

The beam of high-energy electrons used in ESEM can induce chemical reactions or decomposition of the material under the beam. This problem is particularly pronounced when studying energetic materials, as they are of necessity chemically unstable.

2.2 Energy-dispersive X-ray spectroscopy

Energy-dispersive X-ray spectroscopy (EDX) is a technique for determining the distribution of elements on the surface of a sample. It has a spatial resolution

of approximately 1 μm, and used correctly can determine the constituents of an unknown organic sample with an absolute error of 5–10 %. The accuracy improves to 1 % for samples containing heavier elements. The FEG XL30 microscope used for ESEM has an EDX system. This system was used in this research.

In EDX, an electron beam is scanned over the sample. The electrons in this beam provoke secondary electron emission from the atoms in the sample. This emission leaves the resulting ion in an excited state, with a vacancy in a low-energy electron orbital. This can be resolved by an electron in a higher-energy orbital undergoing a transition into this vacancy, emitting an X-ray photon in the process. The photon can then be detected and its energy recorded. The secondary electrons can also be detected, as in ESEM, and EDX and ESEM are commonly combined to produce composite images.

The X-rays detected are typically from $2p \rightarrow 1s$ and $3p \rightarrow 1s$ transitions, often referred to as Kα and Kβ respectively. The energies of these transitions are largely independent of the chemical environment of the atom, but vary considerably between atoms of different elements. The energies of the X-ray photons detected when the electron beam is over a particular point in the sample therefore indicate which elements are present at that point. These X-rays travel through the sample more easily than the secondary electrons used for SEM and ESEM imaging. This limits the resolution of EDX to the size of the volume in which electrons from the probe beam interact with the sample. This volume is called the interaction volume, and can be decreased by using a lower-energy electron beam or a thin foil sample, if increased resolution is required.

2.2.1 X-ray detection

The X-rays are generally detected using a section of intrinsic semiconductor under an electric field. The passage of the X-ray photon produces electron-hole pairs in the semiconductor. The presence of these charge carriers allows a current to flow through the semiconductor, and this current is detected. Each electron-hole pair requires a well-known energy to produce, and the X-ray photon is assumed to dissipate all its energy in the production of such pairs. The detected charge pulse then indicates the energy of the photon.

While this process is similar to that of ionization in a gas, the energy required to create an electron-hole pair is roughly an order of magnitude smaller than the energy required to create an electron-ion pair. This means that more charge carriers are produced by a single photon in a semiconductor, and consequently the energy resolution is improved. Modern semiconductor detectors typically have an energy resolution of about 130 eV. This resolution is due in roughly equal parts to statistical uncertainty in the energy of the charge-carrier pairs and to thermal noise in the processing electronics.

The detector inevitably has a "dead region" some 100–200 nm thick in which the electric field is zero, facing the sample. The lack of electric field means that X-rays absorbed in this region will not be detected. The detector is also covered by a 10–20 nm thick gold electrode. This natural window absorbs all X-rays produced by elements with atomic number $Z < 5$, so boron is the lightest element which can be detected by EDX.

In addition to this natural window, the detector is usually covered by an opaque window. This prevents light within the sample chamber saturating the detector, and protects the detector from dirt and gases in the sample chamber. It also allows the detector to be removed without breaking the sample chamber's vacuum. These were historically made of 7.6 μm thick beryllium, which absorbed all X-rays produced by elements lighter than fluorine. Modern windows consist of a nickel or silicon grid, the gaps in which are filled by a thin layer of some carefully chosen material. They have sufficient strength to withstand a 1 atm pressure difference, are opaque to light, and do not prevent detection of any elements not already blocked by the natural window of the detector. Knoll (1989) and Goldstein et al. (2003) contain more information.

2.3 X-ray microtomography

X-ray microtomography is a non-destructive technique for studying planes in the interior of a sample. It has a minimum spatial resolution of approximately 1 μm. A Skyscan 1072 microtomograph was used for this research.

Multiple views of the X-ray absorption of the sample at different angles θ are taken, as shown in figure 2.2. These are then combined to produce a two-

dimensional image of the sample in the plane perpendicular to the axis of rotation, using a filtered back-projection algorithm (Kak and Slaney, 1988). This computationally expensive process is referred to as reconstruction.

In practice, most X-ray sources are small points, from which X-rays radiate. The back-projection algorithm can be modified to allow reconstruction with diverging X-ray beams. The technique can be further modified to allow reconstruction of the full 3D structure of a sample, in which the X-ray absorption of the sample at each angle θ is measured by a 2D sensor array. This technique is referred to as cone-beam reconstruction (Feldkamp et al., 1984; Kak and Slaney, 1988), and is used in the Skyscan 1072.

Three factors limit the resolution of X-ray microtomography. The first is the resolution of the detector. This limits the density with which $P_\theta(k)$ is sampled, and hence the resolution of the reconstruction. The second, closely related, is the size of the sample. Because X-ray absorption across the entire sample must be measured, the resolution with which a tomographic slice of a sample of maximum diameter d can be reconstructed using a detector with N_d elements cannot exceed $\frac{d}{N_d}$. The third factor affecting resolution of the technique is the finite size of the X-ray source. Penumbral broadening, as illustrated in figure 2.3, will blur $P_\theta(k)$, and hence the reconstruction.

2.4 Screw-driven instrumented press

A screw-driven instrumented press is a tool for applying a uniaxial force to a sample, at a known strain rate. The strain rate can vary from $10^{-7}\,\mathrm{s}^{-1}$ to $1\,\mathrm{s}^{-1}$. Screw driven instrumented presses applying a maximum force of around $10^6\,\mathrm{N}$ are commercially available. This research used an Instron 4466 press, capable of applying a maximum force of $10^4\,\mathrm{N}$. Figure 2.4 shows such a press schematically. The cross-head rests on the thread of the screws. Motors in the base of the apparatus turn the screws and thereby move the cross-head up or down. Since the pitch of the screws is known, the rotation of the motors gives the position of the cross-head. A load cell is mounted on the cross-head, and the sample is attached to that.

In practice, the forces applied cause some elastic deformation of the cross-

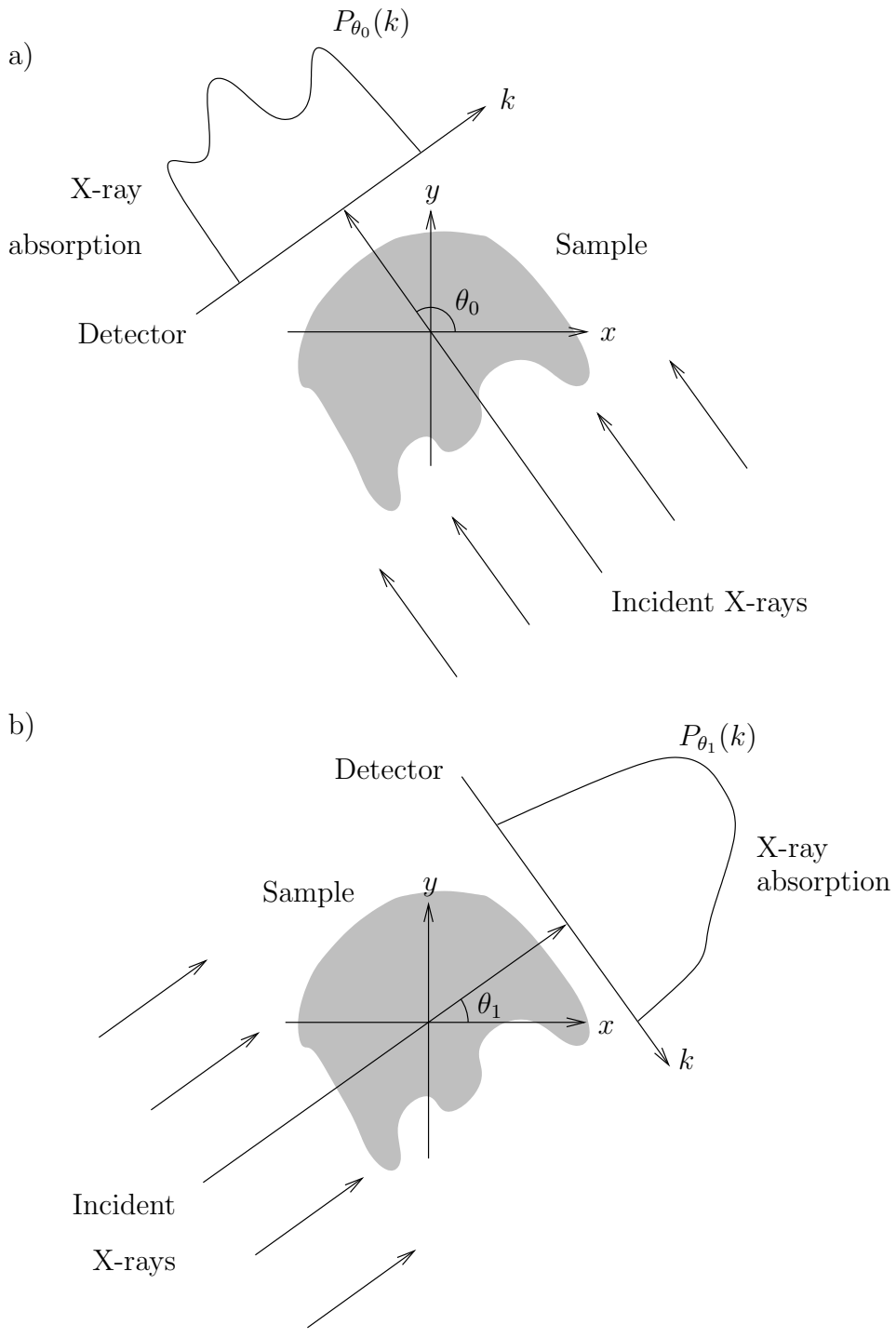

Figure 2.2: Schematic showing X-ray tomography measurements. $P_\theta(k)$ is measured for N_m angles θ between 0° and 180°. In practice N_m is usually in the hundreds and θ is evenly distributed, so $P_\theta(k)$ is measured every few tenths of a degree.

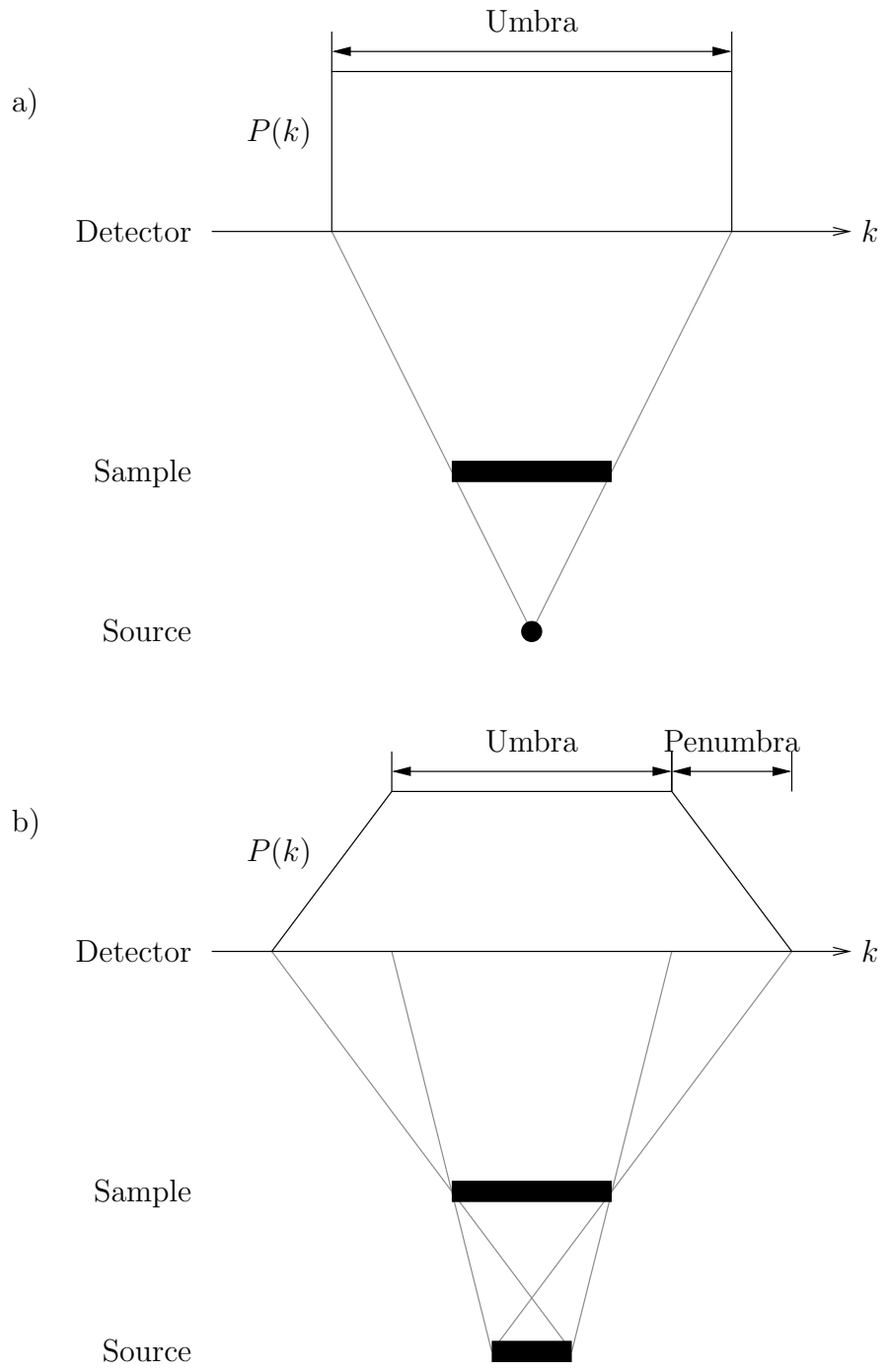

Figure 2.3: Penumbral broadening. (a) With a point source of X-rays, the edges of the sample recorded at the detector are perfectly sharp. (b) With a source of finite size, a penumbral region exists in which the sample only partially obscures the source.

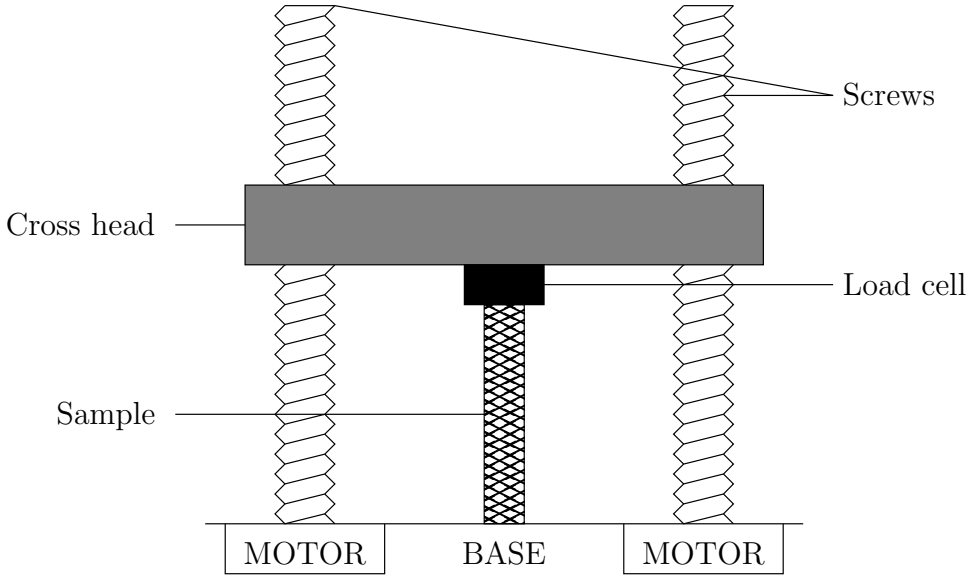

Figure 2.4: Schematic of a screw-driven instrumented press, such as the Instron 4466 used in this research. The motors turn the screws to move the cross head. This in turn deforms the sample. The load cell records the force applied to the sample during this process. Not to scale.

head, drive screws and load cell. It is therefore necessary to measure the reported motion, as a function of measured force, in the absence of any sample. This motion is called the compliance of the system. The compliance can then be subtracted from the reported motion in the presence of a sample to recover the actual sample deformation.

2.4.1 Backlash

Another potential issue with this class of apparatus is that of backlash. There must be some empty space between the threads of screws to allow motion. If the direction of motion is reversed, this free space is rearranged. In the case of this apparatus, this results in uncertainty as to the position of the cross-head. As several useful experiments require the direction of motion of the cross-head to be reversed (for example, any cyclical loading experiment), most instrumented presses take steps to eliminate backlash.

Backlash is usually eliminated by preloading. The cross-head contacts each

drive screw in two locations. These positions are held apart by a spring, applying a force greater than any the drive screws are expected to exert on the cross head. With this arrangement there is sufficient free space for the screws to function, but this space will not be rearranged when the direction of motion of the cross-head is reversed. The drawback to this approach is that the contact forces between the cross-head and the drive screw are considerably increased. This increases the friction between the drive screws and the cross head, and hence reduces the efficiency of the motors in moving the cross-head. To ameliorate this problem, a highly efficient screw design, such as the ball screw, is used for the drive screws.

2.5 Load cell

A load cell, also known as a force transducer, is a device for measuring force along an axis. The most common design is a Wheatstone bridge strain gauge load cell. This design is incorporated into the drop weight and Instron 4466 used in this research. The SHPB uses a much simpler load cell design discussed in section 2.7.

The principle underlying the strain gauge load cell is that a stressed material will deform. A cylindrical block of some material, chosen to remain elastic at the forces the load cell will measure, is instrumented with uniaxial resistive strain gauges as shown in figure 2.5. These gauges act as resistors, with a resistance $R = R_0(1 + G\varepsilon)$, where ε is the strain along the gauge axis and R_0 and G are properties of the gauge. They are arranged in a Wheatstone bridge (Horowitz and Hill, 1989), as shown in figure 2.6.

The variable resistor R_v is set so that the output voltage V_o is zero when the applied force is zero. This is referred to as balancing the bridge. The strain gauges are typically manufactured to identical specifications with very tight tolerances, so that R_v is very small. It is henceforth ignored, and the four strain gauges assumed to have identical values of R_0 and G.

When the load cell is subjected to a force, it will deform. The axial strain gauges A_1 and A_2 will record a different strain to the circumferential gauges P_1 and P_2. We assume the load cell does not bend. Then, if the strain recorded by the axial gauges is ε, that recorded by the circumferential gauges will be $-\nu\varepsilon$. ν is Poisson's ratio for the material of which the load cell is made.

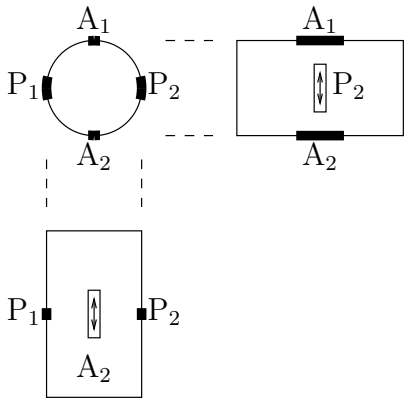

Figure 2.5: Arrangement of strain gauges on a Wheatstone bridge load cell. Not to scale. The gauges are only sensitive to strain along the indicated axes. Labels are as used in figure 2.6 and equation 2.1.

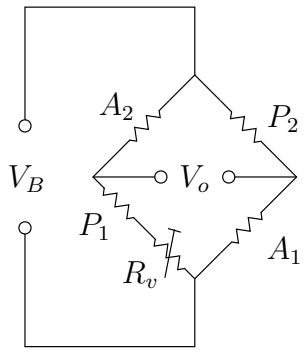

Figure 2.6: Circuit diagram of strain gauges in a Wheatstone bridge load cell. Labels are as used in figure 2.5 and equation 2.1.

This difference will unbalance the bridge, resulting in a non-zero output voltage which is amplified and recorded. The output of an unbalanced Wheatstone bridge is

$$V_o = V_B \left(\frac{P_2}{P_2 + A_1} - \frac{A_2}{A_2 + P_1} \right). \tag{2.1}$$

Substituting in the resistance of the gauges, this gives

$$V_o = -V_B \left(\frac{G\varepsilon(1+\nu)}{2R_0 + G\varepsilon(1-\nu)} \right). \tag{2.2}$$

Using binomial expansion to convert this to a linear form gives

$$V_o \approx -\frac{V_B G(1+\nu)}{2}\varepsilon \pm \frac{G^2(1-\nu^2)}{4}\varepsilon^2. \tag{2.3}$$

The load cell material and strain gauges are usually chosen so that the error due to assuming $V_o \propto \varepsilon$ is very small. For example, in the drop weight load cell the fractional error from this source is approximately 10^{-5}. As the load cell material is elastic, the force applied to the cell is proportional to the strain. Hence, to good approximation, the output voltage is proportional to the force on the cell. A load cell is typically calibrated by applying a known force and recording the output, rather than by calculation from the material and gauge properties.

2.5.1 Bending of the load cell

The gauges are mounted in pairs to reduce the extent to which flexing of the load cell will affect the output voltage. If the load cell bends such that one gauge is in compression, the opposite gauge will be in tension. Assuming that the load cell is initially balanced, and it flexes so that gauge A_1 experiences a small strain ε, gauge A_2 will experience the strain $-\varepsilon$. From equation 2.1, the output of the bridge will be

$$V_o = V_B \left(\frac{R_0}{R_0 + R_0(1+G\varepsilon)} - \frac{R_0(1-G\varepsilon)}{R_0(1-G\varepsilon) + R_0} \right). \tag{2.4}$$

This simplifies to

$$V_o = \frac{V_B G^2}{4 - G^2\varepsilon^2}\varepsilon^2. \tag{2.5}$$

As we have already assumed that ε is small, this gives $V_o \propto \varepsilon^2$, which will be very small.

2.6 Drop Weight

The drop weight is a tool for applying uniaxial stress to a sample, at a strain rate of order $10^3\,\mathrm{s}^{-1}$. The stress that can be applied is limited by the materials of which the sample-facing surfaces are constructed. Typically the maximum stress is a few gigapascals. The advantages of a drop weight system over an SHPB are the high maximum strain to which the sample can be taken, the robustness of the system, and the relative ease of imaging through the sample.

As its name suggests, the central feature of a drop weight is a weight that falls on the sample, crushing it. The weight typically weighs a few kilograms and runs on rails to prevent off-axis motion of the weight and ensure a planar impact. The sample rests on top of an anvil, which remains elastic throughout the experiment. The impact velocity of the weight is commonly measured using a light gate system. The anvil often rests on top of a load cell, to measure the force applied to the sample. If the sample is not expected to be approximately in mechanical equilibrium during the experiment, an accelerometer may be added to the weight.

2.6.1 Sensitivity of explosives

Drop weights are routinely used to measure the sensitivity of explosives. The standard approach is to test multiple samples of the explosive of interest to find the drop height which has a 50 % probability of causing explosion (AMCP 706-180). However, not all of the potential energy of the weight will be transferred to the explosive sample: some will be stored as elastic deformation of the weight. The fraction of the weight's energy transferred to the explosive at the moment of ignition will depend on several factors, including the construction of the drop

weight. The drop weight used for sensitivity testing must therefore be standardized. Refinements have been suggested (Coffey and DeVost, 1995) to eliminate some of the factors affecting energy deposition in the explosive sample.

2.6.2 The Cavendish drop weight

Figure 2.7 shows the usual arrangement of the Cavendish drop weight. In this configuration, two maraging steel anvils and a load cell are restricted to vertical movement by a cylindrical anvil guide. The sample is placed between the anvils, and the weight falls on the upper anvil. The attraction of this approach is that the sample is guaranteed to experience uniaxial stress. In order to allow the weight to move freely, the carriage guides are not pressed tightly against the guide rails. The weight can therefore tip slightly during impact. Were the impact plate to strike the sample directly, this tipping would result in off-axis forces being applied to the sample. The upper anvil and anvil guide practically eliminate these forces.

2.6.3 Materials testing

In this configuration, the drop weight is conventionally used to find the stress-strain response of a material at a particular strain rate. The sample is usually a cylinder with height and diameter both of a few millimetres, and is assumed to have its top and bottom faces in mechanical equilibrium. Given this assumption, and the combined mass m of the weight and top anvil, the acceleration of the weight can be recovered from the force recorded by the load cell:

$$a = \frac{F}{m} \ . \tag{2.6}$$

If the velocity of the weight at impact is measured, its position, and hence the length of the sample, can be recovered by numerically integrating the force

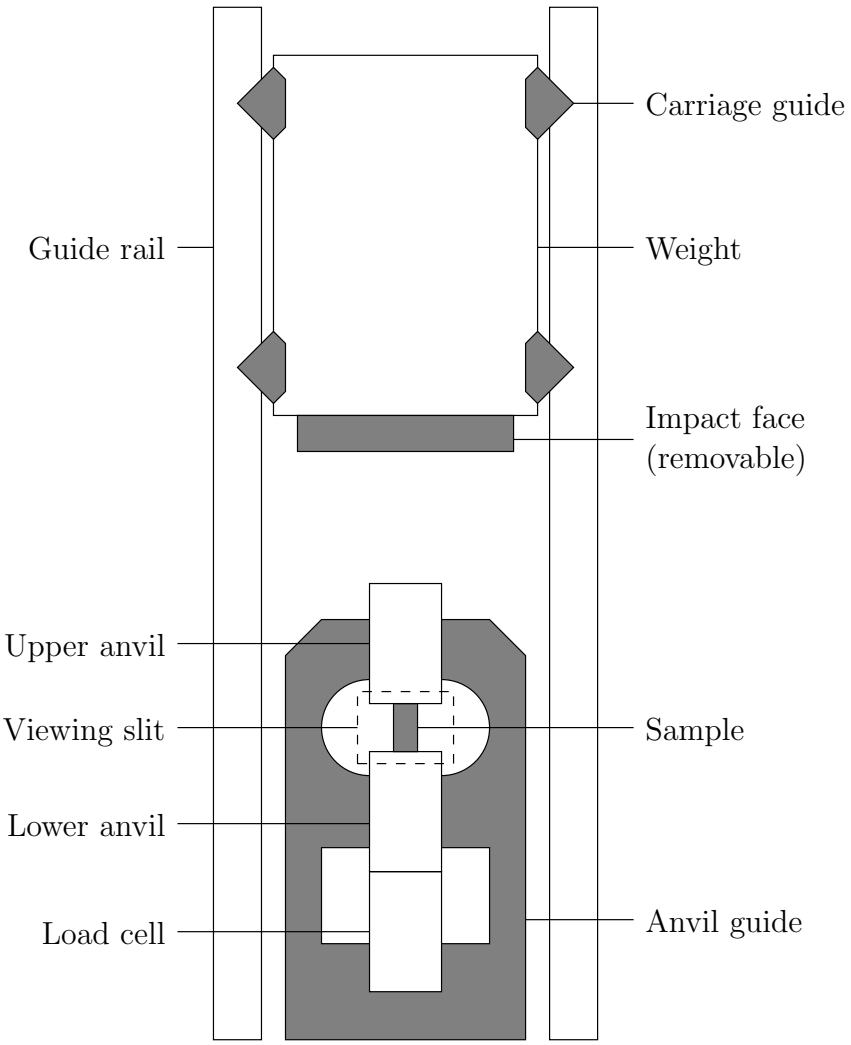

Figure 2.7: Usual arrangement of the Cavendish drop weight system. Not to scale.

twice:

$$\begin{aligned} l &= l_0 - \int v \, \mathrm{d}t, \\ l &= l_0 - \int \left(v_i - \int \frac{F}{m} \, \mathrm{d}t \right) \mathrm{d}t, \\ l &= l_0 - v_i t + \frac{1}{m} \iint F \, \mathrm{d}^2 t. \end{aligned} \tag{2.7}$$

The strain $\varepsilon(t) = \ln \frac{l(t)}{l_0}$ is then easy to find. To find the true stress, the sample's cross-sectional area at a given time is required; the strains involved are too great to assume that the cross-sectional area is constant. To find the cross-sectional area, we assume first that the sample deforms uniformly along its length, and second that the sample's volume is conserved. To achieve the first condition, the faces of the upper and lower anvils are usually lubricated. In the absence of this lubrication, the top and bottom faces of the sample stick to the anvil, and the sample preferentially expands at its mid-point. Lubrication eliminates this "barrelling". Under these assumptions, the cross-sectional area A is given in terms of the initial, measured cross-sectional area A_0 by

$$\begin{aligned} Al &= A_0 l_0, \\ A &= \frac{A_0 l_0}{l}. \end{aligned} \tag{2.8}$$

As l is already known from equation 2.7, it is now easy to find the stress $\sigma = \frac{F}{A}$.

2.6.4 Calibrating the load cell

The load cell in the drop weight is calibrated by dropping the weight on the anvils in the absence of a sample. The impact and rebound velocities u_i and u_r of the weight are measured. Given the mass m of the weight, the impulse J applied to the weight in this impact can then be calculated:

$$J = \Delta p = m(u_i - u_r). \tag{2.9}$$

As established in section 2.5, the load cell's output $V_o(t)$ may be assumed to be proportional to the force applied to the cell. Given this, we have

$$J = \int F(t)\,\mathrm{d}t = A \int V_o(t)\,\mathrm{d}t, \tag{2.10}$$

where A is a constant. From equations 2.9 and 2.10 we get the calibration factor

$$A = \frac{m(u_i - u_r)}{\int V_o(t)\,\mathrm{d}t}\ . \tag{2.11}$$

2.6.5 Imaging through the sample

The drop weight can also be configured with a light path through the sample area, allowing images to be taken along the loading axis as the sample deforms (Field et al., 1982; Heavens and Field, 1974). Figure 2.8 shows the light path in this case. This configuration is often useful in studying the mechanical processes which lead to ignition in energetic materials. In this research, the camera was a C4 rotating mirror camera, described in section 2.8.1.

2.7 Split Hopkinson Pressure Bar

The split Hopkinson Pressure Bar (SHPB), also known as a Kolsky bar, is a tool for applying uniaxial stress to a sample, at a strain rate of order $10^3\,\mathrm{s}^{-1}$. In this respect it is much like the drop weight. Also like the drop weight, the maximum stress that can be applied is limited by the yield stress of the sample-facing surfaces, and is typically a few gigapascals. The chief advantage of an SHPB over a drop weight is the SHPB's greater accuracy in measuring stress and strain. While elastic deformation of a drop weight introduces uncertainty to measurements made with that apparatus, this deformation is a central feature of an SHPB (Gray, 2000).

A compressive SHPB is illustrated schematically in figure 2.9. The striker bar is accelerated by some means to a few metres per second, and strikes the input bar. All the bars are made of the same material and are of equal diameter, and the

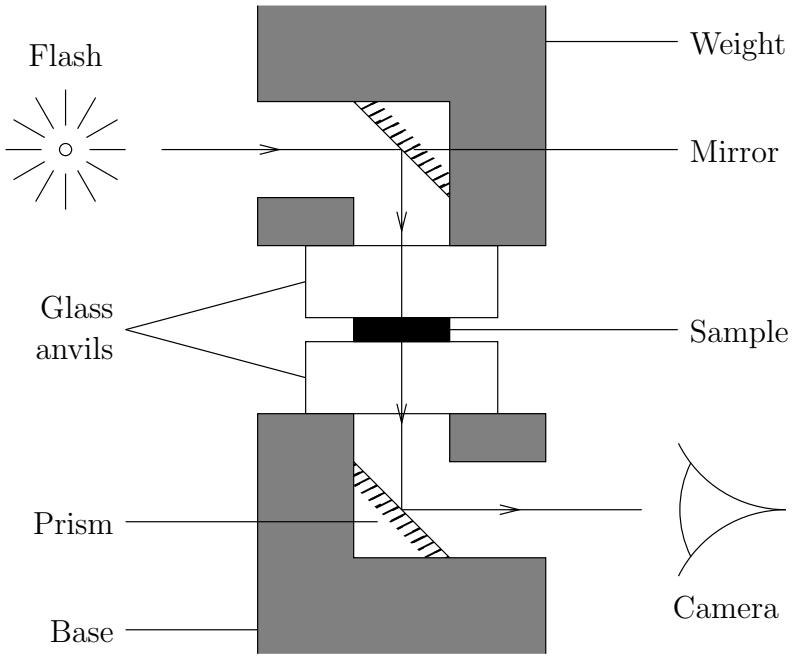

Figure 2.8: Light path through the sample in drop weight. Not to scale.

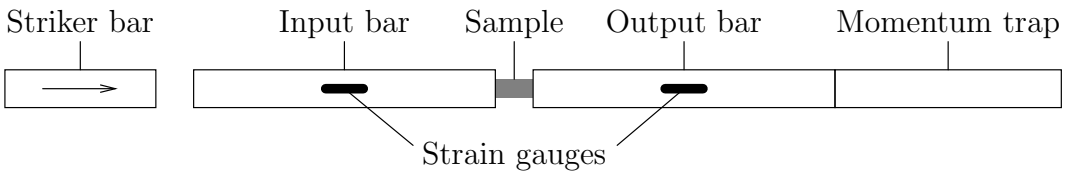

Figure 2.9: A compressive split Hopkinson pressure bar system (SHPB). Not to scale. In practice the ratio of bar length to bar diameter is of order 100:1.

striker bar velocity is chosen to ensure that they behave elastically throughout the experiment. The impact will therefore produce a well-defined, very nearly rectangular pressure pulse in the input bar, and bring the striker bar to rest. This pressure pulse will be recorded by the strain gauge on the input bar. This is the incident pulse.

When the incident pulse reaches the sample, some fraction is reflected and some is transmitted. The transmitted pulse is recorded by the strain gauge on the output bar. The reflected pulse is recorded by the strain gauge on the input bar. This requires that the incident pulse is shorter than the round trip between the input gauge and the sample, so that the incident and reflected pulses do

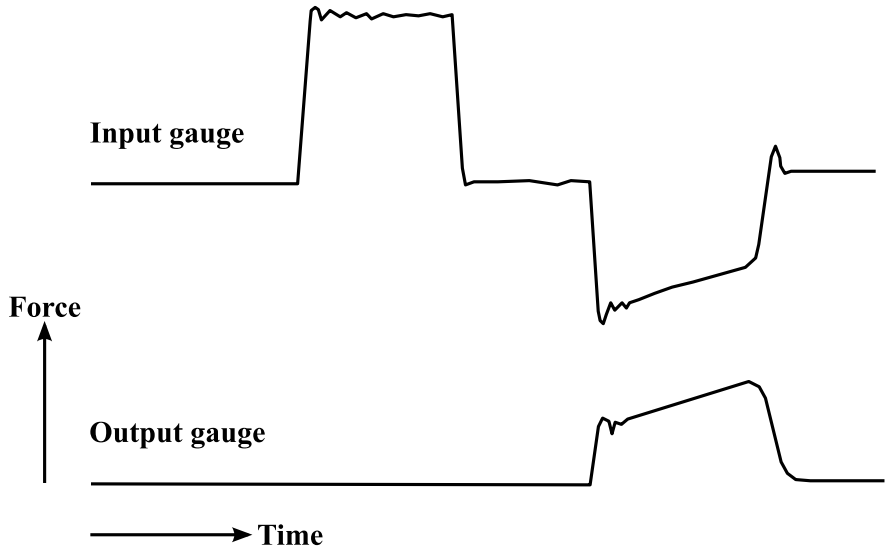

Figure 2.10: Approximate gauge outputs for a compressive SHPB. In this case, as is usual for SHPB experiments, the sample impedance is lower than the bar impedance.

not overlap. Figure 2.10 shows an example of the gauge outputs for this situation. Note that the tensile reflected pulse indicates that the sample was of lower impedance than the bars; this is the default situation in an SHPB experiment.

2.7.1 The momentum trap

The transmitted pulse enters the momentum trap. There is no impedance mismatch between the momentum trap and the output bar. There will, therefore, be no reflected wave from the interface between the output bar and the momentum trap. The reflected wave from the far end of the momentum trap will, however, be tensile. As the momentum trap and the output bar are not secured to each other, this tensile wave will be unable to pass the interface between the two. The momentum trap will therefore be ejected with a large fraction of the momentum of the striker bar.

The momentum trap serves two purposes. First, it prevents the reflection of the transmitted pulse separating the interface between the sample and the output bar, which could interfere with recovery of the sample for subsequent tests. Second, by isolating most of the bulk motion of the apparatus into the

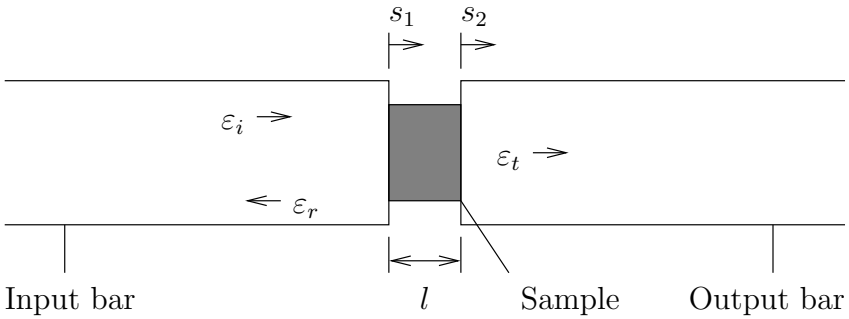

Figure 2.11: Symbols used in SHPB analysis. ε_i, ε_r and ε_t are the strains associated with the incident, reflected and transmitted waves, respectively. s_1 and s_2 are the displacements of the sample faces from their original positions. l is the thickness of the sample.

inexpensive and robust momentum trap, the momentum trap extends the lifetime of the apparatus. In the original pressure bar experiments of Hopkinson (1914), which predated high-speed data capture, the velocity of the momentum trap was the output of the experiment.

2.7.2 Materials testing

The SHPB, like the drop weight, is normally used to find the stress-strain response of a material. Also like the drop weight, the analysis to extract this from the strain gauge readings is not entirely trivial. Throughout this analysis, the bars are assumed to be elastic and non-dispersive. While it is possible to correct for dispersion, the error due to ignoring dispersion is small (Siviour, 2005). This research therefore ignores dispersion. Figure 2.11 shows the symbols used in this analysis.

First, consider the one-dimensional wave equation

$$\frac{\partial^2 s}{\partial x^2} = \frac{1}{c_b^2}\frac{\partial^2 s}{\partial t^2}\ , \tag{2.12}$$

where s is the displacement of a point in the bar, x is the position along the bar, and c_b is the wave speed along the bar. Solutions of this equation are

$$s = f(x - c_b t) + g(x + c_b t), \tag{2.13}$$

where f corresponds to a wave travelling in the positive direction, and g to one travelling in the negative direction. In the input bar, these will be s_i and s_r, the incident and reflected waves, respectively. In the output bar, the wave travelling in the negative direction will be removed by the momentum trap and only the transmitted wave $s_t = h(x - c_b t)$ will be present.

By definition, the strain

$$\varepsilon = \frac{\partial s}{\partial x} \ . \tag{2.14}$$

From this, the strain in the bars will be

$$\varepsilon = f' + g' = \varepsilon_i + \varepsilon_r \ , \qquad \text{Input bar} \tag{2.15}$$

$$\varepsilon = h' = \varepsilon_t \ . \qquad \text{Output bar} \tag{2.16}$$

Using the chain rule, differentiate s with respect to time:

$$\dot{s} = c_b(-f' + g') = c_b(\varepsilon_r - \varepsilon_i), \qquad \text{Input bar} \tag{2.17}$$

$$\dot{s} = -c_b h' = -c_b \varepsilon_t \ . \qquad \text{Output bar} \tag{2.18}$$

Equations 2.15, 2.16, 2.17 and 2.18 are true throughout their respective bars. This allows the strain rate in the sample to be calculated:

$$\dot{\varepsilon} = \frac{\dot{s_1} - \dot{s_2}}{l} = \frac{c_b(\varepsilon_r - \varepsilon_i + \varepsilon_t)}{l}. \tag{2.19}$$

Given the initial length of the sample l_0, and the measurements of $\varepsilon_i(t)$, $\varepsilon_r(t)$ and $\varepsilon_t(t)$ from the strain gauges, this can be numerically integrated to find the strain ε in the sample.

To find the stress in the sample, observe that the forces in the bars are

$$F = AY\varepsilon = AY(\varepsilon_i + \varepsilon_r), \qquad \text{Input bar} \tag{2.20}$$

$$= AY\varepsilon_t \ , \qquad \text{Output bar} \tag{2.21}$$

where Y is the Young's modulus of the bar material and A is the cross-sectional area of the bar.

Averaging these two forces will give the force on the sample. To find the true

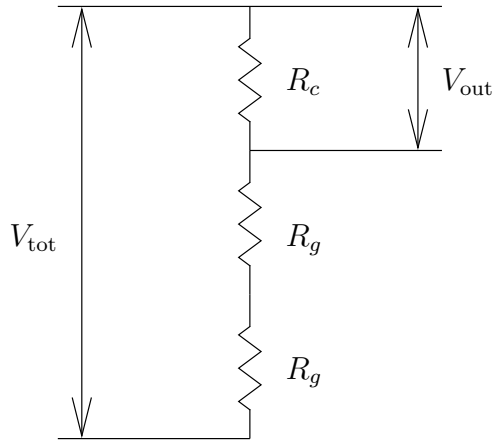

Figure 2.12: Potential divider circuit used in the SHPB. The resistors R_g are strain gauges; the resistor R_c is constant.

stress requires the cross-sectional area of the sample. As with the drop weight, this is obtained by assuming that the sample's volume is conserved, and that it deforms uniformly. Also as with the drop weight, lubrication of the interfaces between the sample and the bars is required to satisfy the second criterion. Then, using equations 2.8, 2.20 and 2.21, the stress σ in the sample is given by

$$\sigma = \frac{AYl(\varepsilon_i + \varepsilon_r + \varepsilon_t)}{2A_0 l_0}, \tag{2.22}$$

where A_0 and l_0 are the measured initial sample area and length, respectively. The instantaneous sample length l is known from numerical integration of equation 2.19.

2.7.3 Strain measurement in the SHPB

The strain gauges in the SHPB are not arranged as a conventional Wheatstone bridge load cell. Instead a single pair of strain gauges is mounted parallel to the bar axis at each measurement point. The gauges are placed on opposite sides of the bar to minimize the effect of bar flexing on the reported strain. They are then placed in a simple potential divider circuit as shown in figure 2.12.

These strain gauges, like those used in a conventional load cell, have a resis-

tance $R_g = R_0(1 + G\varepsilon)$, so this circuit's output will be given by

$$\begin{aligned} V_{\text{out}} &= V_{\text{tot}} \frac{R_c}{R_c + 2R_g} \ , \\ V_{\text{out}} &= V_{\text{tot}} \frac{R_c}{R_c + 2R_0(1 + G\varepsilon)} \ . \end{aligned} \tag{2.23}$$

The oscilloscope recording V_{out} is AC coupled, so it records only the deviation V from the output in the absence of strain:

$$\begin{aligned} V_0 &\equiv V_{\text{out}}(\varepsilon = 0), \\ V_0 &= V_{\text{tot}} \frac{R_c}{R_c + 2R_0} \ . \end{aligned} \tag{2.24}$$

This gives the recorded output on the oscilloscope as a function of strain:

$$V = V_{\text{tot}} R_c \left(\frac{1}{R_c + 2R_0(1 + G\varepsilon)} - \frac{1}{R_c + 2R_0} \right). \tag{2.25}$$

By simple but tedious algebra, this can be rearranged to give the strain as a function of the oscilloscope output:

$$\varepsilon = -\frac{R_c + 2R_0}{2R_0 G} \cdot \frac{V}{V + \dfrac{V_{\text{tot}} R_c}{R_c + 2R_0}} \ . \tag{2.26}$$

This design of strain gauge is much less sensitive to strain than a Wheatstone bridge arrangement. It was chosen because fast-acting amplifiers, of the kind used to amplify a Wheatstone bridge's output, were unavailable when the system was designed. To compensate for its reduced sensitivity, semiconductor strain gauges are used. The gauge factor G of such gauges is typically two orders of magnitude greater than that of the foil gauges used in most Wheatstone bridge load cells. However, semiconductor gauges are also considerably more sensitive to temperature variations than foil gauges. The potential divider system used here ameliorates this temperature sensitivity.

The choice of semiconductor strain gauges has other benefits. Semiconductor gauges are physically smaller than foil gauges, and therefore sample the strain

over a smaller length of the bar. As the temporal structure of the wave is spread along the bar, this smaller sampling range translates directly to improved temporal resolution. This smaller size also makes them more suitable for use in a miniaturized SHPB system (Gorham et al., 1992).

2.7.4 Calibrating the SHPB

Rather than substituting measured values into equation 2.26 to calculate the strain that corresponds to a given oscilloscope output, a dynamic calibration technique similar to that used for the drop weight is employed. First, observe that, if the bars are elastic, equation 2.26 is of the form

$$F = A \cdot \frac{V}{V + B} \ , \tag{2.27}$$

where A and B are constants to be determined. To do so, the bar to be calibrated is set in the place of the input bar, with no sample or output bar. The striker bar is then fired at it at a velocity measured using a light gate system.

By an impedance-matching argument, the pressure pulse produced in the bar must correspond to an impulse exactly sufficient to bring the striker bar to rest. As the striker bar's mass m_s and velocity u_s are known, this impulse is known. If the strain gauge output is approximated as a square wave of duration t and height V, the force applied by the striker bar is given by

$$F = \frac{m_s u_s}{t}. \tag{2.28}$$

The pressure pulse in the bar then gives a single (F, V) data point. Assuming total reflection at the end of the bar, the tensile pulse reflected from that end will give another such point. Several of these points are gathered. A and B can then be determined by model fitting, as described in section 2.12.

Another aspect of the bars that must be calibrated is the wave speed in the bar, c_b. This can in principle be calculated from the properties of the bar material and the geometry of the bars. However, it can be highly sensitive to a variety of factors which are poorly known, such as the thermal and mechanical histories of the bars.

Calibration of c_b is achieved simply by placing the input and output bars in contact and firing the striker bar at the input bar. The pressure pulse will propagate down the bars at c_b. If the distance between the strain gauges is known, the time taken for the pressure pulse to pass from the input strain gauge to the output strain gauge gives c_b.

It is possible to measure c_b in each bar independently by measuring the time taken for the reflection of the incident pulse to return to the bar's strain gauge. In practice, as the bars are manufactured, stored and used as a pair, there is rarely a measurable difference between c_b in the two bars.

2.8 High speed photography

The term "high speed photography" refers to any photographic technique with a frame rate higher than 128 frames per second. There are several high speed photographic techniques (Ray, 1997). This research used high speed cameras of the rotating-mirror and image conversion designs.

2.8.1 Rotating-mirror

A rotating-mirror camera typically records a few tens of frames, with an inter-frame time of a few microseconds. Unlike a conventional film camera, the film in a rotating-mirror camera remains stationary. The rotating mirror for which the camera design is named moves the image across the film, as shown in figure 2.13. The mirror rotates at a constant speed, typically a few hundred r. p. s., and is the only moving part in the system. This rapid rotation subjects the mirror to considerable centrifugal force. The temporal resolution of a rotating-mirror camera will be limited by the mirror's mechanical strength: above a certain rotation speed deformation of the mirror will prevent image formation.

This design of rotating-mirror camera is unable to record continuously: for some time during the mirror's rotation the light from the experiment will fall on the mirror's edge, and not be reflected. The experiment must therefore be carefully synchronized with the mirror's rotation, or the camera will fail to record for some unpredictable part of the experiment. The C4 rotating mirror camera

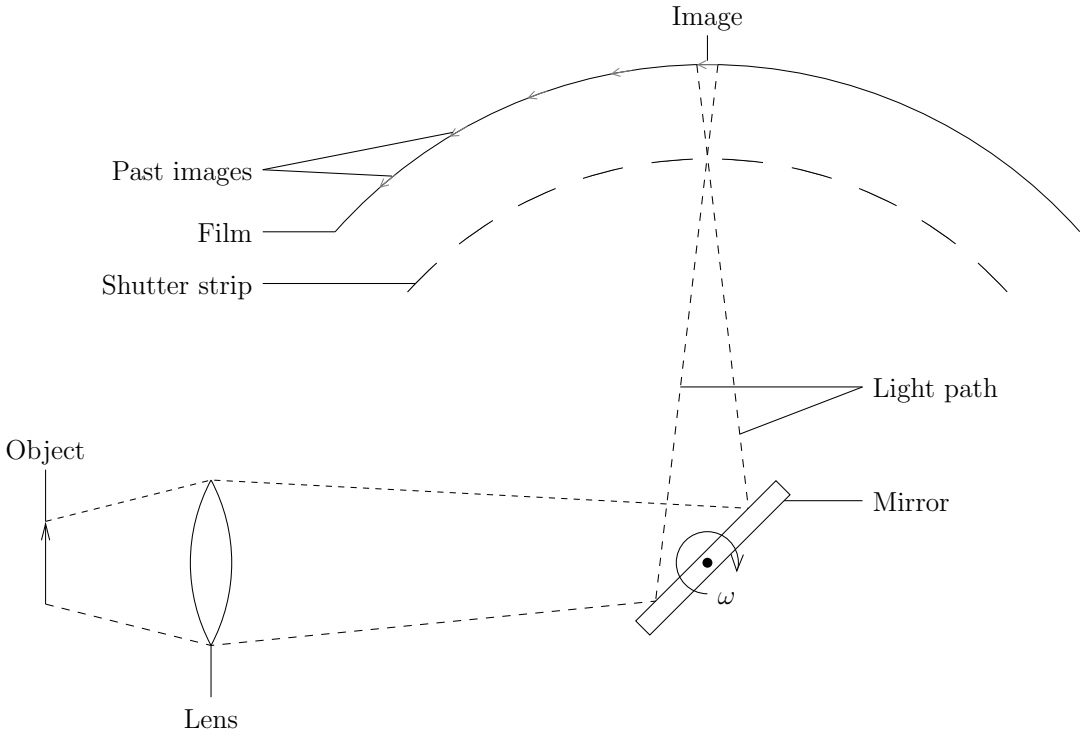

Figure 2.13: Schematic of a simple rotating-mirror camera. The mirror rotates with angular velocity ω. Not to scale.

(Coleman, 1959) uses more complicated optics, shown in figure 2.14, to avoid this problem. Two film tracks are used, and a beam-splitter divides the light from the experiment into two paths. These are arranged so that, when one light path reaches the end of its film track, the other reaches the start of the other film track. While light from the experiment will still strike the edge of the mirror and be lost, this will never occur while that light would otherwise be recorded. Note that this optical arrangement records a full set of images in half a rotation of the central mirror. The design of the C4 camera allows it to record 140 frames.

In this research, the exposure of the film was controlled by use of a short-duration xenon flash. The mirror was rotated at approximately 500 r. p. s. and its precise speed measured using the rotating mirror and photodiode arrangement shown in figure 2.15. The shutter was then opened and the experiment activated. The experiment triggered the flash, which provided illumination for approximately one millisecond. During this time each frame would be exposed once. Some frames received a double exposure, overprinting the initial and final states of the experiment. This can be used to compare these two states directly, and is a useful feature of the C4 camera.

One disadvantage of the C4 camera is that it weighs over a tonne and is effectively immobile. The experiment, therefore, must be brought to the camera, rather than the reverse. This contrasts with an image converter camera, which typically weighs about 20 kg and can be moved to the event being studied.

2.8.2 Image conversion

An image converter camera records roughly ten frames, with an interframe time as low as a few tens of nanoseconds. The camera converts an optical image to an electron beam. This beam is then manipulated electrostatically by altering the charge on deflecting plates. The elimination of moving parts dramatically reduces the minimum interframe time. The temporal resolution is limited by the time taken to charge the deflecting plates (Zavoisky and Fanchenko, 1965).

Figure 2.16 shows the image tube of the Ultranac 501 image conversion camera used in this research (Garfield and Riches, 1991). Light from the experiment is focused using optical lenses (not shown) onto the photocathode. The photocath-

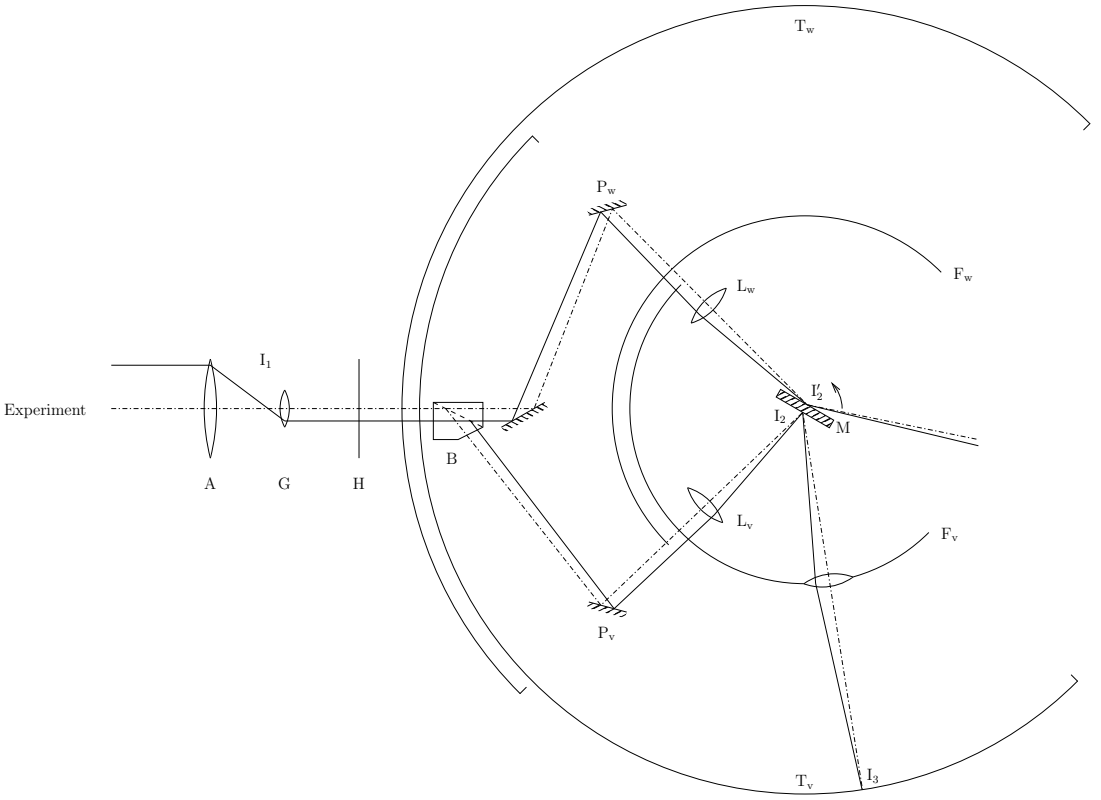

Figure 2.14: Optics of the C4 rotating-mirror camera. Not to scale. The beam splitter B divides the light into two fractions, v and w. These are reflected from their respective fixed mirrors P and focused by lenses L to form an image I_2 on the rotating mirror M. This image is then reflected and refocused by a lens in the static array of lenses F to form an image I_3 on the film track T. Each lens array contains 70 lenses, allowing the system to record a total of 140 images. P, L, F and T are displaced out of the plane of the paper, so that F_w does not obscure T_v and F_v does not obscure T_w. The shutter H controls exposure of the film track. This design allows continuous access: provided the shutter is open, the camera is guaranteed to be able to record an image.

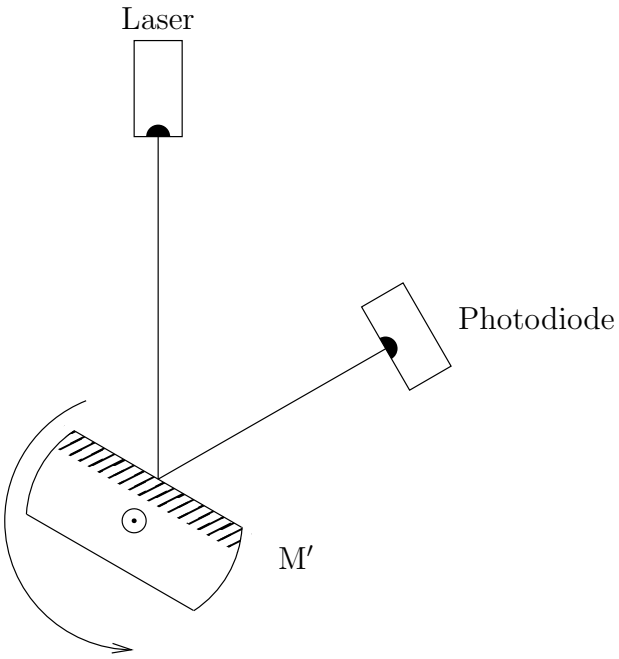

Figure 2.15: System for measuring the rotation speed of the mirror in the C4 camera. Not to scale. The mirror M′ is affixed to the same axle that drives the rotating mirror M in the camera (see figure 2.14). With each rotation, the photodiode will produce a pulse; the frequency of these pulses is measured with a counter-timer.

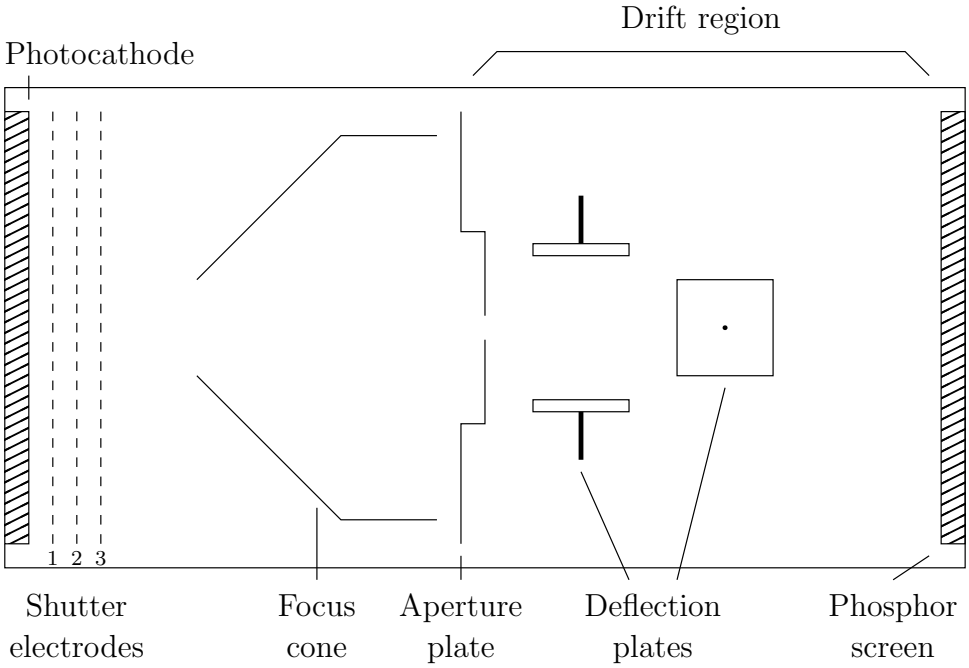

Figure 2.16: Electron optics of the Ultranac 501 image conversion camera. Not to scale. The photocathode and shutter electrodes are held near to 0 V (see figures 2.17 and 2.18 for details). The focus cone is held at +450 V, and the aperture plate and phosphor screen at +15 kV.

ode is constructed from a mixture of compounds of alkali metals and antimony, referred to as S25. This material has a very low work function, and will emit photoelectrons when exposed to visible light (Holtom et al., 1979). Ignoring, for now, the shutter electrodes, these photoelectrons will be accelerated and focused by the focus cone and aperture plate. These two components act as an electrostatic lens, transferring the electron image at the photocathode to the phosphor screen. Within the drift region, there is no axial electric field. The deflection plates move the electron beam across the phosphor screen to produce distinct images or a streak record, as required. The phosphor screen is a thin layer of a mixture of zinc sulphide, cadmium sulphide and silver, referred to as P20. When struck by the accelerated electrons from the photocathode, it emits light. It is coupled by optical fibres to a flat back plate, against which photographic film is pressed to record the images.

Figures 2.17 and 2.18 show the operation of the shutter electrodes. Before

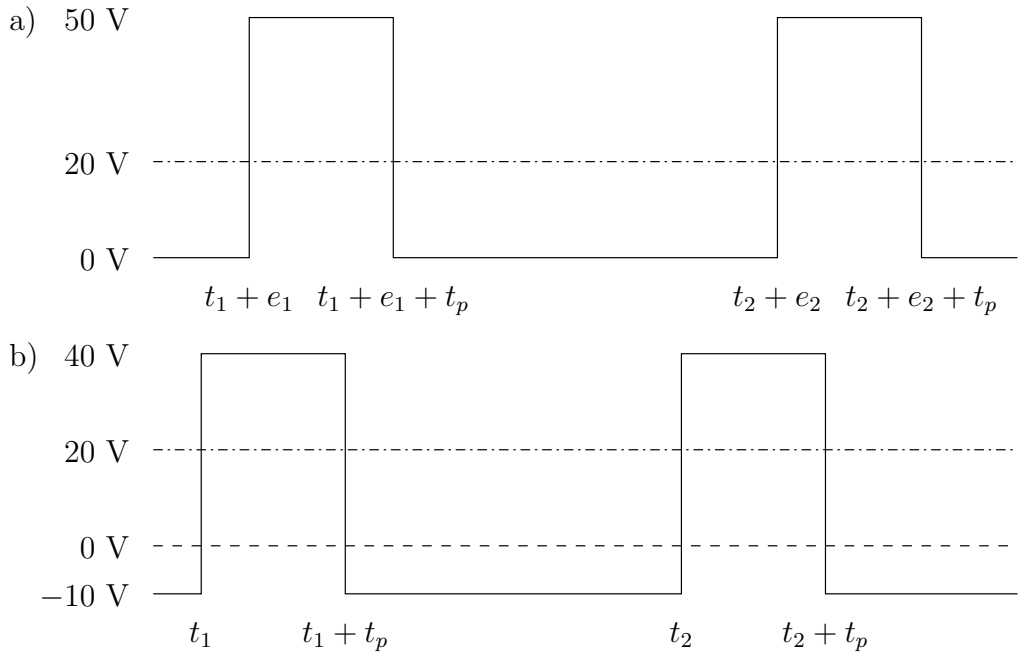

Figure 2.17: Potential of (a) the photocathode and (b) shutter electrode 2 in the Ultranac 501 image conversion camera, as a function of time. Also shown is the constant 20 V potential of shutter electrode 1. Shutter electrode 3 is held at a constant 120 V potential (not shown). Frame n starts at time t_n, and is exposed for a time e_n. t_p is chosen so that $t_n + e_n + t_p < t_{n+1}$, and may vary over the course of an experiment.

the exposure, there is a potential energy minimum at electrode 1. A 50 V pulse of width t_p is generated at the start of an exposure, and fed both to electrode 2 and to a delay generator. The change to the potential at electrode 2 eliminates the potential energy minimum at electrode 1, and admits electrons from the photocathode to the accelerating region of the image tube. The delay generator delays the pulse for the exposure time e_n, then applies it to the photocathode. This produces a potential energy barrier at electrode 1 and consequently prevents electrons passing from the photocathode into the image tube, ending the exposure.

When the camera is used in imaging mode, the distance moved by the electron beam between frames is minimized. This shortens the minimum inter-frame time that can be achieved without image distortion or misalignment. However, it leads

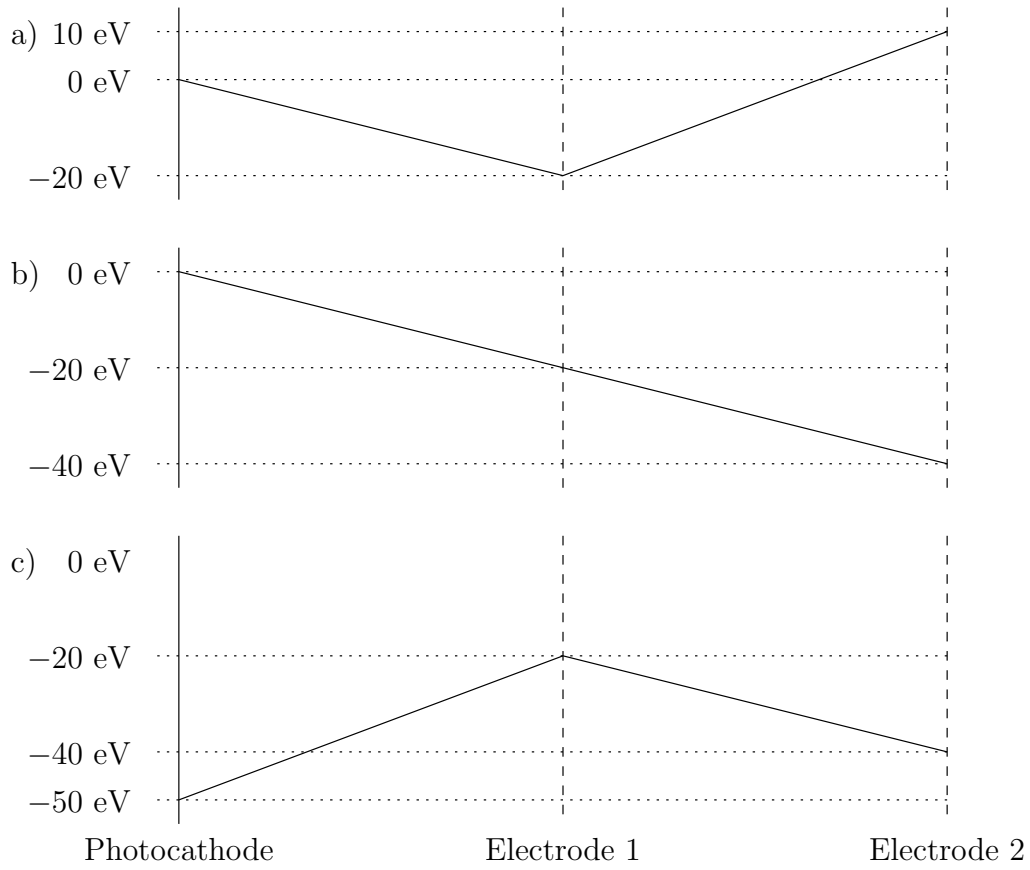

Figure 2.18: Electric potential energy for electrons in the vicinity of the shutter grids in the Ultranac 501 image conversion camera. Potential energy is shown (a) immediately before an exposure, (b) during an exposure, and (c) immediately after an exposure. Horizontal axis not to scale.

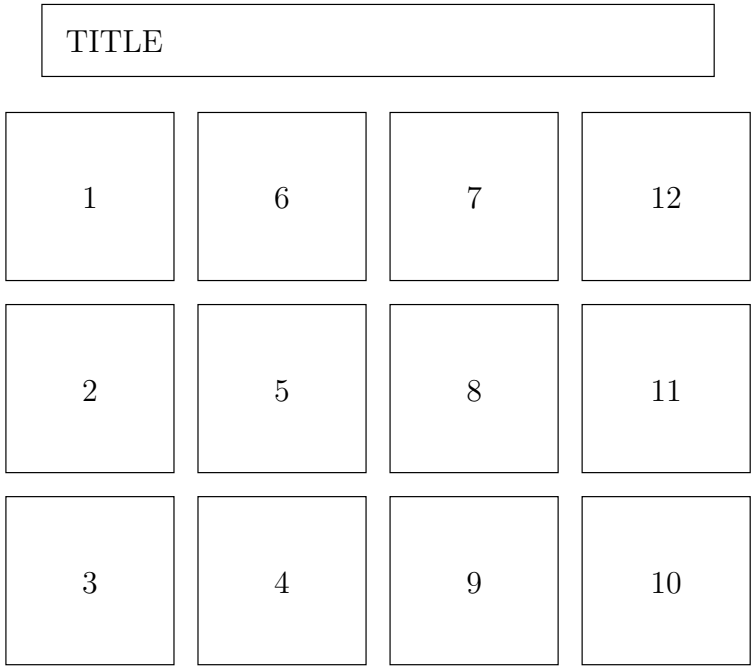

Figure 2.19: Arrangement of output frames in the Ultranac 501 image conversion camera, when configured to produce twelve frames.

to a somewhat counter-intuitive layout of frames on the output film. Figure 2.19 shows the layout of frames produced when the camera is used to produce twelve frames. This mode was used throughout this research.

2.9 Photodiodes

A photodiode is a device for measuring the intensity of light. They typically have a temporal resolution less than a nanosecond, and an intensity resolution of a few milliwatts per square metre, if they are attached to suitably sensitive measurement electronics. An Electro-Optics Technology, Inc. ET-2030 photodiode was used in this research.

The ET-2030 photodiode is a silicon p-type, intrinsic, n-type (PIN) photodiode, operated with a 9 V reverse bias. The photodiode is based on a PIN semiconductor junction, as shown in figure 2.20. The intrinsic semiconductor serves to extend the depletion region that forms at a p-type, n-type (PN) semi-

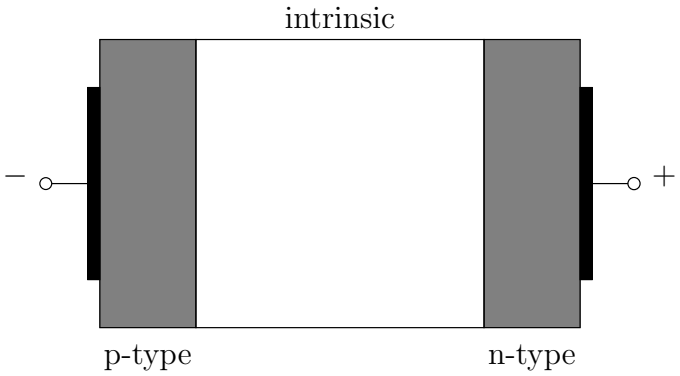

Figure 2.20: PIN semiconductor junction under reverse bias, as used in ET-2030 photodiode. Not to scale.

conductor junction. A photon incident on this extended depletion region excites an electron-hole pair, which allows a certain charge to flow. The current flowing through the photodiode will therefore indicate the photon flux at the photodiode. In practice the average response of the photodiode to a given photon is a function of that photon's energy. The system must therefore be calibrated with light of varying wavelengths. The variation of photon energy with wavelength is typically included in this calibration, giving a wavelength-dependent relationship between output current and incident light intensity.

2.10 Plate impact

Plate impact is a technique for introducing a shock wave to a material. The amplitude of the shock wave may be a few tens of gigapascals, and its duration may be several microseconds. The technique works by accelerating a flat plate of some material (the "flyer plate") to several hundred meters per second and colliding it with a suitably designed sample cell. This research used the small gas gun at the Cavendish to accelerate the flyer plate.

The small gas gun consists of an eight litre gas reservoir, connected to one of a set of interchangeable barrels. The barrel used throughout this research had a 19.6 mm bore. Figure 2.21 shows the gas reservoir. To prepare the system for firing, chamber A is filled to 5 bar above the intended firing pressure using the

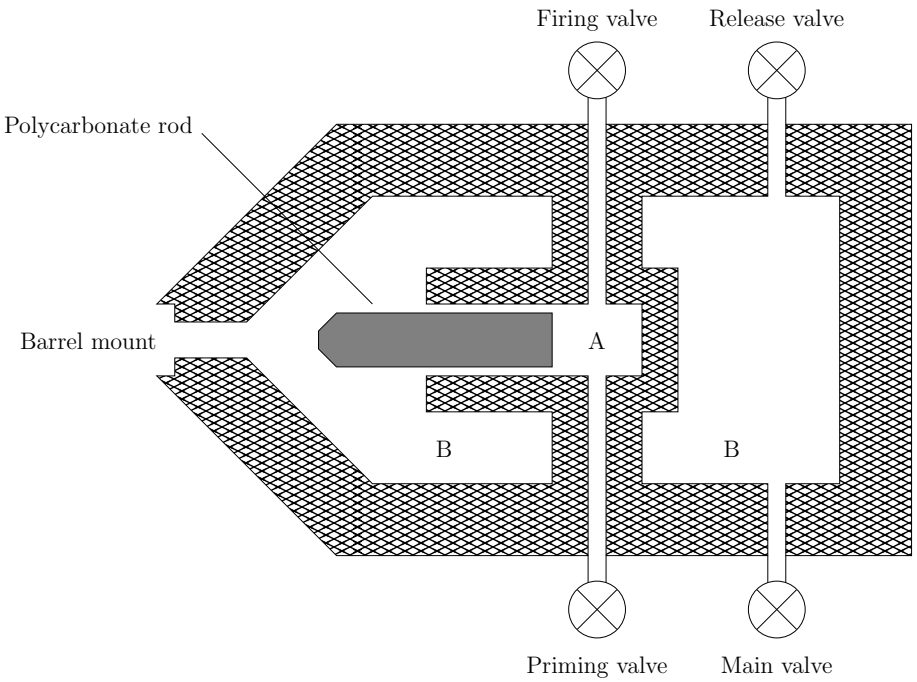

Figure 2.21: Schematic of the firing chamber of the Cavendish small gas gun. Not to scale. The main valve and priming valve are connected to a high-pressure helium cylinder; the release valve and firing valve are connected to atmosphere. The priming chamber, A, is filled through the priming valve and emptied through the firing valve. The firing chamber, B, is in fact a single continuous volume; the two apparently separate regions are connected outside the plane of the diagram. The firing chamber is filled through the main valve; in normal operation it is emptied into the barrel when the gun is fired. The release valve is used to empty the firing chamber without firing the gun.

priming valve. This presses the polycarbonate rod against the inside of chamber B near the barrel mount, sealing chamber B. Chamber B is then filled to the intended firing pressure using the main valve. To fire the gun, the firing valve is rapidly opened. This allows the polycarbonate rod to retreat into chamber A. This in turn opens chamber B to the barrel, firing any projectile loaded therein. The release valve is used to interrupt this process and make the system safe without firing the projectile.

2.11 High-speed optical spectroscopy

Optical spectroscopy is a technique for measuring the energy distribution, as a function of frequency, of electromagnetic radiation. The temporal resolution of the technique is determined by the time for which radiation is gathered. A UV/visible gated spectroscope system produced by Princeton Applied Research Corporation was used in this research. This system was able to record a single spectrum with an exposure time no shorter than 50 ns. It was sensitive to light with wavelengths in the range 200–800 nm.

The system accepts light through a bundle of quartz optical fibres. This light is then dispersed into its spectral components. The spectrum thus formed falls on an image intensifier. An array of photodiodes is coupled to the output of the image intensifier with optical fibres. The output of these photodiodes is recorded. These stages are discussed in more detail below.

2.11.1 Dispersion stage

In this spectroscope system, spectral dispersion is performed by a Princeton Applied Research model 1235 spectrograph. The 1235 is a slight modification of a standard Czerny-Turner monochromator (Czerny and Turner, 1930; Fastie, 1952). The modifications consist of the removal of the output slit, and the addition of plane mirrors R so that the input and output are on opposite sides of the device. Figure 2.22 shows the optics of the spectrograph. The fibre bundle illuminates the input slit. This light is collimated into a parallel beam by the collimating mirror C. This strikes the diffraction grating on one face of the grating turret T and is diffracted. The grating is angled so that the first-order diffracted spectrum strikes the re-focusing mirror F. The dispersed spectrum is then focused on the input plane of the image intensifier.

The grating turret may be rotated. This serves two purposes. First, it allows the grating to be changed, by presenting a different face of the turret to the incident light. Second, it allows the spectral region of interest to be centred on the re-focusing mirror. The re-focusing mirror itself may be moved along its axis to adjust the focus of the spectrum. The gratings themselves are "blazed": their grooves have been cut at an angle, to maximize the energy reflected at that

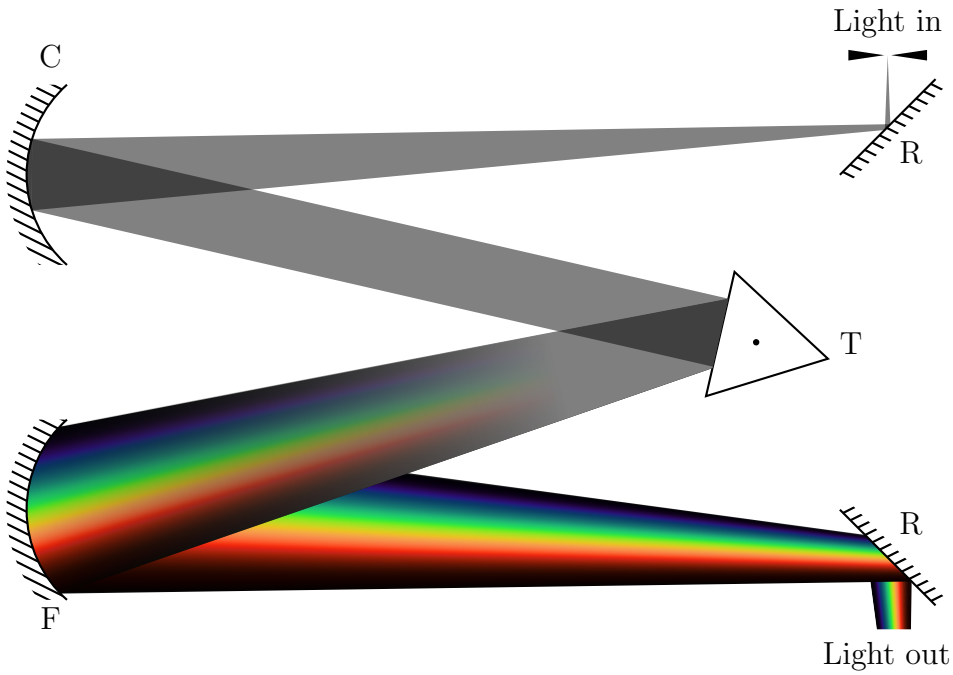

Figure 2.22: Schematic of diffraction stage of Princeton Applied Research model 1235 spectrograph used in this research. The plane mirrors R allow the input and the output to be on opposite sides of the device. The collimating mirror C is arranged so that a parallel beam of light strikes the grating. The grating turret T has a grating on each face, and can be rotated either to change gratings, or to move the diffracted light over the detector. The re-focusing mirror F focuses the diffracted light on the detector plane (not shown). Not to scale.

angle. This angle is chosen to maximize the brightness of the first-order diffracted spectrum; this minimizes the light wasted in spectra which do not strike the refocusing mirror and are not recorded. The wavelength for which this process is optimized is the blaze wavelength. The spectrograph used in this research was supplied with two gratings, etched with 150 and 600 grooves per millimetre respectively. Both were etched with a 500 nm blaze wavelength. Only the first grating was used here.

2.11.2 Image intensifier

The image intensifier and detector array were supplied as a single unit. The combined unit was a Princeton Applied Research model 1455B-700-HQ intensified detector. The intensifier is essentially a generation II image intensifier. This has several similarities with the image conversion camera described in section 2.8.2. Both systems convert the incident optical image to an electron image, manipulate this electron image, then use a phosphor screen to convert it back to an optical image.

Figure 2.23 shows the layout of the intensifier. The interior of the intensifier is evacuated at the time of manufacture, then sealed. The spectrum produced by the spectrograph is focused on the input face. The incident light causes the photocathode to emit photoelectrons. These are accelerated by the 200 V potential difference between the photocathode and the input face of the microchannel plate.

The microchannel plate acts as an array of electron multipliers (Wiza, 1979). The plate consists of an array of glass tubes, aligned at an angle to the plate's normal. This angle is typically a few degrees, and the tubes typically have internal diameters of a few microns. An electron striking the wall of one of these tubes provokes secondary electron emission. These secondary electrons are accelerated by the 1 kV potential difference across the plate. When they strike the tube wall, they also provoke secondary electron emission. This electron cascade results in a gain between 10^3 and 10^5, depending on the design of the microchannel plate and the potential difference applied across it. In this intensifier, the potential difference across the microchannel plate may be varied. This allows the gain of

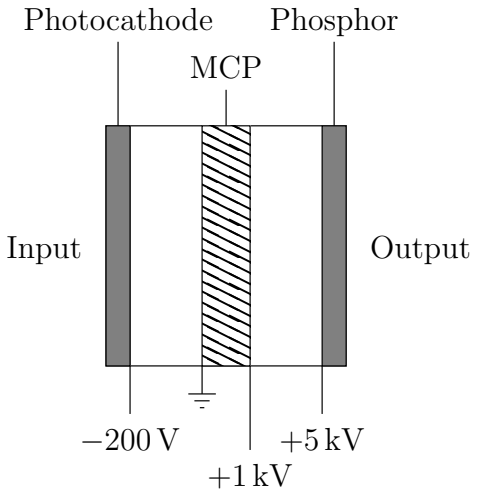

Figure 2.23: Layout of the image intensifier in the Princeton Applied Research model 1455B-700-HQ intensified detector. "MCP" denotes the micro-channel plate. Not to scale. Horizontal axis disproportionately expanded.

the system to be adjusted. Electrons typically exit the plate with energies of a few tens of electron-volts.

The multiplied electrons leaving the microchannel plate are accelerated by the 4 kV potential difference between the output face of the microchannel plate and the phosphor screen. They strike the screen, causing it to emit light. This light is transferred by optical fibre to the detector array. Each stage of the system is proximity focused: the short distance the electrons travel removes the need for any focusing electron optics.

Gating is accomplished by altering the potential at which the photocathode is held. When the intensifier is to be operated in gated mode, the photocathode is held at the same potential as the input face of the microchannel plate. Photoelectrons from the photocathode will therefore not travel to the microchannel plate. To activate the intensifier, a −200 V pulse is applied to the photocathode for the desired duration. This allows electrons to travel from the photocathode to the input face of the microchannel plate, and the intensifier then acts in the fashion described above. The intensifier was capable of a minimum exposure time of 50 ns. The gating pulse was provided by a Princeton Applied Research model 1304 pulse amplifier. This could be triggered by a 5 V TTL pulse from the

experiment. It also provided a 5 V monitoring output. This was high while the intensifier was active. This eliminated uncertainty due to delays in the internal electronics of the pulse amplifier.

2.11.3 Detector array

The detector array is the other component of the Princeton Applied Research model 1455B-700-HQ intensified detector. It is an array of 1024 photodiodes. Seven hundred of these are coupled by optical fibres to a line across the centre of the intensifier's output plate. The remainder are not illuminated. Photodiodes are described in section 2.9. The photodiodes in this array are reverse biased to 5 V, then disconnected from their power source. In this state they are effectively a charged capacitor. Each photon that is absorbed in the depletion region will generate a charge-carrier pair. These charge carriers will act to discharge the capacitor. After the array has been exposed, the potential difference across each photodiode is read in sequence. This will give a quantity proportional to the number of photons absorbed, and hence to the intensity with which the intensifier's output plate was lit. After a photodiode has been read, it is re-biased to 5 V to prepare it for the next exposure. This arrangement requires only a single accurate amplifier to read the entire photodiode array.

The detector array is equipped with a Peltier device for cooling. Cooling the detector reduces the rate at which thermally-generated charge carriers discharge the photodiodes. This "dark current" causes a constant offset in the recorded spectrum. Its magnitude depends on the detector temperature and the time for which the array was exposed between measurements. It cannot be eliminated altogether at non-zero temperature, and must be accounted for.

2.12 Model fitting

Model fitting describes a family of techniques for determining the parameters of a model from some data. It is also known as curve fitting. The technique used in this research was the Levenberg-Marquardt algorithm (Marquardt, 1963; Press et al., 1992). This is an iterative algorithm which attempts to minimize the

χ^2 deviation between the model and the data to be fitted. It does not assume that the model depends linearly on its parameters. This research used the implementations of this algorithm in the SciPy and NumPy suite (Ascher et al., 2001; Jones et al., 2001–), and in the gnuplot software (Williams et al., 2010).

2.12.1 Justification for χ^2 minimization

If the model depends on M parameters, these parameters may be written as the M-element vector $\boldsymbol{a}$. If the independent variable is x, the value of the model is $y(x;\boldsymbol{a})$. The observed data, to which the model is to be fitted, consists of N data points of the form (x_i, y_i); each y_i has some error σ_i which is assumed to be normally distributed. The deviation which is to be minimized is then

$$\chi^2 = \sum_{i=1}^{N} \left[\frac{y_i - y(x_i;\boldsymbol{a})}{\sigma_i} \right]^2 . \tag{2.29}$$

Finding the parameters $\boldsymbol{a}$ for which χ^2 is minimized is an attractive approach to model-fitting. First, it reduces the problem to a special case of function minimization. Second, it is a form of maximum-likelihood method. The probability $P(\boldsymbol{a})$ that a particular set of parameters will produce the set of data (x_i, y_i) is

$$P(\boldsymbol{a}) = \prod_{i=1}^{N} \frac{1}{\sqrt{2\pi\sigma_i^2}} \exp\left[-\frac{(y_i - y(x_i;\boldsymbol{a}))^2}{2\sigma_i^2} \right] . \tag{2.30}$$

This is just the product of the Gaussian probabilities of each data point, assuming that they are centred on $y(x_i, \boldsymbol{a})$ and have standard deviations σ_i. This will be the case if the measurement errors have been correctly assessed, and the model is, in fact, the model that gave rise to these observed data. Equation 2.30 may be rearranged to give

$$P(\boldsymbol{a}) = \frac{1}{\sqrt{2\pi}^N} \exp\left[\sum_{i=1}^{N} - \left[\frac{y_i - y(x_i;\boldsymbol{a})}{2\sigma_i} \right]^2 - \ln \sigma_i \right] . \tag{2.31}$$

This, the probability of the data given some set of parameters $\boldsymbol{a}$, may be

thought of as the likelihood that this set of data was generated by a model with those parameters. The set of parameters which maximizes this likelihood will, assuming the form of the model is correct and subject to some uncertainty due to the measurement errors σ_i, be that responsible for the observed data. The prefactor and $\ln \sigma_i$ terms in equation 2.31 do not depend on $\boldsymbol{a}$, and may therefore be neglected. Further, maximizing a function is equivalent to maximizing its logarithm. Taking these into account, the function to be maximized is

$$-\frac{1}{4}\sum_{i=1}^{N}\left[\frac{y_i - y(x_i;\boldsymbol{a})}{\sigma_i}\right]^2 = -\tfrac{1}{4}\chi^2 \ . \tag{2.32}$$

Therefore maximizing the likelihood that a model gave rise to some data is equivalent to minimizing the χ^2 deviation between the model and the data.

2.12.2 Inverse-Hessian method

The Levenberg-Marquardt algorithm interpolates smoothly between two function-minimization techniques. The first of those, the inverse-Hessian technique, is based on a Taylor expansion to quadratic order of the function to be minimized. Taking a point $\boldsymbol{p}$ as the origin, and expanding about that,

$$\chi^2(\boldsymbol{a}) \approx \gamma - \boldsymbol{d}\cdot\boldsymbol{a} + \tfrac{1}{2}\boldsymbol{a}\cdot\boldsymbol{D}\cdot\boldsymbol{a} \ , \tag{2.33}$$

where

$$\gamma = \chi^2(\boldsymbol{p}) \ , \quad d_k = \left.\frac{\partial\chi^2}{\partial a_k}\right|_{\boldsymbol{p}} \ , \quad D_{kl} = -\left.\frac{\partial^2\chi^2}{\partial a_k \partial a_l}\right|_{\boldsymbol{p}} \ .$$

Differentiating this gives

$$\boldsymbol{\nabla}\chi^2(\boldsymbol{a}) = \boldsymbol{D}\cdot\boldsymbol{a} - \boldsymbol{d} \ . \tag{2.34}$$

If the approximation were exact, this equation would be zero at the value of $\boldsymbol{a}$ that minimized $\chi^2(\boldsymbol{a})$. The approximation becomes increasingly accurate as the minimum is approached. It can therefore be used as the basis for an iteration,

$$\boldsymbol{a}_{n+1} = \boldsymbol{a}_n + \boldsymbol{\delta a} \ , \tag{2.35}$$

where $\boldsymbol{\delta a}$ is found using equation 2.34:

$$\boldsymbol{\delta a} = -\boldsymbol{D}^{-1} \cdot \boldsymbol{d} \ . \tag{2.36}$$

$\boldsymbol{D}$ is referred to as the Hessian matrix of χ^2 at the point $\boldsymbol{p}$. It must be recalculated at each step of the iteration, as $\boldsymbol{a}$ changes. This calculation is not entirely trivial. The form of χ^2 is given in equation 2.29. Differentiating this with respect to the component of $\boldsymbol{a}$ indexed by k gives

$$\frac{\partial \chi^2}{\partial a_k} = -2 \sum_{i=1}^{N} \frac{y_i - y(x_i; \boldsymbol{a})}{\sigma_i^2} \frac{\partial y(x_i; \boldsymbol{a})}{\partial a_k} \ . \tag{2.37}$$

Differentiating this, in turn, by the component of $\boldsymbol{a}$ indexed by l gives

$$\frac{\partial^2 \chi^2}{\partial a_k \partial a_l} = 2 \sum_{i=1}^{N} \frac{1}{\sigma_i^2} \left[\frac{\partial y(x_i; \boldsymbol{a})}{\partial a_k} \frac{\partial y(x_i; \boldsymbol{a})}{\partial a_l} - (y_i - y(x_i; \boldsymbol{a})) \frac{\partial^2 y(x_i; \boldsymbol{a})}{\partial a_k \partial a_l} \right] \ . \tag{2.38}$$

The last term of equation 2.38 is multiplied by $y_i - y(x_i; \boldsymbol{a})$. This is simply the residual between the model and the observed data. If the model fits well, this will be zero when summed over i. The second derivatives of $y(x_i, \boldsymbol{a})$ can therefore be neglected, giving

$$\frac{\partial^2 \chi^2}{\partial a_k \partial a_l} = 2 \sum_{i=1}^{N} \frac{1}{\sigma_i^2} \frac{\partial y(x_i; \boldsymbol{a})}{\partial a_k} \frac{\partial y(x_i; \boldsymbol{a})}{\partial a_l} \ . \tag{2.39}$$

Conventionally, a matrix $\boldsymbol{\alpha}$ and a vector $\boldsymbol{\beta}$ are defined as

$$\beta_k \equiv -\frac{1}{2} \frac{\partial \chi^2}{\partial a_k} \ , \qquad \alpha_{kl} \equiv \frac{1}{2} \frac{\partial^2 \chi^2}{\partial a_k \partial a_l} \ .$$

This eliminates the factor of 2 in equations 2.37 and 2.39. Equation 2.36 is also re-written as a set of linear equations,

$$\sum_{l=1}^{M} \alpha_{kl} \delta a_l = \beta_k \ , \tag{2.40}$$

which are solved for δa_l.

2.12.3 Steepest-descent method

The steepest-descent method is a much simpler approach than the inverse-Hessian method. At each iteration step, the gradient of the function is computed. The parameter vector $\boldsymbol{a}$ is then adjusted to take a step in the direction of the gradient. In the notation used above,

$$\delta a_l = A\beta_l \ , \tag{2.41}$$

where A is a constant chosen to avoid overshooting the downward slope.

This method is very simple, and does not assume the form of χ^2 may be approximated by a quadratic. It is therefore superior to the inverse-Hessian method far from the minimum. However, close to the minimum it tends to converge unacceptably slowly, and the inverse-Hessian method is preferable.

2.12.4 Levenberg-Marquardt algorithm

The Levenberg-Marquardt algorithm combines the inverse-Hessian and steepest-descent methods, switching between them to exploit their strengths and avoid their weaknesses.

The first stage is to consider the dimensionality of the constant A in equation 2.41. $\chi^2(\boldsymbol{a})$ is dimensionless, and therefore β_k will have dimensions of a_k^{-1}. A must therefore have dimensions of a_k^2. There is exactly one component of the Hessian matrix $\boldsymbol{\alpha}$ which has dimensions purely in terms of a_k^2; this is α_{kk}. This has dimensions of a_k^{-2}. α_{kk}^{-1} is therefore a suitable value for A. To err on the side of caution, though, it is divided by a factor ξ, giving

$$\delta a_l = \frac{\beta_l}{\xi \alpha_{ll}} \ . \tag{2.42}$$

This may be rearranged to give

$$\xi \alpha_{ll} \delta a_l = \beta_l \ , \tag{2.43}$$

which closely resembles equation 2.40. The inverse-Hessian and steepest-descent methods may be combined by defining a new matrix $\boldsymbol{\alpha}'$ such that

$$\begin{aligned} \alpha'_{jj} &= (1+\xi)\alpha_{jj} \ , \\ \alpha'_{jk} &= \alpha_{jk} \qquad (j \neq k) \ . \end{aligned} \tag{2.44}$$

Equation 2.40 is used to compute $\boldsymbol{\delta a}$, using $\boldsymbol{\alpha}'$ instead of $\boldsymbol{\alpha}$. When ξ is large, the off-diagonal terms of $\boldsymbol{\alpha}'$ become less significant and the system tends towards the steepest-descent method. When ξ is small, $\boldsymbol{\alpha}'$ becomes close to $\boldsymbol{\alpha}$ and the system tends towards the inverse-Hessian method.

There remains the problem of setting ξ so that it is small when close to the value of $\boldsymbol{a}$ which will minimize $\chi^2(\boldsymbol{a})$, but large when far from that value. The technique used is as follows.

1. Choose an initial value for ξ. 0.001 is usually sensible.
2. Choose a multiplier $\kappa > 1$. 10 is usually sensible.
3. Compute $\chi^2(\boldsymbol{a})$.
4. Solve for $\boldsymbol{\delta a}$ and compute $\chi^2(\boldsymbol{a} + \boldsymbol{\delta a})$.
5. If $\chi^2(\boldsymbol{a} + \boldsymbol{\delta a}) \geq \chi^2(\boldsymbol{a})$ (i.e. this step has probably been away from the minimum), increase ξ by a factor κ and go back to step 4.
6. If $\chi^2(\boldsymbol{a} + \boldsymbol{\delta a}) < \chi^2(\boldsymbol{a})$ (i.e. this step has probably been towards the minimum), decrease ξ by a factor κ. Update $\boldsymbol{a}$ to use the new value $\boldsymbol{a} + \boldsymbol{\delta a}$. Go back to step 4 with the new $\chi^2(\boldsymbol{a})$.

Thus, if the iteration is converging, ξ will decrease and the inverse-Hessian method, which performs well near the minimum, will come to dominate. If the iteration is failing to converge, ξ will increase until the steepest-descent method, which reliably moves the iteration towards a minimum, comes to dominate.

This method will, by default, never terminate. It is necessary to set a halting condition. If subsequent iterations are changing χ^2 very little, then they are providing no statistically significant improvement in the fit. The algorithm is

therefore halted if iterations are changing χ^2 by only some small amount. This is normally a fractional rather than an absolute change. Were it an absolute change, rounding errors in χ^2 could prevent the algorithm from ever terminating. Fractional changes in χ^2 of order 10^{-5} are commonly used as halting conditions.

2.12.5 Error estimation

Without some measure of uncertainty, the parameters found by model fitting are of limited use. A wide range of techniques for estimating this uncertainty are available. The bootstrap method was used in this research (Efron and Tibshirani, 1986; Press et al., 1992). This is a Monte Carlo technique which probes the probability distribution of the model parameters. It is attractive because it does not require information on the error associated with each data point, nor does it make any assumption about the relationship between the parameters and the model. It is also straightforward to implement. It requires that the data used are independent and identically distributed.

The bootstrap method operates on a data set $\boldsymbol{y} = (\boldsymbol{x}_1, \boldsymbol{x}_2, \ldots, \boldsymbol{x}_n)$, N elements long. When subjected to the model-fitting technique of choice (Levenberg-Marquardt here, but the technique is irrelevant), this produces model parameters $\boldsymbol{a}$. The bootstrap method consists of generating some large number B of simulated N-element data sets $\boldsymbol{y}_i^s$ by randomly drawing, with replacement, N members from $\boldsymbol{y}$. Each of these simulated data sets is then subjected to the same model-fitting technique as the original data set, producing B sets of model parameters $\boldsymbol{a}_i^s$. The probability distribution of these simulated model parameters may be shown to approximate the true probability distribution of the real model parameters $\boldsymbol{a}$.

For a model with a single parameter, the standard deviation of the simulated parameter set approximates the standard error in that parameter. For models with M parameters, the M-dimensional probability distribution may be projected onto each of the axes in turn, reducing the problem to that of a single-parameter model. This is the approach normally used in this research. While simple to implement, it neglects interactions between the various model parameters. The simulated probability distribution is discussed qualitatively, where appropriate.

No pre-packaged code for the bootstrap method was available. It was, however, simple to implement.

References

D. Ascher, P. F. Dubois, K. Hinsen, J. Hugunin, and T. Oliphant. Numerical python. Technical Report UCRL-MA-128569, Lawrence Livermore National Laboratory, 2001. http://numpy.scipy.org.

C. S. Coffey and V. F. DeVost. Impact testing of explosives and propellants. *Propellants, Explosives, Pyrotechnics*, 20(3):105, 1995.

K. R. Coleman. The photography of high temperature events. In H. Schardin and O. Helwich, editors, *Kurzzeitphotographie: Fourth international congress on high speed photography*, pages 32–39. Verlag Dr. Othmar Helwich, Darmstadt, 1959.

M. Czerny and A. F. Turner. Über den Astigmatismus bei Spiegelspektrometern. *Zeitschrift für Physik*, 61:792–797, 1930.

G. D. Danilatos. Foundations of environmental scanning electron microscopy. *Advances in Electronics and Electron Physics*, 71:109–250, 1988.

G. D. Danilatos. Theory of the gaseous detector device in the ESEM. *Advances in Electronics and Electron Physics*, 78:1–102, 1990.

B. Efron and R. Tibshirani. Bootstrap methods for standard errors, confidence intervals, and other measures of statistical accuracy. *Statistical Science*, 1:54–75, 1986.

W. G. Fastie. A small plane grating monochromator. *Journal of the Optical Society of America*, 42(9):641–647, 1952.

L. A. Feldkamp, L. C. Davis, and J. W. Kress. Practical cone-beam algorithm. *Journal of the Optical Society of America A*, 1(6):612–619, 1984. doi: 10.1364/JOSAA.1.000612.

J. E. Field, G. M. Swallowe, and S. N. Heavens. Ignition mechanisms of explosives during mechanical deformation. *Proceedings of the Royal Society of London, Series A*, 382:231, 1982.

B. R. Garfield and M. J. Riches. Ultranac – a new programmable image converter framing camera. In P. W. Fuller, B. Garfield, and J. Rendell, editors, *19^{th} International Congress on High-Speed Photography and Photonics*, volume 1358 of *SPIE*, pages 290–299. SPIE, 1991.

J. I. Goldstein, D. E. Newbury, P. Echlin, D. C. Joy, C. E. Lyman, E. Lifshin, L. C. Sawyer, and J. R. Michael. *Scanning Electron Microscopy and X-Ray Microanalysis*. Springer, third edition, 2003.

D. A. Gorham, P. H. Pope, and J. E. Field. An improved method for compressive stress-strain measurements at very high strain rates. *Proceedings of the Royal Society of London, Series A*, 438:153–170, 1992.

G. T. Gray. Classic split-Hopkinson pressure bar testing. In H. Kuhn and D. Medlin, editors, *Mechanical Testing and Evaluation*, volume 8 of *ASM Handbook*, pages 462–476. ASM International, Materials Park, Ohio, 2000.

S. N. Heavens and J. E. Field. The ignition of a thin layer of explosive by impact. *Proceedings of the Royal Society of London, Series A*, 338:77–93, 1974.

R. Holtom, G. P. Hopkins, and P. M. Gundry. Surface studies of multialkali antimonide (S20/S25) photocathodes. *Journal of Physics D*, 12:1169–1180, 1979.

B. Hopkinson. A method of measuring the pressure produced in the detonation of high explosives or by the impact of bullets. *Philosophical Transactions of the Royal Society of London A*, 213:437–456, 1914.

P. Horowitz and W. Hill. *The Art of Electronics*. Cambridge University Press, second edition, 1989.

E. Jones, T. Oliphant, P. Peterson, et al. SciPy: Open source scientific tools for Python, 2001–. http://www.scipy.org.

REFERENCES

A. C. Kak and M. Slaney. *Principles of Computerized Tomographic Imaging*. IEEE Press, 1988.

G. F. Knoll. *Radiation detection and measurement*. John Wiley and sons, second edition, 1989.

D. W. Marquardt. An algorithm for least-squares estimation of nonlinear parameters. *Journal of the Society for Industrial and Applied Mathematics*, 11: 431–441, 1963.

W. H. Press, S. A. Teukolsky, W. T. Vetterling, and B. P. Flannery. *Numerical recipes in Fortran: The art of scientific computing*. Cambridge University Press, second edition, 1992.

S. F. Ray, editor. *High Speed Photography and Photonics*. Focal Press, Oxford, 1997.

C. R. Siviour. *High strain rate properties of materials using Hopkinson bar techniques*. PhD thesis, University of Cambridge, 2005.

AMCP 706-180. *Engineering Design Handbook: Principles of Explosive Behavior*. US Army Materiel Command, 1972.

T. Williams, C. Kelley, and many others. Gnuplot 4.4: an interactive plotting program. http://www.gnuplot.info/, March 2010.

J. L. Wiza. Microchannel plate detectors. *Nuclear Instruments and Methods*, 162:587–601, 1979.

E. K. Zavoisky and S. D. Fanchenko. Image converter high-speed photography with 10^{-9}–10^{-14} sec time resolution. *Applied Optics*, 4:1155–1167, 1965.

Chapter 3

Materials and microstructure

The following sample materials were used in this research. Figure 3.1 shows these materials.

- Low density pure ammonium nitrate prills, produced by the prilling process described in chapter 1, section 1.1. These are made for use in ANFO explosives. They were supplied by Orica as approximately 2 mm roughly spherical pellets, both with and without an organic coating (Lilamin AC-59P, a blend of anionic and cationic surface-active agents) to reduce caking. They are referred to as coated or uncoated Orica prills.

- Mixed ammonium nitrate and dolomite pellets, produced using fluid-bed granulation. These are intended for use as fertilizer, and meet the definition of "Calcium Ammonium Nitrate" in EEC directive 76/116/EEC. They were purchased from a garden centre, and take the form of approximately 4 mm, irregular, rounded pellets. They are referred to as agricultural pellets.

- High density pure ammonium nitrate prills. These are intended for use as fertilizer. Due to their popularity in improvised explosive devices, they are difficult to acquire in the UK. They were supplied by [dstl], as approximately 4 mm, irregular, rounded pellets. They are referred to by their brand name, Nitram.

- Fertilizer pellets containing a variety of fertilizers, not including ammonium nitrate. These were purchased from a garden centre, and used as an inert

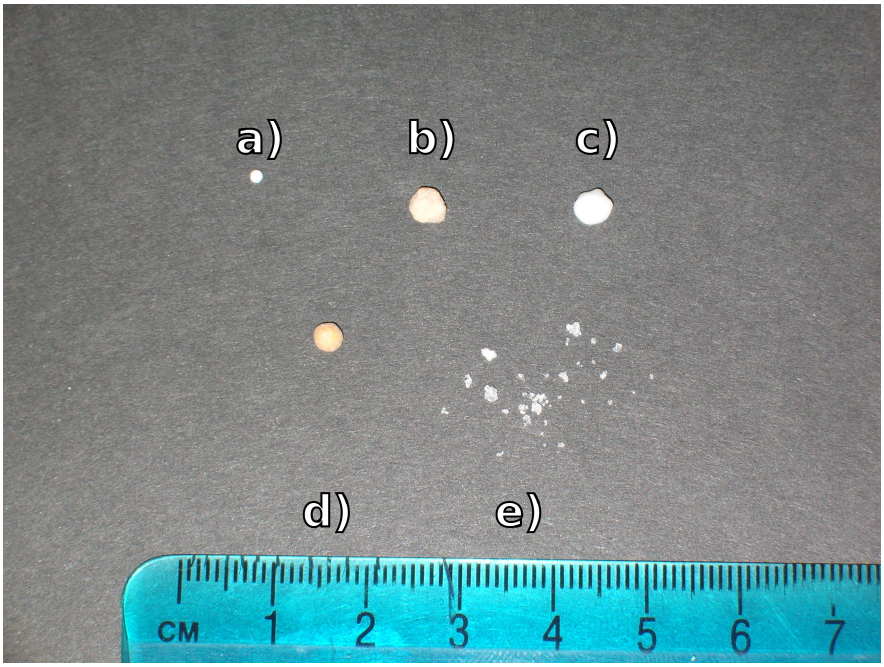

Figure 3.1: Photograph showing the various materials studied. a) Orica explosive prill. b) Agricultural Calcium Ammonium Nitrate fertilizer pellet. c) Nitram fertilizer prill. d) Westland fertilizer pellet. e) Analytical reagent grade ammonium nitrate crystals.

mock for the other pellets. They take the form of approximately 4 mm roughly spherical pellets. They are referred to by their brand name, Westland Feed-All Plant Food, or simply as Westland.

- Analytical reagent grade ammonium nitrate. This was purchased from Aldrich. It was supplied as approximately 1 mm crystals, which were typically ground and sieved before use. This is referred to as ground ammonium nitrate.

If cavity collapse is an important hot-spot mechanism in these materials, the microstructure of the materials studied will be important to understanding their behaviour. The primary tool used to study this was environmental scanning electron microscopy (ESEM). Some initial studies with X-ray microtomography were also performed. The distribution of the different components of the Westland and agricultural materials was studied using energy-dispersive X-ray spec-

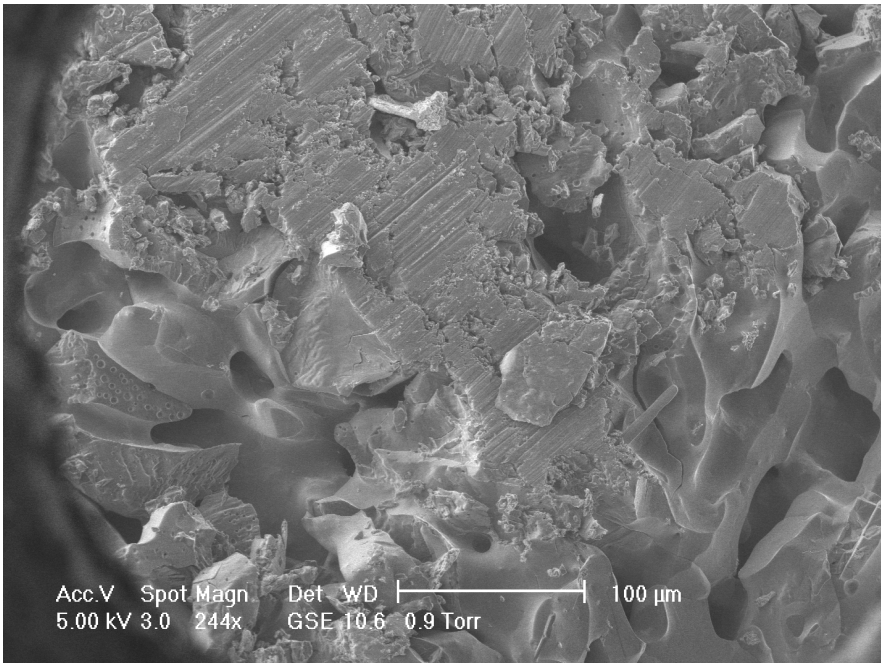

Figure 3.2: ESEM image showing razor damage in uncoated Orica prill. The damage is visible as the region of parallel stripes to the top left.

troscopy (EDX).

3.1 Sample preparation

To image the interior of prills with ESEM and EDX, they were bisected with a razor blade. They were then glued, cut side up, to a stud which was held by the sample stage of the microscope. The glue was a conductive paste known as silver dag. The razor blade caused considerable damage to the microstructure of the prill, as shown in figure 3.2. This damage was, however, localized, and easily identified by the pattern of parallel lines left by imperfections in the razor's edge. To image the surface of prills, the initial sectioning was omitted and the intact prill was glued to the sample stud.

No preparation was required for microtomography.

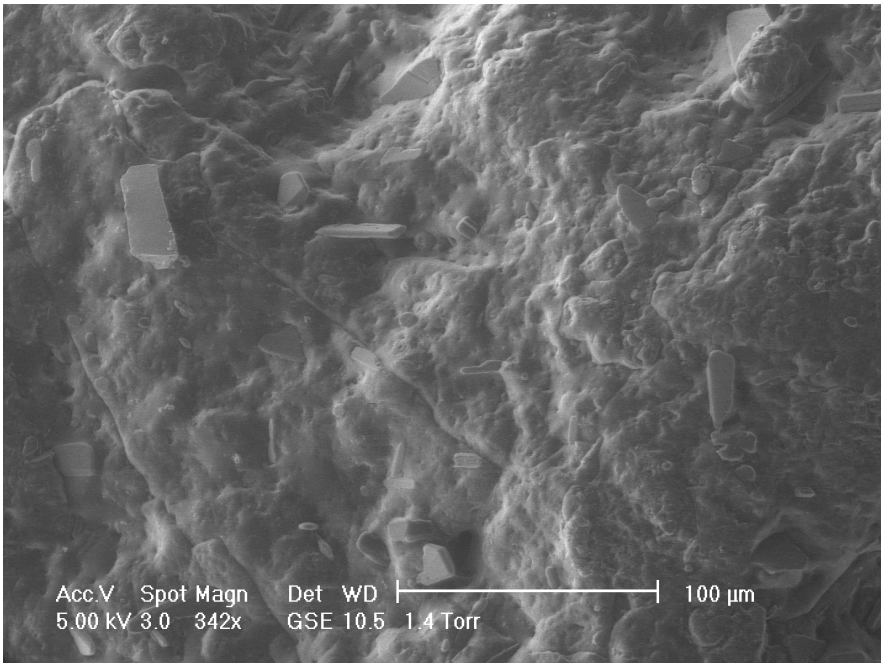

Figure 3.3: ESEM image of outer surface of uncoated Orica prill.

3.2 Orica prills

Figures 3.3 and 3.4 show ESEM images of the outer surface of uncoated and coated Orica prills, respectively. The organic coating is visible as a change in the texture of the surface.

The internal microstructures of coated and uncoated Orica prills are very similar. This is unsurprising, as the coating is applied after the prilling process, and the latter is identical for both kinds of prill. Figure 3.5 shows a typical section of the internal structure of an Orica prill. It has a very high density of voids with sizes of the order of tens of microns. These voids are large enough to form critical hot spots when they collapse, as discussed in chapter 1, section 1.2.2. A high density of such hot spots will spread reaction through the material more quickly than a low density. This is relevant to the performance of a non-ideal explosive, such as ammonium nitrate, as the duration of the reaction zone is comparable to the time taken for reaction to spread. A higher density of critical hot spots is therefore likely to increase the detonation velocity of the explosive.

The voids in the Orica prills appear to form an interconnected network. This

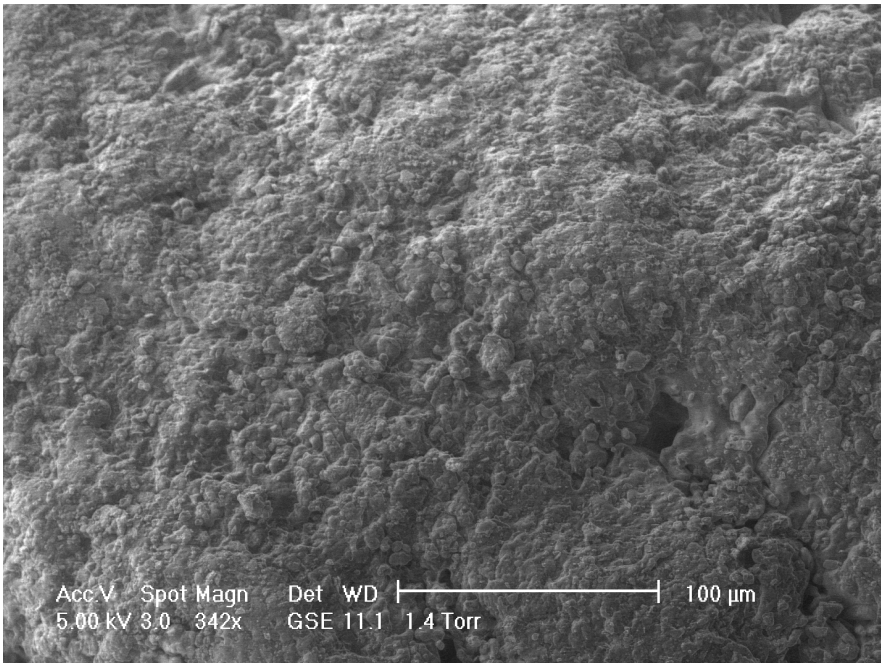

Figure 3.4: ESEM image of outer surface of coated Orica prill.

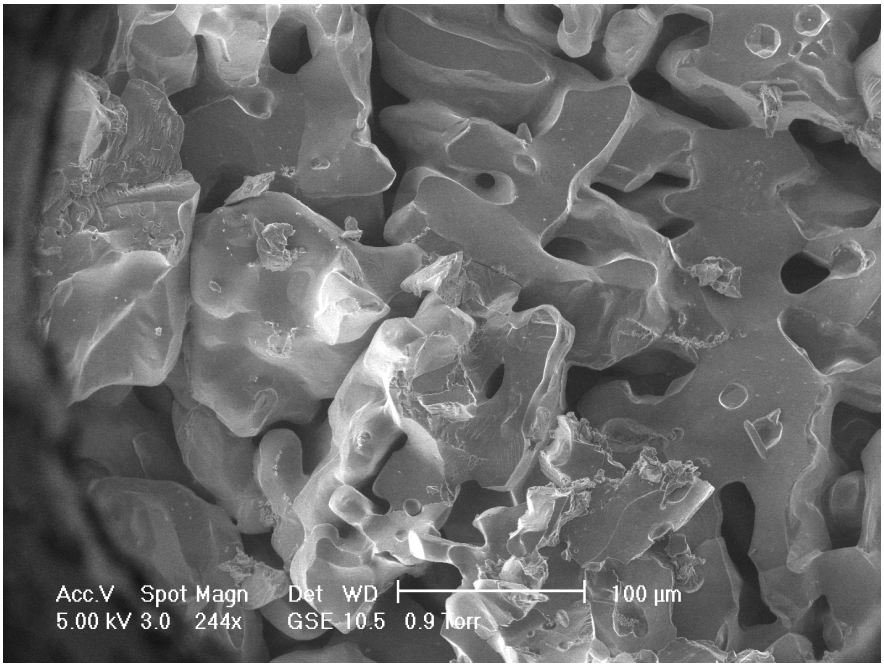

Figure 3.5: ESEM image of body of coated Orica prill, showing network of voids which permeates the material.

may allow fuel oil to penetrate the prill easily, reducing the average distance between the oxidizing ammonium nitrate and the fuel. This will in turn increase the heat of reaction within the reaction zone, again increasing the detonation velocity.

Figure 3.6 shows a tomographic slice approximately through the centre of an Orica uncoated prill. It shows the interconnected network of voids, as well as the expected central void. Figure 3.7 uses ESEM to show the microstructure near that void in another Orica prill. The plates of ammonium nitrate that make up the prill appear to have aligned with the wall of the central void. The microstructure also appears to have become considerably more dense. Figure 3.8 shows a similar effect at the outer edge of the prill.

Although X-ray microtomography is intended to show the interior structure of a sample, figure 3.6 shows a few indentations in the exterior. Marked with a J on figure 3.6, these indentations could, if shocked from the correct direction, produce a jet (see chapter 1, section 1.2.2.4) directed away from the prill. While this effect could not cause a hot spot in the originating prill, many prills are often combined to form a bed. In such a prill bed, the jet from an indentation on one prill could strike an adjacent prill, creating a hot spot.

Figure 3.7 also shows some pitting of the ammonium nitrate surface. This could be due to beam damage. To determine the effect of beam damage, the beam current was increased and the beam was restricted to a small area of the sample. This would be expected to increase the frequency of any artefacts of beam damage in that area. No such increase in the density of pits was observed. This leaves two possible explanations for the pits. First, they could be small pores present within the prill structure. Second, they could be due to corrosion of the ammonium nitrate surface by the low-pressure water vapour in the ESEM. Unfortunately the X-ray microtomograph has insufficient resolution to detect these pores and discriminate between these two possibilities.

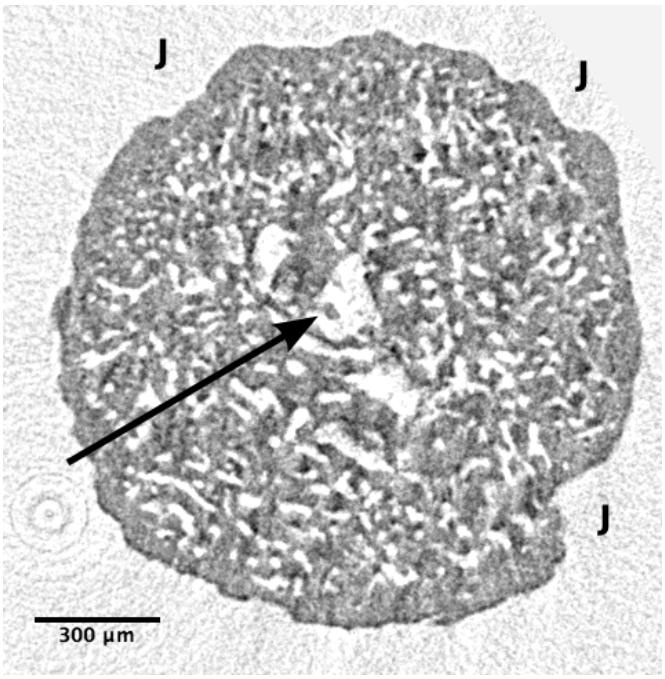

Figure 3.6: Tomographic slice approximately through the centre of an uncoated Orica prill, showing the central void (arrowed) and exterior indentations (marked with J).

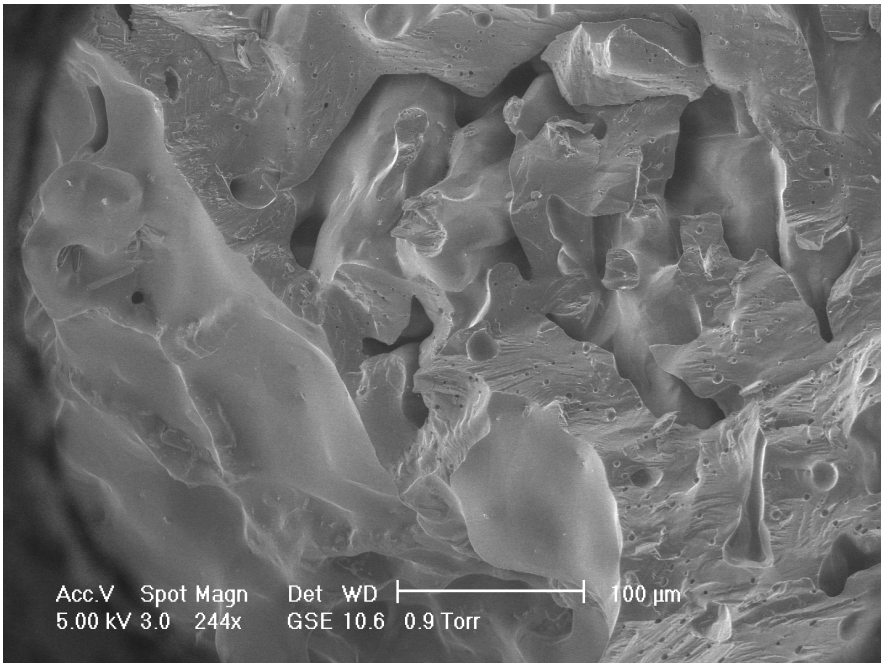

Figure 3.7: ESEM image of body of coated Orica prill, showing microstructure around the central void. The void itself is to the bottom left of the image.

3.3 Agricultural calcium ammonium nitrate pellets

Figure 3.9 shows a typical region of the interior of an agricultural pellet. Here there are fewer, larger voids, and the voids do not appear to form any kind of network. It is possible that these "voids" are in fact caused by the material failing along a line of weakness during sample preparation. The pitting observed in the Orica prills is also present here. There is also no sign of the plate-like structures present in the Orica prills, with blocky crystals dominating instead. There was no sign of a large central void. As the pellets were not produced by prilling, this is unsurprising.

These pellets contain a mixture of ammonium nitrate and dolomite grains, to reduce explosive sensitivity. Dolomite is a calcium magnesium carbonate. It can therefore be distinguished from ammonium nitrate using element mapping: dolomite contains no nitrogen, and ammonium nitrate contains no calcium or

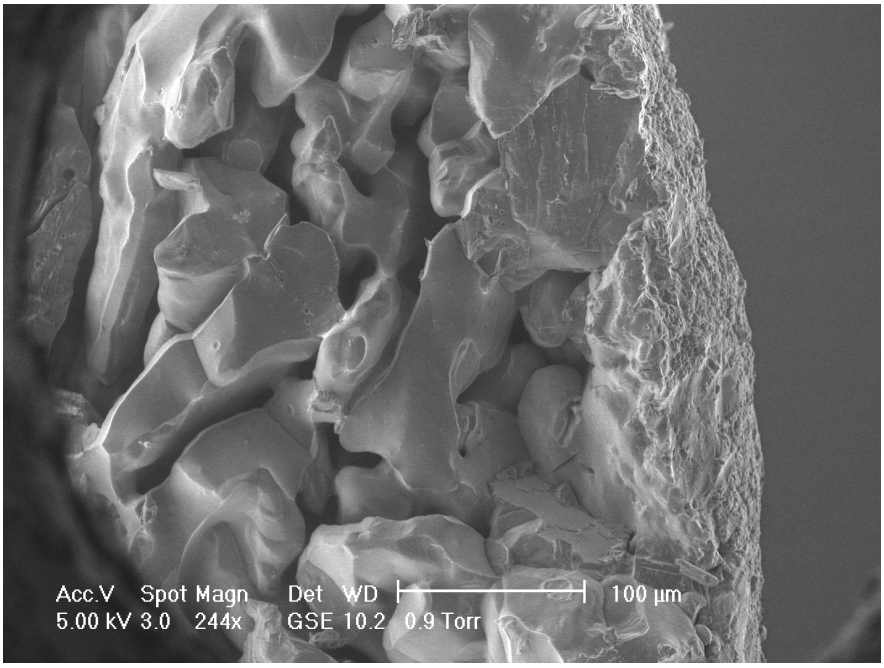

Figure 3.8: ESEM image of body of coated Orica prill, showing microstructure near the outer surface of the prill. The main body of the prill is left of the field of view.

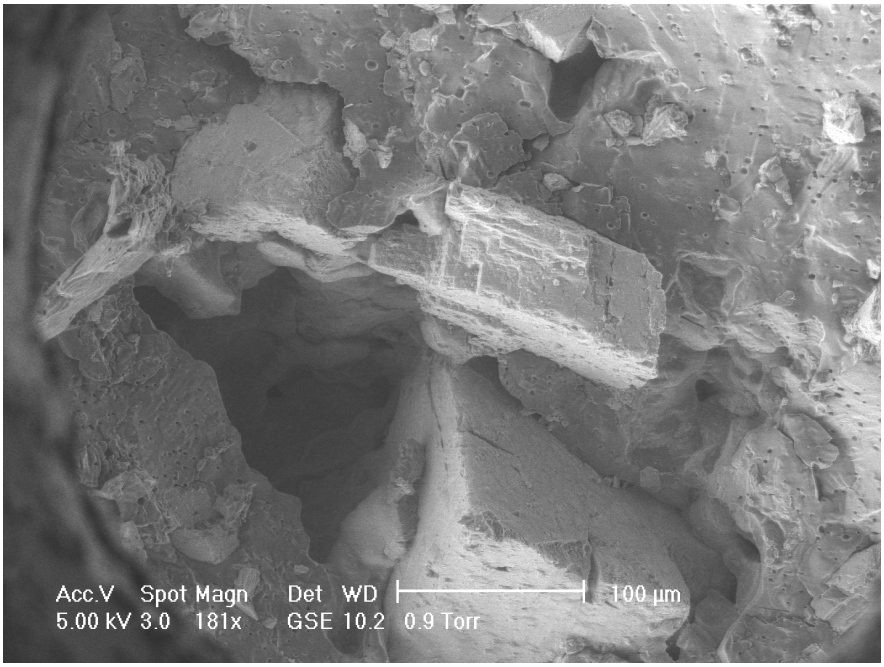

Figure 3.9: ESEM image of the interior of an agricultural calcium ammonium nitrate pellet.

magnesium. The sizes of the dolomite and ammonium nitrate crystals may be relevant to the energetic properties of these pellets. Figure 3.10 shows an ESEM image of a region within an agricultural pellet. Figure 3.11 shows a composite image of the same region generated using EDX. It shows a pair of dolomite grains roughly 50 μm in size in the centre, surrounded by larger ammonium nitrate grains. There are a few smaller dolomite grains scattered around the field of view.

3.4 Nitram prills

Figure 3.12 shows a typical patch of the microstructure of a Nitram prill. The microstructure appears to be very dense, with very few passages down which fuel oil or hot gases could pass. The few passages that exist are also considerably narrower than those in the Orica prills. Although this material was produced by a prilling process, there was no evidence of a central void. There were, however,

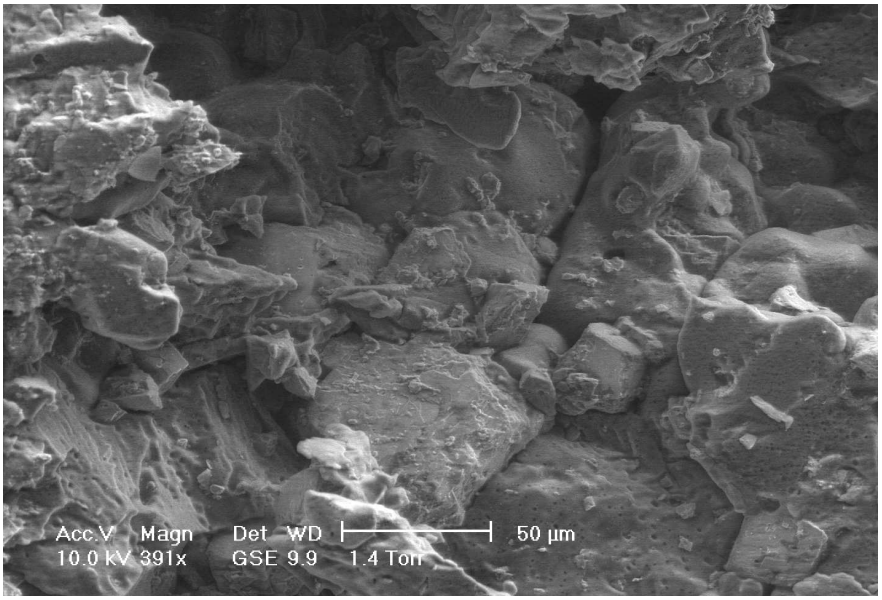

Figure 3.10: ESEM image of the interior of an agricultural calcium ammonium nitrate pellet. This image covers the area shown in the composite EDX image, figure 3.11.

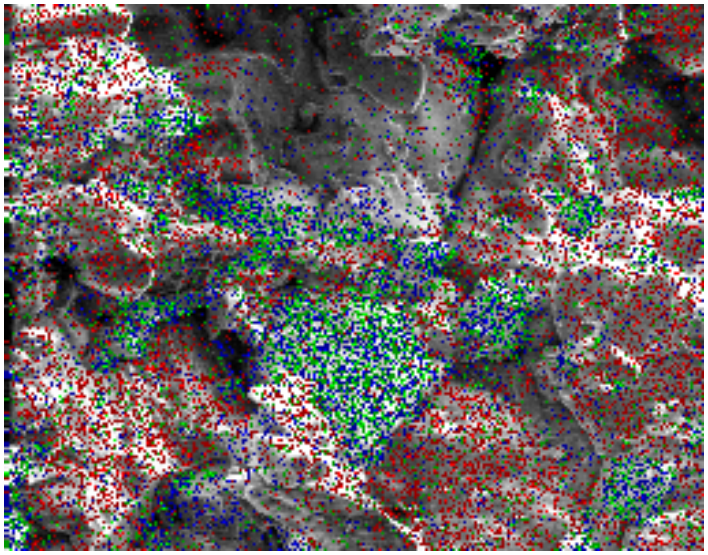

Figure 3.11: Composite image of the interior of an agricultural calcium ammonium nitrate pellet. The background image was generated using ESEM. The green pixels indicate that magnesium was detected in that pixel; the blue, calcium; and the red, nitrogen. Green and blue pixels therefore correspond to dolomite, and red pixels to ammonium nitrate.

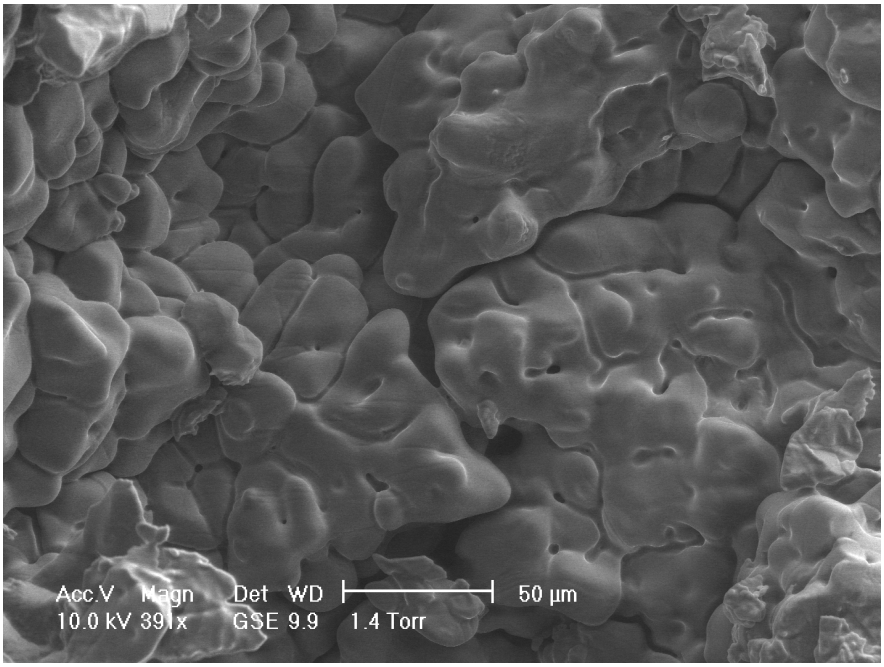

Figure 3.12: ESEM image of the microstructure of a Nitram prill.

several smaller voids of the kind shown in figure 3.13. As with the calcium ammonium nitrate pellets, these voids could be an artefact of sample preparation.

3.5 Westland pellets

The advertised composition of these pellets is shown in table 3.1. This brand was chosen because its low nitrate content implied a low ammonium nitrate content, which in turn suggested it might provide a usable inert mock for ammonium nitrate prills and pellets. The product as purchased consisted of orange-brown roughly spherical pellets, roughly 4 mm in diameter, mixed with black irregular pellets a few millimetres long. These black pellets were ignored, as their shape rendered them obviously unsuitable mocks for the roughly spherical AN pellets and prills. Their size and distinctive colour made them easy to remove from any experiments using this material.

Figure 3.14 shows a patch of the microstructure of one of the larger orange pellets. It appears to contain very few voids, and there is, again, no evidence of a

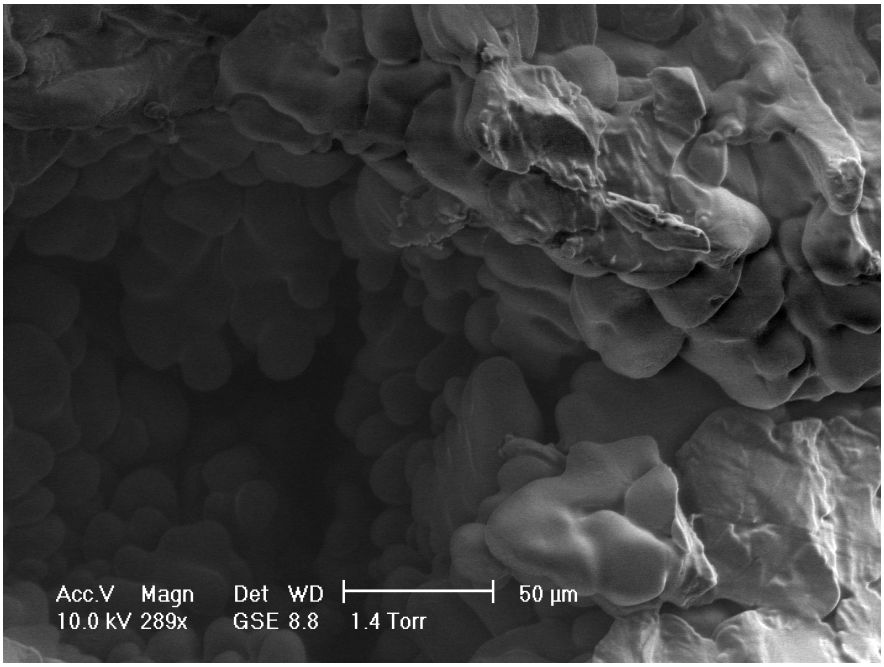

Figure 3.13: ESEM image of a void within a Nitram prill. The void is to the lower left of the image.

connected network of voids. The orange colour of the pellet was due entirely to a coating applied to the outside; the interior of the pellet was white. This coating was probably intended to slow the release of nutrients from the fertilizer pellet.

Figure 3.15 shows the spatially-unresolved EDX spectrum for this pellet. This suggests that the pellet is almost pure P_2O_5. Close inspection of the Westland pellets suggested that there were at least three visually distinct types of orange-brown roughly spherical pellet: the large orange ones studied here, smaller, paler ones, and smaller, darker ones. Figures 3.16 and 3.17 show the EDX spectra for the paler and darker small pellets, respectively. These suggest that the paler pellets consist of potassium carbonate[1], and that the darker consist of urea.

Figure 3.18 shows a region near the centre of one of the potassium carbonate pellets. The large void suggests that the pellet was produced by prilling. There

[1]Note that, while the advertised composition includes potassium oxide, this is simply an assaying convention; typically other potassium compounds are substituted (potassium carbonate in this case), and the mass of potassium oxide which would contain an equal amount of potassium is quoted.

Component	Percentage
Nitric nitrogen	1.3 %
Ammoniacal nitrogen	8.3 %
Ureic nitrogen	5.4 %
Phosphorous pentoxide	6.0 %
Potassium oxide	30.0 %
Water soluble boron	0.025 %
Total copper	0.012 %
Total iron	0.150 %
Total manganese	0.075 %
Total zinc	0.150 %
Total chlorine	< 0.600 %

Table 3.1: Advertised composition of Westland Feed-All Plant Food.

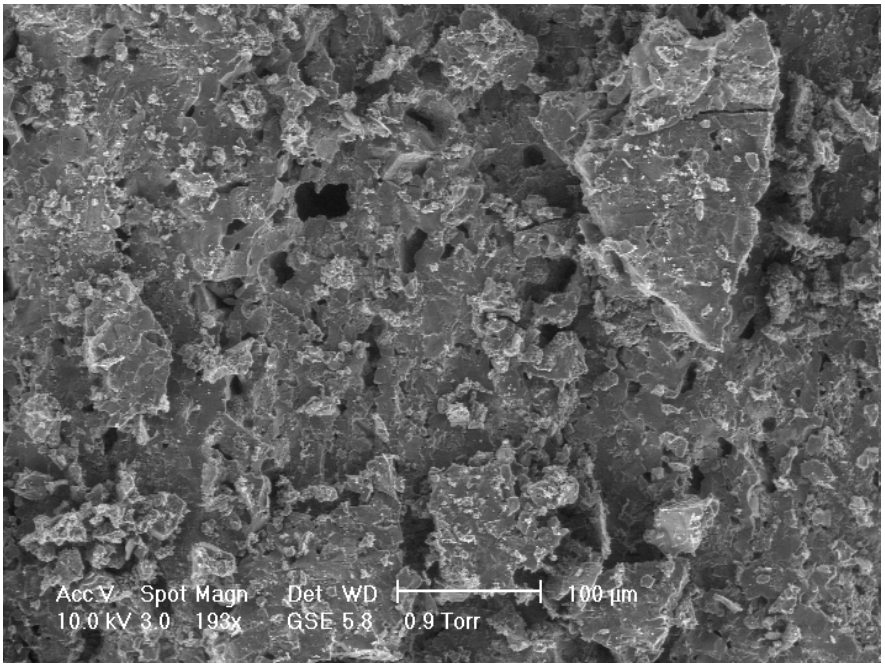

Figure 3.14: ESEM image of the microstructure of one of the larger Westland pellets.

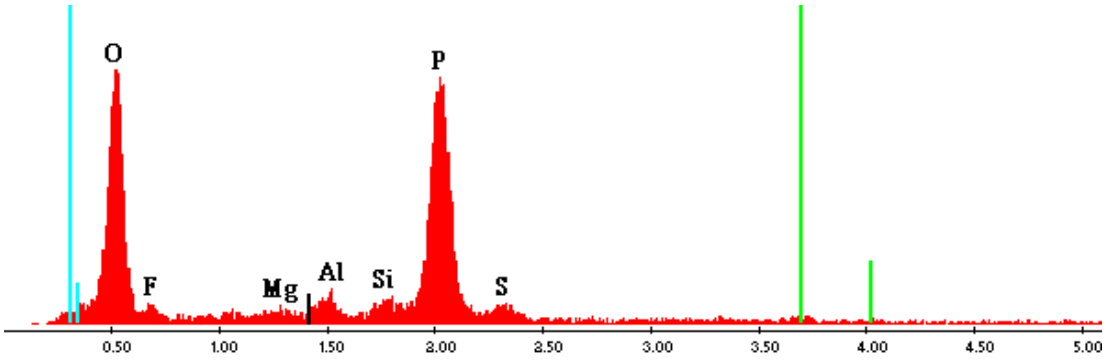

Figure 3.15: Spatially-unresolved EDX spectrum of one of the larger Westland pellets. Horizontal scale is X-ray energy in keV. Labels indicate the element to which each peak corresponds.

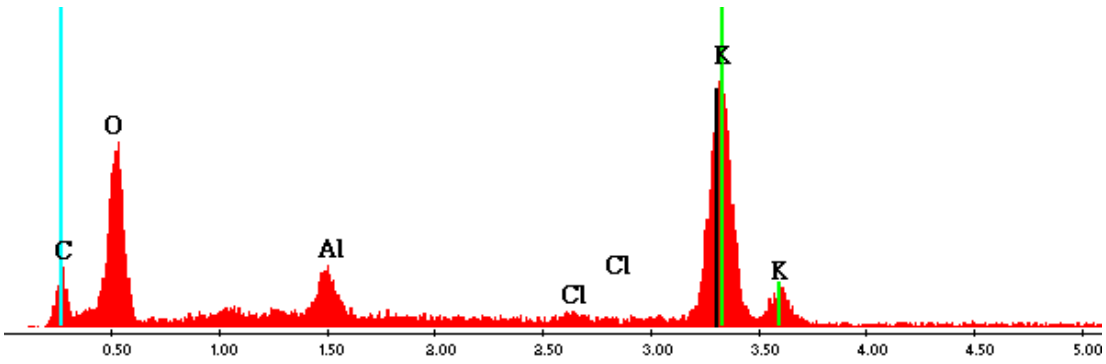

Figure 3.16: Spatially-unresolved EDX spectrum of one of the small, pale Westland pellets. Horizontal scale is X-ray energy in keV. Labels indicate the element to which each peak corresponds.

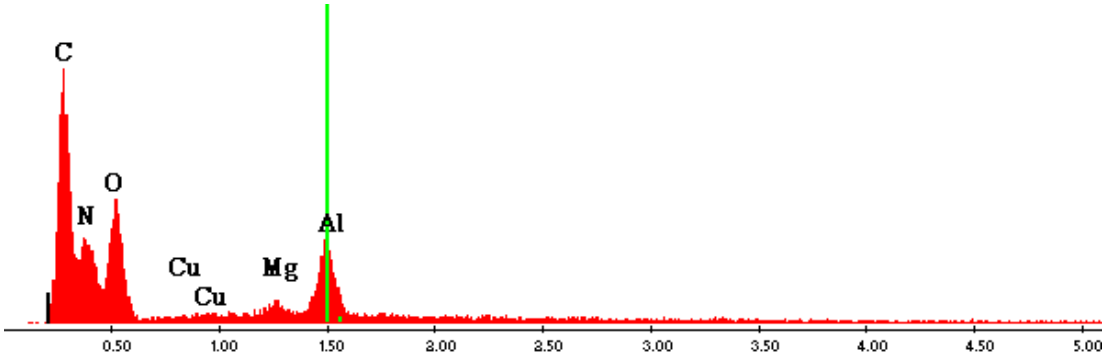

Figure 3.17: Spatially-unresolved EDX spectrum of one of the small, dark Westland pellets. Horizontal scale is X-ray energy in keV. Labels indicate the element to which each peak corresponds.

appears to be very little porosity apart from this void. Figure 3.19 shows a similar region on one of the urea pellets, again suggesting that the pellet is a prill and indicating very low porosity.

3.6 Conclusions

- Orica's explosive prills have a much more open microstructure than agricultural grades of ammonium nitrate, with a network of connected voids.
- This open microstructure allows good mixing between fuel and ammonium nitrate in ANFO formulations.
- This open microstructure also increases the density of hot spots when Orica prills are shocked.
- Features of the exterior of Orica prills could lead to inter-prill jetting and hot spot formation when beds of these prills are shocked.
- The dense microstructures of agricultural ammonium nitrate formulations increase their mechanical strength and packing density, both desirable features in a commercial material.
- EDX is a useful technique for studying the physical distribution of chemicals in these samples.

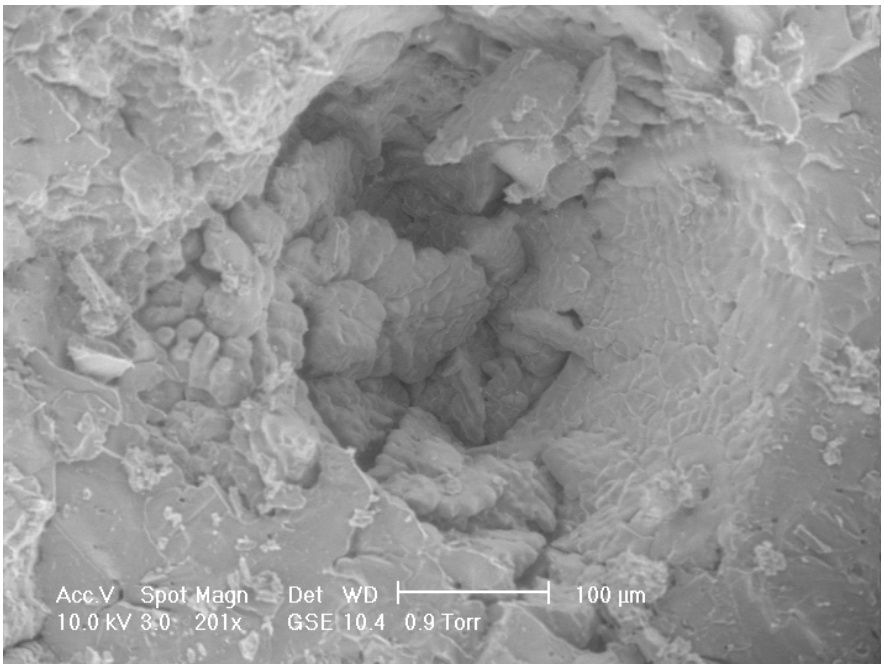

Figure 3.18: ESEM image of the microstructure near the centre of a Westland potassium carbonate pellet, showing central void.

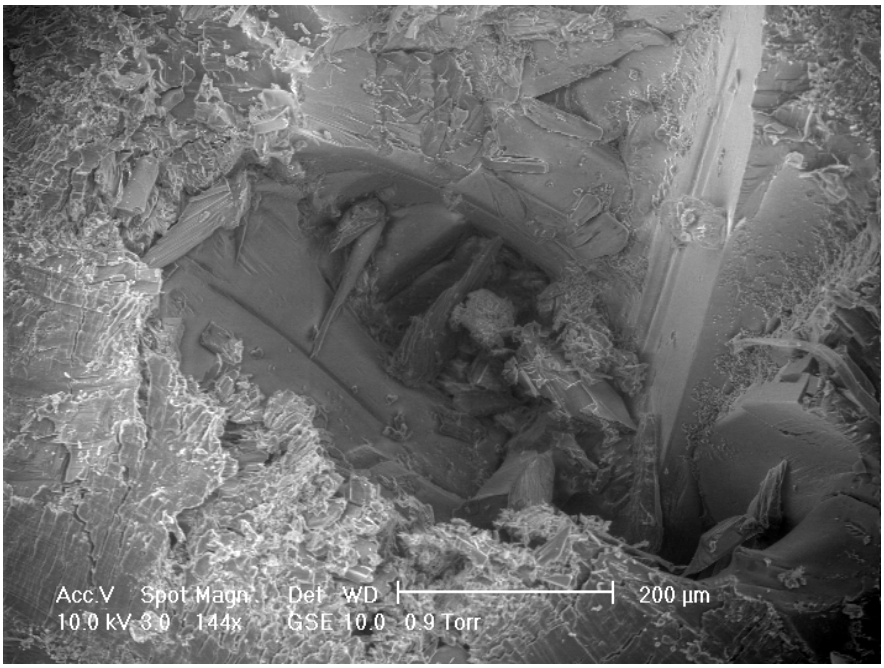

Figure 3.19: ESEM image of the microstructure near the centre of a Westland urea pellet, showing central void.

- It is difficult to study internal voids using ESEM, as the sectioning technique used may introduce false voids.
- The resolution of X-ray microtomography is sufficient to study most, but not all, internal voids in the prilled samples studied here.
- Westland plant food is likely to be a suitable mock for agricultural grades of ammonium nitrate. It may be less suitable for explosive grades.

Chapter 4

Compaction

Compaction describes the various processes by which a porous material becomes less porous in response to load. Several of these processes (for example, cavity collapse) are also hot spot mechanisms. Study of the compaction behaviour of ammonium nitrate is therefore relevant to understanding hot spots in ammonium nitrate.

Compaction is generally considered in terms of the relationship between applied pressure and porosity. Porosity can be expressed either as void fraction (the fraction of the bulk material that is empty) or as fractional theoretical maximum density (the density of the bulk material as a fraction of the density the material would have, were all the voids filled).

Several techniques developed for compressive testing of materials can be modified to study compaction. This research used a screw-driven instrumented press to study compaction at a strain rate of roughly $10^{-4}\,\mathrm{s}^{-1}$ and a drop weight to study compaction at a strain rate of roughly $100\,\mathrm{s}^{-1}$. This research also used a split Hopkinson pressure bar system (SHPB), with limited success.

4.1 Experimental methods

4.1.1 Quasi-static compaction

A confinement cell of the form shown in figure 4.1 was constructed. Initially, the end cap and outer jacket were made from PMMA, and the plunger was made

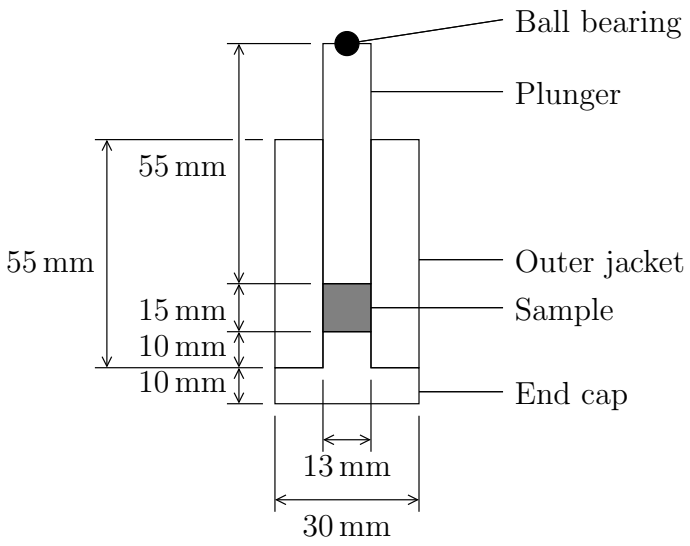

Figure 4.1: Confinement cell used for compaction experiments. All measurements are approximate. Load is applied vertically to the ball bearing.

from mild steel. Early experiments, though, found that the plunger would plough into the soft outer jacket, damaging it. This also invalidated the results from that experiment: the quantity probed was the resistance of PMMA to cutting by mild steel, rather than the resistance of the sample to compaction. The confinement cell was therefore remade using stainless steel for all components, which was found to eliminate the problem.

The ball bearing was intended to ensure there was a single point of contact between the plunger and the driving force. This would ensure that the loading was entirely axial. However, it was found that the ball bearing indented the sample-facing surface used. It was therefore removed for most of these experiments.

For some of the later experiments, the sample-facing surface was replaced with a synthetic diamond anvil and the ball bearing replaced. This presented the reverse problem, that the ball bearing deformed. If the ball bearing was rotated slightly between tests so that the flat surface thus produced did not contact the diamond anvil, this deformation was found to be repeatable. The deformation was therefore simply included in the compliance measurement for the system. Whether data were gathered with or without a ball bearing is indicated in the results.

The load was provided by an Instron 4466 as described in chapter 2, section 2.4. All experiments were performed at a constant loading rate of $0.333\,\mathrm{mm\,min^{-1}}$, and a maximum force of 10 kN. The compliance was obtained by placing the confinement cell in the Instron without any sample. This ensured that any elastic deformation of the plunger would be accounted for in the compliance.

A known mass m_s of the sample material was poured into the confinement cell, and the plunger added gently. The plunger was then held in place as the system was shaken several times, then allowed to fall onto the sample bed. The protrusion of the plunger from the confinement cell was measured; combined with the known dimensions of the various components of the confinement cell, this gave the initial sample length l_0.

The filled confinement cell was then placed in the Instron and loaded. The moment when the recorded force first exceeded the load cell's noise level of 0.27 N was taken to be the moment of contact between the loading surface and the plunger. Given that the weight of the plunger was approximately 6 N, this seemed both reasonable and unlikely to lead to undetected deformation of the sample bed.

It was possible to recover the compacted pellet after an experiment. The length of the recovered pellet was measured with calipers to assess the reliability of the length measured during the experiment.

4.1.1.1 Analysis

The goal is to relate the pressure applied to the sample to the fractional theoretical maximum density (TMD) of the sample. This is quite straightforward in the Instron, which gives the applied force F and the change in length Δl directly. Having measured the initial length l_0 of the sample, the mass m_s of the sample, and the cross-sectional area A of the confinement, the bulk density ρ of the sample is given by

$$\rho = \frac{m_s}{A(l_0 - \Delta l)} \ . \tag{4.1}$$

The fractional TMD can be recovered easily if the TMD is known. For Nitram and Orica prills, this TMD is that of ammonium nitrate, which is well known. For Westland and agricultural pellets, the TMD was assumed to be the bulk density after pressing to 50 kN.

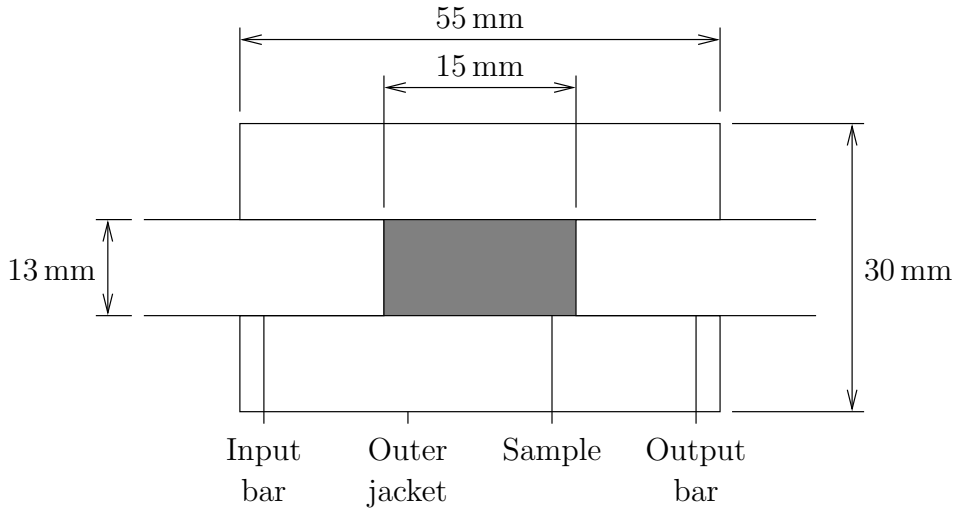

Figure 4.2: Arrangement of sample and confinement for SHPB compaction testing. All measurements are approximate.

Recovering the applied pressure is simple: the applied force F and the area A over which that force is applied are known, so the pressure P is given by

$$P = \frac{F}{A} \, . \tag{4.2}$$

4.1.2 Higher rate compaction: SHPB

An SHPB system, as described in section 2.7, was used in an attempt to probe compaction at higher strain rates than the Instron. To achieve this, a tubular PMMA confinement was constructed and arranged as shown in figure 4.2. Aluminium bars were used throughout this experiment.

The confinement was filled with a known mass m_s of sample material, and the bars of the SHPB inserted to seal it. The bars were then gently pressed together as the confinement was rotated, until the sample bed was firmly held in place. The length of the sample l_0 was then measured by aligning calipers with the bar ends visually. The lensing effect of the PMMA ameliorated the associated parallax errors, but they still reduced the accuracy of the measurement considerably. This somewhat unsatisfactory measurement technique was chosen because it did not permit rearrangement of the sample bed.

The confined sample bed was then subjected to an SHPB test. The degree of compaction achieved during this test was small, so the experiment was repeated on the compacted specimen. After a few such tests, the sample was sufficiently compacted that it held firmly to the walls of the confinement. Its length could then be measured using the more precise approach of plunger protrusion employed in the quasi-static tests. Typically, ten tests on a given sample were required to reach 85–90 % TMD.

4.1.2.1 Analysis

Much of the analysis from chapter 2, section 2.7.2 is applicable to the problem of recovering a pressure-porosity relation from these experiments. Equation 2.19 gives the strain rate in the bed:

$$\dot{\varepsilon} = \frac{\dot{s_1} - \dot{s_2}}{l} = \frac{c_b(\varepsilon_r - \varepsilon_i + \varepsilon_t)}{l}. \tag{2.19}$$

Just as in conventional materials testing, this can be numerically integrated to find the sample length l as a function of time, given the measured initial sample length l_0. The bulk sample density ρ, and hence the fractional TMD, can then be recovered, almost exactly as in section 4.1.1.1.

The force applied to the sample can be found from equations 2.20 and 2.21:

$$F = \tfrac{1}{2}AY(\varepsilon_i + \varepsilon_r + \varepsilon_t). \tag{4.3}$$

This analysis differs from the conventional SHPB analysis, though, in that it assumes the cross-sectional area A_s of the sample is constant and equal to the bar diameter, and that the volume $A_s l$ of the sample is not conserved. The applied pressure P is then given by

$$P = \tfrac{1}{2}Y(\varepsilon_i + \varepsilon_r + \varepsilon_t). \tag{4.4}$$

4.1.3 Higher rate compaction: drop weight

The short duration of the loading pulse in the SHPB severely limited the degree of compaction reached in a single experiment. Repeating the SHPB experiments

to achieve a higher degree of compaction produced results which were difficult to interpret and suffered from a low signal-to-noise ratio. The drop weight, with its much longer loading pulse, seemed an obvious way to avoid this problem.

The confinement cell shown in figure 4.1, without a ball bearing, was used for these experiments. The sample was weighed, loaded and measured as in section 4.1.1. The loaded confinement was placed in the drop weight as shown in figure 4.3. The length of the confinement cell required the removal of the upper anvil. The confinement cell was held securely by the anvil guide; combined with the length of the outer jacket and plunger, this reduced the off-axis forces applied to the system.

Initially, the analysis presented in chapter 2, section 2.6.3 was used to find the sample length, and the fractional TMD was calculated from this. This analysis showed that the sample was being compacted past its TMD by quite modest forces. While this is not impossible for samples of a sufficiently small bulk modulus K, it was thought far more likely that accumulating errors in the analysis resulted in the length of the sample being underestimated. A separate method for measuring the sample length was therefore sought.

4.1.3.1 The line laser

A line laser projects a fan of laser light. With appropriate optics, this can be used to measure the position of an opaque obstruction, such as the falling mass in a drop weight. The line laser used in this research was a Power Technology, Inc. PM01(635-5)L71. This produces a fan whose intensity is uniform along its length, apart from lobes at the ends which are easily eliminated with a mask. It was arranged using optical benches as shown in figure 4.4.

When the weight passes through this fan, it will reduce the intensity of the light falling on the photodiode as shown in figure 4.5. The photodiode will then produce an output dependent on the position of the weight. Assuming the optics are ideally aligned, as depicted here, the output will be proportional to the height of the weight above the bottom of the fan. In practice such alignment was difficult to achieve.

The quantity to be measured by the line laser is the total length of the sample.

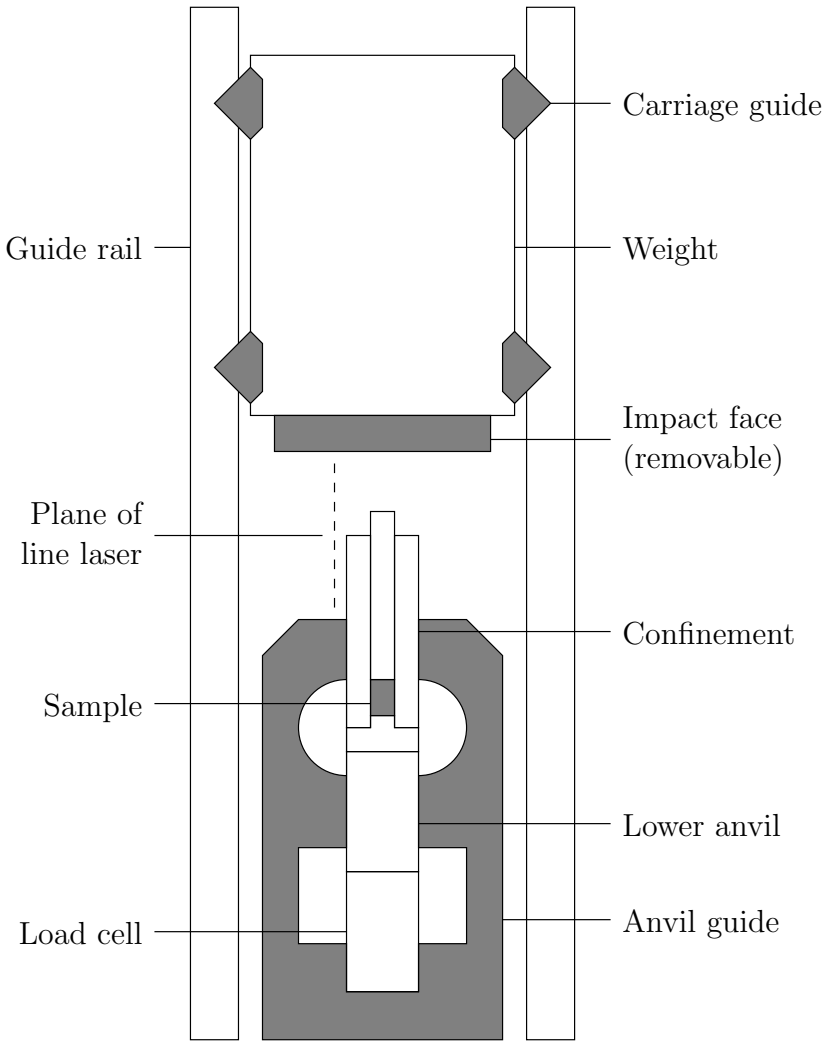

Figure 4.3: Arrangement of drop weight used for compaction experiments. Not to scale.

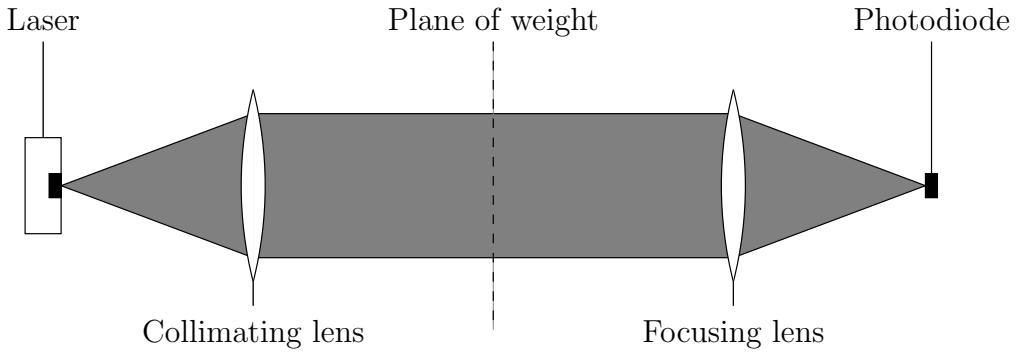

Figure 4.4: Arrangement of line laser used to measure position of drop weight. Weight passes along the plane indicated, partially blocking the laser beam. Not to scale.

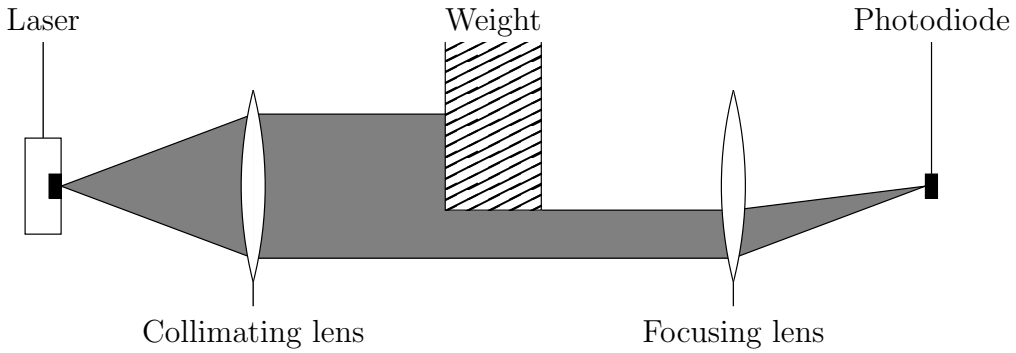

Figure 4.5: Effect of adding an obstruction to the line laser system. Obstruction partially blocks laser beam, reducing light incident on photodiode. Not to scale.

It was therefore aligned to measure in the plane indicated in figure 4.3. To calibrate the output of the photodiode, the confinement was placed, with no sample, into the drop weight. The weight was then lowered to rest on it. Various spacers of known thickness were added between the confinement and the weight, and the photodiode output corresponding to that thickness recorded.

As with the quasi-static experiments, it was desirable to measure the length of the pellet after each experiment and compare this against that recorded during the experiment. However, recovery of the pellet proved more difficult in these experiments. The plunger protrusion was therefore measured with calipers; as the plunger did not undergo plastic deformation, this was equivalent to measuring the pellet thickness.

4.1.3.2 Analysis

The output of the calibrated photodiode directly measures the length l of the sample, and the load cell measures the force F applied. A pressure-porosity relationship can therefore be recovered almost exactly as in section 4.1.1.1.

4.2 Results and discussion

4.2.1 Quasistatic results

Figures 4.6 to 4.10 show the pressure-porosity curves obtained by Instron experiments on beds of various prills. There are a few noteworthy features at this stage.

Most obviously, in several of the experiments, the sample bed is pressed past its TMD. Measurements of the bed length after the load is removed suggest that this is due to elastic compression of the bed. Attempts to assess this compression using these measurements, however, had an uncertainty in excess of 80 %. No attempt was therefore made to correct for it.

After the experiments on agricultural pellet beds, a clear, colourless, oily liquid was found on the surface of the compacted bed. This is believed to be oil, added to the pellets to reduce caking.

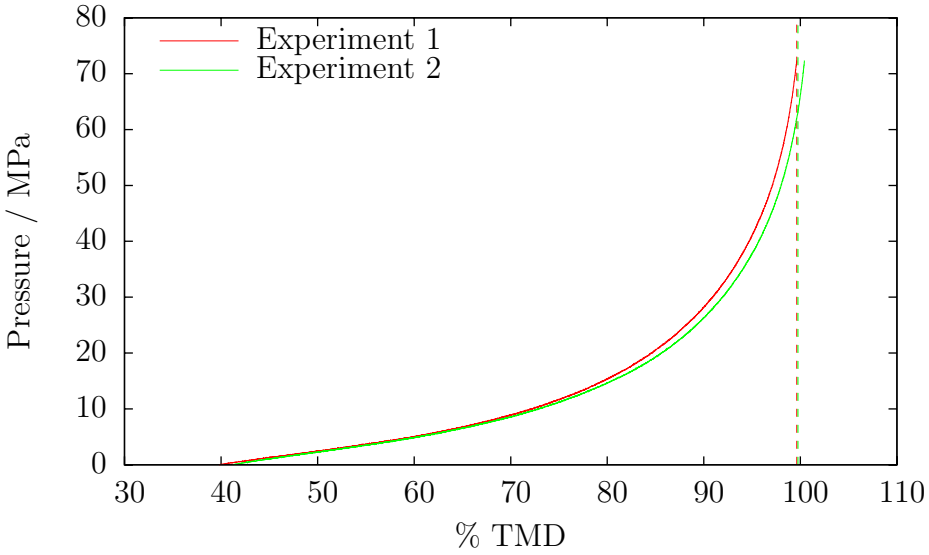

Figure 4.6: Pressure-porosity curves from two Instron experiments on uncoated Orica prill beds. Initial strain rate $4 \times 10^{-4}\,\mathrm{s}^{-1}$. Vertical dashed lines indicate fractional TMD of recovered pellets.

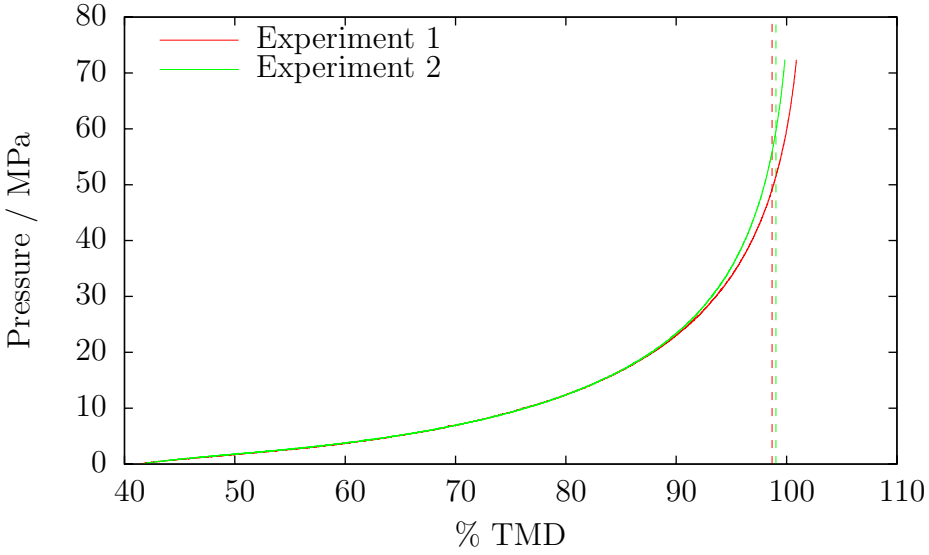

Figure 4.7: Pressure-porosity curves from two Instron experiments on coated Orica prill beds. Initial strain rate $4 \times 10^{-4}\,\mathrm{s}^{-1}$. Vertical dashed lines indicate fractional TMD of recovered pellets.

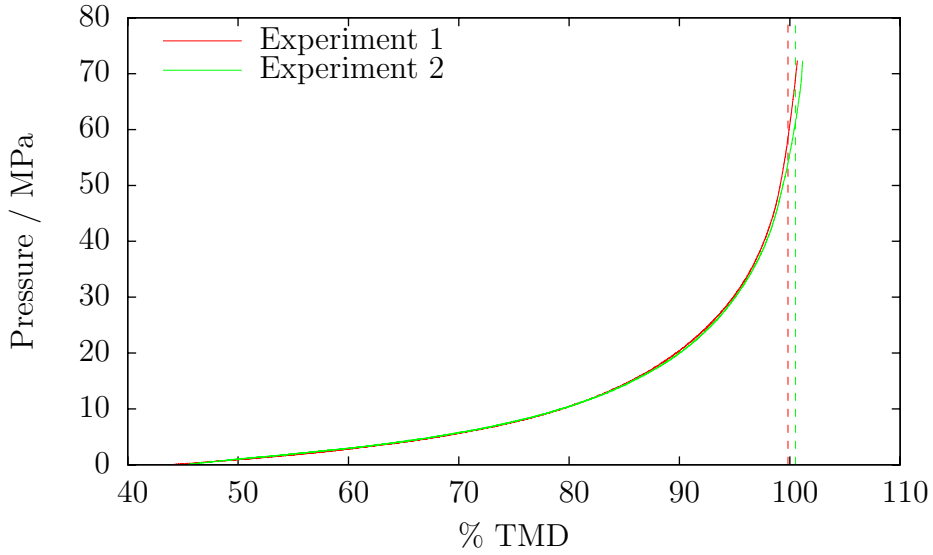

Figure 4.8: Pressure-porosity curves from two Instron experiments on agricultural pellet beds. Initial strain rate $4 \times 10^{-4}\,\mathrm{s}^{-1}$. Vertical dashed lines indicate fractional TMD of recovered pellets.

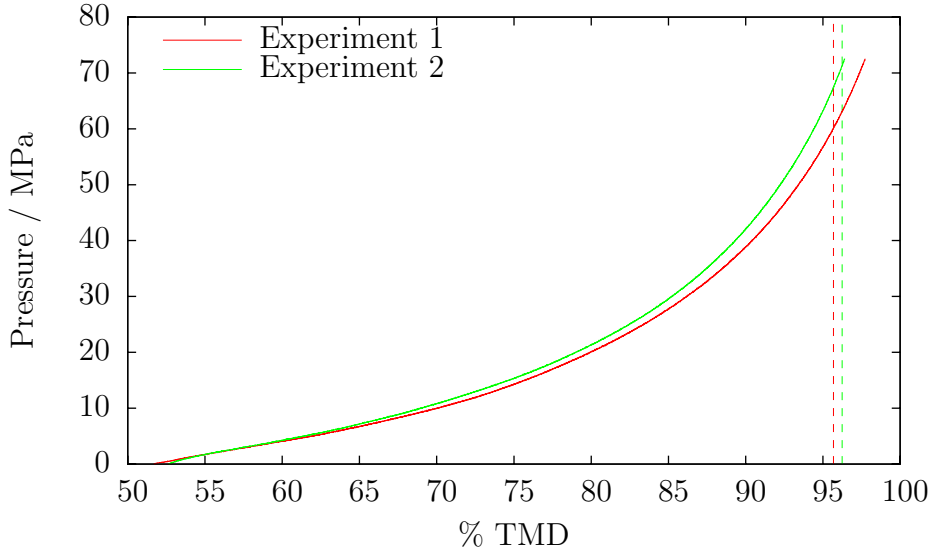

Figure 4.9: Pressure-porosity curves from two Instron experiments on Nitram prill beds. Initial strain rate $4 \times 10^{-4}\,\mathrm{s}^{-1}$. Vertical dashed lines indicate fractional TMD of recovered pellets.

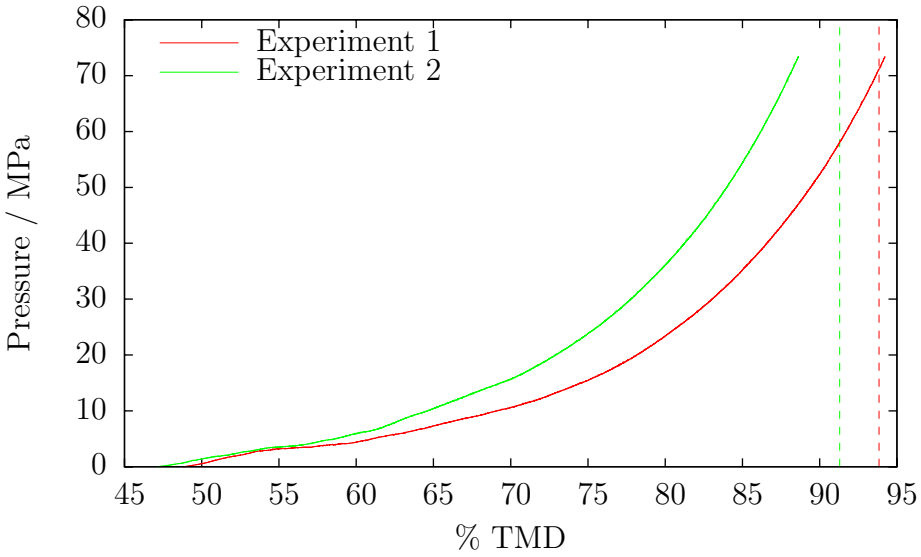

Figure 4.10: Pressure-porosity curves from two Instron experiments on Westland prill beds. Initial strain rate $4 \times 10^{-4}\,\mathrm{s}^{-1}$. Vertical dashed lines indicate fractional TMD of recovered pellets. Ball bearing used for uniaxial loading. Note the poor repeatability; this is discussed in section 4.2.8.

4.2.1.1 Pressure oscillations in Instron traces

Figure 4.11 shows small-amplitude pressure oscillations in the results of Instron experiments. Fourier analysis using the NumPy software (Ascher et al., 2001) shows these oscillations to have a frequency of $0.5143 \pm 0.0010\,\mathrm{Hz}$, whether a ball bearing was used or not. To assess the amplitude of these oscillations, a high-pass filter with a cut-off frequency of $0.4\,\mathrm{Hz}$ was applied to the data. The oscillations were found to follow a linearly growing sinusoid, of the form $(At + B)\sin(\omega t + \theta)$. The rate A at which the amplitude of the oscillations increased was found to be $25.8 \pm 1.1\,\mathrm{Pa\ s}^{-1}$. The initial amplitude B was found to be less repeatable: $2.0 \pm 1.0\,\mathrm{kPa}$.

In these experiments, the plunger was driven into the confinement cell at a constant rate of $5.55\,\mu\mathrm{m\,s}^{-1}$. The contact area between the jacket of the confinement cell and the plunger will therefore increase linearly with time. That the amplitude of these oscillations increases linearly with time suggests that some feature of the interaction between the jacket and the plunger may be responsi-

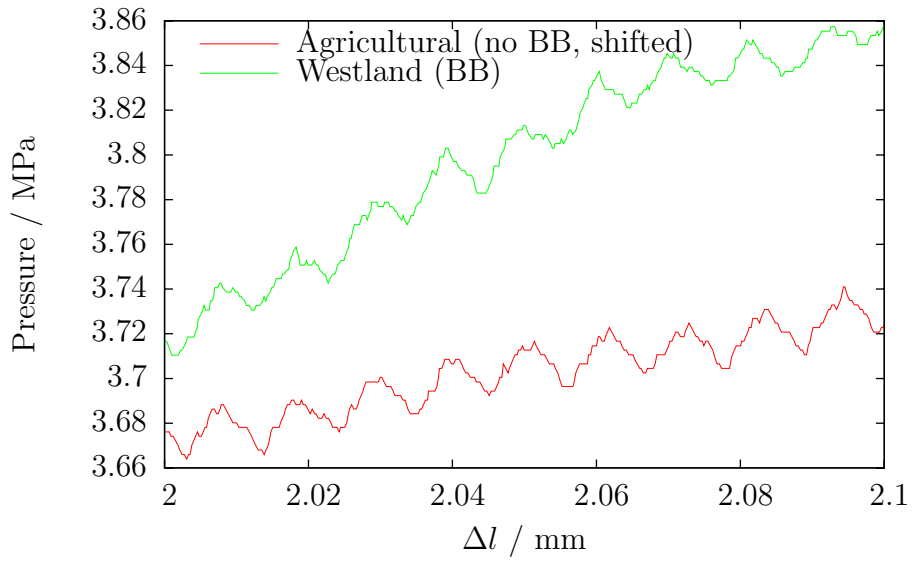

Figure 4.11: Force oscillations in Instron experiments, showing structure and repeatability of oscillations. A ball bearing was used to achieve uniaxial loading for the experiment on a Westland prill bed, while none was used for the experiment on an agricultural pellet bed. The latter has been vertically shifted by 2.65 MPa to aid comparison.

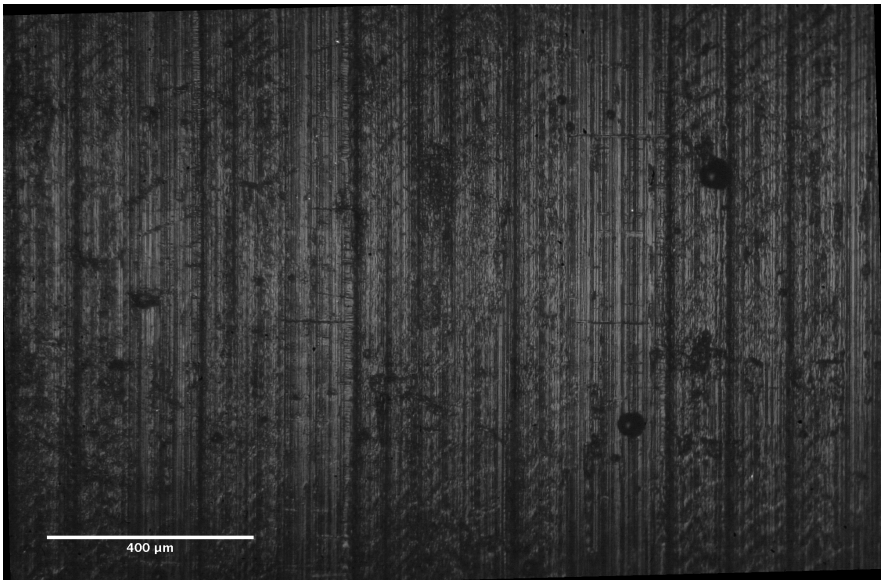

Figure 4.12: Optical microscope image of epoxy cast of interior of confinement jacket, showing striations at various length scales. The axis of the confinement cell is horizontal.

ble for them. From the known frequency of the oscillations, and the constant speed of the plunger, the features responsible are expected to be separated by $10.79 \pm 0.02\,\mu$m. Such features would be detectable by optical microscopy.

Examination of the plunger revealed no suitable features. Directly imaging the interior of the confinement jacket was difficult. Instead, a cast was made using fast cure epoxy (National Adhesives Bondmaster Double Bubble Mix & Fix). This was left for twelve hours to cure, then broken from the jacket. The resulting cast was suitable for microscopy. Figure 4.12 shows an image of this cast. Features normal to the axis of the confinement cell, formed when the jacket was produced, are visible. The broad dark lines, spaced irregularly a few hundred microns apart, were caused by the manual removal of the cutting tool after the jacket's fabrication. They are too widely-spaced and irregular to be responsible for the oscillations observed in this experiment. The finer lines between them were caused by the cutting tool as it hollowed out the confinement jacket. During this process it was moved automatically, explaining the regular spacing of these lines.

This spacing was assessed by averaging the rows of the image to find its average brightness as a function of horizontal position, then taking the Fourier transform

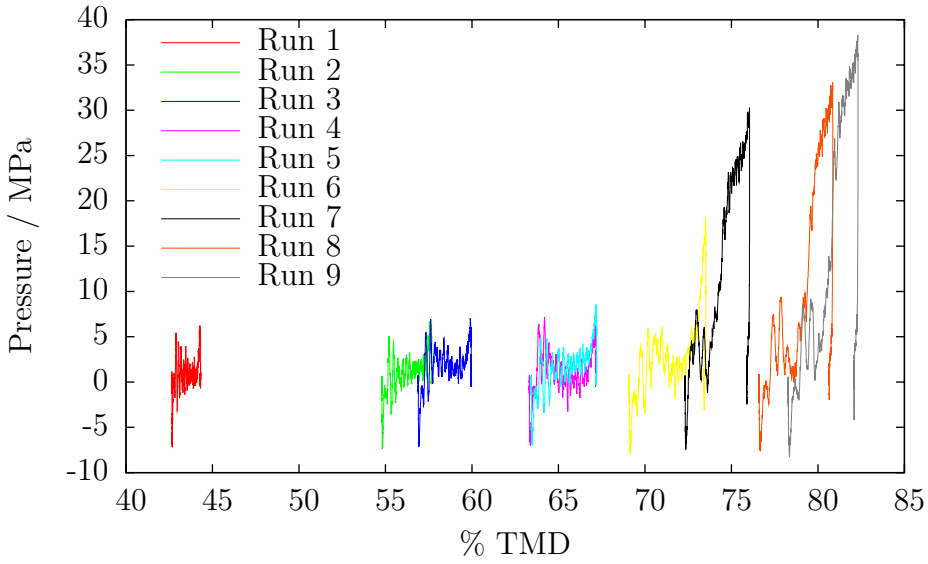

Figure 4.13: Pressure-porosity curves from repeated SHPB experiments on a single uncoated Orica prill bed. Initial strain rate $450\,\mathrm{s}^{-1}$.

of that function. This clearly shows a feature with period $20.3 \pm 1.7\,\mu$m, double that of the force oscillations when error is considered. The most likely explanation for the doubled frequency of the oscillations involves the helical nature of these features. The plunger could be pushed across the bore of the confinement jacket, interacting with the peaks of these grooves on diametrically opposed sides of the bore. This would result in the frequency-doubling seen here.

4.2.2 SHPB results

Figure 4.13 shows the results from a series of nine experiments on an uncoated Orica prill bed. Each experiment compacts the bed for the subsequent experiment. In principle, these traces should give the complete pressure-porosity curve for the bed. Examination, however, suggests quite strongly that this is not the case. Most notably, the end of one trace does not match the beginning of the subsequent trace.

Several of these mismatches, for example the gap between runs 1 and 2, can be explained by reloading. The compressive incident pulse will reflect from the sample as a tensile wave. This tensile wave will reflect from the striker end of the

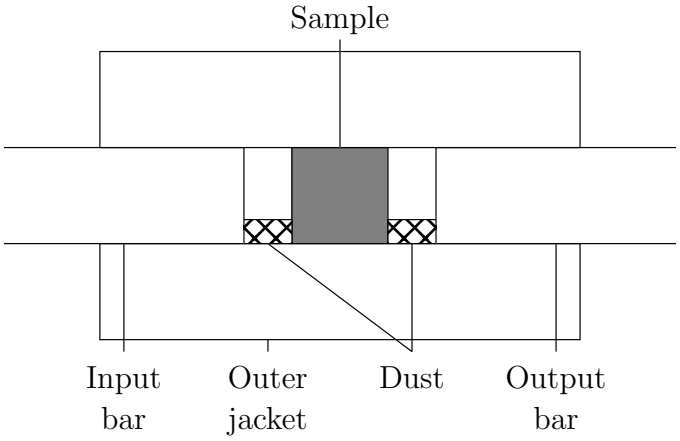

Figure 4.14: Sample geometry encountered in later SHPB compaction runs. Dust falls from the sample after each experiment. This produces a buffer which prevents the bars from probing the true response of the sample. Not to scale.

bar as a compressive wave, and apply load to the sample after data recording has ceased. This will result in unrecorded compaction of the sample.

Several other traces, however, overlap the previous trace. The most extreme example is that of runs 4 and 5, which overlie each other completely. While some reversible elastic compression will occur, it seems unlikely that this can account for such a great degree of overlap.

A more likely explanation for this overlap involves dust. At the high strain rates used in this experiment, some of the prills in the sample bed will fracture, producing dust. At the end of each run, the compressive force will be removed and dust at the end of the compacted bed will fall down. Rather than compacting a cylindrical bed, the next experiment encounters a bed of the form shown in figure 4.14. The thin layer of loosely-packed dust will extend the initial sample length, leading to overlap of the kind seen between several of the later runs.

The presence of dust also explains the low applied pressure at the start of the later runs. Figure 4.15 shows run 9 from figure 4.13. Before about 81 % TMD it demonstrates much less resistance to compaction than would be expected. This would be consistent with rearrangement of a thin layer of dust.

Figures 4.13 and 4.15 also demonstrate the very low signal-to-noise ratio of this technique. The low impedance of the beds relative to the bars results in

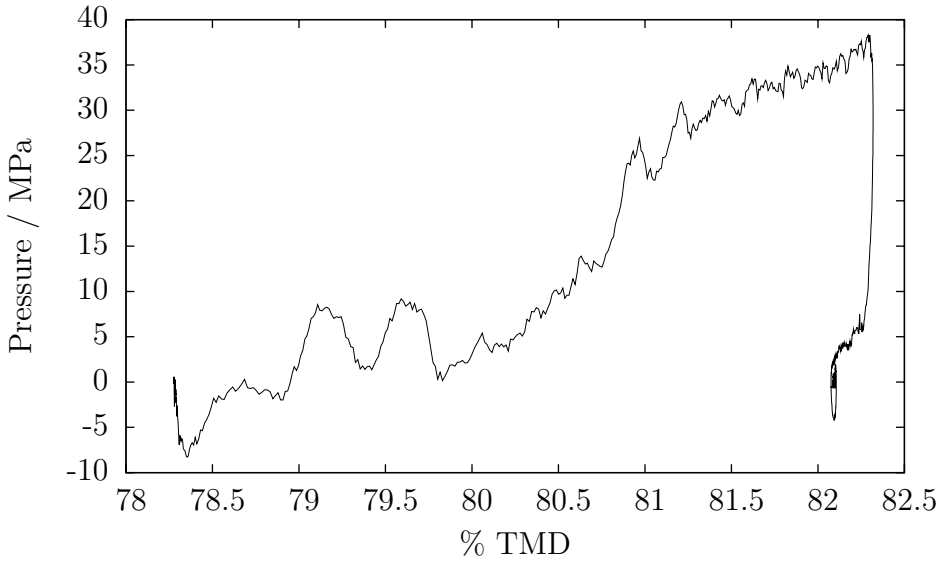

Figure 4.15: Pressure-porosity curve generated by ninth SHPB experiment on uncoated Orica prill bed.

a very high fraction of the incident pulse being reflected. This leads naturally to a poor signal-to-noise ratio after analysis. The conventional solution to this problem is to use lower-impedance bars. However, these data were taken using the lowest-impedance solid metal bars available. While it is possible to achieve lower impedances, by using tubular or polymer bars, dispersion in such bars is significant.

While none of the problems with this technique are insurmountable, it was deemed more efficient to employ a technique which circumvented them than to attempt to overcome them.

4.2.3 Drop weight results

Figure 4.16 shows a pressure-porosity curve generated using the drop weight, with sample length measured by the line laser. The low spatial resolution of the line laser is apparent from the large error in the fractional TMD. The output of the photodiode, even when the laser fan was unobstructed, was roughly 80 mV. This led to considerable digitization error when the output was recorded. However, the temporal resolution of the technique was far higher than necessary: 10 μs in

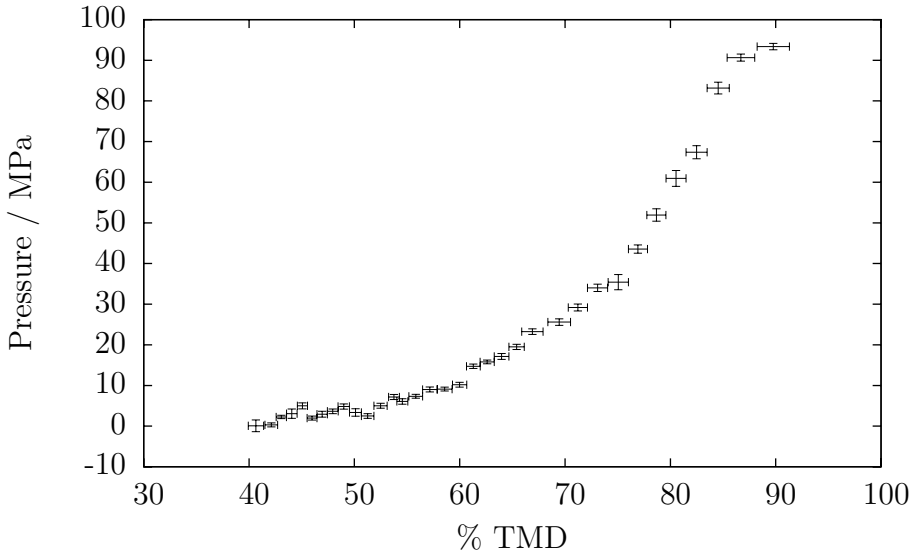

Figure 4.16: Pressure-porosity curve from drop weight experiment on uncoated Orica prill bed. Initial strain rate $170\,s^{-1}$.

an experiment lasting a few milliseconds. A moving average, with a window size of five samples, was therefore applied to the data, sacrificing temporal for spatial resolution.

Figures 4.17 to 4.26 show the pressure-porosity curves generated using this technique. To vary the strain rate, the height from which the weight was dropped was varied. All the results presented here were produced by dropping the weight from either 32 cm or 17 cm above the top of the plunger.

4.2.4 Effect of coating

Figure 4.27 compares pressure-porosity curves for coated and uncoated Orica prill beds. There is no significant difference between these curves. Figure 4.28 shows that this is also the case at higher strain rates.

4.2.5 Effect of strain rate

Figure 4.29 shows the effect of a large change in strain rate on the compaction response of a bed of uncoated Orica prills. The other bed materials demonstrated

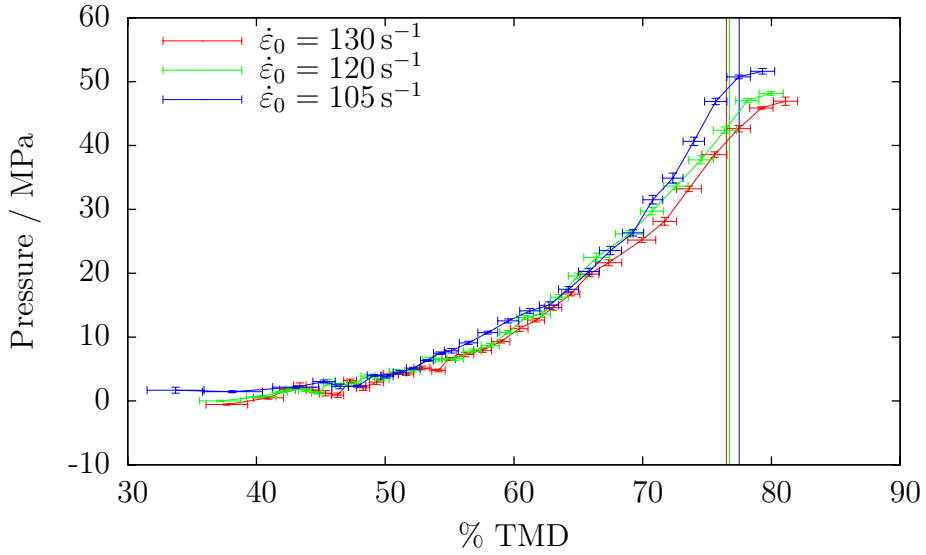

Figure 4.17: Pressure-porosity curves from drop weight experiments on uncoated Orica prill beds. Weight dropped from 17 cm. Vertical lines indicate fractional TMD measured after experiment.

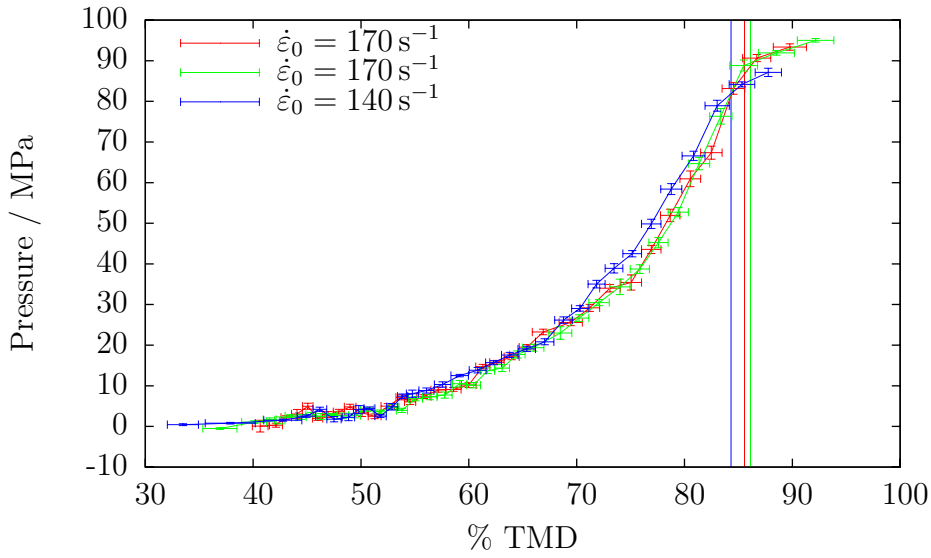

Figure 4.18: Pressure-porosity curves from drop weight experiments on uncoated Orica prill beds. Weight dropped from 32 cm. Vertical lines indicate fractional TMD measured after experiment.

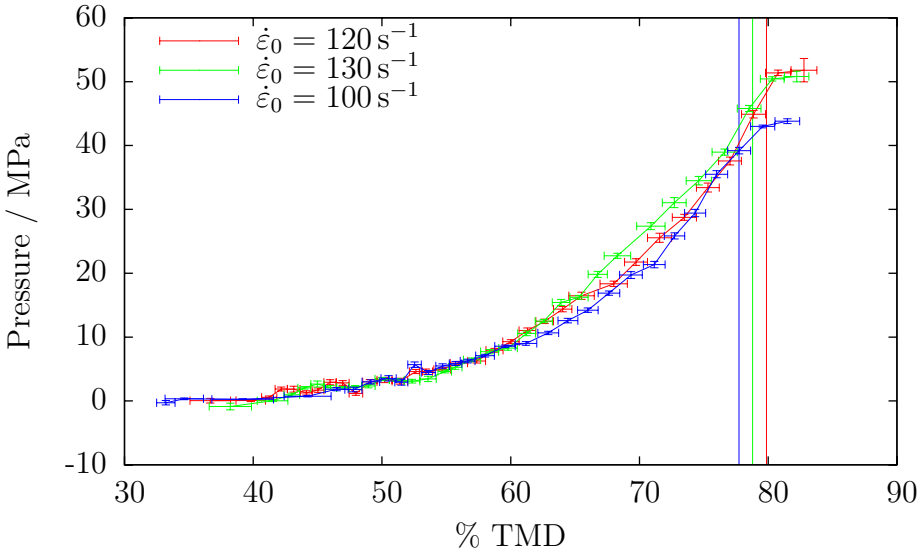

Figure 4.19: Pressure-porosity curves from drop weight experiments on coated Orica prill beds. Weight dropped from 17 cm. Vertical lines indicate fractional TMD measured after experiment.

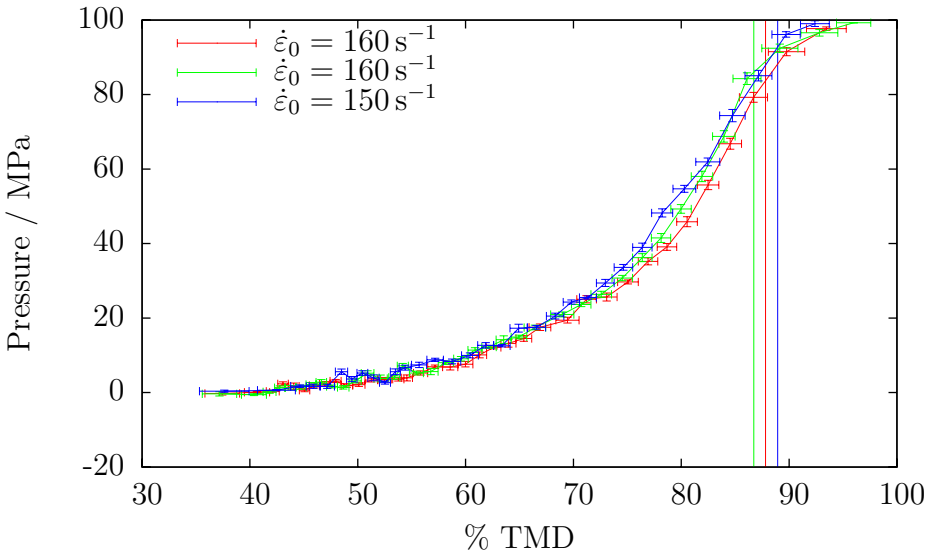

Figure 4.20: Pressure-porosity curves from drop weight experiments on coated Orica prill beds. Weight dropped from 32 cm. Vertical lines indicate fractional TMD measured after experiment.

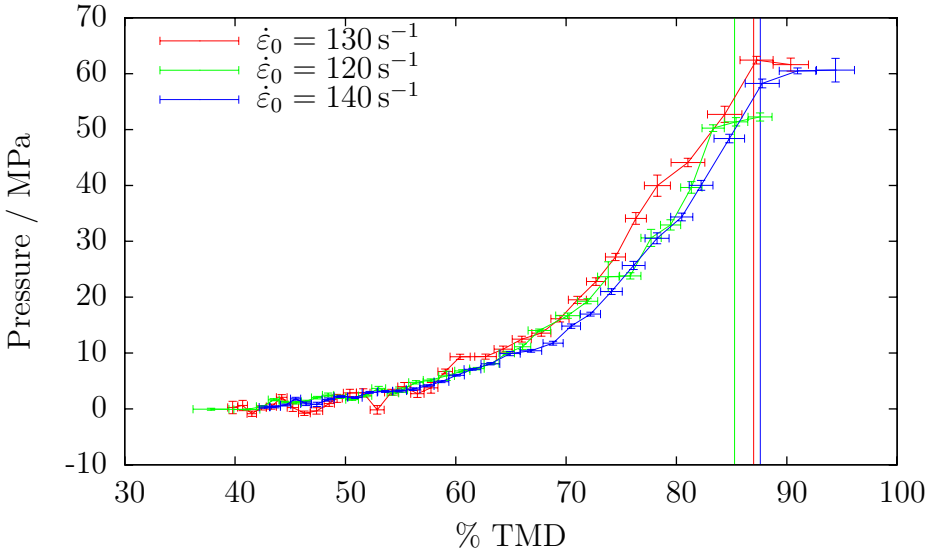

Figure 4.21: Pressure-porosity curves from drop weight experiments on agricultural pellet beds. Weight dropped from 17 cm. Vertical lines indicate fractional TMD measured after experiment.

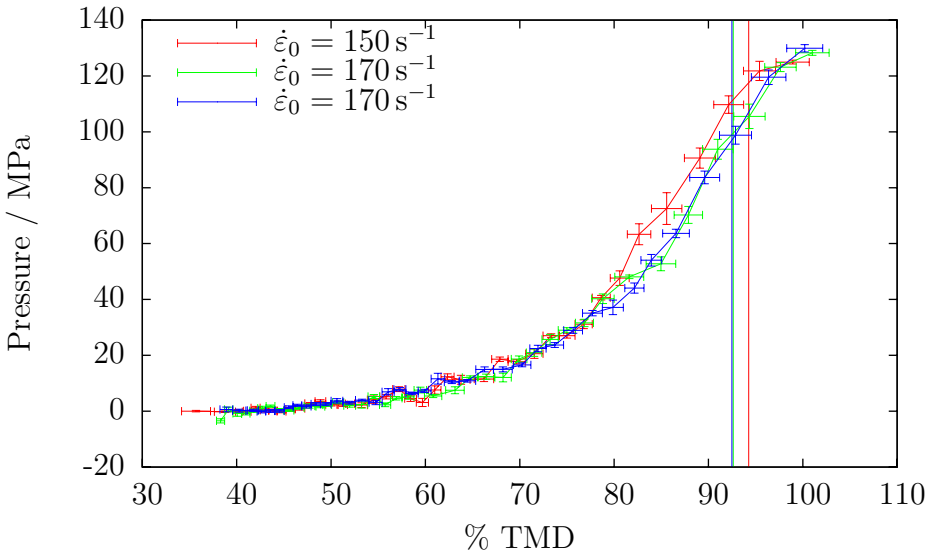

Figure 4.22: Pressure-porosity curves from drop weight experiments on agricultural pellet beds. Weight dropped from 32 cm. Vertical lines indicate fractional TMD measured after experiment.

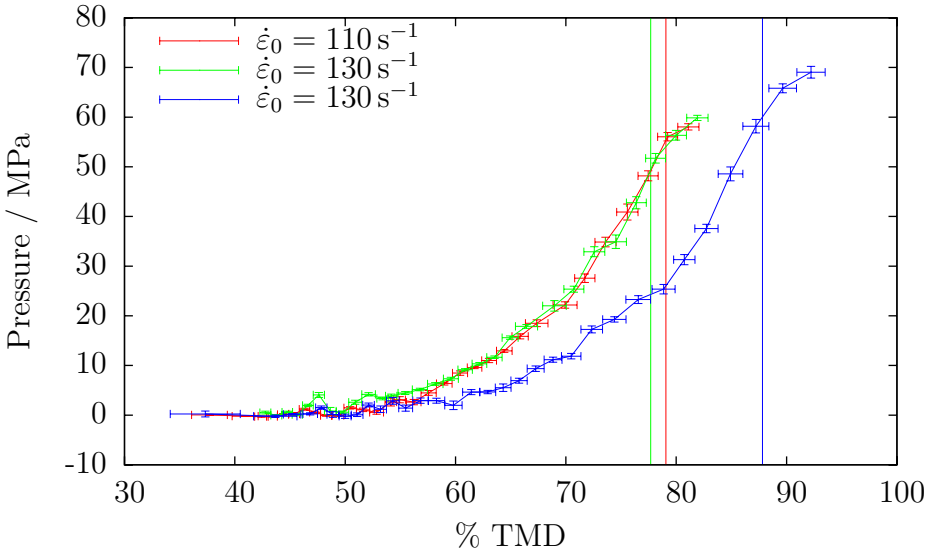

Figure 4.23: Pressure-porosity curves from drop weight experiments on Nitram prill beds. Weight dropped from 17 cm. Vertical lines indicate fractional TMD measured after experiment.

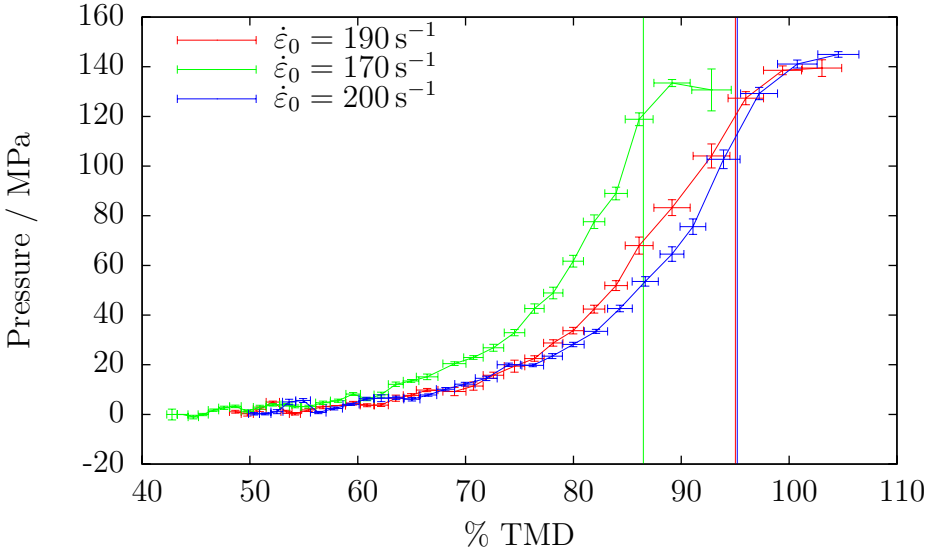

Figure 4.24: Pressure-porosity curves from drop weight experiments on Nitram prill beds. Weight dropped from 32 cm. Vertical lines indicate fractional TMD measured after experiment.

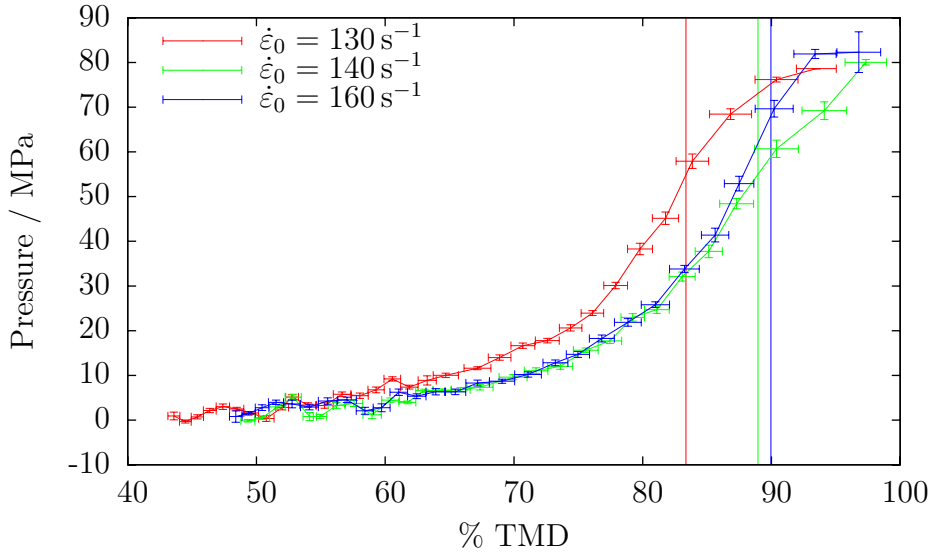

Figure 4.25: Pressure-porosity curves from drop weight experiments on Westland prill beds. Weight dropped from 17 cm. Vertical lines indicate fractional TMD measured after experiment.

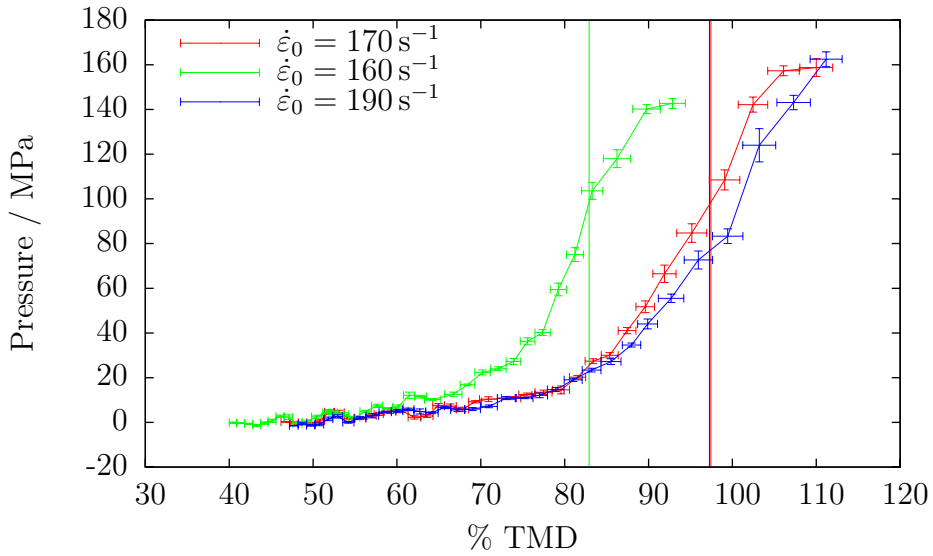

Figure 4.26: Pressure-porosity curves from drop weight experiments on Westland prill beds. Weight dropped from 32 cm. Vertical lines indicate fractional TMD measured after experiment.

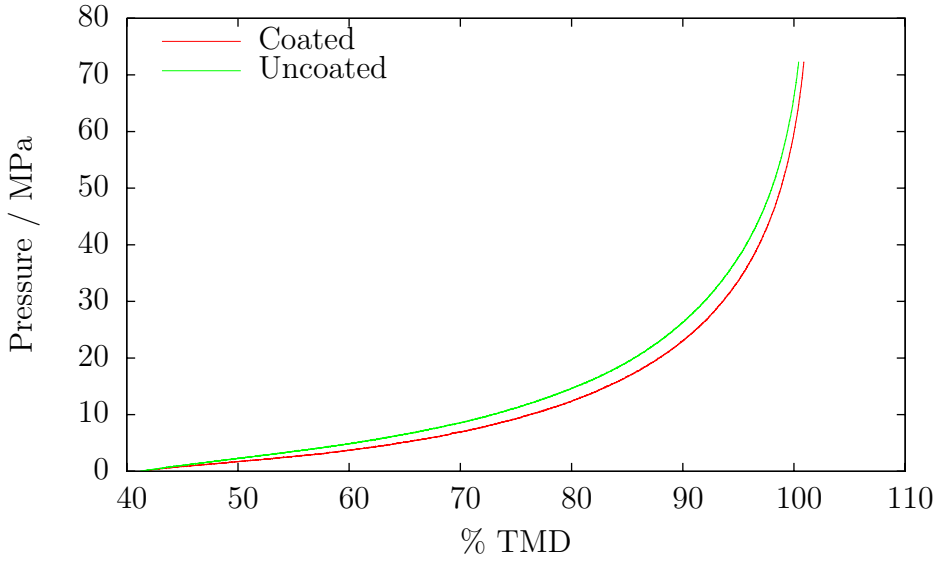

Figure 4.27: Pressure-porosity curves from Instron experiments on coated and uncoated Orica prill beds. Initial strain rate $4 \times 10^{-4}\,\mathrm{s}^{-1}$.

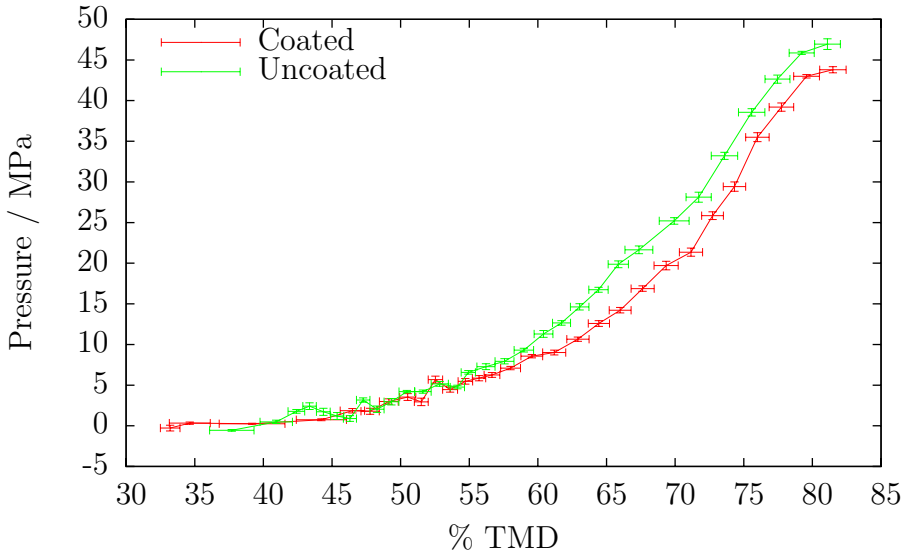

Figure 4.28: Pressure-porosity curves from drop weight experiments on coated and uncoated Orica prill beds. Initial strain rates $100\,\mathrm{s}^{-1}$ and $120\,\mathrm{s}^{-1}$ for coated and uncoated bed respectively.

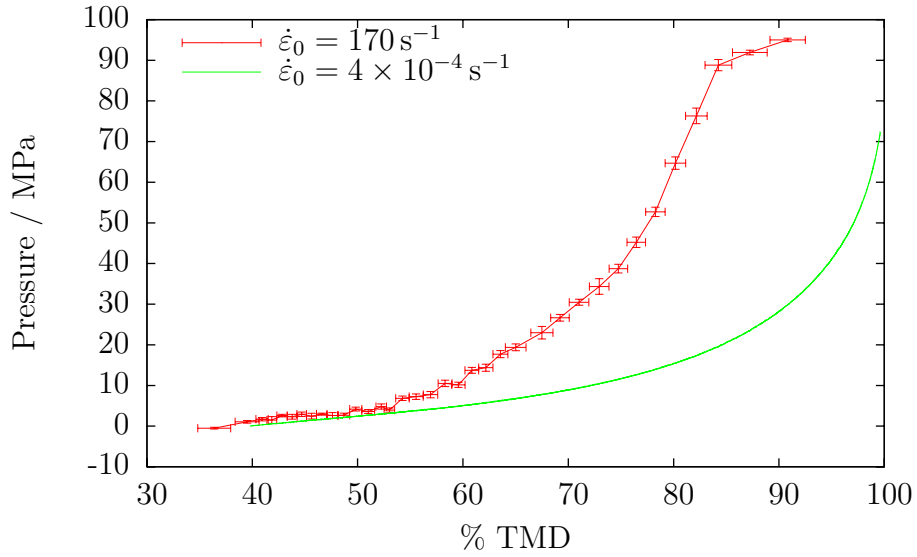

Figure 4.29: Pressure-porosity curves from both Instron and drop weight experiments on uncoated Orica prill beds, showing enhanced resistance to compaction at higher strain rate.

a similar response. At a higher rate, the bed demonstrates markedly increased resistance to compaction.

Compaction necessarily involves rearrangement of material within the bed. Material must be accelerated to move it from one location to a vacancy, so that the bed is more efficiently packed. At the quasistatic strain rates achieved in Instron experiments, the acceleration involved is negligibly small. At the higher strain rates of the drop weight experiments, though, the force required to provide this acceleration could conceivably increase the pressure required to achieve a given degree of compaction. This mechanism is considered in section 4.2.5.1, below.

Second, the higher-rate experiments caused considerably more fracture in the bed materials than the quasi-static experiments, as observed in section 4.2.2. This energy-absorption mechanism is considered in section 4.2.5.2, below.

A smaller relative change of strain rate, as shown in figure 4.30, has very little effect on the compaction behaviour of a bed. Again, all the sample materials exhibited this behaviour. This lack of change may indicate that the processes which increase resistance to compaction at higher strain rate are sensitive to relative,

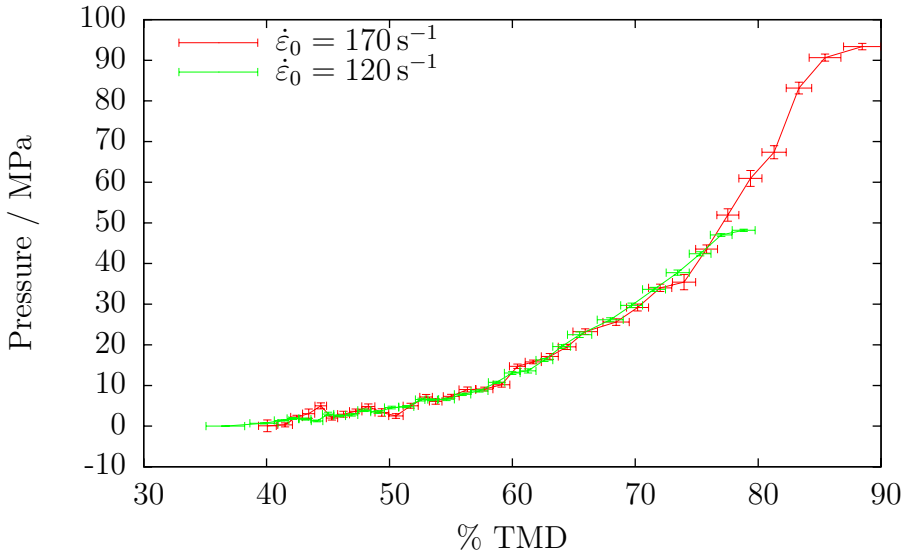

Figure 4.30: Pressure-porosity curves from drop weight experiments on uncoated Orica prill beds, showing no significant variation in bed response with strain rate. The weight was dropped from a different height for each experiment to vary the strain rate.

rather than absolute, changes in strain rate. Alternatively, it may indicate that there exists some threshold strain rate, between those probed with Instron and with drop weight experiments, above which an additional compaction-resisting mechanism becomes active. Distinguishing between the two would require additional experiments at intermediate strain rates.

4.2.5.1 Momentum effects

To within an order of magnitude, the effect of momentum on the resistance of the bed to compaction can be found by considering the applied pressure required to accelerate the bed from rest to the plunger velocity over the duration of the experiment. This gives a stress

$$\sigma = \frac{mv}{\frac{1}{4}\pi d^2 t} \ , \tag{4.5}$$

where m is the bed mass, v is the plunger velocity, d is the plunger diameter, and t is the duration of the experiment. For a typical drop weight experiment,

$m = 1.5\,\mathrm{g}$, $v = 3\,\mathrm{m\,s^{-1}}$, $d = 13\,\mathrm{mm}$, and $t = 3\,\mathrm{ms}$. This gives $\sigma = 1.1\,\mathrm{MPa}$.

This is approximately the difference between high-rate and low-rate compaction curves in the early stages of compaction; however, it is also approximately the size of the uncertainty in the high-rate compaction curves at this stage. As the compaction process continues, the difference between high-rate and low-rate compaction curves increases until it is much greater than can be accounted for by momentum considerations.

4.2.5.2 Fracture effects

The higher-rate experiments caused considerably more fracture in the bed materials than the quasi-static experiments, as observed in section 4.2.2. While the drop weight experiments do not suffer from the presence of dust as the SHPB experiments did, this fracture is an energy-absorption mechanism. The surface energy for the new surfaces opened by fracture must be supplied by the kinetic energy of the falling weight. A simple calculation can assess the likely effect of this fracture on the compaction behaviour of the bed.

First, note that during a compaction experiment nearly all the kinetic energy of the weight is dissipated in compaction of the bed. This kinetic energy

$$E_k = \frac{1}{2}mu^2. \tag{4.6}$$

In these experiments, the mass of the weight $m \approx 6\,\mathrm{kg}$, and the impact velocity $u \approx 2\,\mathrm{m\,s^{-1}}$. This gives $E_k \approx 12\,\mathrm{J}$.

To assess the energy dissipated in fracture, assume the sample is composed of cubic crystallites, exactly filling the sample volume, each of which is bisected by fracture. The surface energy required to bisect a single such crystallite will be

$$E = \gamma a^2, \tag{4.7}$$

where γ is the fracture surface energy of the sample material and a is the length of one side of a crystallite. The total number of crystallites, and hence the number

of these fracture events, will be

$$N = \frac{\text{Volume}}{a^3} = \frac{\pi l d^2}{4a^3} \ , \tag{4.8}$$

where l and d are the length and diameter of the confinement cell. This gives the energy dissipated by fracture in this simple model as

$$E_{\text{frac}} = NE = \frac{\gamma \pi l d^2}{4a} \ . \tag{4.9}$$

Based on the electron micrographs in chapter 3, $100\,\mu$m is a reasonable value for a. For all these experiments, $l \approx 15\,$mm and $d \approx 13\,$mm. Due to the difficulty of obtaining large, high-quality ammonium nitrate crystals, the fracture surface energy of ammonium nitrate is unknown. However, several other explosive materials have been investigated (Palmer and Field, 1982) and found to have fracture surface energies of order $0.1\,\text{J}\,\text{m}^{-2}$. Taking this as a value for γ gives $E_{\text{frac}} = 2.0\,$mJ. This is a negligibly small fraction, 1.7×10^{-4}, of the kinetic energy E_k of the weight.

4.2.6 Effect of initial porosity

The results from drop weight experiments on beds of Nitram prills, shown in figures 4.23 and 4.24, appear to be highly variable. This does not seem to be an effect of the strain rate at which the experiment was carried out. As figure 4.31 shows, this variability is almost eliminated by simply shifting the pressure-porosity curve by the initial porosity of the bed.

This indicates that the pressure required to compact these beds depends primarily on the amount of compaction already performed. How near they are to their theoretical maximum density appears to be of secondary importance. This is discussed further in section 4.2.10.

This effect is most noticeable in Nitram prill beds, probably because the large, irregular Nitram prills are capable of a wider range of initial porosities than the other bed materials. However, it seems to be present to some degree in beds of all materials.

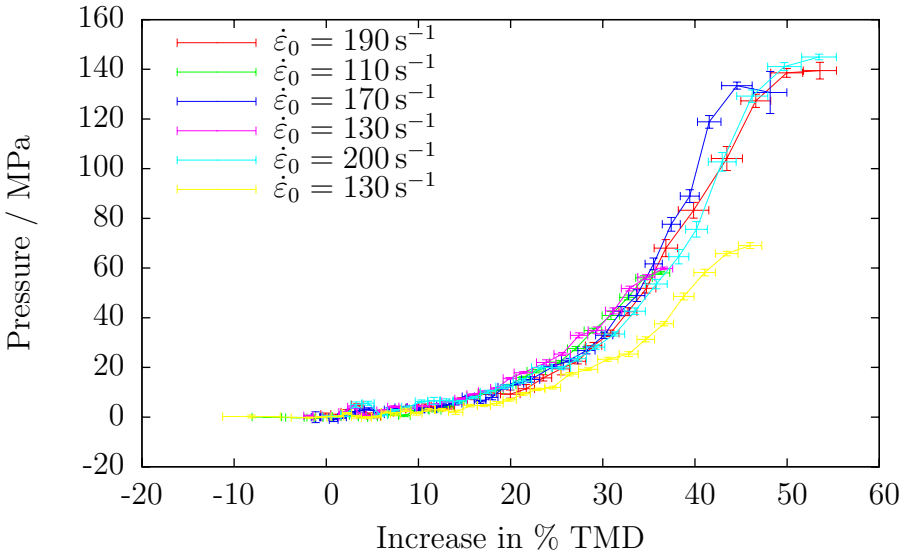

Figure 4.31: Pressure-porosity curves from drop weight experiments on Nitram prill beds. All curves have been shifted by their initial fractional TMD, greatly improving experiment repeatability.

4.2.7 Effect of microstructure

As discussed in chapter 3, Nitram prills and Orica prills are very similar chemically, being composed of nearly pure ammonium nitrate. However, their microstructure differs, with Nitram prills being considerably denser than Orica prills. This increases the initial fractional TMD of Nitram beds, which in turn makes direct comparison of the compaction data shown in figures 4.6 and 4.9 difficult. Following the reasoning in section 4.2.6, though, figure 4.32 compares the results of Instron experiments on Nitram and Orica prill beds, shifted by their initial porosity.

The bed of Nitram prills is clearly more resistant to compaction than the bed of Orica prills, despite their similar chemical composition. This suggests that the denser microstructure of Nitram prills must enhance their resistance to compaction. Denser prills are likely to be mechanically stronger and more resistant to disintegration; if the primary mechanism by which prill beds undergo compaction is one of prill disintegration, this alone would explain the Nitram beds' increased resistance to compaction.

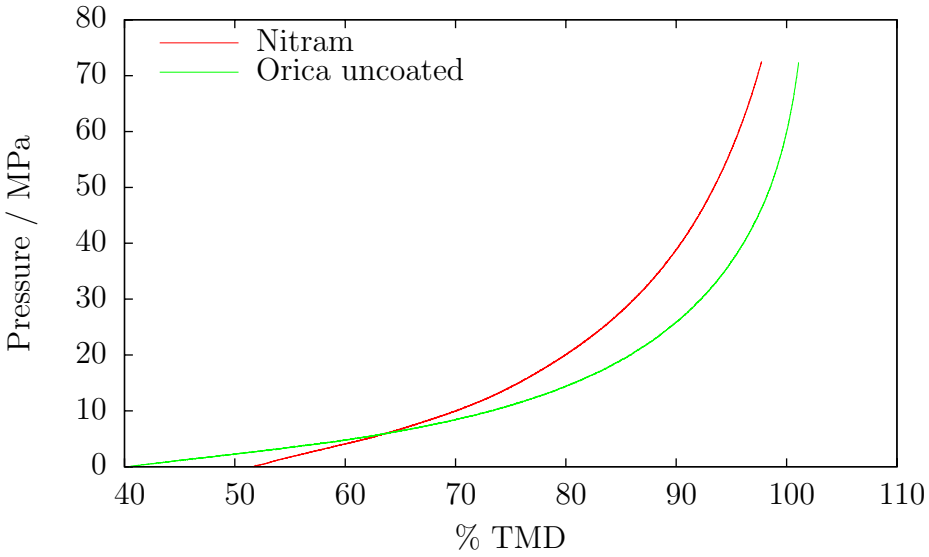

Figure 4.32: Pressure-porosity curves obtained by Instron experiments on beds of Nitram and uncoated Orica prills, showing greater resistance to compaction in Nitram prill bed. Initial strain rate 4×10^{-4} in both cases.

Other results in this section, however, suggest that compaction is dominated by plastic flow of the bed material. The enhanced resistance of beds of denser prills to compaction can also be explained in this case. In order for a bed to compact, material must flow into voids in the bed's structure. The dense microstructure of Nitram prills increases the mean distance between material and void. In order to achieve a given rate of compaction, the rate at which material enters voids must be constant. Therefore, at a given compaction rate, a bed of denser prills must contain more material in motion, or that material must be moving faster, than a bed of less dense prills. This will increase the amount of energy dissipated by plastic work in the flowing material, and hence the bed's resistance to compaction.

4.2.8 Effect of composition

Comparing the compaction properties of agricultural pellets and Westland prills with those of the pure AN prills is challenging. Both the chemical content and microstructure of these materials differ from those of the pure AN prills.

Agricultural pellet beds offer very similar resistance to compaction to coated Orica prill beds (see figures 4.7, 4.8, 4.19, 4.20, 4.21, and 4.22). This is surprising for a few reasons. First, the ESEM images presented in chapter 3 indicate that the microstructure of the agricultural pellets is roughly as dense as that of the Nitram prills, and considerably denser than that of the Orica prills. Following the reasoning in section 4.2.7, this should give beds of agricultural pellets considerably greater resistance to compaction than beds of Orica prills. Second, the inert additive in these agricultural pellets is dolomite, a mechanically stronger material than ammonium nitrate (Robertson, 1955; Ross et al., 1945). It would be unusual for the addition of a stronger material to make the resulting composite weaker, all else being equal.

One possible explanation for the anomalously low resistance a bed of agricultural pellets offers to compaction involves the fluid-bed granulation method by which the pellets are manufactured. This method is essentially one of controlled caking, in which dissolution and recrystallization are used to bond individual crystals together into a pellet. The resulting pellet will be markedly less resistant to disintegration than the interlocking network of crystals produced by prilling. This may, in turn, lower a pellet bed's resistance to compaction. It is also possible that oil in the pellet beds, noted in section 4.2.1, is relevant. By lubricating the motion of crystallites over each other, this oil could reduce the bed's resistance to compaction.

Beds of Westland prills offer more resistance to compaction than most other beds studied, and very similar resistance to beds of Nitram prills (see figures 4.10, 4.25 and 4.26). This is not unexpected given the dense microstructure of Westland prills (see chapter 3). The pressure-porosity traces from experiments on Westland prill beds also appear to be more variable than those from experiments on other beds. As figure 4.33 shows, this variability is not eliminated by the shifting technique used in section 4.2.6. This is probably because of the multiple different kinds of prill present in a sample of Westland prills, as determined by EDX in chapter 3. While these prills are easily distinguishable by sectioning and EDX, they are harder to distinguish by eye. A sample contains roughly a hundred prills, and therefore the composition of each sample could vary significantly. This would naturally affect the sample's compaction behaviour.

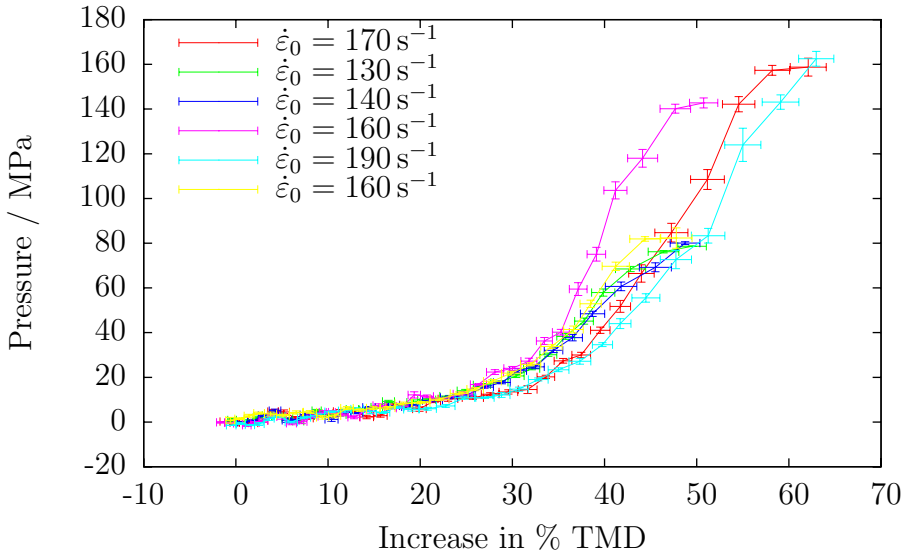

Figure 4.33: Pressure-porosity curves from drop weight experiments on Westland prill beds. All curves have been shifted by their initial porosity. This has not eliminated variation between experiments.

The shape of the pressure-porosity curves for quasistatic compaction of Westland prill beds shown in figure 4.10 is interesting. While the curves for other materials increase smoothly at an ever-increasing rate, bumps and plateaux are visible on the Westland curve. The most obvious such feature is between 55 % and 60 % TMD on the red curve in figure 4.10. This behaviour is likely due to the heterogeneous nature of the prill bed. Some prills will yield at considerably lower stresses than others; once the bed is sufficiently compacted that such a prill is loaded, that prill's deformation will briefly dominate the compaction behaviour of the bed until stronger prills support the load.

4.2.9 Compaction modelling

As discussed in chapter 1, section 1.4.2, several models of compaction exist. It is useful to compare two of the most popular to these data.

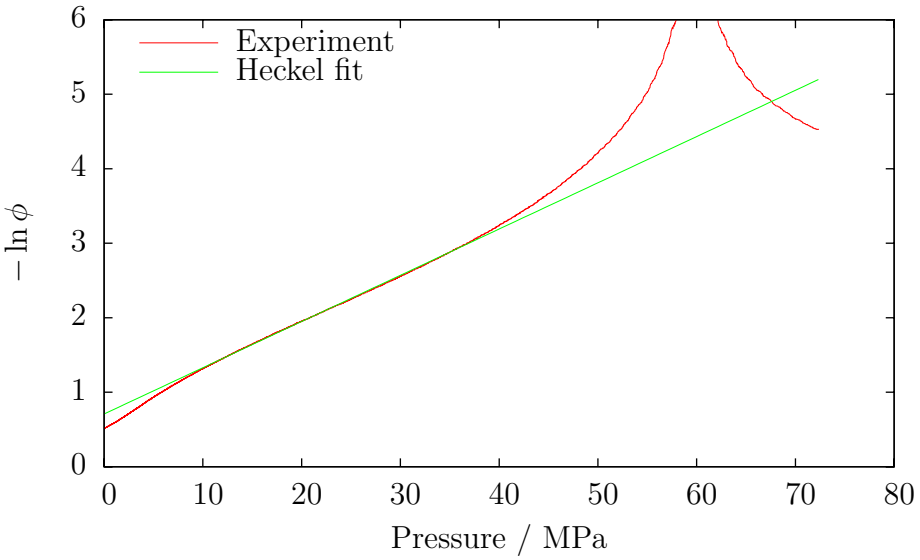

Figure 4.34: Heckel plot for quasistatic compaction of uncoated Orica prills, showing linear region between 10 and 40 MPa. Initial strain rate $4 \times 10^{-4}\,\mathrm{s}^{-1}$. Heckel parameters $\phi_0 = 49.232 \pm 0.014 \times 10^{-2}$, $\alpha = 62.059 \pm 0.013\,\mathrm{GPa}^{-1}$. Note severe deviation from linearity near 60 MPa; this corresponds to the bed reaching its ambient-pressure TMD, causing the Heckel model to fail.

4.2.9.1 Heckel model

The Heckel model is described in chapter 1, section 1.4.2.1. It gives the pressure-porosity relationship

$$\ln \frac{1}{\phi} = \ln \frac{1}{\phi_0} + \alpha P \ , \tag{1.10}$$

where ϕ is the void fraction of the material at applied pressure P, ϕ_0 is the void fraction at zero applied pressure, and α is a constant. Plots of $\ln \frac{1}{\phi}$ against P, referred to as Heckel plots, typically show a curved region at low applied pressure, then become straight. This curved region means that the intercept of the straight region is not, in fact, the observed ϕ_0.

Figure 4.34 shows a typical Heckel plot for quasistatic compaction of a prill bed. There is clearly a region in which the Heckel model applies. However, it is just as clear that this is only a limited region of the compaction curve. Figure 4.35 reproduces this plot in the more usual pressure-porosity space.

At higher strain rates, the disagreement between the Heckel model and the

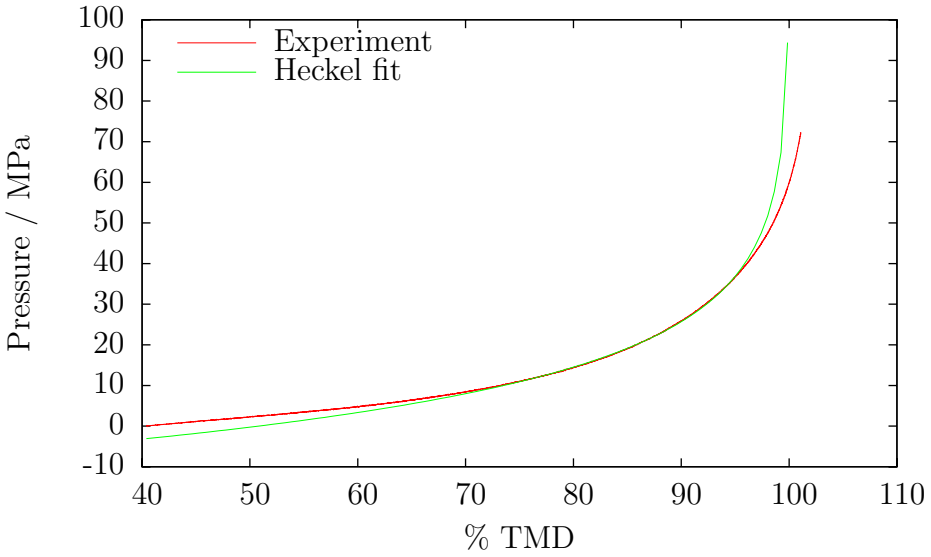

Figure 4.35: Pressure-porosity graph for quasistatic compaction of uncoated Orica prills, showing limited agreement of Heckel model with experiment. Initial strain rate 4×10^{-4} s^{-1}. Heckel parameters $\phi_0 = 49.232 \pm 0.014 \times 10^{-2}$, $\alpha = 62.059 \pm 0.013\,\mathrm{GPa}^{-1}$.

data becomes more pronounced. Figure 4.36 shows a typical Heckel plot for drop weight compaction of a prill bed. As in the quasi-static case, there exists a region over which the linear relationship predicted by the Heckel model appears to be obeyed. However, as figure 4.37 shows, outside this region the predictions of the Heckel model match the data very poorly.

The Heckel model also predicts that the slope α of the linear region is related to the yield stress σ_0 of the material by

$$\sigma_0 = \frac{1}{3\alpha} \,. \tag{4.10}$$

Apart from the Westland prills, all the prills studied here are made mostly or entirely of ammonium nitrate. They should all, therefore, have the same value of σ_0 as given by equation 4.10. Table 4.1 collects these measurements. The measured yield stress clearly varies with prill type and strain rate. This provides further indication that the Heckel model does not adequately predict the behaviour of these prill beds.

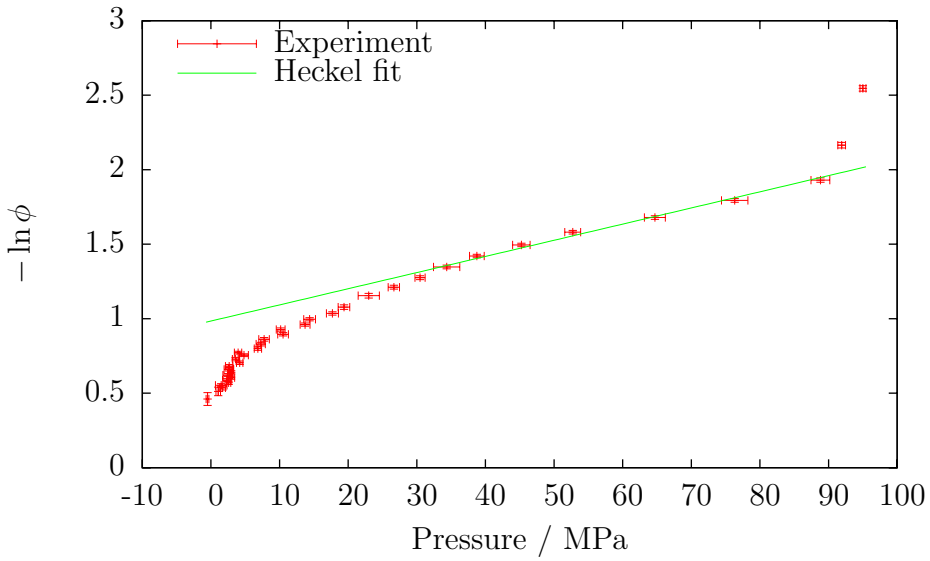

Figure 4.36: Heckel plot for drop weight compaction of uncoated Orica prills, showing linear region between 40 and 80 MPa. Initial strain rate $170\,\mathrm{s}^{-1}$. Heckel parameters $\phi_0 = 37.4 \pm 1.2 \times 10^{-2}$, $\alpha = 10.8 \pm 0.6\,\mathrm{MPa}^{-1}$.

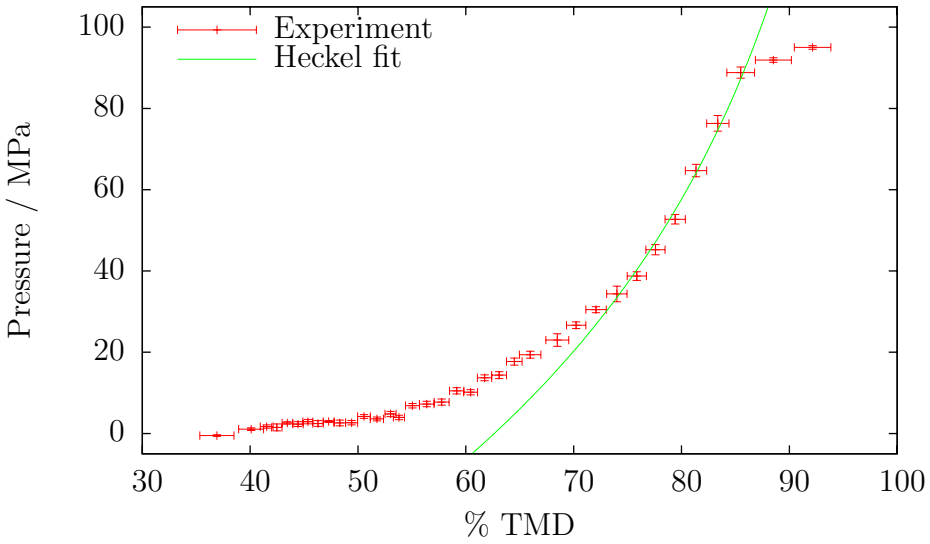

Figure 4.37: Pressure-porosity graph for drop weight compaction of uncoated Orica prills, showing discrepancy between Heckel model and experiment. Initial strain rate $170\,\mathrm{s}^{-1}$. Heckel parameters $\phi_0 = 37.4 \pm 1.2 \times 10^{-2}$, $\alpha = 10.8 \pm 0.6\,\mathrm{GPa}^{-1}$.

Material	Yield stress / MPa		
	Quasistatic	Drop weight	
		17 cm	32 cm
Orica uncoated	5.1 ± 0.3	20.7 ± 1.6	29.4 ± 0.5
Orica coated	4.61 ± 0.19	19.2 ± 0.8	24 ± 3
Agricultural	4.78 ± 0.08	19 ± 2	22 ± 3
Nitram	9.5 ± 0.5	24 ± 3	28 ± 7
Westland	17 ± 4	21 ± 2	21 ± 7

Table 4.1: Table indicating the yield stress measured by Heckel's model from compaction experiments on a range of prills. Apart from the Westland prills, all prills studied are composed primarily or wholly of ammonium nitrate. This suggests that they should all have the same yield stress. That they do not is interesting.

The Heckel model was developed for metal powders, and assumes that the deformation of the bed is dominated by particles undergoing plastic yield at their contact points. Its failure to model AN prill beds suggests that the behaviour of these beds is not so dominated.

4.2.9.2 Kawakita model

The Kawakita model is described in chapter 1, section 1.4.2.2. It gives the pressure-volume relation

$$\frac{P}{e} = \frac{1}{AB} + \frac{P}{A} \,, \tag{1.13}$$

where e is the engineering strain $\frac{\Delta l}{l}$ of the confined uniaxial bed, P is the applied pressure, and A and B are constants.

Figure 4.38 shows a typical Kawakita plot for quasistatic compaction of a prill bed. Most Kawakita plots show deviation from linearity at low pressures, and this bed is no exception. However, usually $\frac{P}{e}$ is lower than expected at low pressures; here, it is higher. It is likely that this unusual behaviour is due to the tendency of ammonium nitrate to "cake", forming a rigid network of bonds at contact points between particles. Until the applied force becomes large enough to break this network, an ammonium nitrate bed will show anomalously high resistance to compaction. As figure 4.39 shows, this discrepancy does not seriously affect the agreement between the Kawakita model and experiment in pressure-porosity

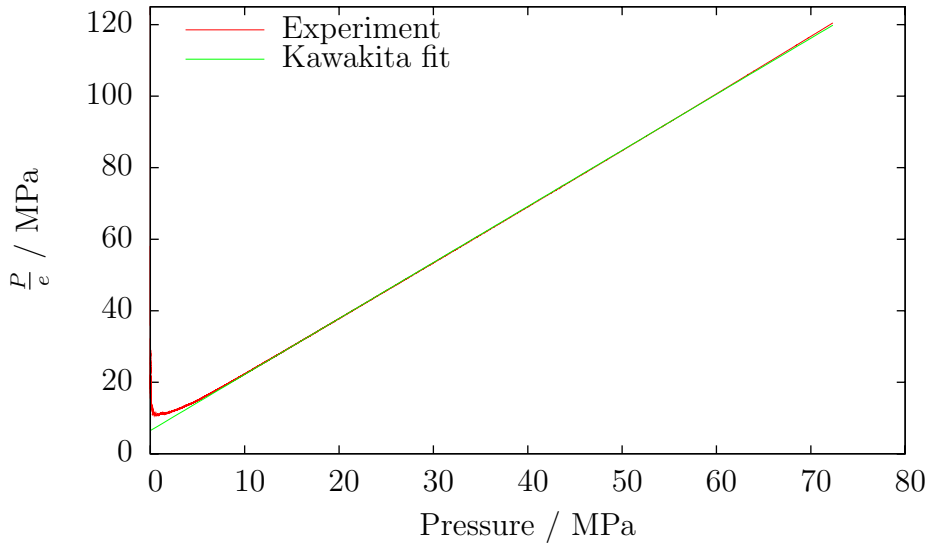

Figure 4.38: Kawakita plot for quasistatic compaction of uncoated Orica prills, showing linear relationship above 10 MPa. Initial strain rate $4 \times 10^{-4}\,\mathrm{s}^{-1}$. Kawakita parameters $A = 63.800 \pm 0.003 \times 10^{-2}$, $B = 241.97 \pm 0.09\,\mathrm{GPa}^{-1}$.

space.

At higher strain rates, the model still performs quite well. Figure 4.40 shows a typical Kawakita plot for drop weight compaction of a prill bed. It is interesting to note that the low-pressure behaviour of the bed is the reverse of that for quasistatic compaction: the bed offers less resistance to compaction than the Kawakita model predicts. It is possible that the caking network of the ammonium nitrate breaks as the bed is achieving mechanical equilibrium, and therefore does not have any effect on the recorded results. Figure 4.41 shows this plot in pressure-porosity space. Unsurprisingly, the Kawakita model agrees very well with the data over the linear region of figure 4.40. Its agreement is less good outside that range, but it captures the broad shape of the data up to 85% TMD. Above that the model fails completely to follow the data. This relatively flat region of the drop weight compaction curve is interesting, and will be discussed further in section 4.2.10. However, it has little bearing on the model.

The Kawakita model appears to provide good agreement with experimental data overall. Adams and McKeown (1996) found that the Kawakita parameter B for a bed of agglomerates was related to the failure stress of a single agglomerate.

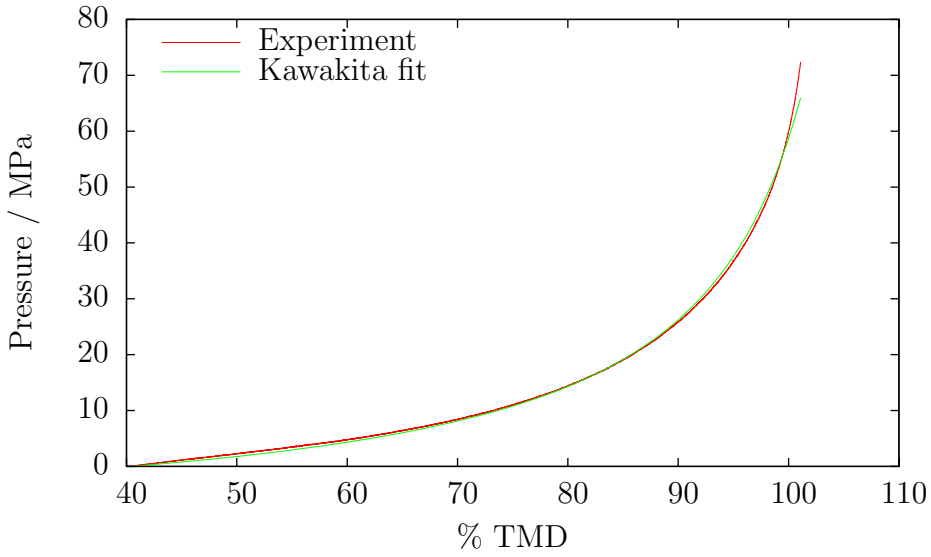

Figure 4.39: Pressure-porosity graph for quasistatic compaction of uncoated Orica prills, showing good agreement with Kawakita model. Initial strain rate $4 \times 10^{-4}\,\mathrm{s}^{-1}$. Kawakita parameters $A = 63.800 \pm 0.003 \times 10^{-2}$, $B = 241.97 \pm 0.09\,\mathrm{GPa}^{-1}$.

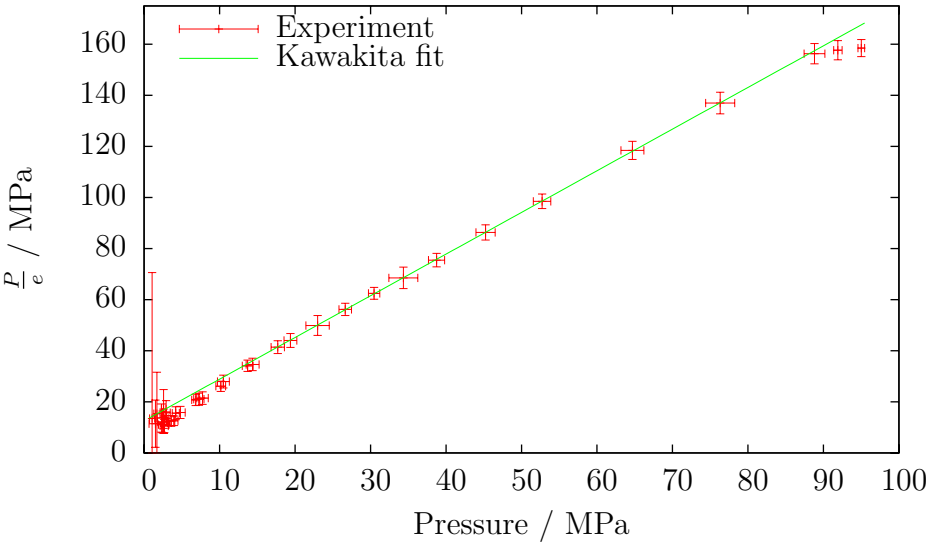

Figure 4.40: Kawakita plot for drop weight compaction of uncoated Orica prills, showing linear region from 20 to 80 MPa, and small deviations from linearity outside that range. Initial strain rate $170\,\mathrm{s}^{-1}$. Kawakita parameters $A = 61.30 \pm 0.18 \times 10^{-2}$, $B = 130 \pm 2\,\mathrm{GPa}^{-1}$.

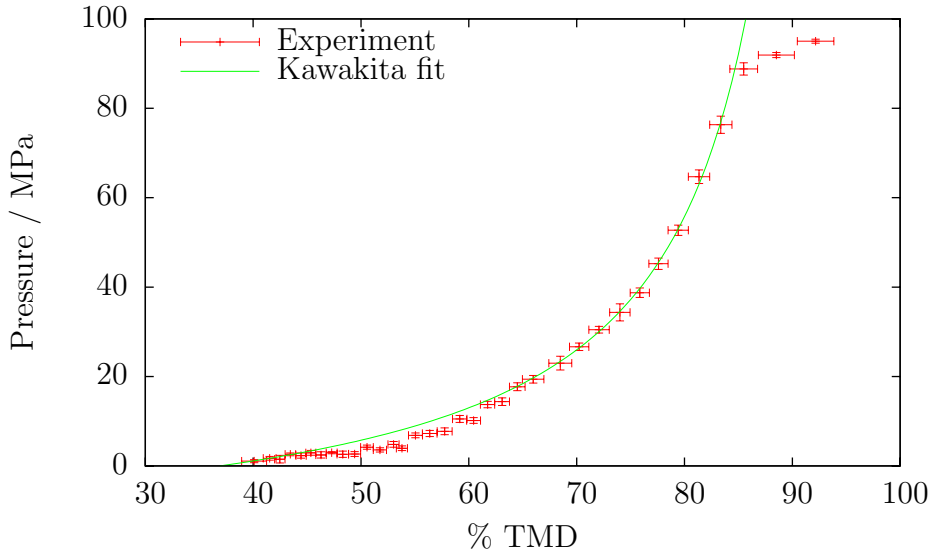

Figure 4.41: Pressure-porosity graph for drop weight compaction of uncoated Orica prills, showing broad agreement between experiment and Kawakita model. Model reliably over-predicts required pressure from 45% to 60% TMD, and fails to reproduce tail at 85% to 95% TMD. Initial strain rate $170\,\mathrm{s}^{-1}$. Kawakita parameters $A = 61.30 \pm 0.18 \times 10^{-2}$, $B = 130 \pm 2\,\mathrm{GPa}^{-1}$.

As this closely resembles the situation here, it would be interesting to study the failure stress of individual prills and compare this with that found from bed compaction.

4.2.10 Discussion

These compaction data suggest that the compaction behaviour of prill beds is dominated by viscoplastic flow of material over distances comparable to the prill diameter.

The enhanced resistance of the bed to compaction at higher strain rates (section 4.2.5) may be explained in this light. At higher strain rates, the material must flow more rapidly to compact, and will consequently dissipate more energy as plastic work. A similar argument applies to the enhanced resistance to compaction of beds of denser prills (section 4.2.5): denser prills require material to flow further to accommodate compaction.

Finally, and most tellingly, the bed undergoes compaction during the unloading cycle of a drop weight experiment. This is most clearly shown in figure 4.41 as a flat region at high pressure and fractional TMD, which the Kawakita model does not follow. Here the bed density is increasing at constant applied pressure, in a clear indication of plastic flow.

4.3 Conclusions and future work

- The short duration of the loading in an SHPB experiment renders the technique unsuitable for investigation of compaction.
- The addition of a line laser system to a drop weight produces a suitable technique for investigation of compaction at a strain rate of around $100\,\mathrm{s}^{-1}$.
- A screw-driven instrumented press is a suitable technique for investigation of compaction at a strain rate of around $10^{-4}\,\mathrm{s}^{-1}$.
- Increasing the rate at which compaction occurs increases the resistance of the bed to compaction. This is probably due to the increased speed at which

the material flows, and thus the increased energy dissipation in plastic work of the material.

- The increased force required to accelerate the bed material, and the increased degree of fracture seen at higher compaction rates, are unlikely to have any effect on the bed's resistance to compaction.

- Further compaction experiments at rates intermediate between those chosen here would help to quantify this effect.

- The porosity of the bed at the start of a compaction experiment has minimal effect on the shape of the pressure-porosity curve produced by that experiment.

- Beds of ammonium nitrate prills become more resistant to compaction if the microstructure of the prills is denser. This is probably due to the greater distance material must move to achieve compaction, and is likely to be true regardless of the material from which the prills are made.

- Beds of agricultural ammonium nitrate pellets show anomalously little resistance to compaction, compared to beds of ammonium nitrate prills. This is likely to be due partly to the pellets' relatively low resistance to disintegration, and partly to the lubricant effect of oil added to the pellets by the manufacturer as an anti-caking agent.

- Heckel's compaction model does not agree with the compaction data gathered here.

- Kawakita's compaction model agrees quite well with the compaction data gathered here.

- Experiments on the failure stress of individual prills would help assess the physical relevance of Kawakita's model to these data.

References

M. J. Adams and R. McKeown. Micromechanical analyses of the pressure-volume relationships for powders under confined uniaxial compression. *Powder Technology*, 88:155–163, 1996.

D. Ascher, P. F. Dubois, K. Hinsen, J. Hugunin, and T. Oliphant. Numerical python. Technical Report UCRL-MA-128569, Lawrence Livermore National Laboratory, 2001. http://numpy.scipy.org.

S. J. P. Palmer and J. E. Field. The deformation and fracture of β-HMX. *Proceedings of the Royal Society of London, Series A*, 383:399–407, 1982.

E. C. Robertson. Experimental study of the strength of rocks. *Bulletin of the Geological Society of America*, 66:1275–1314, October 1955.

W. H. Ross, J. Y. Yee, and S. B. Hendricks. Properties of granular and monocrystalline ammonium nitrate. *Industrial and Engineering Chemistry*, 37(11):1079–1083, 1945.

Chapter 5

Light output

As an explosive, ammonium nitrate reacts rapidly and exothermically. Reacting regions will therefore become very hot, and consequently emit light. The initiation, spread and rate of reaction can then be assessed by following this light output. In this research, plate impact was used to initiate reaction in beds of ammonium nitrate a few millimetres thick. High speed photography and photodiodes were then used to study the light output of, and hence reaction propagation within, these beds.

5.1 Granular beds

The light emitted during shock-induced reaction of granular beds of ammonium nitrate was studied. To facilitate this, a copper-fronted, glass-backed cell was constructed to hold a bed a few millimetres thick. A shock was introduced to the bed by plate impact of a copper-fronted flyer on the copper front of the cell. The glass window permitted light to leave the back face of the bed; this light was then captured and analysed. To contain harmful debris, the experiments took place in a sealed chamber. This chamber was evacuated to 100 mbar to prevent a dangerous overpressure developing.

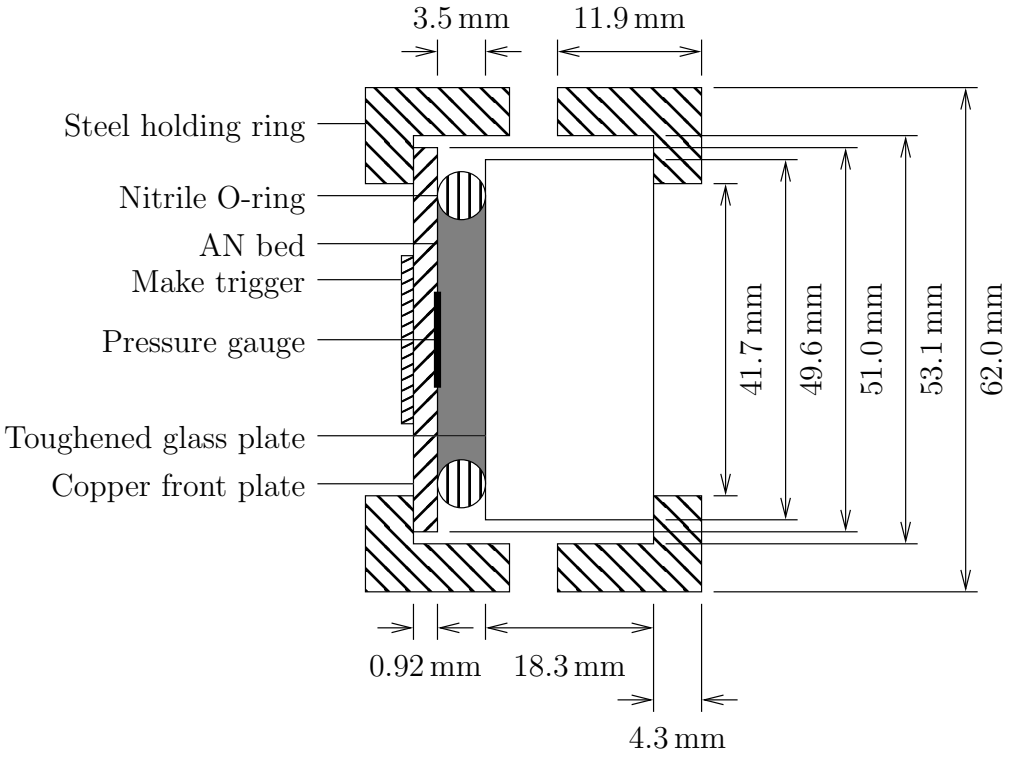

Figure 5.1: The sample cell used for holding granular beds in shock-induced reaction experiments. The projectile approaches the cell from the left.

5.1.1 Cell and flyer design

Figure 5.1 shows the design of the cell used in these experiments. The O-ring was a nominally 3.5 mm thick, $1\frac{3}{4}''$ (44.45 mm) internal diameter nitrile O-ring, supplied by Polar Bearings. The toughened glass plate was a nominally 19 mm thick, 50 mm diameter toughened float glass anvil, supplied by W. H. Constable & co. The steel holding ring was machined from $2\frac{1}{2}''$ (63.5 mm) bright mild steel bar. The copper front plate was made from copper sheet using a $2''$ (50.8 mm) circular punch.

5.1.1.1 Triggering

The make trigger serves to provide a triggering pulse to the various instruments directed at the experiment. It consists of layered one thou (25.4 μm) copper foil and double-sided Sellotape. The arrangement is shown in figure 5.2. The make

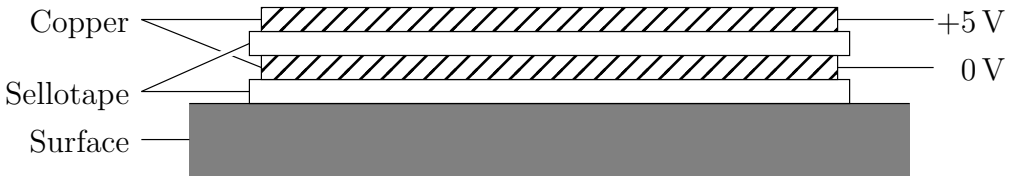

Figure 5.2: Design of make trigger used in these experiments. Not to scale.

trigger is connected to the input of a delay generator, set to a 5 V trigger level and a 500 Ω input impedance. The delay generator is configured to be triggered by a negative-going edge. When the projectile strikes the cell, it will cut through the make trigger. Its copper front plate will form an electrical connection between the two copper layers of the make trigger, causing the potential difference between them to fall. This in turn will trigger the delay generator, the outputs of which may be connected to instruments. It was found that arranging the make trigger with the positive foil away from the sample cell, as shown in figure 5.2, reduced the triggering system's sensitivity to electrical noise.

5.1.1.2 Pressure gauge

While the make trigger is suitable for triggering instrumentation, it is valuable to know the time at which a shock wave is introduced to the AN bed. The delay between the projectile striking the make trigger and the trigger activating is subject to considerable uncertainty. To eliminate this uncertainty, a thin pressure gauge was placed between the AN bed and the copper front plate. The design of the pressure gauge was based on that used in Obara et al. (1995), and is shown in figure 5.3.

The sensing element of this pressure gauge is a small disc of polyvinylidene difluoride (PVDF). PVDF is a piezoelectric polymer. It was biaxially stretched and poled in a strong electric field to form a thin film with a well-defined piezoelectric direction normal to that film. This film was then coated with an alloy of gold and platinum, to provide a good electrical connection to the PVDF film. The resulting sheet was 25 μm thick and provided by Piezotech S. A. S. Discs were cut from this sheet by pressing a 1.6 mm diameter circular cutter through the sheet and into a layer of paper. The same cutter was used to produce a

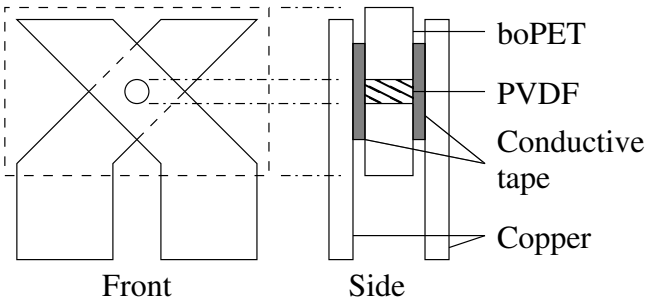

Figure 5.3: Design of pressure gauge used in these experiments. The PVDF is the sensing element. Not to scale. The gauge was assembled on double-sided Sellotape (not shown).

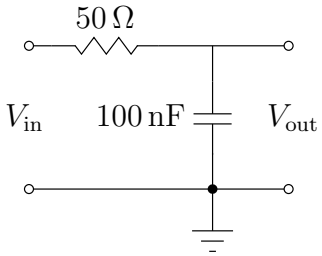

Figure 5.4: Circuit diagram of charge integrator for PVDF gauges.

hole in a 24 μm sheet of biaxially orientated polyethylene terephthalate (boPET; Mylar). This sheet served to insulate the two copper legs of the completed gauge from each other. 3M conductive double-sided tape was applied to one side of this pierced sheet. The PVDF disc was aligned with the hole by feel and eye, with its positive face arranged so that it would face the shock in the completed gauge. The conductive tape was then used to affix this sheet to the legs, cut from one thou (25.4 μm) copper foil.

As a piezoelectric sensor, the PVDF gauge will produce a charge dependent on the pressure applied to it. To convert this to a voltage, the gauge was connected to a charge integrator (figure 5.4). The output of this integrator was recorded with an oscilloscope.

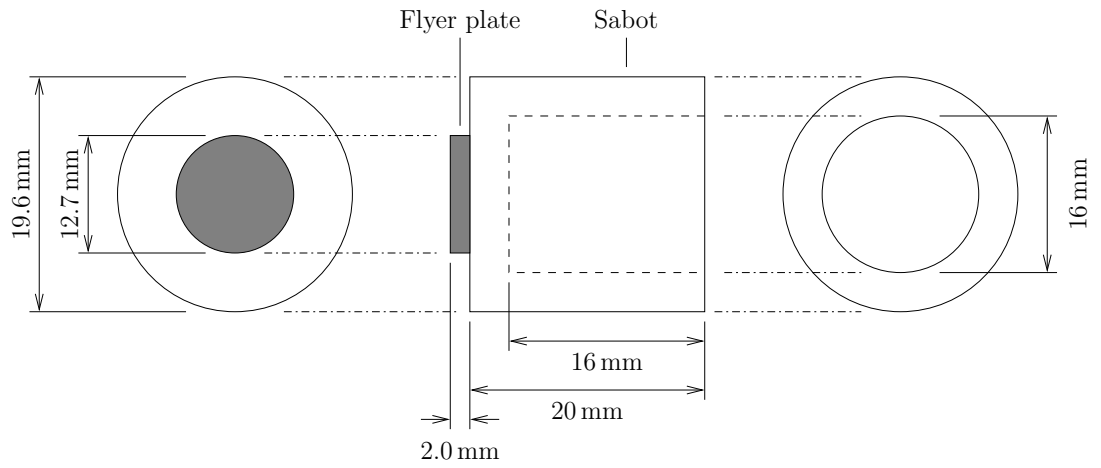

Figure 5.5: Flyer design used in these experiments. The flyer plate strikes the front plate of the sample cell shown in figure 5.1. The flyer plate is made of copper, and the sabot is made of POM.

5.1.1.3 Flyer

The design of the flyer is shown in figure 5.5. The purpose of the sabot is to carry the flyer plate along the gun barrel, and ensure that the plate strikes the sample cell at normal incidence. The flyer plate was made from 14 gauge copper sheet using a circular punch. This punching left a burr on the flyer plate, which interfered with attaching the plate to the sabot. The burr was therefore filed off. The sabot was made from 20 mm diameter polyoxymethylene (POM; acetal) rod, using a lathe. It was hollowed out to reduce the flyer's mass, and hence increase the impact velocity achievable with the small gun. The production technique left a nipple on the front face of the sabot, which was removed using a knife. The flyer plate was attached to the sabot using double-sided Sellotape. To align the plate with the sabot axis, the assembled flyer was placed, plate down, on a flat surface. Firm pressure was then applied to the rear of the sabot by hand. This was found to align the plate and sabot to within 3 milliradians. Each flyer had a mass of 6.3 ± 0.3 g.

5.1.1.4 Bed construction

To obtain consistent particle sizes, the raw bed material was ground and passed through a pair of sieves of different mesh size. The fraction passing through the coarser sieve and retained by the finer was used to manufacture the bed. The sizes of these two sieves were used to identify the distribution of particle sizes in a given bed. For most of these experiments, 150–212 μm particles were used. These were ground using a pestle and mortar. Some experiments used 20–40 μm particles. These were ground by rotating a cylinder containing the bed material and steel ball bearings at 60 r. p. m. for eight hours.

The sample cell was constructed, face down, with the make trigger, glass plate, and rear holding ring left off. The ground and sieved bed material was poured into the sample cell, and the glass plate and rear holding ring attached. This process will reduce the porosity of the bed. The confinement cell shown in chapter 4, figure 4.1 was used to assess this effect. The free-pour density of 150–212 μm AN was found to be $54 \pm 4\,\%$ TMD. Inserting the plunger with force similar to that used to apply the back plate of the sample cell increased the density to $58.2 \pm 1.3\,\%$ TMD.

5.1.1.5 Projectile velocity

The muzzle of the gun was equipped with a pair of light gates, 14.955 ± 0.009 mm apart. This allowed the velocity of the projectile to be measured. The velocity is expected to depend on the mass of the projectile and the firing pressure of the gun. While the barrel diameter and length will also affect the projectile velocity, these are constant throughout this research.

Neglecting friction between the barrel and projectile, the pressure in the target chamber, and the volume of the barrel, the muzzle velocity of the projectile will be

$$u = \sqrt{\frac{2PAl}{m}}\ , \tag{5.1}$$

where P is the firing pressure, A is the cross-sectional area of the barrel, m is the projectile mass, and l is the barrel length. As noted above, A and l are constant

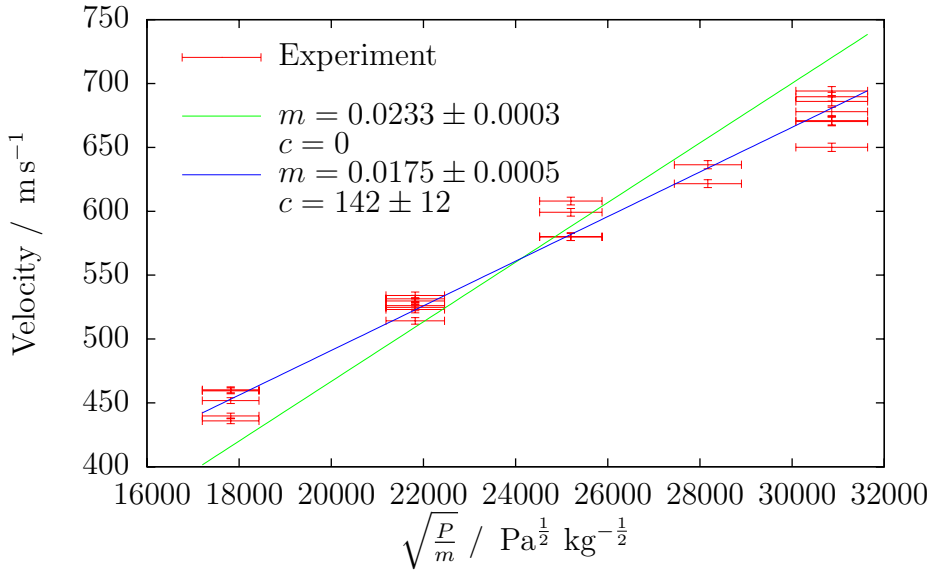

Figure 5.6: Projectile velocity calibration graph for the Cavendish small gun, using helium propellant and the 19.6 mm barrel. Two best-fit lines, one of the form $y = mx$ and one of the form $y = mx + c$, are shown.

between shots, giving

$$u \propto \sqrt{\frac{P}{m}} \,. \tag{5.2}$$

Figure 5.6 shows the projectile velocity as a function of this mass-adjusted firing pressure $\sqrt{\frac{P}{m}}$. The large y-intercept of the best-fit line suggests that this model's assumptions are not wholly justified. However, it serves as a useful aid when selecting firing pressures.

5.1.1.6 Fibre and mirror mounts

Capturing and analysing the light leaving the rear of the sample cell required that mirrors and fibres be mounted on the cell. Two designs of mount were used, depending on whether framing photography was required. The first is shown in figure 5.7. This design was used with framing photography. A large batch of these mounts was cut from a single 9.8 mm PMMA sheet using a bandsaw and appropriately angled jigs. The hole was then drilled using a pillar drill and another suitable jig. In use, the surface labelled $*$ was attached to the rear of

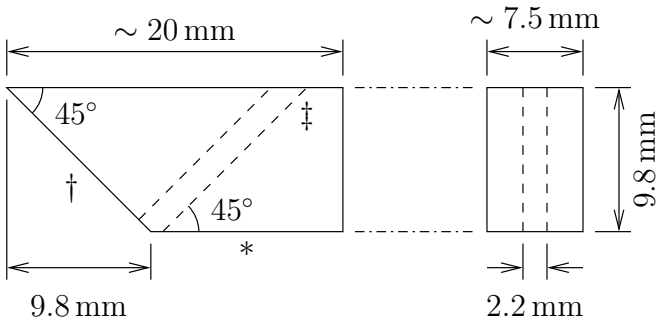

Figure 5.7: Fibre mount design when framing photography is required. Measurements prefixed with ∼ are approximate, and vary between individual mounts. The surface labelled † is attached to the rear of a front-silvered mirror using double-sided tape. The surface labelled ∗ is similarly attached to the rear steel holding ring of the sample cell. An optical fibre is inserted through the hole labelled ‡, and held in place by friction.

a front-silvered mirror using double-sided tape. The surface labelled † was then similarly attached to the rear steel holding ring shown in figure 5.1, so that the mirror would reflect light from the AN bed. This allowed the camera to be placed out of the line of fire of the gun. An optical fibre was then fed through the drilled hole labelled ‡, and held in place by friction with the hole walls. This arrangement pointed the end of the fibre at the centre of the AN bed, to improve light capture.

The second design of mount was used to affix fibres to the rear of the toughened glass plate at normal incidence. When the mount was placed at the centre of the plate, this improved light capture. However, this arrangement was incompatible with framing photography. Figure 5.8 shows this design. The mounts were, again, made in a batch. The starting material in this case was $\frac{1}{2}''$ (12.7 mm) square-section aluminium-alloy bar. A groove was cut in this using a rotary side-and-face cutter, and individual mounts were cut from the resulting grooved bar using a bandsaw. Holes to accept the fibres were then drilled. The surfaces labelled ∗ were affixed to the back plate using double-sided tape, and fibres fed into the holes. As with the first mount design, friction held the fibres in place.

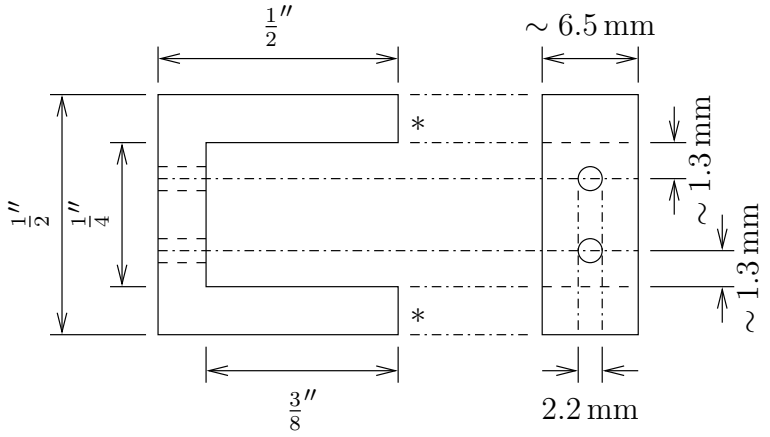

Figure 5.8: Fibre mount design when framing photography is not required. Measurements prefixed with $\sim$ are approximate, and vary between individual mounts. The surfaces labelled $*$ are attached to the rear of the glass back plate of the sample cell using double-sided tape.

5.1.2 Framing photography

Framing photography using an Ultranac 501 camera provided a useful sanity check for other diagnostics and models. Figure 5.9 shows framing photography typical of this experiment. It clearly shows an induction time of $2.5 \pm 0.5\,\mu$s between the arrival of the shock in the bed and the peak light output of the bed. This is followed by a decay of similar duration, leaving very little light output $6\,\mu$s after impact. Saturation of the detector, and the low temporal resolution of the technique, leads to large uncertainty in the induction and decay times.

During the decay, structure can be seen within the emitted light. The most obvious is a ring around the bright region. This is most likely to be due to the construction of the projectile (figure 5.5). The hollow centre of the projectile will cause the centre of the flyer plate to be released more quickly, and to a lower pressure, than the edges of the flyer plate. This in turn will lead to regions of the bed near the edges of the flyer plate experiencing high pressure for longer than regions near the centre. This could easily cause those regions to emit more brightly than the centre in the late stages of the experiment. In frame 8, when this structure is first visible, the ring is $11.0 \pm 0.5\,\mathrm{mm}$ in diameter. Subsequently it grows, reaching $15.3 \pm 0.8\,\mathrm{mm}$ across in frame 11, the last frame in which

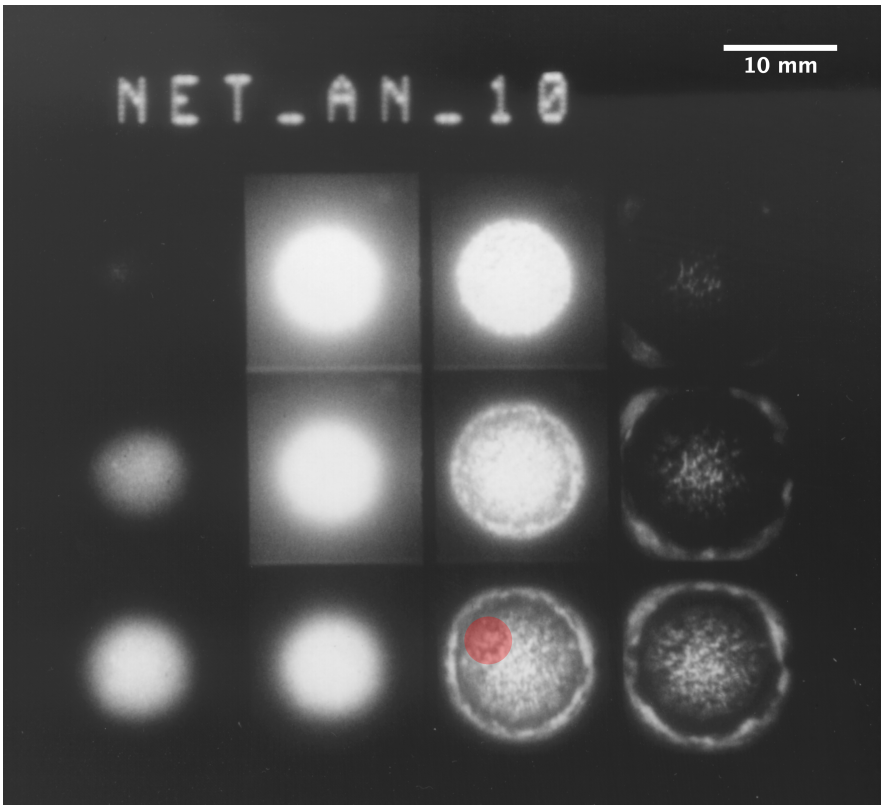

Figure 5.9: Framing photography of 150–212 μm ammonium nitrate granular bed. Camera was triggered 110 ± 30 ns before shock entered bed. 700 ± 40 m s^{-1} impact velocity, 460 ns exposure time, 40 ns interframe time. Taken using Ultranac 501 camera; frame order as shown in figure 2.19.

it is sufficiently visible to measure. This suggests that the flyer is spreading laterally under the applied load. Recovered flyers suggest that this interpretation is reasonable: they are broader and thinner than pristine flyers, and dished with the concave face towards the direction of travel.

It is useful to consider the very similar experiments of Proud et al. (2003). By performing the experiment on a bed of 150–212 μm sugar, they were able to eliminate triboluminescence and compression of trapped gas as significant sources of light in this experiment. Despite increasing the exposure time to 10 μs and employing image intensification, very little light was seen from the sugar bed. Sugar was chosen for its strong triboluminescence and similar density to AN. The density of sugar is 1587 $\mathrm{kg\,m^{-3}}$, versus 1720 $\mathrm{kg\,m^{-3}}$ for AN.

The speckled pattern visible from frame 8 onward is interesting. A similar pattern was seen in Proud et al., but could not be distinguished from noise due to the image intensifier. Here, comparison with frame 2 suggests that this speckle is not an artefact of the photographic film on which the image is recorded. It has a scale of the order of a few hundred microns. This is comparable to that of the ammonium nitrate grains in the bed; it seems reasonable to assume that the grains are the source of this structure. It is also apparent that features of this structure are persistent between frames. The loop highlighted with a red circle in frame 9 is the most obvious of these. It is visible from frame 7 to frame 11. The presence of such apparent structures is unremarkable: a random speckle pattern is likely to contain apparent structures simply because human perception is adapted for detecting such structures. Their persistence, however, is interesting for two reasons. First, it provides a method for assessing lateral expansion of the bed. The distance between two features which remain visible from frame 9 onward can be measured, and changes in this distance can be converted to a strain. This indicates a strain of 0.11 ± 0.07 between frames 9 and 10, with no measurable lateral motion from frame 10 onward. Second, it indicates that no new light sources are appearing; each emitting region is simply dimming.

The behaviour of this speckle pattern suggests that it is caused by the region of reacting material surrounding a hot spot. Each hot spot will cause the surrounding material to react, emitting light. The reaction then ceases, and the emitting region dims over time. A success of this technique is that the resolution

is good enough to see the individual grains of AN, and observe the late evolution of these emitting regions. However, the early evolution of the emitting region is obscured. In the earlier frames, unreacted AN between the emitting regions and the camera prevents observation. Once the AN at the face of the sample towards the camera starts to react, the light output from previously ignited AN saturates the camera, preventing observation. Proud et al. avoided this problem by using a 0.4 mm thick bed. By using very short exposure times and image intensification, they were able to observe the formation and growth of emitting regions. Premature decay of some emitting regions, believed to be associated with a sub-critical hot spot, was also observed.

The 501 camera's variable exposure time could be used to reduce the uncertainty in measurements of induction and decay time. However, the temporal resolution would be limited by the time-dependent light output of the reacting bed. Optimizing temporal resolution, and avoiding saturation of the detector, would require careful synchronization between the bed's light output and the camera's exposure. In light of the variable delay between the make trigger and the arrival of the shock in the bed, this synchronization would depend heavily on luck. The higher dynamic range, finer temporal resolution, and longer recording time of a photodiode would avoid these problems.

5.1.3 Photodiode measurements

Optical fibre was used to connect an ET-2030 photodiode to the rear of the sample cell. This allowed the photodiode to be placed outside the capture chamber in which the experiment took place, thereby reducing the chance that part of the sample cell would damage the photodiode. The fibre used was cut with a razor, then polished using diamond polishing paper. The fibre was polished first on 30 μm paper, then on 3 μm, 1 μm and finally 0.3 μm paper. The output of the photodiode was connected to a digital oscilloscope. Initially, the oscilloscope input was set to 1 MΩ impedance. The resulting photodiode traces indicated that bright light was emitted for tens of microseconds following the impact. This is inconsistent with the framing photography described above, which shows the light fading several microseconds after impact.

Further investigation found that this result was due to the photodiode's internal capacitance of $146.4 \pm 0.7\,\mathrm{pF}$ discharging across the oscilloscope's input impedance. The resulting RC circuit had a time constant of $146.4 \pm 0.7\,\mu\mathrm{s}$, and was therefore unsuitable for following an experiment whose duration is of the order of microseconds. The oscilloscope's input impedance was therefore set to $50\,\Omega$. This reduced the time constant of the system to $7.32 \pm 0.08\,\mathrm{ns}$, which was suitable for this experiment. The sensitivity of the photodiode-oscilloscope system was, however, reduced. This is because the photodiode produces a current dependent on the intensity of the light incident on it, while the oscilloscope records the potential difference produced when that current flows through its input impedance. The limiting factor on the system's sensitivity will be electrical noise in the oscilloscope, which is not affected by the input impedance. Therefore, reducing the oscilloscope's input impedance by a factor of 20,000 will reduce the system's sensitivity by a like factor. This reduced sensitivity was, however, still adequate for this experiment.

Figure 5.10 shows the photodiode output corresponding to the framing photography shown in figure 5.9. This shows the same growth and fall noted in section 5.1.2. The induction time can be seen from the photodiode trace to be $2.49 \pm 0.05\,\mu\mathrm{s}$. This agrees with that found using framing photography, but is, as expected, more precise. The photodiode output clearly shows the decay of the light output. It also shows a bump in that decay from 3.5 to $4\,\mu\mathrm{s}$, in which the light output rises again. Comparison with framing photography indicates that this coincides with the formation of a bright ring structure, also discussed in section 5.1.2. Interestingly, this bump was not observed in every experiment – of the 52 granular-bed experiments for which photodiode data were gathered, 11 showed this bump.

The decay of the bed's light output is best illustrated by figure 5.11. This shows the same data as figure 5.10, but with a logarithmic y axis. That the decay follows a straight line when so plotted strongly suggests that the decay is exponential. Such a decay may be written

$$V(t) = V_0 e^{-\frac{t}{\tau}}, \tag{5.3}$$

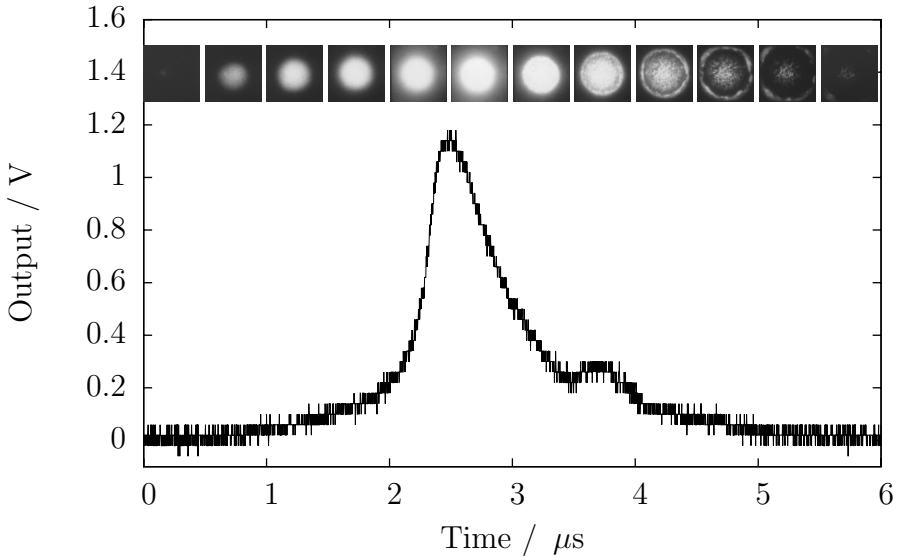

Figure 5.10: Photodiode output of 150–212 μm ammonium nitrate granular bed under $700 \pm 40\,\mathrm{m\,s^{-1}}$ flyer impact. Superimposed images show framing photography of the experiment. Horizontal extent of image indicates duration for which shutter was open. Experiment also shown in figure 5.9.

where V_0 is the output at $t = 0$ and τ is the time constant of the decay. V_0 is of little interest: it depends upon the precise time at which the trigger is activated, and the efficiency with which light from the experiment is gathered. τ, however, is purely a property of the light output of the experiment. Taking logarithms, equation 5.3 may be re-written as

$$\ln V = \ln V_0 - \frac{1}{\tau} t \ . \tag{5.4}$$

Using equation 5.4, V_0 and τ were found by a linear regression fit to the photodiode output data. Errors were assessed by using the bootstrap method.[1] For this experiment, $V_0 = 125 \pm 5\,\mathrm{V}$ and $\tau = 547 \pm 4\,\mathrm{ns}$.

The induction time, and the time constant of the decay, were investigated for 150–212 μm granular beds of ammonium nitrate.

[1] See chapter 2, section 2.12.5

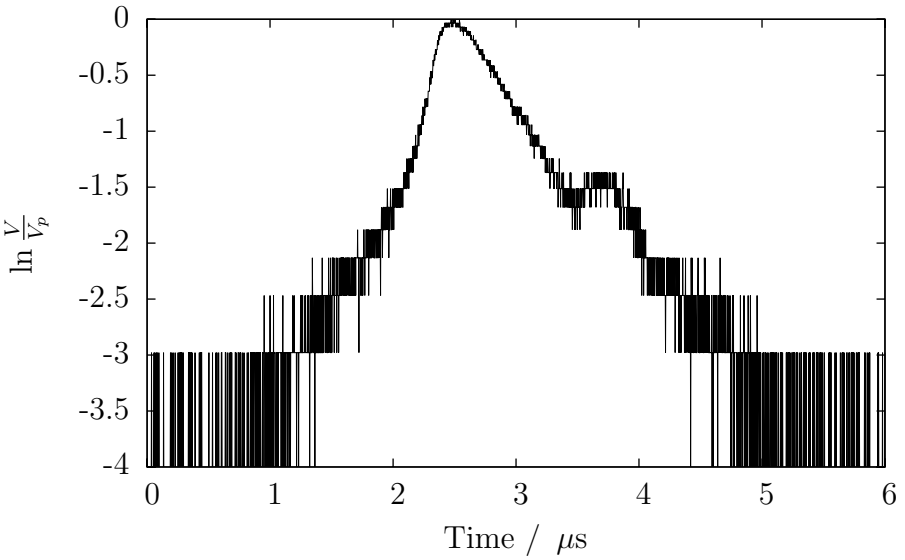

Figure 5.11: Photodiode output of 150–212 μm ammonium nitrate granular bed under $700 \pm 40\,\mathrm{m\,s^{-1}}$ flyer impact, with logarithmic y axis. V_p is the maximum output recorded in the experiment. In this case $V_p = 1.18\,\mathrm{V}$. Experiment also shown in figures 5.9 and 5.10.

5.1.3.1 Induction time

The induction time is the delay between the arrival of the shock wave in the bed, and the peak of the bed's light output. Given the observations in section 5.1.2, this peak marks the time at which ignition of fresh AN grains ceases. Several shots on cells of the form shown in figure 5.1, filled with 150–212 μm ground ammonium nitrate, were performed. The induction time was taken as the time between the first rise of the front PVDF gauge output and the peak of the photodiode output. Uncertainty in the induction time was due to the duration of these features.

Figure 5.12 shows the results of these experiments. At impact velocities below $450\,\mathrm{m\,s^{-1}}$ no light was seen; this could be because the granular bed did not react. Alternatively, the slow-moving projectile may not have activated the make trigger while the bed was reacting. Recovered debris from these low-velocity experiments indicated that the projectile did not breach the copper front shim. As the make trigger must be cut through to activate, this lends some support to the latter suggestion. Rather than re-design the trigger mechanism, the exper-

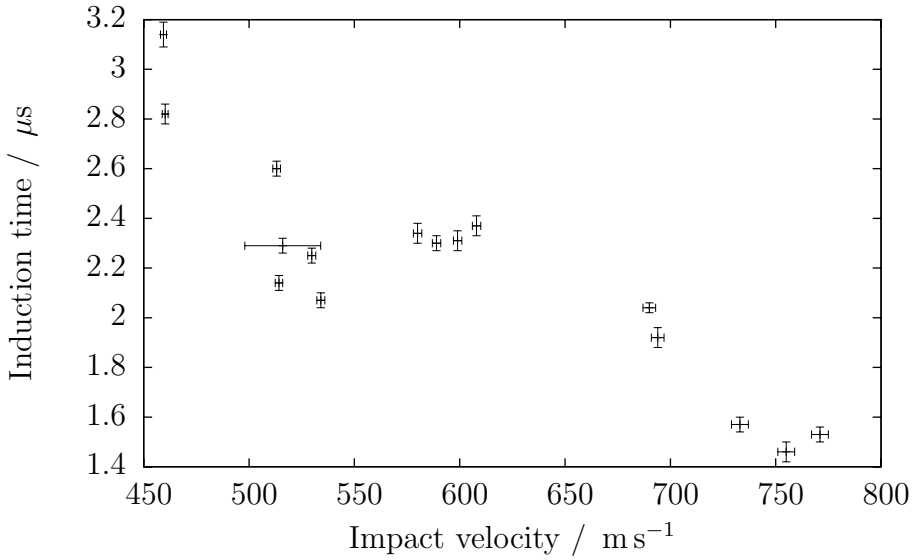

Figure 5.12: Induction times for granular ammonium nitrate beds, impacted at a range of velocities.

iment was restricted to velocities in excess of $450\,\mathrm{m\,s^{-1}}$. The results show that the induction time falls as the projectile velocity increases. This is intuitively attractive: supplying more shock energy to the explosive causes it to react more quickly. However, there are competing explanations to consider.

The variable induction time may be due to variation in the duration of the pressure pulse in the bed. This pulse is caused by the collision between the flyer plate and the front shim of the sample cell. When the pulse ends, it is possible that ignition of AN ceases. After this time, the light output of the bed will decay as reacting regions cool down and are not replaced. This will produce the peak and decay seen in photodiode records of the bed's light output.

If lateral release waves from the edge of the flyer plate are neglected, this problem is analytically tractable. Figure 5.13 shows the X-T diagram for the experiment. The flyer approaches the front shim from the left at a velocity u_i. On impact, shock waves are propagated forward into the shim and backward into the flyer. After some time t_s the forward-going shock reaches the interface between the shim and the AN bed. This is the start of the pressure pulse in the bed. The release wave reflected from this interface is neglected in this treatment,

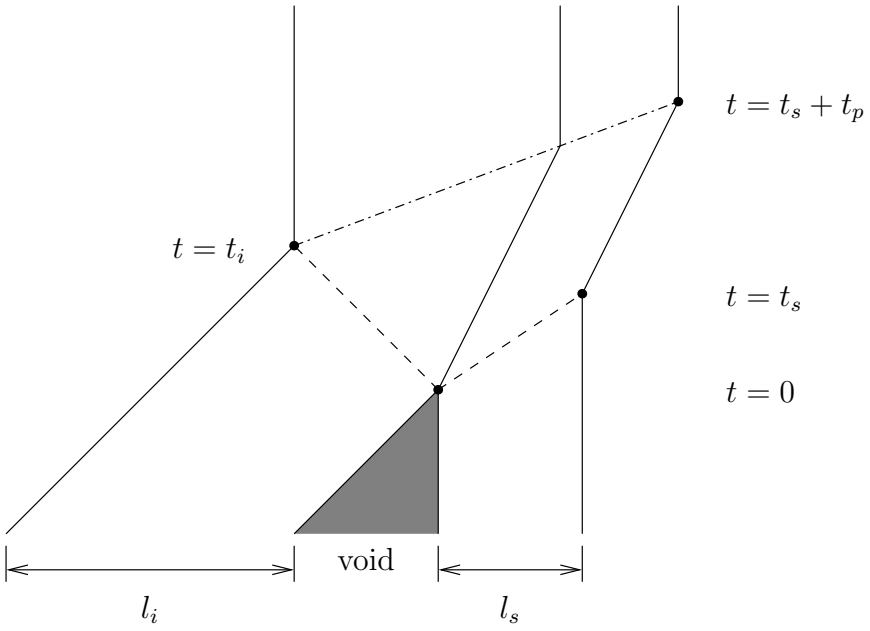

Figure 5.13: X-T diagram of the collision between the flyer plate and the front shim of the experimental cell, in the lab's frame of reference. l_i is the initial thickness of the flyer plate. l_s is the initial thickness of the front shim. t_s is the time taken for the shock to travel through the front shim, while t_i is the time taken for the shock to travel through the flyer plate. t_p is the duration for which the back face of the front shim is held at its shock pressure, and is to be found.

because its properties depend strongly on the unknown properties of the reacting AN bed. Meanwhile, the backward-going shock from the impact is travelling towards the rear face of the flyer. It reaches this face at a time t_i, and is reflected as a release wave. This travels through the flyer and front shim, which are now in a uniform shocked state. The release wave reaches the bed-shim interface at a time $t_s + t_p$, and ends the pressure pulse in the AN bed.

Copper is widely used in plate impact experiments, and therefore its shock properties are well known. For this problem, the relationship between shock velocity and the particle velocity behind the shock is required. This is simply

$$u_s = c_0 + s u_p \tag{5.5}$$

where u_s and u_p are the shock and particle velocities respectively, and c_0 and s

are experimentally-determined constants. The speed with which a release wave propagates through the material is also required. During this experiment, the copper experiences pressures of approximately 10 GPa. In this regime, the release wave travels at approximately the longitudinal sound speed c_l of the material. For copper, $c_0 = 3.940\,\mathrm{km\,s^{-1}}$, $s = 1.489$ (Asay and Shahinpoor, 1993) and $c_l = 4.76\,\mathrm{km\,s^{-1}}$ (Marsh, 1980). These references did not state any errors; for purposes of error analysis the error has been assumed to be 5 in the least significant figure. The velocity of the interface between the flyer and the shim is also required. Since the two are of the same material, a simple symmetry argument shows this to be

$$u_j = \tfrac{1}{2}u_i \tag{5.6}$$

where u_i is the impact velocity.

Calculating the travel times of the various shock and release waves in this system is simplified by careful choice of reference frames. The simplest reference frame in which to consider a shock is the rest frame of the unshocked material. The simplest reference frame in which to consider a release wave is the rest frame of the unreleased material. Since the velocities of these frames relative to the lab frame are not relativistic, travel times calculated in these frames remain valid in the lab frame without further transformation.

Bearing this in mind, the time t_s for the forward-going shock to reach the bed-shim interface is easily calculated. The rest frame of the unshocked material is also the lab frame, so the particle velocity behind the shock will simply be the interface velocity u_j. Equation 5.5 then gives the velocity of this shock

$$u_f = c_0 + \tfrac{1}{2}su_i \ . \tag{5.7}$$

This shock must cross the thickness l_s of the front shim, giving

$$t_s = \frac{l_s}{c_0 + \frac{1}{2}su_i} \ . \tag{5.8}$$

The time t_i for the backward-going shock to reach the rear of the flyer is only slightly more challenging. In this case the simplest frame is the rest frame of the

incoming flyer, which is moving at u_i in the positive x direction. In this frame, the particle velocity behind the shock will be

$$\begin{aligned} u_p &= u_i - u_j \\ &= \tfrac{1}{2}u_i \end{aligned} \tag{5.9}$$

in the negative x direction. By equation 5.5, the shock velocity in this frame will then be

$$u_b = c_0 + \tfrac{1}{2}su_i \tag{5.10}$$

in the negative x direction. In this frame of reference, the rear of the flyer is stationary. The shock must therefore cover a distance l_i to reach the back face, giving

$$t_i = \frac{l_i}{c_0 + \frac{1}{2}su_i} \ . \tag{5.11}$$

The time t_r for the release wave to travel from the rear of the flyer to the bed-shim interface requires a little more thought. All the material through which the release travels will have been shocked to a uniform state. This material will be travelling at $\frac{1}{2}u_i$ in the positive x direction, providing an obvious frame of reference in which the release will simply travel at c_l through stationary material to reach the stationary bed-shim interface. However, the material will also have been compressed by the shock waves. The distance the release must travel will therefore not be simply $l_s + l_i$. The new thickness of the material can most easily be found by considering the shock wave itself. Both the shocks considered in this problem have travelled at a velocity u_s into stationary material of some density ρ_0, accelerating it to a velocity $\frac{1}{2}u_i$ and compressing it to a density ρ_s. Conserving mass across the shock gives

$$\begin{aligned} \rho_0 u_s &= \rho_s \left(u_s - \tfrac{1}{2}u_i\right) \\ \rho_0 \left(c_0 + \tfrac{1}{2}su_i\right) &= \rho_s \left(c_0 + \tfrac{1}{2}(s-1)u_i\right) \qquad \text{from equations 5.5 and 5.6} \\ \frac{\rho_0}{\rho_s} &= \frac{c_0 + \frac{1}{2}(s-1)u_i}{c_0 + \frac{1}{2}su_i} \ . \end{aligned} \tag{5.12}$$

This compression ratio immediately gives the distance the release wave must

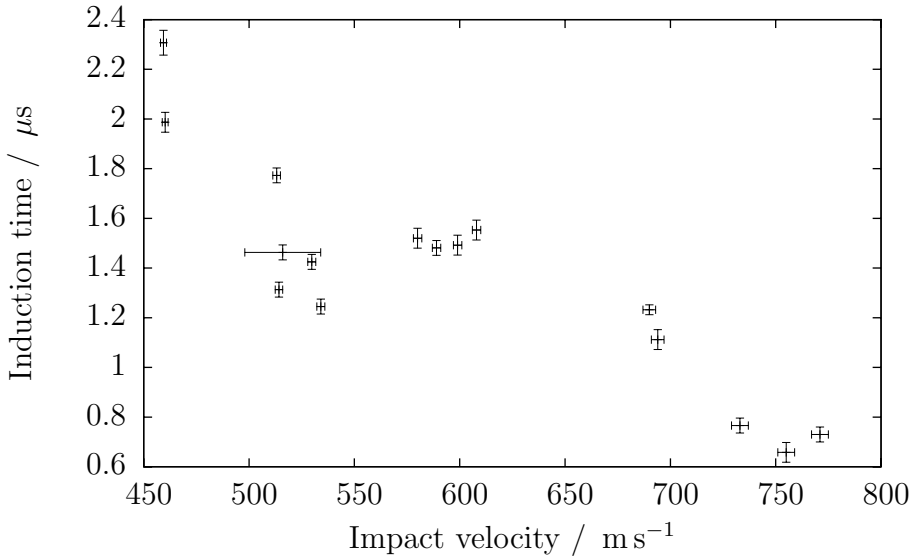

Figure 5.14: Induction times for granular ammonium nitrate beds, impacted at a range of velocities. The calculated loading pulse duration for each impact velocity has been subtracted from these induction times.

travel, and hence the time it takes doing so. This time

$$t_r = \frac{l_i + l_s}{c_l} \cdot \frac{c_0 + \frac{1}{2}(s-1)u_i}{c_0 + \frac{1}{2}su_i} \,. \tag{5.13}$$

The total pulse duration t_p can thus be found:

$$\begin{aligned} t_p &= t_i + t_r - t_s \\ &= \frac{l_i}{c_0 + \frac{1}{2}su_i} + \frac{l_i + l_s}{c_l} \cdot \frac{c_0 + \frac{1}{2}(s-1)u_i}{c_0 + \frac{1}{2}su_i} - \frac{l_s}{c_0 + \frac{1}{2}su_i} \\ &= \frac{1}{c_0 + \frac{1}{2}su_i} \left(\frac{l_i + l_s}{c_l} \left[c_0 + \frac{1}{2}(s-1)u_i \right] + l_i - l_s \right). \end{aligned} \tag{5.14}$$

Figure 5.14 shows the effect of applying this correction to the experimental results. Induction time still clearly decreases with increasing impact velocity. This is inconsistent with the hypothesis that the variation in induction time is due to reaction ceasing when the loading pulse ends. Were that the case, subtracting the duration of the loading pulse from the induction time should give a constant.

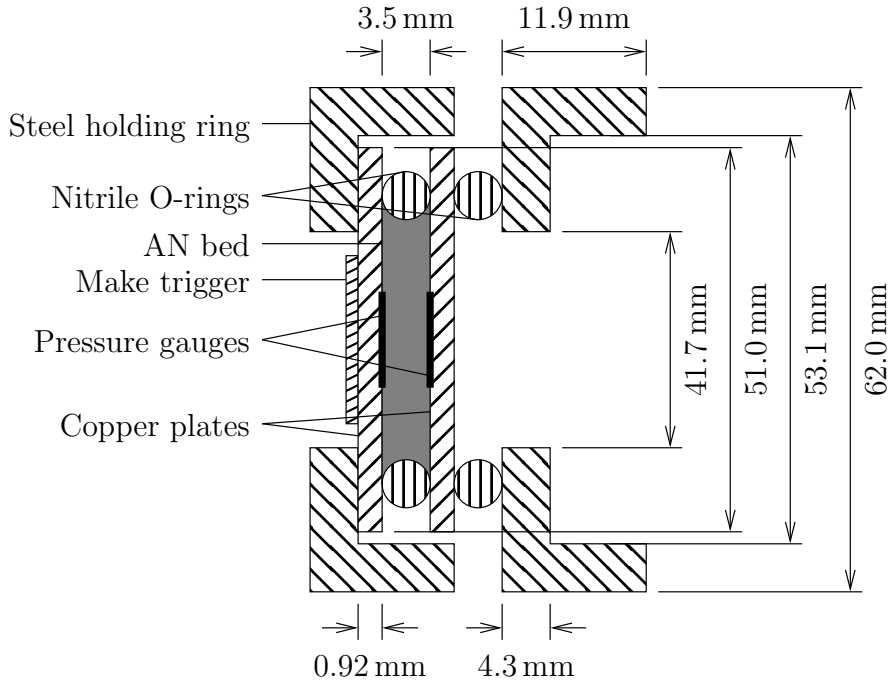

Figure 5.15: Arrangement of modified AN cell used to measure the travel time of pressure waves through the bed.

Another possible explanation for this variability in induction time is based on the opacity of the ammonium nitrate bed. The bed contains many AN-air interfaces which will scatter light. This will attenuate light emitted far from the glass back plate of the bed. If this attenuation is significant on the scale of the bed's thickness, only the region of the bed close to the back plate will contribute to the recorded light output. The pressure wave introduced by the impact will take some time to reach this observable volume. This delay between impact and observation may be sufficient to explain the variation in induction time with impact velocity.

The relationship between impact velocity and travel time in a reactive granular bed is difficult to model. However, the sample cell used in these experiments may be modified to measure this relationship directly. Figure 5.15 shows the modified sample cell. This design was chosen to avoid the need to produce new parts, while also eliminating the glass back-plate.

Figure 5.16 shows the results of this experiment. The vertical error bars are

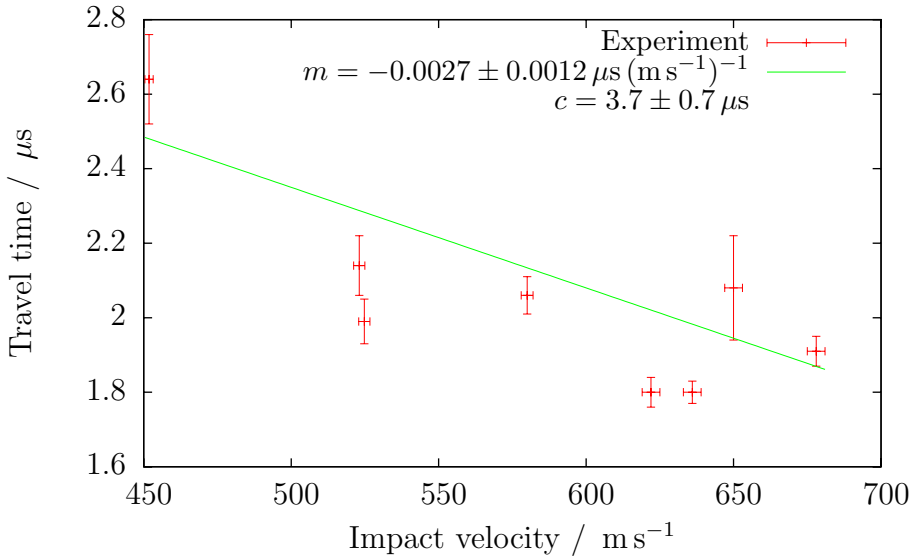

Figure 5.16: Travel time of pressure wave through 3.5 mm thick 150–212 μm AN granular bed. A best-fit line of the form $y = mx + c$ is plotted. Note uncertainty on fit parameters.

based on uncertainty in the individual measurement. The broad spread of the data suggests that there is some source of shot-to-shot variation for which this does not account. The best-fit line shown in figure 5.16 was used to calculate the travel time for each experiment in figure 5.12. This travel time was then subtracted from the induction time.

Figure 5.17 shows the result of this subtraction. The large error bars are due to uncertainty in the best-fit line calculated in figure 5.16. Subject to these errors, however, the induction time is entirely eliminated by accounting for this travel time. This suggests that the opacity of the granular AN bed is significant on the 3.5 mm length-scale of this experiment, and that this opacity is sufficient to explain the observed dependence of induction time on impact velocity.

The large uncertainty in the travel time of pressure waves through the bed weakens this conclusion considerably. One simple way to reduce this uncertainty would be to take additional measurements of the travel time. A more elegant approach, though, would be to take travel time and induction time data simultaneously. This would eliminate the shot-to-shot variation seen in figure 5.16. However, the sample cell would need to be re-designed. Both light output and

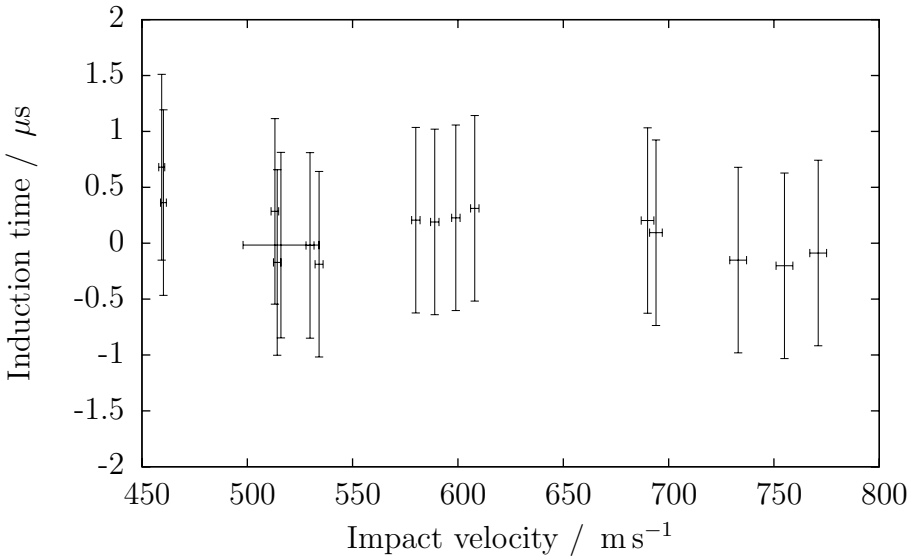

Figure 5.17: Induction times for granular ammonium nitrate beds, impacted at a range of velocities. The calculated travel time of the input pressure wave through the bed has been subtracted from these induction times.

back-face pressure should be measured close to the loading axis. The PVDF gauges used in this experiment are opaque. The gauges would therefore need to be slightly re-designed to place the sensing element as close as possible to the edge of the copper. By careful placement of this modified PVDF gauge and the photodiode fibre, off-axis effects on both the light output and the rear-face pressure reading would be minimized.

5.1.3.2 Decay time

After the light output has reached a maximum, it decays. As is observed in chapter 6, the bed is emitting as a black body during this time. This decay can be interpreted as the hot regions cooling, and therefore emitting less light.

To probe this, all emitting regions were taken to be identical. This allowed a single emitting region to be considered: the output of the bed as a whole will be a constant multiplier of the output of this one region. Further, this emitting region was taken to be defined by an instantaneous release of heat at a single point in the bed: a delta function in space and time. This was assumed to cool

by conduction into the surrounding bed. It is immediately apparent that such a delta function does not, in fact, exist. The infinite spike in temperature would be quite obvious. However, the heat profile of any small heat source cooling by conduction will quickly converge to that of a delta function. The time taken for this convergence can be accounted for by shifting the initial delta function in time.

The heat equation for an isotropic material (Carslaw and Jaeger, 1947) is

$$\frac{\partial T}{\partial t} = \frac{K}{\rho C_p} \nabla^2 T \ , \tag{5.15}$$

where K is the conductivity of the material, ρ is its density, and C_p is its specific heat capacity at constant pressure. Given the problem, spherical polar coordinates are appropriate. In this system,

$$\nabla^2 T = \frac{1}{r^2}\frac{\partial}{\partial r}\left(r^2 \frac{\partial T}{\partial r}\right) + \frac{1}{r^2 \sin\theta}\frac{\partial}{\partial \theta}\left(\sin\theta \frac{\partial T}{\partial \theta}\right) + \frac{1}{r^2 \sin^2\theta}\frac{\partial^2 T}{\partial \phi^2} \ . \tag{5.16}$$

Since the problem is spherically symmetrical, only the term in $\dfrac{\partial T}{\partial r}$ is non-zero. This gives

$$\frac{\partial T}{\partial t} = \frac{K}{\rho C_p} \cdot \frac{1}{r^2}\frac{\partial}{\partial r}\left(r^2 \frac{\partial T}{\partial r}\right) \ . \tag{5.17}$$

The appropriate solution to this (Carslaw and Jaeger, 1947) is

$$T = Q\left(\frac{1}{2\pi\zeta t}\right)^{\frac{3}{2}} \exp\left(-\frac{r^2}{2\zeta t}\right) \ , \tag{5.18}$$

where Q is the heat energy in the emitting region and $\zeta = \dfrac{2K}{C_p \rho}$. The peak temperature in the emitting region, $T(r = 0)$, will therefore be

$$T(r=0) = \left(\frac{1}{2\pi\zeta}\right)^{\frac{3}{2}} \frac{1}{t^{\frac{3}{2}}} \propto t^{-\frac{3}{2}} \ . \tag{5.19}$$

Assuming the light is black-body radiation, the power radiated will follow the Stefan-Boltzmann law

$$\dot{W} = A\varepsilon\sigma_B T^4 \ , \tag{5.20}$$

where A is the emitting area, T is the temperature of the black body, ε is its emissivity, and σ_B is the Stefan-Boltzmann constant $\frac{2\pi^5 k_B^4}{15c^2h^3}$. The expected form of $T(t)$ is given by equation 5.19. The variation of area with time must also be considered. The Gaussian component of equation 5.18 provides a means to do so. Its characteristic length

$$\langle r^2 \rangle = 2\zeta t \propto t, \tag{5.21}$$

and thus we expect $A \propto t$, dimensionally. The power radiated will therefore be

$$\dot{W} \propto t \cdot \left(\frac{1}{t^{\frac{3}{2}}} \right)^4 = t^{-5} \ . \tag{5.22}$$

Assuming the photodiode captures some constant fraction of the light output, the photodiode output should follow this t^{-5} dependence. It is worth noting that this is not the exponential decay expected based on figure 5.10. Figure 5.18 shows that there is a significant difference between these two models. The agreement is superficially convincing, but the model is clearly failing to capture some of the physics of the situation.

There are three possible explanations for this. The first is that the temperature distribution in an emitting region takes non-negligible time to relax to the gaussian of equation 5.18. Probing this would require a more sophisticated heat-conduction model, or direct observations of the evolution of an emitting region. The second possibility is that the emitting regions of the bed are initiated at a range of times, with a range of thermal energies. In this case, the photodiode output could be used to test a statistical model for the distribution of initiation times and energies. Finally, the release of heat in each emitting region may not be instantaneous: as the energy comes at least partially from chemical reaction of AN, the kinetics of that reaction may distort the light output.

5.1.4 Particle size

Some work was performed on 20–40 μm ground AN, produced as described in section 5.1.1.4. This production technique was somewhat unsatisfactory. The only grinding balls available were steel, and the resulting rust contamination was sufficient to impart a visible pink colour to the ground AN. Figure 5.19 shows

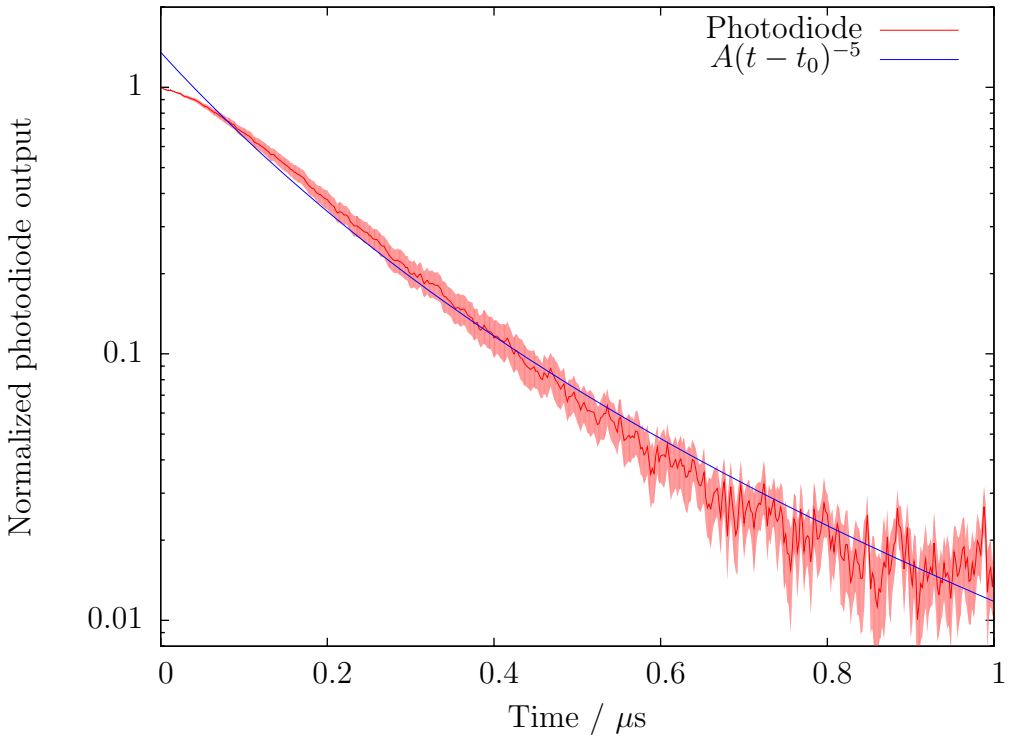

Figure 5.18: Log-linear plot comparing light-emission model with average normalized photodiode output, and showing failure of the model. Note systematic under-prediction between 0.08 and 0.4 μs and after 0.9 μs, and over-prediction before 0.08 μs and between 0.4 and 0.9 μs. $A = 0.136 \pm 0.003$, $t_0 = -0.632 \pm 0.003$ μs.

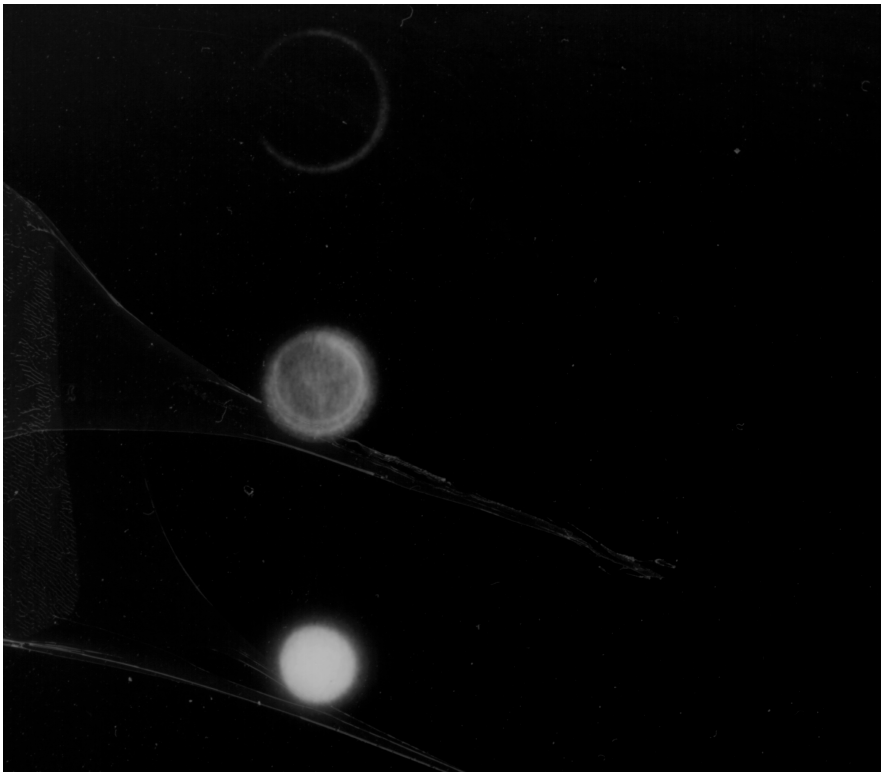

Figure 5.19: Framing photography of 20–40 μm ammonium nitrate granular bed. Camera was triggered 274 ± 17 ns before shock entered bed. $683 \pm 3\,\mathrm{m\,s^{-1}}$ impact velocity, 460 ns exposure time, 40 ns interframe time. Taken using Ultranac 501 camera; frame order as shown in figure 2.19.

framing photography of a $700 \pm 40\,\mathrm{m\,s^{-1}}$ impact on a 3.5 mm bed of this ground AN, and figure 5.20 shows the corresponding photodiode output.

These differ from those of a 150–212 μm AN bed (figures 5.9 and 5.10) in a few interesting respects. The light output of the 20–40 μm bed is much dimmer than that of the 150–212 μm bed. It also rises and falls more quickly. The ring structure seen in the late stages of the light output of both beds is sharper in the finer bed.

All these features are consistent with increased bed opacity in the finer bed. A more opaque bed will permit light from a narrower region near the glass back plate to escape and be detected. This will result in the dimmer light output observed. As the reaction front travels through the bed at a finite speed, sampling a narrower region of the bed will naturally lead to the faster rise and fall in light

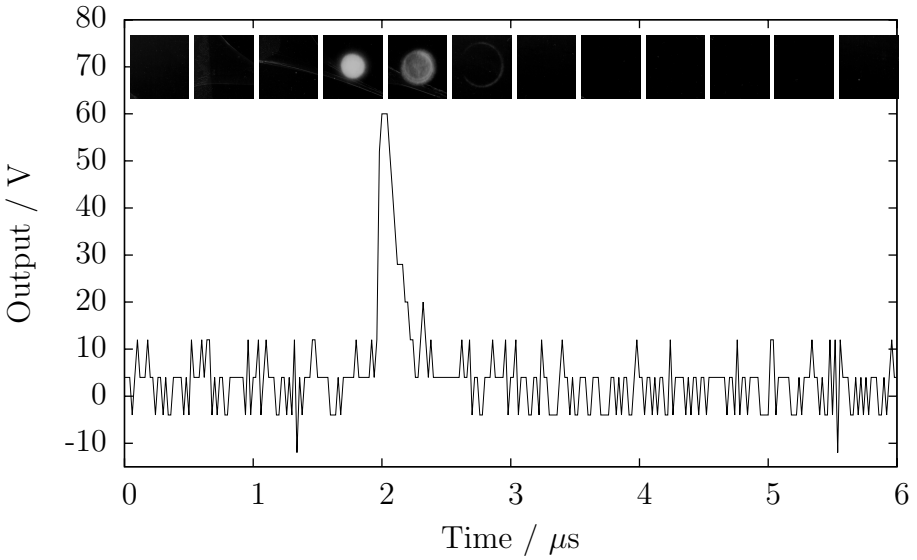

Figure 5.20: Photodiode output of 20–40 μm ammonium nitrate granular bed under 683$\pm$3 m s^{-1} flyer impact. Superimposed images show framing photography of the experiment. Horizontal extent of image indicates duration for which shutter was open. Experiment also shown in figure 5.19.

output observed. The light emitted by the ring structure will not be scattered as far by a more opaque bed, explaining its sharper definition.

There is also a faint speckle pattern with a length scale of approximately 200 μm visible in frame 5 (2–2.5 μs). Comparison with early frames of figure 5.9 suggests that this may be due to the grain of the film used here.

The increased opacity of the finer bed is readily explained. Ammonium nitrate is a transparent material. The opacity of the bed will therefore be dominated by scattering from AN-air interfaces. This effect could in principle be quantified and compared to experiment. However, both the time and voltage resolution of the photodiode data obtained in this experiment are too coarse for this to be useful. Given the shortcomings of the milling technique used, further experiments were not performed. This could prove an interesting avenue of study in future.

5.2 Prill beds

While granular beds are a useful system to experiment on, ammonium nitrate is normally used in prill form. Some experiments were therefore performed on prill beds. Prills are typically a few millimetres in diameter. The small-scale experiments performed here only contain tens of prills. The conclusions drawn from them are therefore mostly qualitative.

Beds of each prilled formulation were investigated using framing photography and photodiode output. Beds containing a single reactive prill were investigated using the same techniques. The bulk of these beds consisted of Westland prills. These served as an inert mechanical mock for the reactive prills. The various prill types used here are described in chapter 3.

5.2.1 Bed construction

The cells and flyers used in these experiments were nearly identical to those used for granular beds. See section 5.1.1 for details. The bed itself was a single randomly-packed layer of prills. Prills with diameters within 0.1 mm of the thickness of the bed were chosen by sieving through circular holes. As with the granular bed, the sample cell was constructed, face down, with the make trigger, glass plate, and rear holding ring left off. The sieved prills were poured in and spread to form a uniform layer. The remainder of the cell was then assembled.

The nitrile O-rings used as spacers for the granular bed experiments were 3.5 mm thick. Most of the prilled formulations here had a significant population of prills with diameters within 0.1 mm of this thickness. For these formulations, the cell design used for granular bed experiments was not modified. The Orica prills, however, were smaller. A ring was punched from 2 mm copper sheet. This was used instead of the nitrile O-ring for experiments on Orica prills. This fabrication technique was chosen simply to avoid the delay associated with ordering different O-rings.

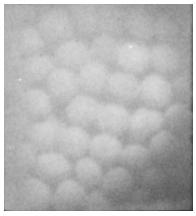

Figure 5.21: Static image of the bed of 3.4–3.6 mm Westland prills impacted in figure 5.22. To scale with, and taken with the same apparatus as, figure 5.22.

5.2.2 Westland prills

Westland Feed-All Plant Food was used as an inert mechanical mock for the reactive prills studied here. It was necessary to check that these prills were in fact inert in this experiment. A bed consisting entirely of Westland prills was constructed. Figure 5.21 shows the bed. This bed was then impacted at $700 \pm 40\,\mathrm{m\,s^{-1}}$, and framing photography and photodiode readings recorded. Figure 5.22 shows the framing photography, and figure 5.23 shows the photodiode output.

A very small amount of light is emitted by the bed. The light is dim enough that it could be due to compression of trapped gas or triboluminescence of fracturing prills, rather than reaction of the bed material. Most relevantly, it is much dimmer than the light emitted by the reactive prills studied later in this chapter. Therefore Westland prills are suitable for use as an inert mock of reactive prills in these experiments.

5.2.3 Orica prills

There was no discernible difference between coated and uncoated Orica prills. They are therefore discussed together.

5.2.3.1 Reactive prill bed

The bed shown in figure 5.24 was shocked; figure 5.25 shows the resulting framing photography. Due to the small size of the Orica prills, the beds used here were 2 mm thick. Many of the features observed when impacting granular beds are repeated here; see section 5.1.2 for discussion. Note that the work of Proud et al. (2003) discussed there is not directly comparable to these results: that work was

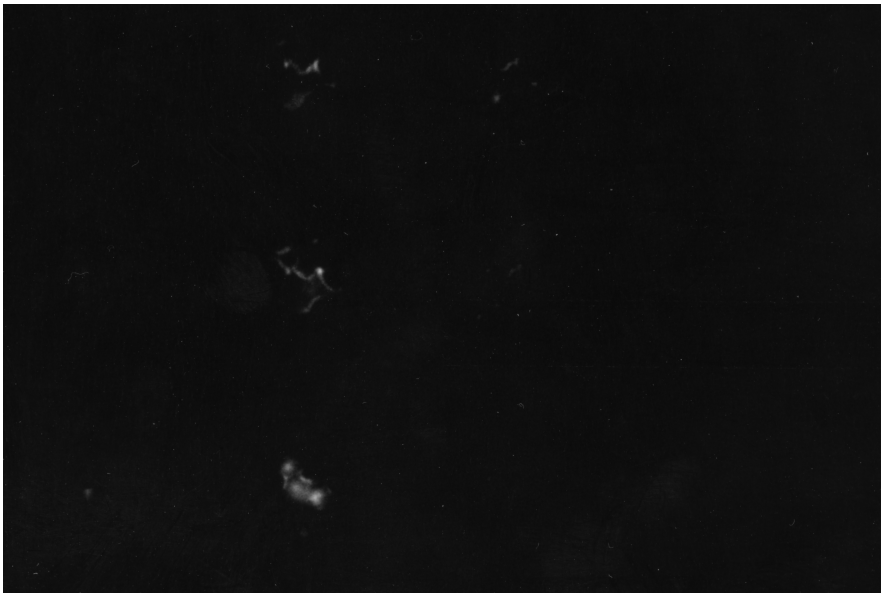

Figure 5.22: Framing photography of a bed of 3.4–3.6 mm Westland prills impacted at $700 \pm 40\,\mathrm{m\,s^{-1}}$. 460 ns exposure, 40 ns interframe time. Taken using Ultranac 501 camera; frame order as shown in figure 2.19. Static image of bed, to the same scale, shown in figure 5.21.

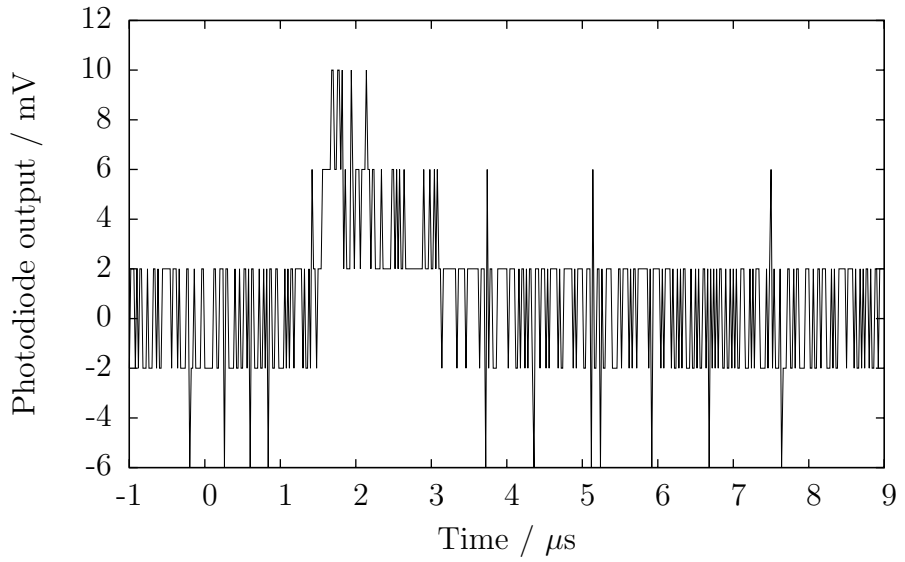

Figure 5.23: Photodiode output from a bed of 3.4–3.6 mm Westland prills impacted at $700 \pm 40\,\mathrm{m\,s^{-1}}$. Experiment also shown in figure 5.22.

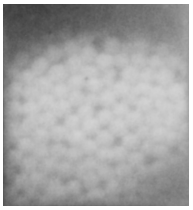

Figure 5.24: Static image of the bed of 1.9–2.1 mm Orica prills impacted in figure 5.25. To scale with, and taken with the same apparatus as, figure 5.25.

concerned solely with granular beds. The behaviour observed here deviates in a few interesting ways from that of a granular bed.

First, frames 1 and 2 (0–1 μs) show the undisturbed prill bed, with light between the prills. There are two possible explanations for this. The first is that reaction starts in the inter-prill region; the light from this initial reaction would therefore be visible only in the voids between prills. The second involves the finite speed with which the shock wave travels through the prill bed. Figure 5.26 shows the situation when the shock has recently entered the prill bed. Reaction will only start in those regions into which the shock wave has passed. The unshocked material will neither move nor react, and will block light from the reacting material. The camera will therefore observe these unshocked prills, with light from the reaction visible only between them.

The second interesting feature is the structure of the light output in frames 7 onward (3 μs onward). Heterogeneity of a scale comparable to that of the prills persists. This suggests that at least substantial fragments of the prills, and possibly entire prills, survive the reaction. This in turn indicates that the reaction of the bed was arrested before consuming all available AN. This is unsurprising: the scale of the experiment is much smaller than the critical diameter for pure AN, and the loading pulse provided by the flyer is of very short duration. It is also interesting to note that the prills are not entirely reduced to dust over the timescale studied here. Inspection of the debris after the experiment, however, found no prill fragments.

Finally, frame 12 (5.5–6 μs) appears to show limited re-ignition of the central region of the bed. This is rather surprising. While the unreacted prill fragments provide reagent, there is no clear energy input to initiate reaction at this time.

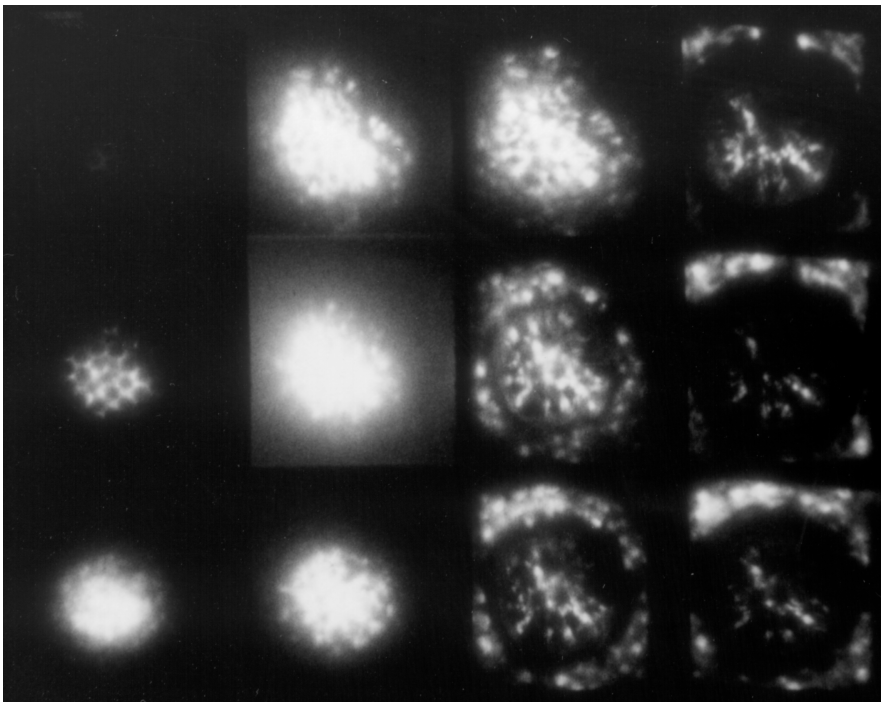

Figure 5.25: Framing photography of a bed of 1.9–2.1 mm Orica prills impacted at $700 \pm 40\,\mathrm{m\,s^{-1}}$. 460 ns exposure, 40 ns interframe time. Taken using Ultranac 501 camera; frame order as shown in figure 2.19. Static image of this bed, to the same scale, shown in figure 5.24.

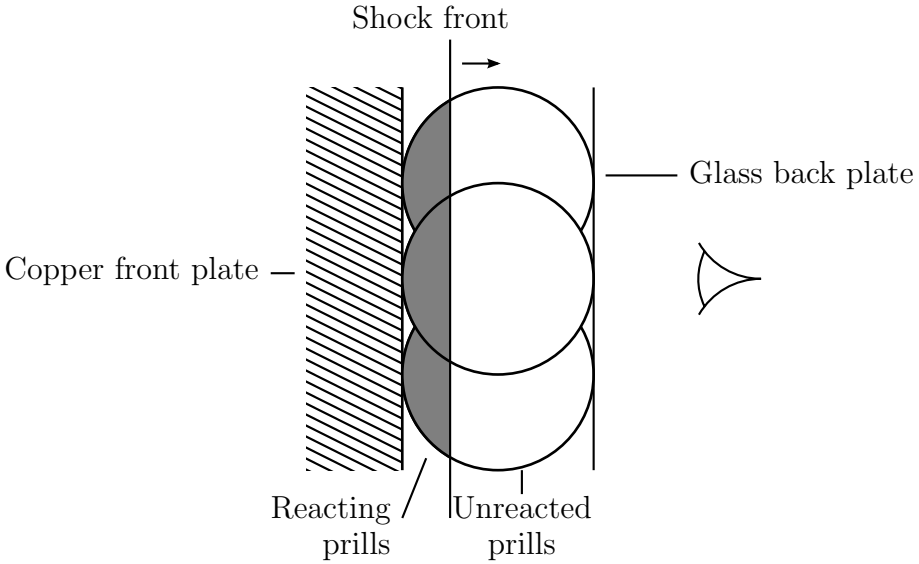

Figure 5.26: Illustration of a prill bed through some of which a shock has travelled.

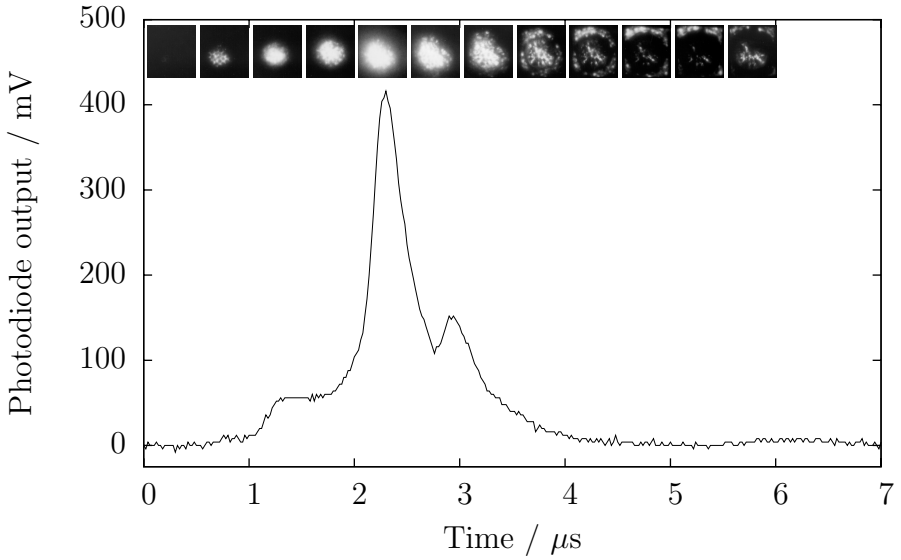

Figure 5.27: Photodiode output of a bed of 1.9–2.1 mm Orica prills impacted at $700 \pm 40\,\mathrm{m\,s^{-1}}$. Superimposed images show framing photography of the experiment. Horizontal extent of image indicates duration for which shutter was open. Experiment also shown in figure 5.25.

The most likely explanation is that these unreacted fragments have "cooked off": the uniformly high temperature in the sample cell has caused them to decompose exothermically. Cook-off events are associated with a random delay, which would explain why this re-ignition is not directly associated with any event in the experiment. It would also make a detailed study exceedingly difficult.

Figure 5.27 shows the output of the photodiode attached to this experiment. The reignition seen in frame 12 of the framing photography is visible here. It causes a slight rise in the photodiode output between 5.5 μs and 7 μs.

The overall form of the photodiode output is similar to that produced by a granular bed. It rises to a peak, then decays. The bump in the decay at 3 μs is similar to that seen in some of the granular bed experiments. However, here it is much more pronounced.

The photodiode output also shows a plateau in light output between 1.2 and 1.7 μs. The photodiode viewed the experiment through an optical fibre. It was thought that the narrow acceptance angle of this fibre might be responsible for both this plateau and the bump observed at 3 μs. Therefore a polished fibre was

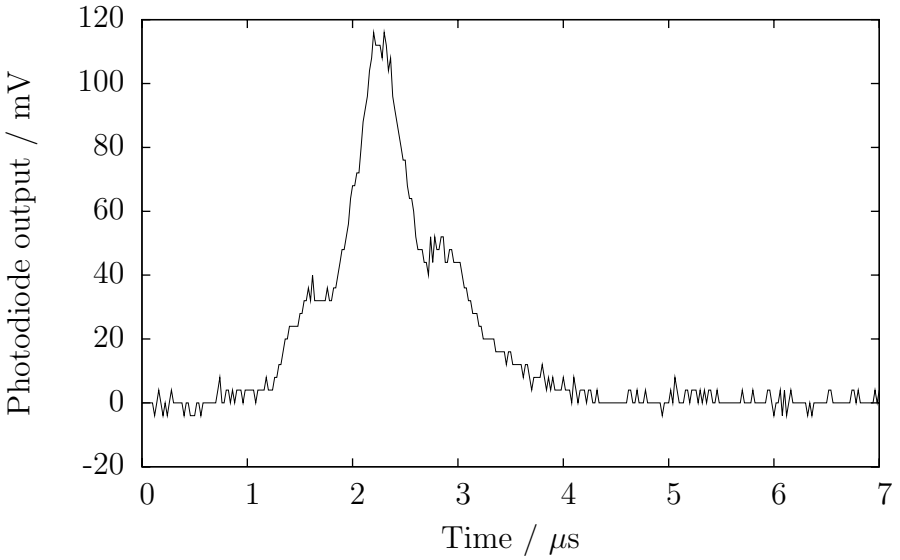

Figure 5.28: Photodiode output from bed of 1.9–2.1 mm Orica prills, impacted at $700 \pm 40\,\mathrm{m\,s^{-1}}$. Fibre end roughened with 30 μm polishing paper.

deliberately roughened using 30 μm polishing paper, and the experiment repeated. Figure 5.28 shows the result of this experiment. While the duration of the plateau is reduced, it is still clearly present. Its brightness relative to the bed's peak light output is increased. The bump during the light's decay also remains, and has also become relatively more prominent.

One possible interpretation of the plateau region is that the light output indicates the rate at which AN is reacting. Under this interpretation, the plateau indicates that the reaction temporarily reaches a steady state. This may be due to some feature of the kinetics of AN. However, in that case it would also be observed in granular beds of AN. Figure 5.10 shows that this is not the case. A more likely explanation involves the structure of the prills themselves. As the framing photography shows, significant fragments of the prills survive until late in the experiment. Their structure is therefore likely to be relevant in the early stages of the experiment. In chapter 3 it was seen that the outside of Orica prills is denser and less permeable than the interior. It is likely, therefore, that reaction will spread through the interior of the prills before the outside begins to react. During this time, the opaque outer shell of the prill will block the light produced

by the reacting interior. The light output will therefore reach a plateau. This will end when the shells of the prills either react or break to such an extent that they no longer block light.

5.2.3.2 Single reactive prill

A bed of inert Westland prills was constructed, and a single Orica prill placed near the centre. The size distributions of the two prill types had very little overlap. Therefore the bed was constructed of 3.4–3.6 mm prills: it was easier to find a single oversized Orica prill than to find enough undersized Westland prills to fill an entire bed. It was possible that the prill thus selected would have an unusual microstructure. Unfortunately tomographic imaging was not available at the time, and bisecting the prill to investigate would have rendered it unsuitable for this experiment.

This bed is shown in figure 5.29. The red circle highlights the Orica prill. The dark mark on its surface was added with a pen to identify it. The bed was then impacted at $700 \pm 40\,\mathrm{m\,s^{-1}}$. Figure 5.30 shows framing photography of this impact. The light output seen here gives some support to the conclusions of section 5.2.3.1. Apart from a little light in frame 1 (0–0.5 μs), the bed is dark until frame 4 (1.5–2 μs). By frame 5 (2–2.5 μs) the light output is clear, and there are visible fragments where the Orica prill has disintegrated. The light output in frame 4 may be due to break-up of the side of the prill away from the camera. In frames 4–8 (1.5–4 μs), light can clearly be seen away from the reacting prill. This may be due to hot, glowing gas from the prill spreading through the inert prill bed. Alternatively it may be because the light from the prill illuminates distant parts of the inert prill bed.

Figure 5.31 shows the output of the photodiode attached to this experiment. The initial plateau is again reduced in size but increased in prominence, relative to figure 5.28. The plateau appears to coincide with frame 4. This further supports the explanation that the plateau is due to the outer layers of the prill blocking light from reaction within the prill. The bump during decay of light output is also present.

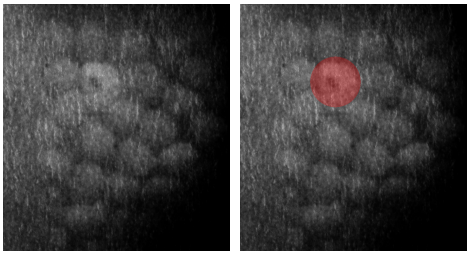

Figure 5.29: Two copies of a static image of the bed of 3.4–3.6 mm Westland prills, with a single 3.5 mm Orica prill, impacted in figure 5.30. To scale with, and taken with the same apparatus as, figure 5.30. Position of Orica prill is highlighted with a red circle in the right-hand image.

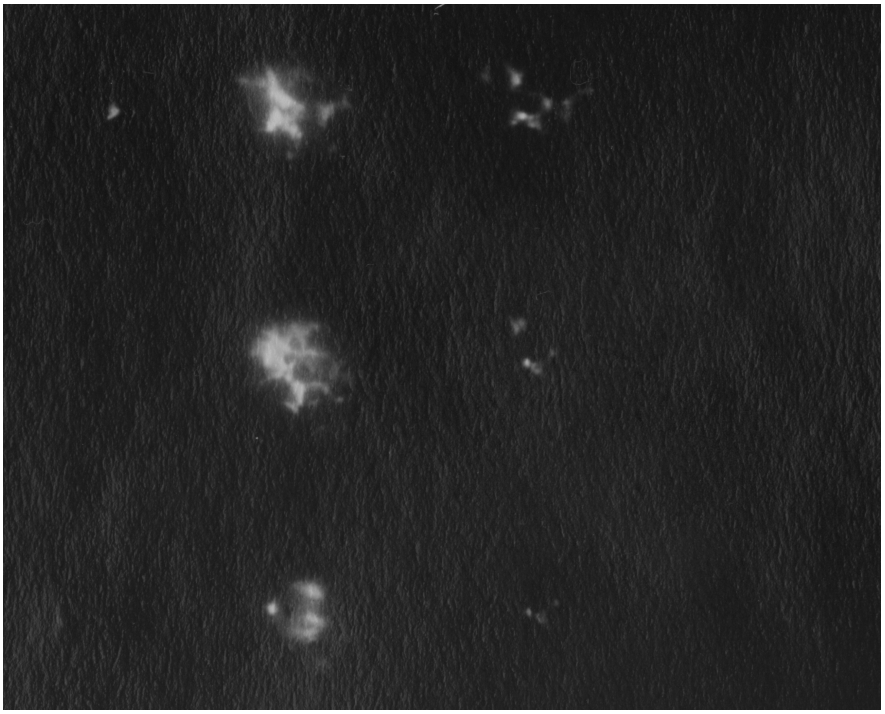

Figure 5.30: Framing photography of a bed of 3.4–3.6 mm Westland prills, with a single 3.5 mm Orica prill, impacted at $700 \pm 40\,\mathrm{m\,s^{-1}}$. 460 ns exposure, 40 ns interframe time. Taken using Ultranac 501 camera; frame order as shown in figure 2.19. Static image of bed, to the same scale, shown in figure 5.29.

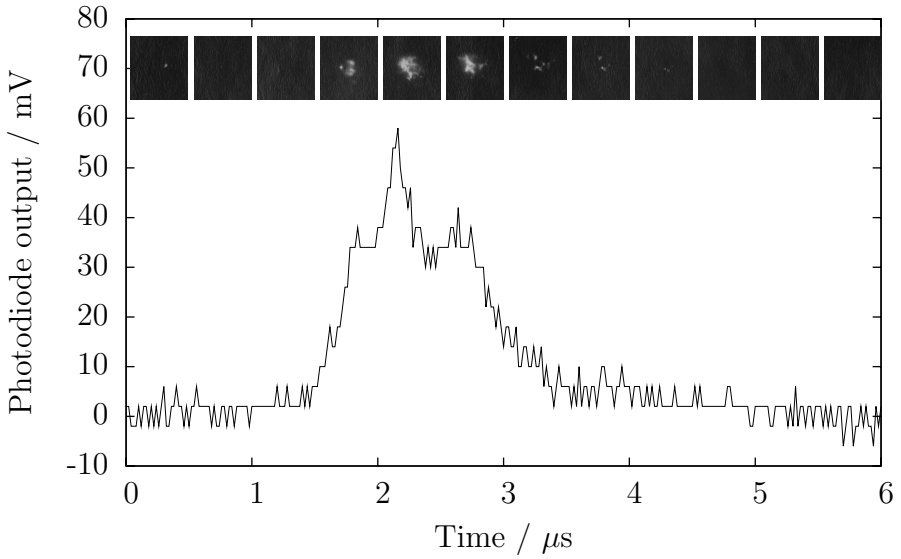

Figure 5.31: Photodiode output of a bed of 3.4–3.6 mm Westland prills, with a single 3.5 mm Orica prill, impacted at $700 \pm 40\,\mathrm{m\,s^{-1}}$. Superimposed images show framing photography of the experiment. Horizontal extent of image indicates duration for which shutter was open. Experiment also shown in figures 5.29 and 5.30.

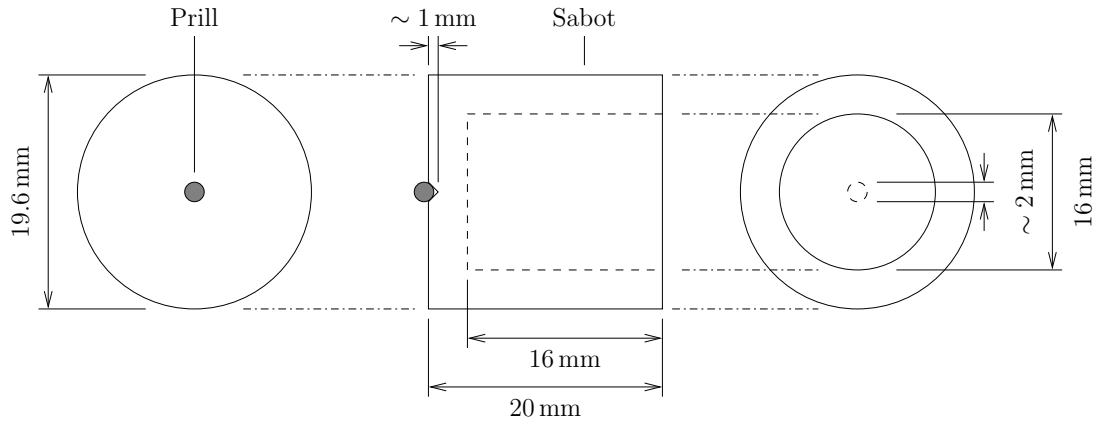

Figure 5.32: Sabot design for direct impact experiments. Measurements prefixed with ∼ are approximate, and vary between individual sabots. Sabot is made from POM.

5.2.3.3 Direct impact

Several features of these experiments involved activity on the side of the prill facing the shock wave. The design of the experiment prevented observation of this part of the prill. Therefore a direct impact experiment was designed, with the intention of circumventing this limitation.

In this experiment, the flyer was re-designed. The copper front plate was removed, and the acetal sabot re-designed to carry a single prill. A small indentation was made in the centre of the front face using the tip of a drill bit. The prill was then held in this indentation with a small amount of silicone vacuum grease. This was chosen to avoid potentially introducing an organic fuel to the prill. Figure 5.32 shows the re-designed sabot, with prill attached. The sample cell was also re-designed: the bed and front face were removed, so that the prill would strike the glass rear plate directly. As in the prill and granular bed experiments, framing photography and a photodiode were directed at the rear of the glass plate.

Triggering the diagnostics presented a problem. The addition of an opaque make trigger would prevent direct observation of the prill's impact, and thus defeat the point of the experiment. Instead, a time-of-flight computer was used. This took input from the light gate used to measure the flyer's velocity. It then

waited some pre-defined multiple of the delay between the light gates' activation before triggering the apparatus. The distance between the light gates is known, and the projectile is assumed to travel at constant velocity for the duration of the experiment. The position of the projectile when the apparatus is triggered can then be controlled by modifying the multiplier.

This experiment produced extremely bright light, saturating the photodiode and camera. Further investigation showed that this light coincided with the arrival of the acetal sabot at the glass target plate. The light was found to be independent of the presence or otherwise of the prill, or the silicone grease used to attach the prill. It was therefore interpreted as being due to compression of air trapped between the flyer and the glass target plate. There was no visible light coinciding with the arrival of the prill at the target plate. This implies that the prill disintegrated or was dislodged before impact. In the absence of any way to reduce the loading experienced by the prill, the technique was abandoned.

5.2.3.4 Drop weight experiments

The early stages of the reactive prill bed experiment showed light between the prills (see figure 5.25). One possible explanation for this light was inter-prill reaction. It was therefore interesting to search for possible mechanisms for this reaction. Any such mechanism will involve material being ejected from the prill's surface. A drop weight experiment, with imaging through the sample, was used to search for this ejected material. The general technique is described in chapter 2, section 2.6.5.

Experiments were performed on 1.9–2.1 mm uncoated Orica prills, mixed with 5.8 % diesel by weight. The fuel was added to sensitize the prills. The loading in the drop weight experiments was slower than that in the plate impact experiments, and reached a lower maximum pressure. It was hoped that sensitization would allow the prills to react under these circumstances.

Figure 5.33 shows the arrangement of prills initially used. In similar experiments (Field et al., 1982; Me-Bar and Walley, 1994) on liquid propellants, a jet formed from the interface of drops 1 and 2. This jet then struck drop 3, causing reaction. This geometry was chosen because jets were thought to be the most

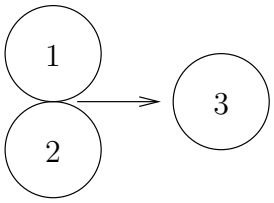

Figure 5.33: Sample geometry for jet-based initiation. The jet forms between objects 1 and 2, and follows the path indicated by the arrow.

likely cause of inter-prill initiation. If a jet forms, this geometry should make it visible. Figure 5.34 shows the result of this experiment. No jet is visible: the prills simply disintegrate. There is no evidence of reaction or melting in the resulting mass of prill fragments. The open microstructure of the prills will diffuse the shock wave resulting from contact between the prills. The geometry of the experiment also differs from that of a liquid-drop experiment: the prills are spherical at the time of contact, while the liquid drops are cylindrical. Both these factors will inhibit jet formation in this experiment.

The fashion in which the prills disintegrate is interesting. In the early stages (42–105 μs) cracks appear to propagate from the edges towards the centre of the prills. These separate the prills into a small number of cohesive fragments, which separate (140–245 μs) and are crushed (350 μs onward). This behaviour is due to the inhomogeneity of the prills. As figure 3.6 in chapter 3 shows, Orica prills consist of a porous centre surrounded by a dense outer shell. In uniaxial compression, this shell will experience tensile loading around its circumference (as seen by the camera). Referring again to chapter 3, figure 3.6, we see numerous indentations in the circumference. These could initiate crack growth in the outer shell, resulting in the form of disintegration seen here.

It is possible that limited reaction took place, but was obscured by unreacted AN. This was tested in a second experiment. Maraging steel anvils were used, as described in chapter 2, section 2.6. The arrangement of prills shown in figure 5.35 was placed between the anvils. A layer of heat-sensitive film was placed in contact with the prill layer, as shown in figure 5.36. Heat-sensitive film is a transparent plastic that undergoes a permanent colour change when heated above some temperature (Swallowe et al., 1986). This temperature depends on the time

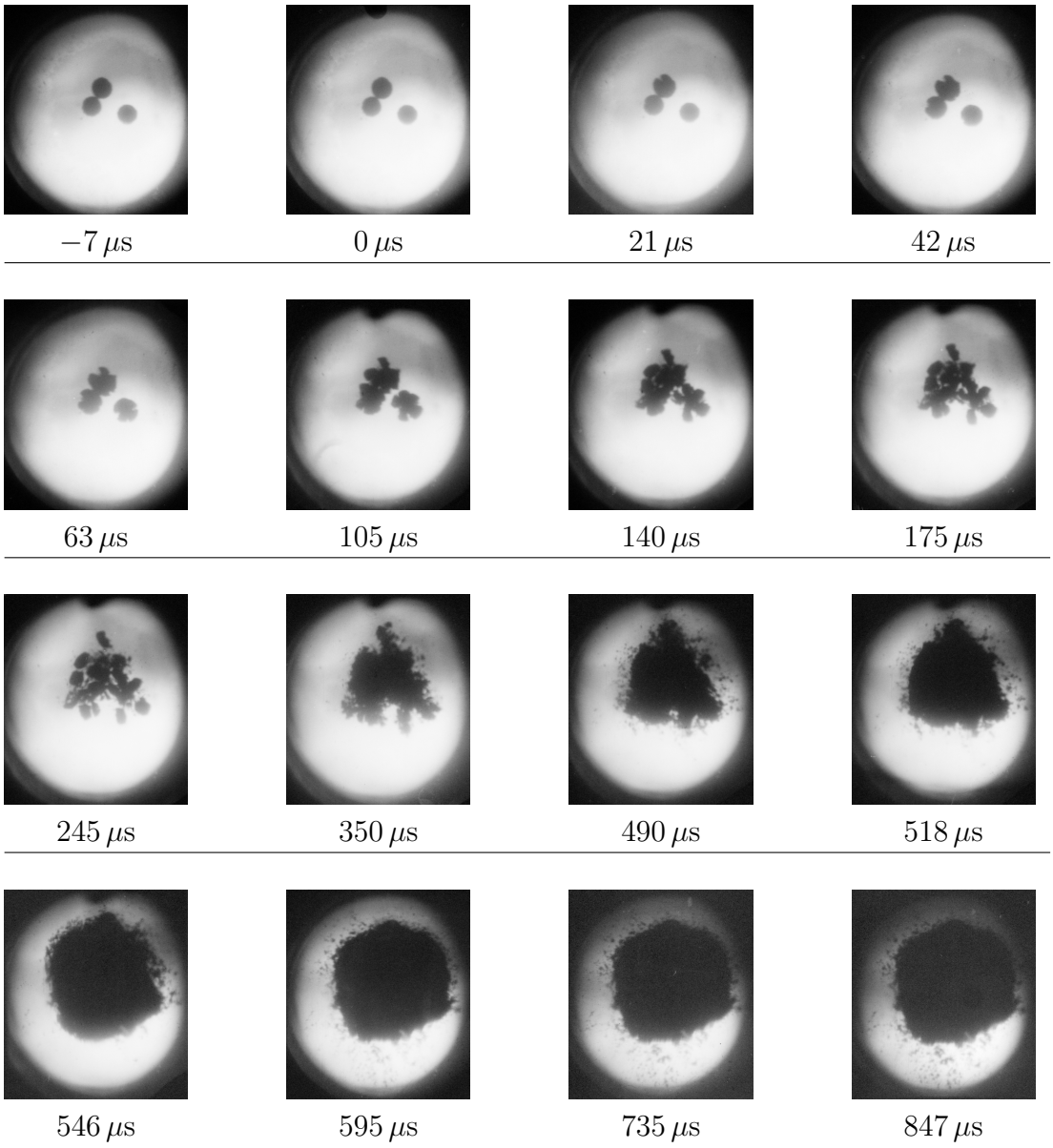

Figure 5.34: Photography through sample in drop weight experiment on 2 mm ANFO prills taken using C4 camera. Time is relative to first detectable deformation of prills. No jetting or reaction is visible.

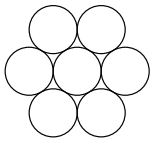

Figure 5.35: Arrangement of prills for heat-sensitive film experiment.

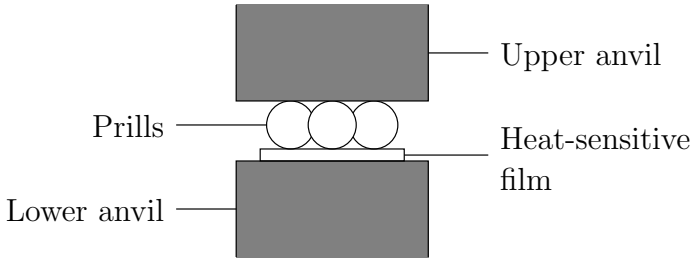

Figure 5.36: Layout of heat-sensitive film experiment. The anvils are those of the drop weight. Not to scale.

for which the film is heated, but is always at least 180 °C. As seen in chapter 1, section 1.1.2, AN will thermally decompose at this temperature. Figure 5.37 shows the film recovered from this experiment. The darkening of the film clearly shows that it has been heated. There must therefore have been limited reaction in the mass of disintegrated AN. However, there is no evidence that this reaction began in the inter-prill spaces. The darker spots at the right-hand edge of the film are similar in size and position to the prills. This suggests that there is significant heating within the prills themselves, before they fragment.

5.2.4 Nitram prills

5.2.4.1 Reactive prill bed

The bed shown in figure 5.38 was shocked; figure 5.39 shows the resulting framing photography. The bed behaves very similarly to the Orica bed studied in section 5.2.3.1. The structure of the light output is coarser, but this is due to the larger prill size used here. There is also no evidence of re-ignition of the bed, as was seen in section 5.2.3.1. Given the random nature of cook-off, this is unremarkable.

Figure 5.40 shows the output of the photodiode attached to this experiment.

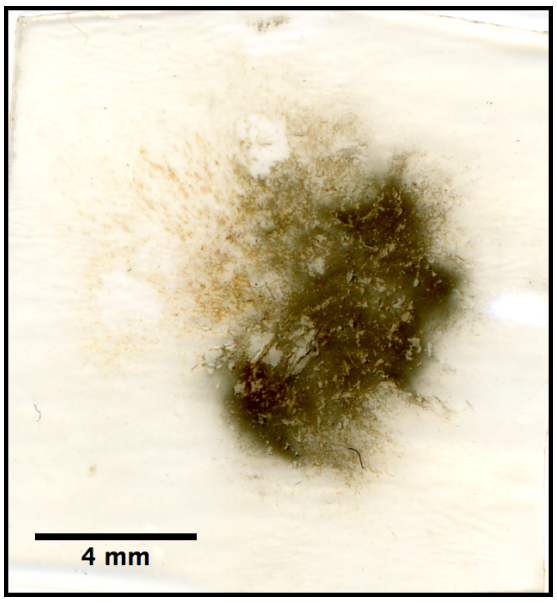

Figure 5.37: Recovered heat-sensitive film after drop weight experiment on hexagonal arrangement of prills.

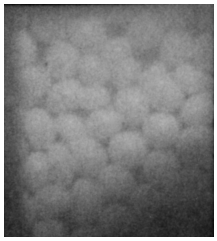

Figure 5.38: Static image of the bed of 3.4–3.6 mm Nitram prills impacted in figure 5.39. To scale with, and taken with the same apparatus as, figure 5.39.

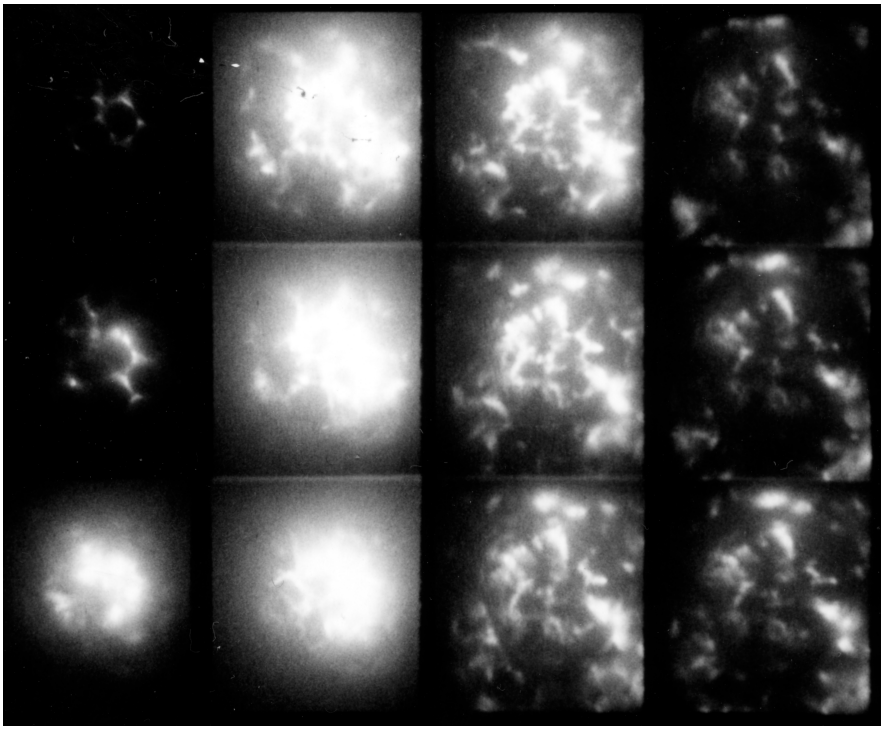

Figure 5.39: Framing photography of a bed of 3.4–3.6 mm Nitram prills impacted at $700 \pm 40\,\mathrm{m\,s^{-1}}$. 460 ns exposure, 40 ns interframe time. Taken using Ultranac 501 camera; frame order as shown in figure 2.19. Figure 5.38 shows a static image of this bed, to the same scale.

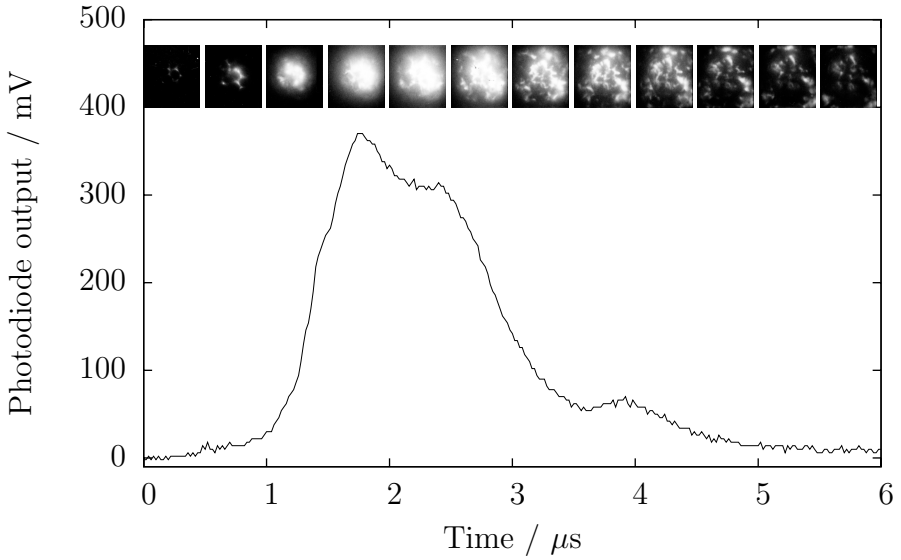

Figure 5.40: Photodiode output of a bed of 3.4–3.6 mm Nitram prills impacted at $700 \pm 40\,\mathrm{m\,s^{-1}}$. Superimposed images show framing photography of the experiment. Horizontal extent of image indicates duration for which shutter was open. Experiment also shown in figures 5.38 and 5.39.

This differs quite markedly from figure 5.27, the equivalent for a bed of Orica prills. No plateau region is visible. After rising to a peak at $1.75\,\mu$s, the light output falls in three stages, arrested at $2.4\,\mu$s and $3.9\,\mu$s. The second of these closely resembles the bump in light output seen in both granular beds and Orica prill beds.

Nitram prills have a uniformly dense microstructure. Unlike Orica prills, they do not become more dense near the surface of the prill. The absence of a plateau in figure 5.40 therefore provides some support for the second possible explanation of the plateau in section 5.2.3.1. There is no low-density interior to the Nitram prills, through which reaction may spread without contributing to the observed light output of the bed.

5.2.4.2 Single reactive prill

A bed of Westland prills was constructed, and a single Nitram prill placed near the centre. This bed is shown in figure 5.41. The dark mark on the Nitram prill

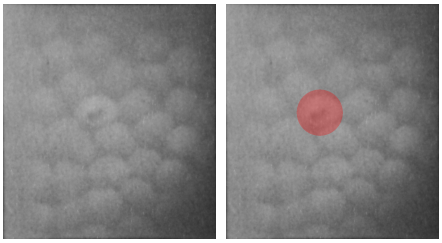

Figure 5.41: Two copies of a static image of the bed of 3.4–3.6 mm Westland prills, with a single 3.5 mm Nitram prill, impacted in figure 5.42. To scale with, and taken with the same apparatus as, figure 5.42. Position of Nitram prill is highlighted with a red circle in the right-hand image.

was added with a pen to identify it. The bed was then impacted at $700 \pm 40\,\mathrm{m\,s^{-1}}$. Figure 5.42 shows framing photography of this impact. This reaction is noticeably brighter than that induced in an Orica prill (figure 5.30). Because of this enhanced brightness, the spread of light through the bed is visible as highlights on the inert prills in frames 5 to 9 (2–4.5 μs). Some disintegration of prills near the reactive prill is visible in frame 5 ($2 - 2.5\,\mu$s).

Figure 5.43 shows the photodiode output of this experiment. It is broadly similar to that seen in the prill-bed experiment (figure 5.40). The first fall after the peak (1.75–2.5 μs) is steeper than that seen in the prill-bed experiment.

The enhanced light output of a Nitram prill relative to an Orica prill is interesting. Nitram prills have a denser microstructure than Orica prills. A single Nitram prill will therefore contain more energetic material; assuming that it reacts completely, it will therefore produce more light. However, prill-bed experiments indicate that this is not the case: unreacted prill fragments are visible throughout the experiments (figures 5.25 and 5.38). The open microstructure of the Orica prills should introduce additional hot spots, resulting in more complete reaction of the Orica prills. This in turn would result in greater energy release and brighter light output from Orica prills.

One possible explanation of this discrepancy involves the mechanical strengths of the prills involved. It was found in chapter 4 that Orica prills were less resistant to compaction than Westland prills. If this is the case at the higher strain rate of these experiments, the inert Westland prills will support the Orica prill. Nitram prills, meanwhile, show very similar compaction resistance to Westland prills.

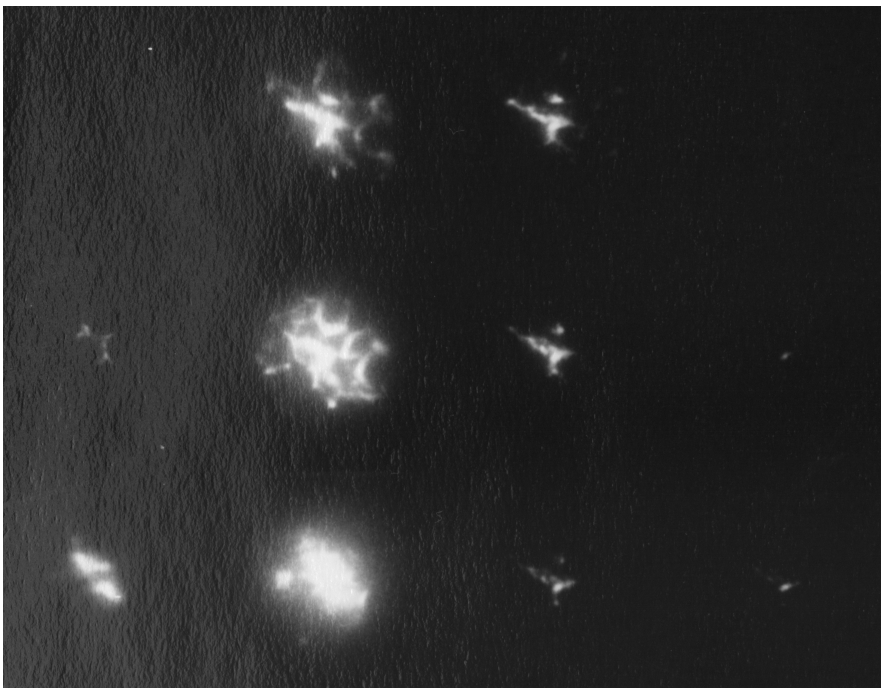

Figure 5.42: Framing photography of a bed of 3.4–3.6 mm Westland prills, with a single 3.5 mm Nitram prill, impacted at $700 \pm 40\,\mathrm{m\,s^{-1}}$. 460 ns exposure, 40 ns interframe time. Taking using Ultranac 501 camera; frame order as shown in figure 2.19. Figure 5.41 shows a static image of the bed, to the same scale.

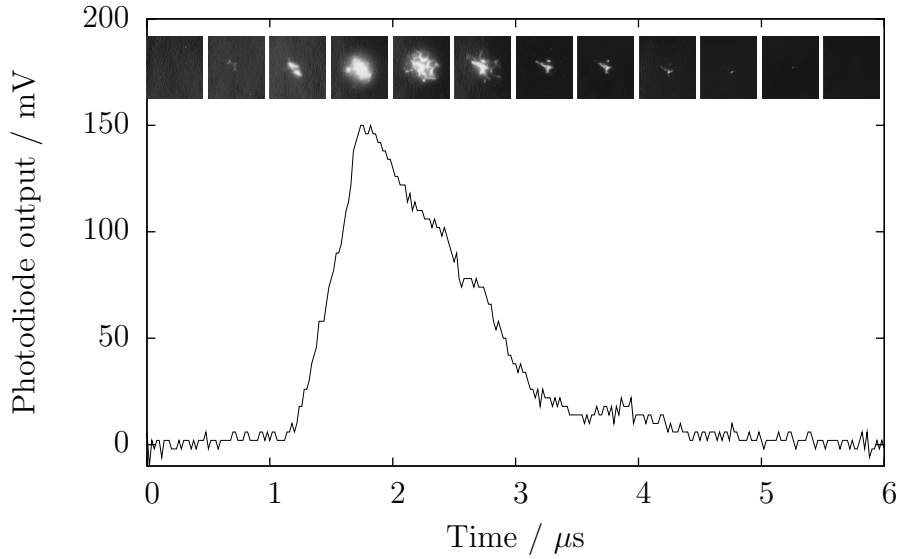

Figure 5.43: Photodiode output of a bed of 3.4–3.6 mm Westland prills, with a single 3.5 mm Nitram prill, impacted at $700 \pm 40\,\mathrm{m\,s^{-1}}$. Superimposed images show framing photography of the experiment. Horizontal extent of image indicates duration for which shutter was open. Experiment also shown in figures 5.41 and 5.42.

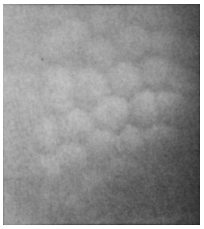

Figure 5.44: Static image of the bed of 3.4–3.6 mm agricultural pellets impacted in figure 5.45. To scale with, and taken with the same apparatus as, figure 5.45.

More shock energy would therefore be deposited in the Nitram prill than in the Orica prill, even if the beds were loaded identically. This could account for the brighter light output of the Nitram prill in this experiment.

5.2.5 Agricultural pellets

5.2.5.1 Reactive pellet bed

The bed shown in figure 5.44 was shocked; figure 5.45 shows the resulting framing photography. The structure of the light output is similar to that from a Nitram prill bed (figure 5.39). However, the light fades more rapidly. Agricultural AN pellets contain additives intended to absorb heat and hence inhibit reaction. This rapid fading indicates that the additives are behaving as intended. It also provides additional confirmation that the light seen here is due to reaction of AN, and that this reaction is thermally activated. There is no evidence of the ring structure seen in Nitram and Orica prill beds, probably because of the rapid decay of the light output.

Figure 5.46 shows the photodiode output of this experiment. As in other AN experiments, the light output rises to a peak, in this case at 1.7 μs, then falls. Unlike other experiments, this fall is linear, with gradient $-295 \pm 5\,\mathrm{V\,ms^{-1}}$. The gradient of the fall appears to reduce after 3 μs, but digitization of the photodiode output makes this difficult to assess.

The photodiode output of a repeat experiment is shown in figure 5.47. In this experiment, the region of linear fall runs from the peak at 1.55 μs to 2.15 μs. The linear region has gradient $-329 \pm 9\mathrm{V\,ms^{-1}}$. It is succeeded by a non-linear fall with a bump at 3.75 μs, as expected in prill-bed experiments.

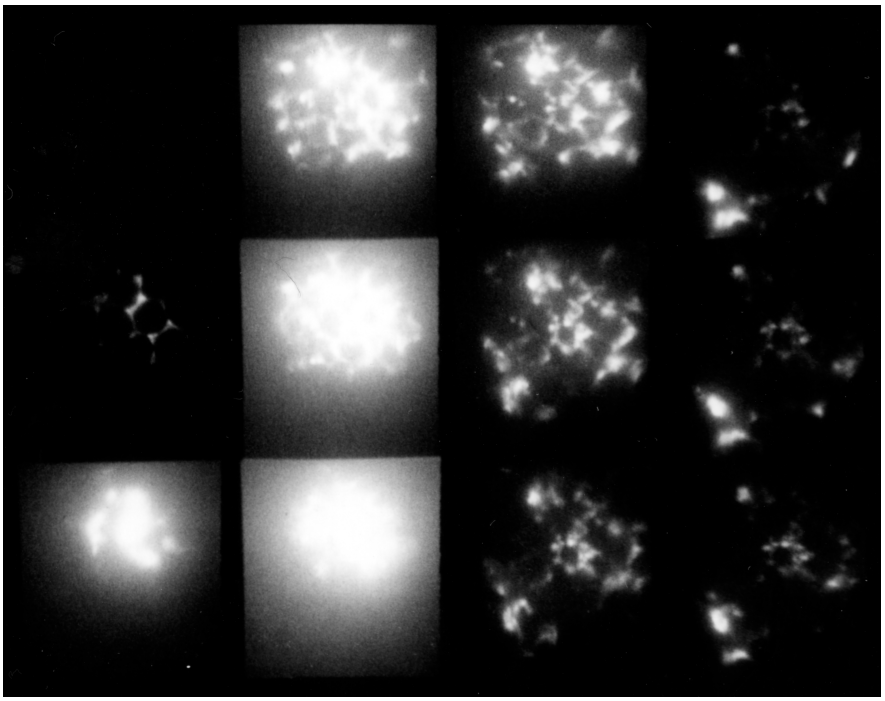

Figure 5.45: Framing photography of a bed of 3.4–3.6 mm agricultural pellets impacted at $700 \pm 40\,\mathrm{m\,s^{-1}}$. 460 ns exposure, 40 ns interframe time. Taken using Ultranac 501 camera; frame order as shown in figure 2.19. Figure 5.44 shows a static image of the bed, to the same scale.

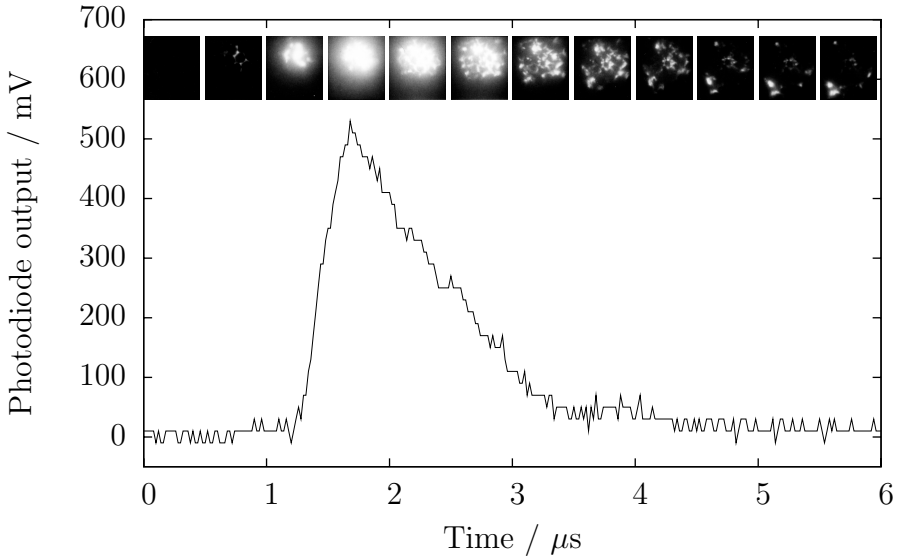

Figure 5.46: Photodiode output of a bed of 3.4–3.6 mm agricultural pellets impacted at $700 \pm 40\,\mathrm{m\,s^{-1}}$. Superimposed images show framing photography of the experiment. Horizontal extent of image indicates duration for which shutter was open. Experiment also shown in figures 5.44 and 5.45.

The linear fall seen in figures 5.46 and 5.47 may be due to the dolomite added to these pellets. It is added to absorb heat without reacting. This absorption, and later re-radiation, may account for the linear region. The greater extent and prominence of the linear region in figure 5.46 compared with figure 5.47 may be due to excess dolomite in the pellets used in the former experiment.

5.2.5.2 Single reactive pellet

A bed of Westland prills was constructed, and a single agricultural pellet placed near the centre. This bed is shown in figure 5.48. The dark mark on the agricultural pellet was added with a pen to identify it. The bed was then impacted at $700 \pm 40\,\mathrm{m\,s^{-1}}$. Figure 5.49 shows framing photography of this impact. The light output appears similar to that from a single Nitram prill (figure 5.42). However, in frames 6 onward (2.5 μs onward), the reactive prill appears to have remained mostly intact. There is also a small region near the reactive prill which remains brightly lit for significantly longer than in the Nitram experiment. Both are likely

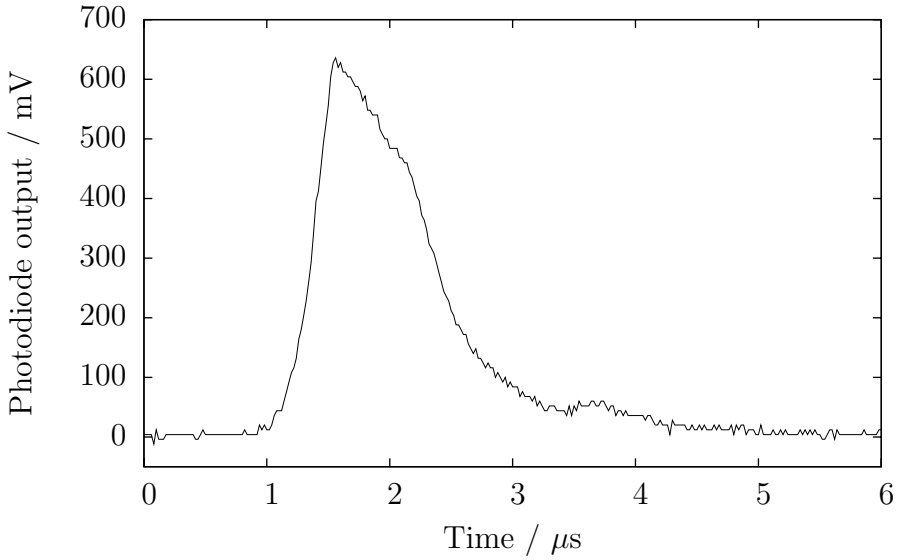

Figure 5.47: Photodiode output of a bed of 3.4–3.6 mm agricultural pellets impacted at $700 \pm 40\,\mathrm{m\,s^{-1}}$.

due to the inert additives in the agricultural pellet. These additives will reduce the rate and extent of reaction in the pellet. This will prevent the pellet's disintegration, and preserve reactive material later in the experiment. This will result in the small, long-lasting bright region seen here.

Figure 5.50 shows the output of the photodiode attached to this experiment. Digitization and noise in the output make it difficult to determine whether the linear fall observed in agricultural pellet bed experiments is repeated here.

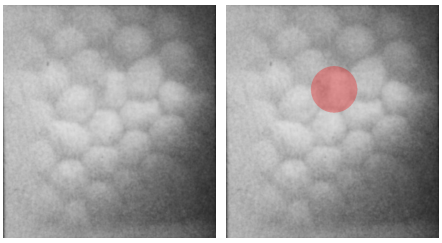

Figure 5.48: Two copies of a static image of the bed of 3.4–3.6 mm Westland prills, with a single 3.5 mm agricultural pellet, impacted in figure 5.49. To scale with, and taken with the same apparatus as, figure 5.49. Position of agricultural pellet is highlighted with a red circle in the right-hand image.

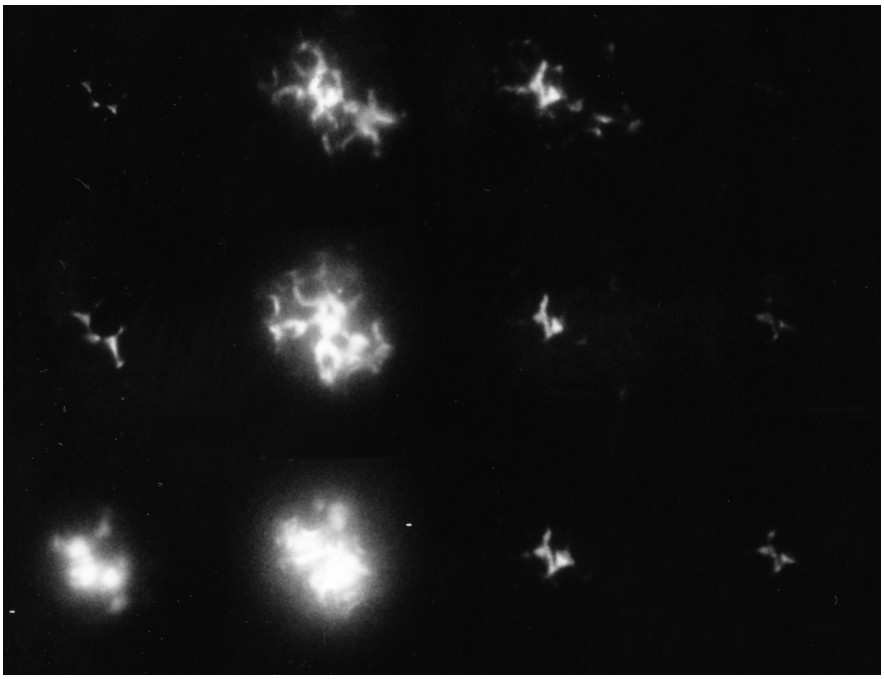

Figure 5.49: Framing photography of a bed of 3.4–3.6 mm Westland prills, with a single 3.5 mm agricultural pellet, impacted at $700 \pm 40\,\mathrm{m\,s^{-1}}$. 460 ns exposure, 40 ns interframe time. Taken using Ultranac 501 camera; frame order as shown in figure 2.19. Figure 5.48 shows a static image of the bed, to the same scale.

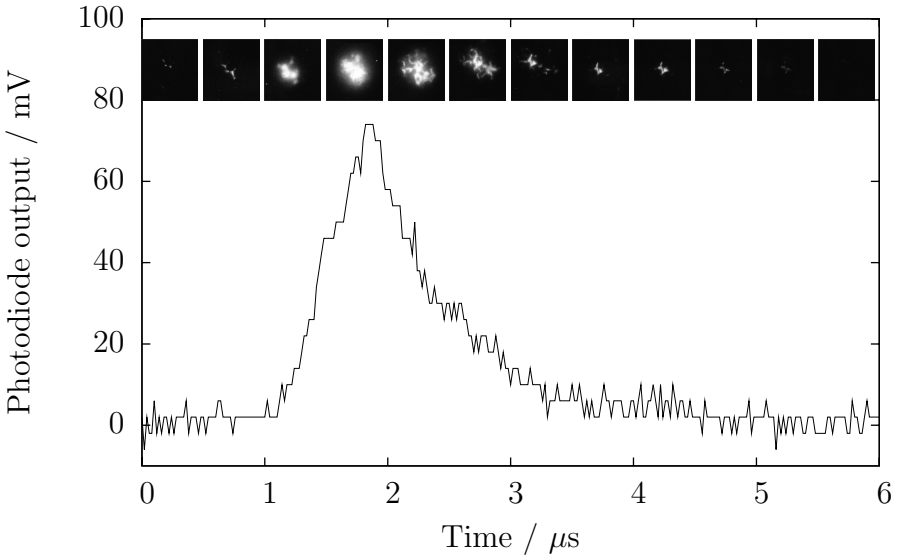

Figure 5.50: Photodiode output of a bed of 3.4–3.6 mm Westland prills, with a single 3.5 mm agricultural pellet, impacted at $700 \pm 40\,\mathrm{m\,s^{-1}}$. Superimposed images show framing photography of the experiment. Horizontal extent of image indicates duration for which shutter was open. Experiment also shown in figures 5.48 and 5.49.

5.3 Conclusions and future work

- Using the projectile and bed design detailed in section 5.1.1, a flyer velocity of $450\,\mathrm{m\,s^{-1}}$ is sufficient to induce reaction in a bed of 150–212 μm granular ammonium nitrate.
- The induction time between introduction of a shock to a granular ammonium nitrate bed, and the outbreak of light in that bed, may be explained by the travel time of the shock through the bed.
- A slightly re-designed sample cell would allow the above conclusion to be probed more rigorously, by allowing simultaneous observation of light output and shock travel time.
- The decaying light output of a shocked granular ammonium nitrate bed is not fully explained by conductive cooling of a large number of identical instantaneous delta-function heat sources.
- Therefore, either the heat sources are not approximately delta functions, they are not identical, or they are not instantaneous.
- Direct measurement of the evolution of one of these heat sources would determine how closely they approximate a delta function.
- The decaying light output could be used to test a model of the population distribution of these heat sources, or the chemical kinetics involved in their generation.
- In prill and pellet bed experiments, and in some granular bed experiments, the decay of light output was interrupted by a rise. This "bump" remains unexplained, and bears further study.
- Westland prills are suitable for us as an inert mock for agricultural pellets and Nitram prills.
- Differences in size distribution and mechanical strength make Westland prills less suitable as an inert mock for Orica prills.

- Beds of Orica and Nitram prills, and agricultural pellets, undergo incomplete reaction when impacted with a flyer velocity of $700 \pm 40\,\mathrm{m\,s^{-1}}$.

- The variation of light output with time for such beds shows features characteristic of the type of prill or pellet from which the bed is constructed. For Orica and Nitram prills, these features are visible when a single prill is used in an inert bed. This indicates that the features originate in the structure of the prills, rather than in inter-prill interactions. For agricultural pellets, the data neither support nor rule out this conclusion.

- More sensitive light-output experiments on inert beds would determine whether the above conclusion also applied to agricultural pellets.

- The light output from both beds of Orica prills and individual Orica prills reaches a plateau before growing to a peak. This plateau is due to spread of reaction through the porous interior of the prills.

- The peak of the light output of beds of Nitram prills and agricultural pellets shows structure which remains unexplained and bears further study.

- Direct prill impact experiments would provide useful information on the early stages of reaction in individual prills. Such experiments, however, require impractically high vacuum.

- Drop weight experiments find no indication that inter-prill jetting is responsible for reaction of Orica prills.

References

J. R. Asay and M. Shahinpoor, editors. *High-Pressure Shock Compression of Solids*. Springer-Verlag, 1993.

H. S. Carslaw and J. C. Jaeger. *Conduction of Heat in Solids*. Oxford University Press, 1947.

J. E. Field, G. M. Swallowe, and S. N. Heavens. Ignition mechanisms of explosives during mechanical deformation. *Proceedings of the Royal Society of London, Series A*, 382:231, 1982.

S. P. Marsh. *LASL Shock Hugoniot Data*. University of California Press, Berkeley, 1980.

Y. Me-Bar and S. M. Walley. Impact ignition of liquid explosives. Technical Report R&D 6541-AN-09, European Research Office, United States Army, London, W1, England, 1994.

T. Obara, N. K. Bourne, and Y. Mebar. The construction and calibration of an inexpensive PVDF stress gauge for fast pressure measurements. *Measurement Science and Technology*, 6:345–348, 1995.

W. G. Proud, E. J. W. Crossland, and J. E. Field. High-speed photography and spectroscopy in determining the nature, number and evolution of hot-spots in energetic materials. In C. Cavailler, G. P. Haddleton, and M. Hugenschmidt, editors, *25th International Congress on High-Speed Photography and Photonics*, volume 4948 of *SPIE*, pages 510–518, Physics and Chemistry of Solids Group, Cavendish Laboratory, University of Cambridge, 2003. SPIE.

G. M. Swallowe, J. E. Field, and L. A. Horn. Measurements of transient high temperatures during the deformation of polymers. *Journal of Materials Science*, 21:4089–4096, 1986.

Chapter 6

Spectra

It was seen in chapter 5 that reacting regions in ammonium nitrate beds reach a high temperature. To measure this temperature, the spectrum of the light emitted by these reacting regions was studied using a high-speed optical spectroscope. If they are black- or grey-body emitters, this spectrum will have a characteristic shape determined by their temperature (Planck, 1901). Curve-fitting tools were used to extract the emitter temperature from the recorded spectra.

6.1 Apparatus and calibration

The cell and flyer used were described in chapter 5, section 5.1.1. The fibre mount shown in chapter 5, figure 5.8 was used; no framing photography was taken during these experiments. Two optical fibres were taken from the rear of the sample cell. One of these led to a photodiode, as discussed extensively in chapter 5. The other led to the light input of the spectroscope.

The spectroscope is described in chapter 2, section 2.11. It was configured with a 0.21 s exposure time. Since reading the photodiode array takes 30 ms, this gave a $\frac{1}{7}$ probability that the photodiode array would be read during an experiment. In this case, one photodiode would report an erroneous value. This was deemed acceptable. This exposure time is the time between array readings, and should not be confused with the duration for which the image intensifier is active. The detector was cooled to $-15\,^{\circ}\mathrm{C}$; this required water cooling of the

Peltier device.

The image intensifier was triggered by a TTL pulse, remaining active for as long as the pulse was high. This pulse also signalled that the controlling computer should record the output of the photodiode array when next it was read. In this experiment, the pulse was produced by a delay generator, which in turn was triggered by the make trigger on the sample cell. The delay and duration of the pulse could be adjusted. This allowed the spectrum of light emitted by the experiment at a particular time after impact to be recorded.

6.1.1 Dark current

The dark current in the photodiode array adds an approximately constant intensity offset to the recorded spectrum. This offset depends on the array's exposure time, the temperature of the array, and the construction of the photodiodes in the array. There is also a random factor due to the probabilistic nature of thermal charge-carrier generation. The simplest way to account for this offset is to model it as exactly constant. The array is configured as for an experiment, and a single spectrum captured with the image intensifier gated off. Such a dark-current spectrum is shown in figure 6.1. The average intensity of this spectrum would then be taken as the dark current offset for these array parameters.

However, it was found that there was some repeatable structure to the spectra produced for this purpose. This is likely to be due to variations between the photodiodes in the array. Figure 6.2 illustrates this repeatability. $I_d(\lambda)$ is a dark current spectrum, while $I_e(\lambda)$ is some experimental spectrum. For illustrative purposes, another dark current spectrum has been chosen for $I_e(\lambda)$. Subtracting each element of I_d from its corresponding element in I_e produces a markedly smaller spread of points[1] than subtracting the mean dark current $\bar{I}_d$ from each element of $I_e(\lambda)$. The former approach was therefore adopted for this research.

The outlier at approximately 630 nm, -60 counts in figure 6.2 bears some mention. Occasionally, with probability of order 10^{-3}, a photodiode will record an anomalously low or high dark current. The element-wise subtraction approach used here does not suppress this anomaly, and it will propagate to later stages of

[1] The standard deviation $\sigma(I_e(\lambda) - \bar{I}_d) = 20.3$ counts, while $\sigma(I_e(\lambda) - I_d(\lambda)) = 2.43$ counts.

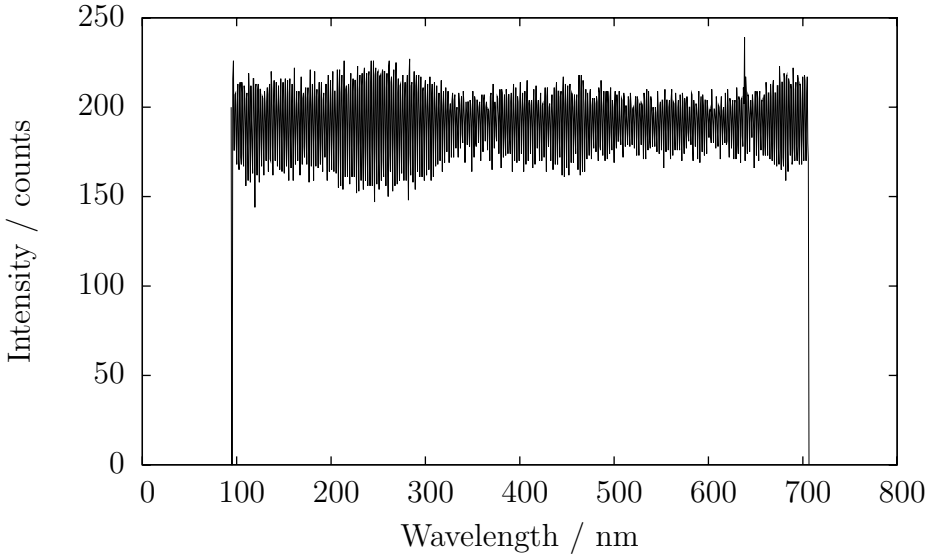

Figure 6.1: Example dark current spectrum. Exposure time 0.21 s, detector temperature −15 °C.

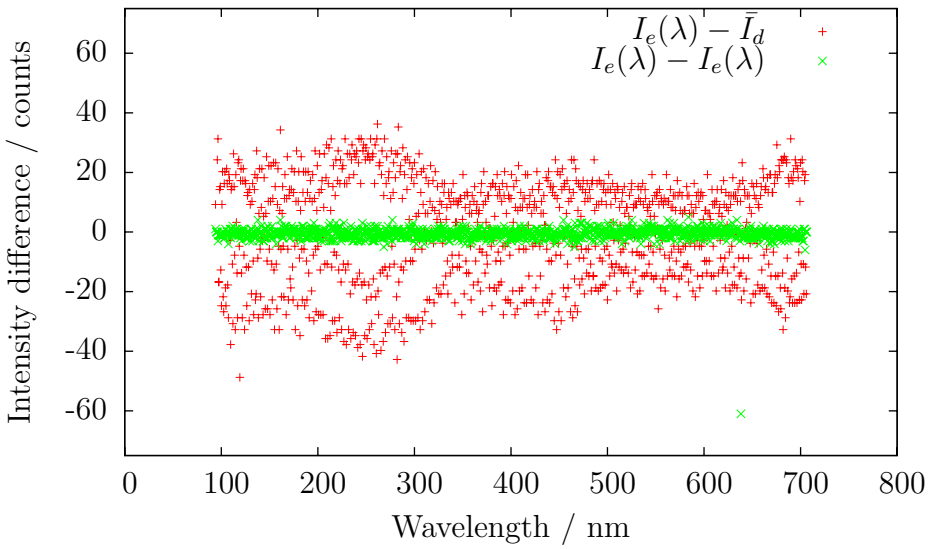

Figure 6.2: Illustration of repeatability of apparently-random noise in dark current for two dark current spectra, $I_d(\lambda)$ and $I_e(\lambda)$. That the green points are much more tightly grouped than the red points indicates that the structure of the dark current spectrum, despite appearing random, is in fact highly repeatable.

analysis. As those later stages are robust to a single point suffering an error of a few tens of counts, these anomalies are ignored.

6.1.2 Wavelength calibration

For the output of the detector array to be useful, the wavelength of light corresponding to each detector must be determined. The design of the array is such that the wavelength change between two adjacent detectors is constant. Therefore any source with multiple sharp spectral features at known wavelengths is suitable for this calibration. A mercury vapour lamp is recommended in the spectroscope documentation. A calibration using such a source was carried out long before this research began. It was then found that the fluorescent room lights used in the laboratory also produced light suitable for this calibration[1]. The wavelengths of several sharp features of the spectrum from these lights were recorded with the spectroscope. These recorded wavelengths were then used as the basis of subsequent wavelength calibrations of the spectroscope, including that performed in this research.

Figure 6.3 shows the spectrum of the room lights used for this calibration. In all cases the observed spectral features differed by less than 0.6 nm from the recorded values for calibration. As the resolution of the spectroscope with this grating is 0.6 nm, no further adjustment was deemed necessary.

6.1.3 Relative intensity calibration

Several components of the experiment reduce the intensity of light passing through them in a wavelength-dependent fashion. As this experiment is based on fitting a model to the relationship between intensity and wavelength of light emitted by the experiment, this wavelength-dependence must be accounted for. To do so, the light path of the experiment between the granular bed and the spectroscope was constructed. In place of the reacting granular bed, though, a light source of continuous, known spectrum was used.

[1] Unsurprisingly, given the similarity between a standard fluorescent lamp and a mercury vapour lamp.

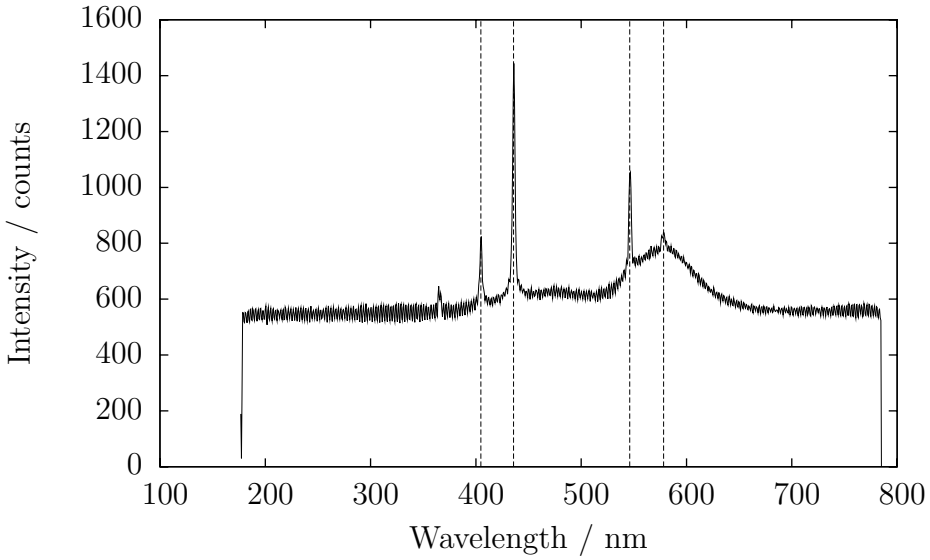

Figure 6.3: Recorded spectrum of fluorescent room lights. Dark current correction not applied. Superimposed lines are the nominal wavelengths of the features used for calibration, at 404.7, 535.8, 546.1 and 578.2 nm.

Figure 6.4 shows the arrangement used for this calibration. The light source was an incandescent bulb, determined by the National Physical Laboratory (NPL) to produce a 2856 K black body spectrum when a current of 3.549 A was passed through it. This current was supplied by a stabilized power supply and monitored with a multi-meter. The potential difference across the bulb was monitored with a second multi-meter, to ensure it remained at the 7.29 V observed by the NPL. This bulb would not fit into the confinement used for the granular bed. It was therefore possible for light to bypass the glass back-plate and distort the calibration. The shroud shown in figure 6.4 was used to eliminate this possibility. A windowless room was used for this calibration, and the room lights were switched off; no other steps were taken to eliminate stray light.

To record the spectrum of the light source, the image intensifier was gated on. The detector array was then exposed and read 50 times, and the resulting outputs automatically added. This reduced the random error in the recorded spectrum. This composite spectrum was then corrected for dark current and compared to the calculated black-body spectrum emitted by the light source. Figure 6.5 shows such a comparison. At each wavelength λ for which the spectroscope recorded an

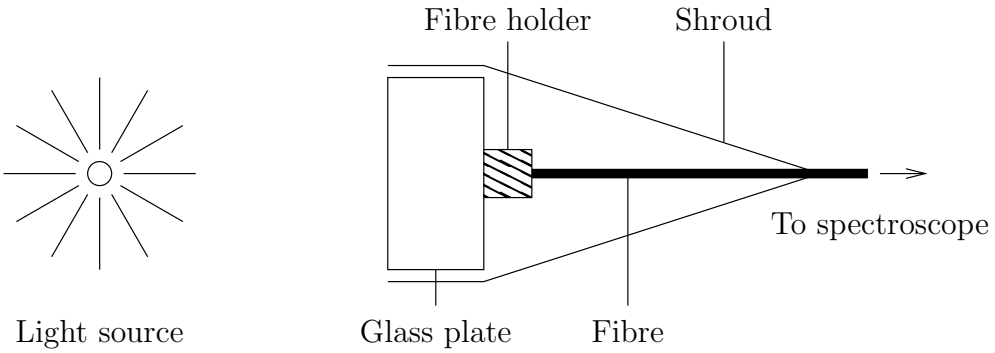

Figure 6.4: Arrangement used for relative intensity calibration of spectroscope. Fibre holder, glass plate and fibre are identical to those used in plate impact experiments (see chapter 5, figures 5.1 and 5.8). Shroud is black paper, folded and taped to exclude light from rear of glass plate.

intensity, this intensity was divided by the intensity predicted for that wavelength for a black body at 2856 K. The set of ratios thus produced was referred to as the sensitivity curve $S(\lambda)$. This process was repeated three times to assess repeatability. Figure 6.6 shows the sensitivity curve calculated by this method. The sensitivity of the apparatus was very low below 380 nm and above 615 nm. Therefore, only the spectral region between these two values was considered. Note that the vertical axis is now in arbitrary units. The fraction of the radiation emitted by the calibration source that is captured by the spectroscope is unknown, as is the emitting area of the calibration source. Therefore it is not possible to find the absolute sensitivity of the spectroscope without considerably refining the system used for calibration. Such refinement was unnecessary, as the analysis techniques used assumed a grey-body emitter. Calibration of the variation in sensitivity with wavelength was therefore sufficient.

It was found that the sensitivity $S(\lambda)$ varied as the gain of the intensifier was varied. It was therefore decided that only integer numbers of turns of the ten-turn gain-control potentiometer would be used in experiments, and a separate calibration would be performed for each such gain. This presented a new problem. While continuous illumination of the detector was possible at low gain, at high gain this would saturate the detector. This prevented acquisition of a useful spectrum and risked damage to the detector. To avoid this, the detector was

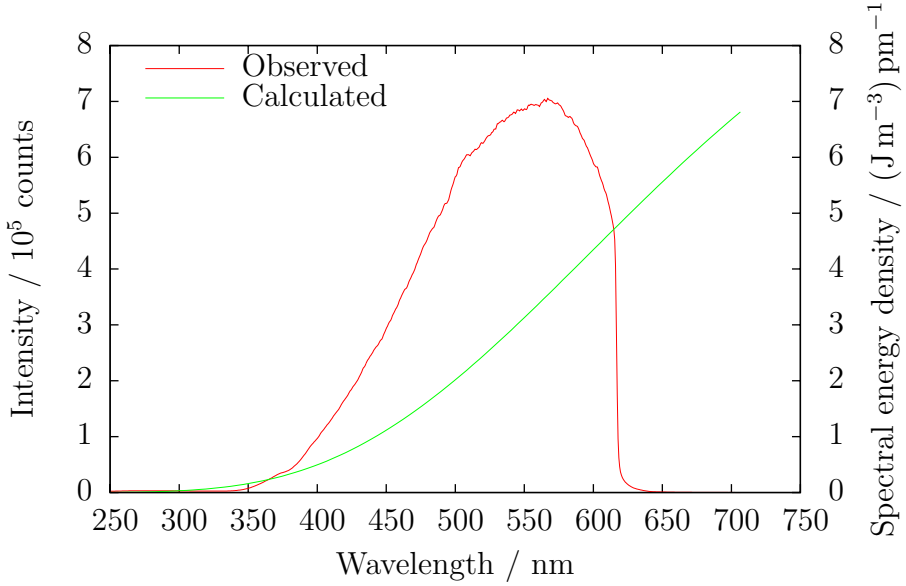

Figure 6.5: Comparison of the observed spectrum of a 2856 K black body source (left axis) with the calculated spectral energy density of such a source (right axis). At each wavelength of interest, the value of the red curve is divided by the value of the green curve. This gives the sensitivity S of the apparatus at that wavelength. Observed spectrum gathered with 50 exposures each of 0.21 s duration, detector temperature −15 °C, intensifier gain set to "0".

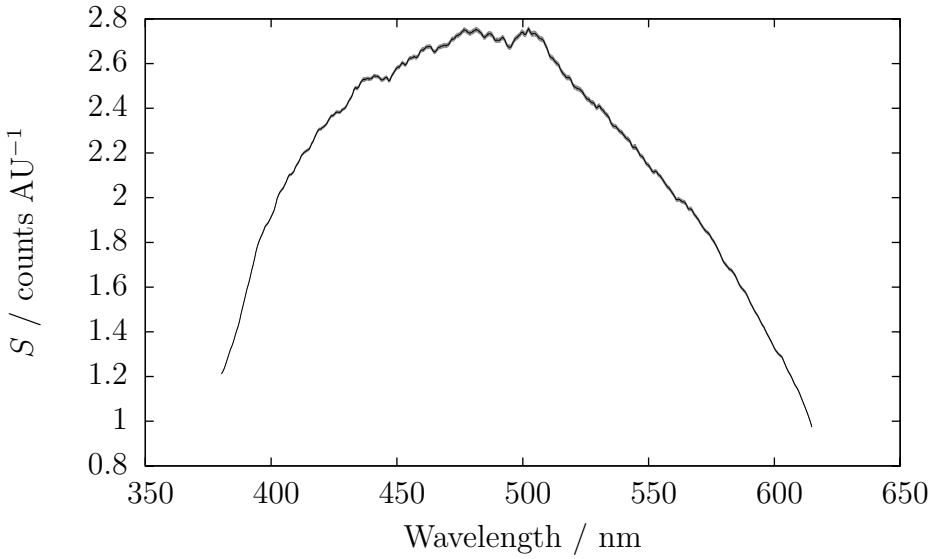

Figure 6.6: Sensitivity curve for apparatus with 0.21 s exposure time, detector temperature −15 °C, intensifier gain set to "0".

used in gated mode. A pulse generator was used to produce a TTL pulse of a certain duration in response to user input. This was connected to the input of the pulse amplifier, so that the intensifier would be active as long as the output of the pulse generator was high. The duration of the TTL pulse was chosen so that, at the intensifier gain under investigation, the detector would produce a clear spectrum without saturation. The detector was then exposed and read multiple times, just as for continuous illumination. During this time, the pulse generator was manually triggered ten times, taking care to wait at least one exposure time (0.21 s) between triggers.

Given an experimental spectrum $I(\lambda)$ and the corresponding sensitivity curve $S(\lambda)$, the sensitivity-corrected spectrum

$$I_{\text{corr}}(\lambda) = \frac{I(\lambda)}{S(\lambda)} \,, \tag{6.1}$$

i.e. for each wavelength of interest, the intensity reported by the spectroscope is divided by the previously-obtained wavelength-dependent sensitivity for that wavelength, $S(\lambda)$. Assuming that no properties of the spectroscope or the optical path leading to it have changed since $S(\lambda)$ was measured, this will eliminate all wavelength dependence of the observing apparatus from the corrected spectrum I_{corr}. As previously discussed, relating this to the actual energy output of the source requires multiplication by some unknown value. The calibration performed here, though, ensures that this multiplier is independent of wavelength.

6.1.4 Fibre effects

In these experiments, inexpensive optical fibre was used to carry light from the experiment to the spectroscope. This protected the spectroscope from being physically damaged by the experiment. The fibre used was supplied by RS Components, with stock number 368-047, and had a 1 mm PMMA core. The degree to which this fibre attenuates light passing through it depends on the wavelength of that light. Altering the length of the fibre will therefore alter the shape of the spectrum as received by the spectroscope. This in turn can modify the temperature the system records. The effect of the fibre must therefore be quantified.

If one end of a fibre of attenuation coefficient $\alpha(\lambda)$ is exposed to a spectrum of intensity $I_0(\lambda)$, the spectrum emitted from the other end will be

$$I(\lambda) = I_0(\lambda)e^{-\alpha(\lambda)l}. \tag{6.2}$$

The dependence of the attenuation coefficient α on wavelength can be determined by a simple experiment. A fibre of length l_0 is used to carry light from some suitable source (in this case, the 2856 K lamp used for calibration) to the spectroscope, and the transmitted spectrum recorded. This is then repeated using a fibre of length l_1. By rearranging equation 6.2,

$$\begin{aligned} \alpha(\lambda) &= \frac{1}{l_1 - l_0} \ln A \frac{I(\lambda, l_0)}{I(\lambda, l_1)}, \\ &= \frac{\ln A}{l_1 - l_0} + \frac{1}{l_1 - l_0} \ln \frac{I(\lambda, l_0)}{I(\lambda, l_1)}, \end{aligned} \tag{6.3}$$

where A is a constant to account for the varying alignment between the fibre and the light source.

Figure 6.7 shows $\alpha(\lambda)$ for $l_0 = 1.79 \pm 0.01$ m, $l_1 = 4.43 \pm 0.01$ m. Note the large error in α, particularly at longer wavelengths. This is due to the multimodal nature and relatively short length of the fibre. There are multiple modes by which light may propagate down the fibre, and each will impose a different wavelength-dependent attenuation on that light. The differences will arise for two reasons. First, light propagating in different modes will pass through different amounts of the core material. Second, the different modes will couple differently with the cladding and sheath of the fibre. The extent to which the various modes of the fibre are excited will, in short fibres such as those used in this research, depend strongly on the precise orientation of the fibre itself, and on the alignment between the fibre and the light source (Wilson and Hawkes, 1989). Rolling the fibre into a coil of ~ 0.2 m diameter eliminated this variability in attenuation measurements, as would be expected if it was due to variable mode populations. However, as the arrangement of the experiment itself required a length of un-coiled fibre, it was more appropriate to treat this variability as a random error.

In practice, the length of fibre used varied by ~ 0.5 m from the length for

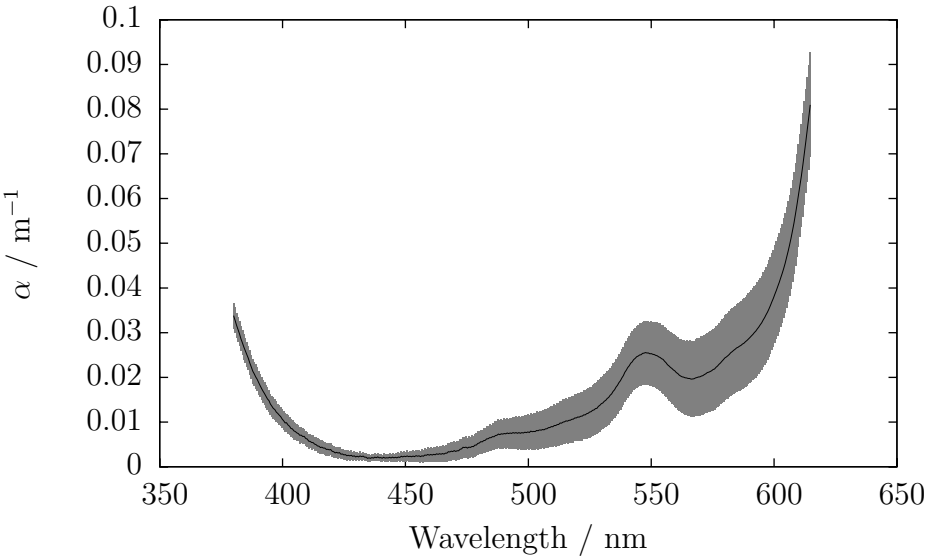

Figure 6.7: Attenuation coefficient α as a function of wavelength for RS 368-047 PMMA-cored fibre, measured using 1.79 m and 4.43 m fibres. All traces had $\frac{\ln A}{l_1 - l_0}$ set so that $\alpha = 0$ at the lowest point of the curve.

which the spectroscope was calibrated. This allows the error in temperature introduced by the variable fibre length and mode excitation to be assessed. Using equation 6.2, the recorded spectrum from an experiment can be adjusted to simulate the addition or removal of 0.5 m of fibre. Black-body curves can then be fitted to the two modified spectra thus produced, providing two temperatures. These temperatures then set bounds on the error introduced to temperature measurements by fibre variations in that experiment. Figure 6.8 demonstrates the technique. This shows that the temperature error introduced by fibre variations is of similar magnitude to that introduced by the fitting program.

6.2 Results

The spectra observed during these experiments fell into one of two categories, approximately divided by the peak light output of the reacting bed. "Reaction-like" spectra were captured before this peak, while "cooling-like" spectra were captured after this peak. Reaction-like spectra were dominated by spectral lines

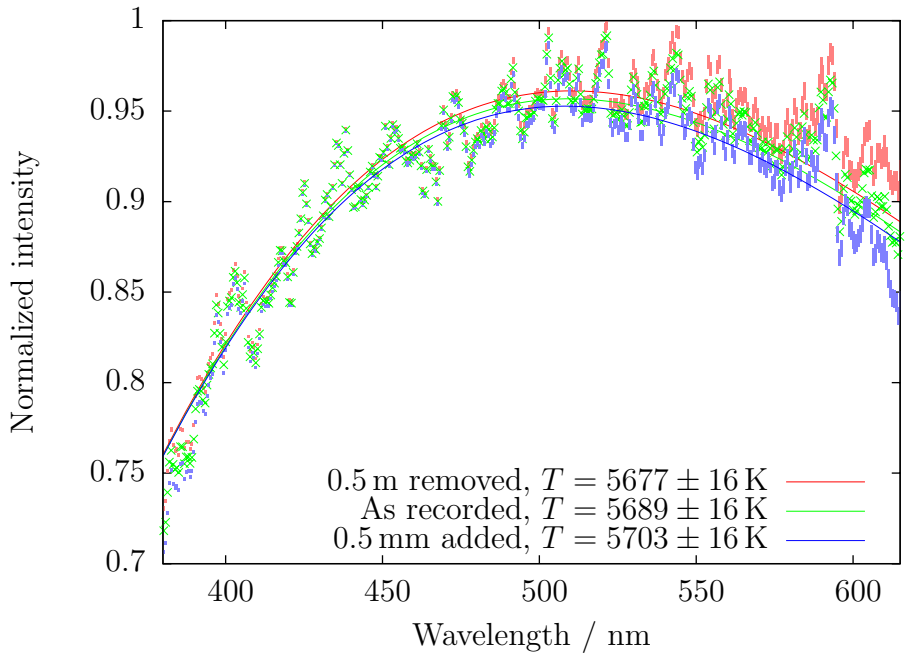

Figure 6.8: Spectrum captured $0.5 \pm 0.3\,\mu$s after photodiode peak during AN impact ($700 \pm 40\,\mathrm{m\,s^{-1}}$ impact on 3.5 mm thick cell of 150–212 μm AN) adjusted to simulate addition and removal of 0.5 m of fibre and with black-body curves fitted between 400 nm and 530 nm, illustrating the effect of fibre variations on measured temperature. Quoted errors found using bootstrap method. Accounting for both errors, the measured temperature is 5690 ± 20 K.

and were unsuitable for temperature measurements. Cooling-like spectra followed a black-body shape and were useful for temperature measurements.

6.2.1 Reaction-like spectra

Figure 6.9 shows a typical reaction-like spectrum. It shows clear peaks at 385, 424, 557 and 591 nm. Apart from these peaks, the light output increases with wavelength. This underlying continuum could be due to the chemiluminescent reaction

$$\mathrm{O} + \mathrm{NO} \longrightarrow \mathrm{NO}_2 \ , \tag{6.4}$$

(Young and Sharpless, 1963) or to radiation from a black body at $\sim 10^3\,\mathrm{K}$. Disambiguating the two would require spectroscopy in the range 600–1000 nm; this may also allow temperature measurements in the latter case.

The peaks at 557 and 591 nm are consistent with the N_2 first positive bands (Becker et al., 1972; Guerra et al., 2004; Kurzweg and Broida, 1959; Young and Sharpless, 1963), caused by the radiative transition $N_2(\mathrm{B}\,^3\Pi_\mathrm{g} \rightarrow \mathrm{A}\,^3\Sigma_\mathrm{u}^+)$. The upper state of this transition is populated by the combination of atomic nitrogen to form an excited N_2 molecule. This transition also involves a change in the vibrational energy quantum number of the N_2 molecule. The broad peak at 557 nm is due to transitions in which this number falls by 5, while the sharper peak at 591 nm is due to transitions in which this number falls by 4. The sharpness of the 591 nm peak is interesting: it implies that the $\nu' = 9$ vibrational energy level of the excited N_2 state is much more populous than the other vibrational energy levels. Apart from this anomaly, these two peaks simply confirm that N_2 is being formed in this reaction.

The peaks at 385 and 424 nm may be due to NO β bands (Young and Sharpless, 1963). These are caused by the radiative transition $\mathrm{NO}(\mathrm{B}\,^2\Pi \rightarrow \mathrm{X}\,^2\Pi)$. Similarly to the N_2 first positive bands, the upper state of this transition is populated by the combination of atomic nitrogen and oxygen to form an excited NO molecule. Again, the transition involves a change in the vibrational energy of the NO molecule. The peak at 424 nm could be due to either the $\mathrm{NO}(\mathrm{B}\,^2\Pi, \nu' = 3 \rightarrow \mathrm{X}\,^2\Pi, \nu'' = 15)$ or the $\mathrm{NO}(\mathrm{B}\,^2\Pi, \nu' = 0 \rightarrow \mathrm{X}\,^2\Pi, \nu'' = 13)$ transition, the peaks for which overlap. The peak at 385 nm could be due to the

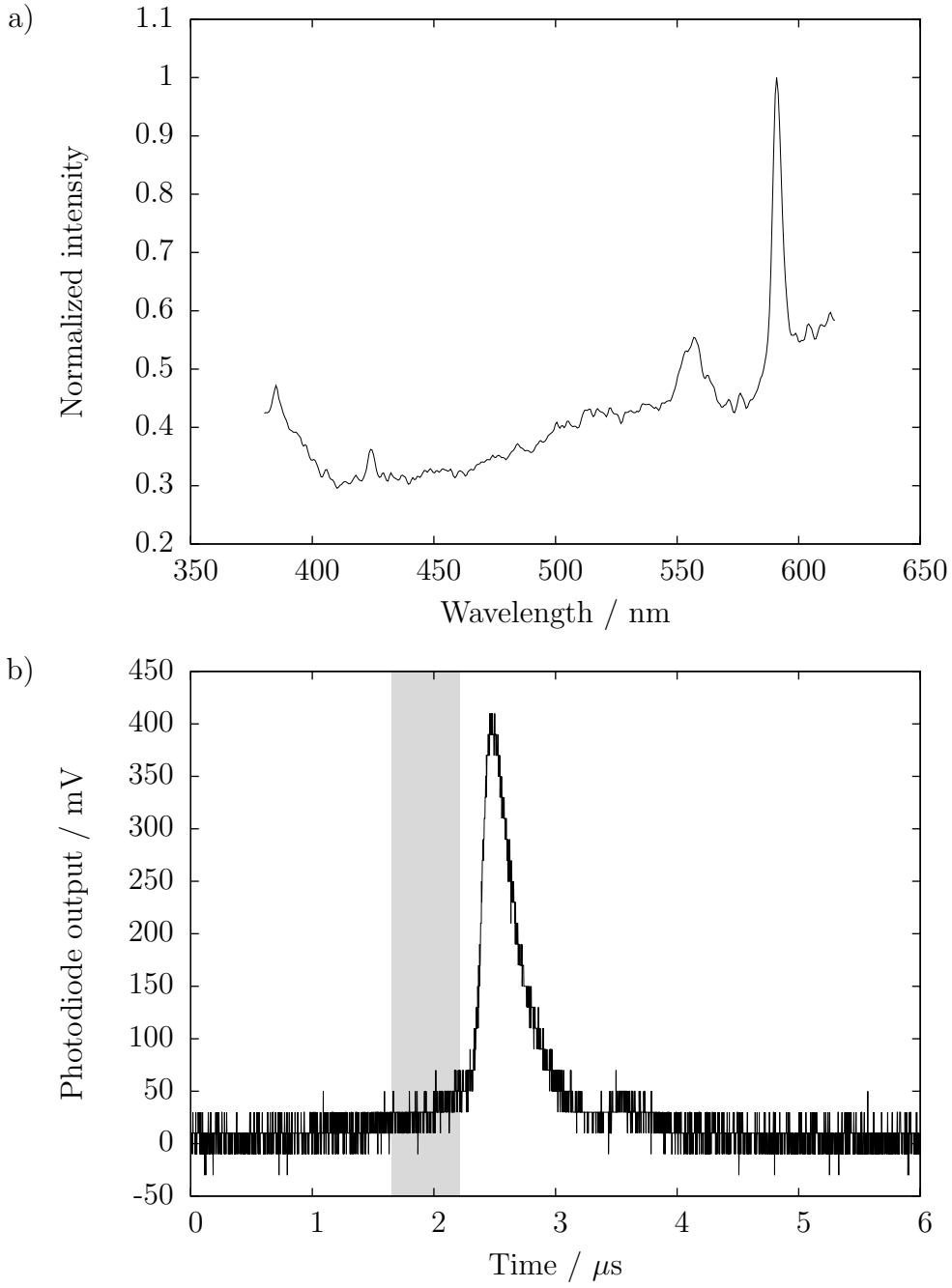

Figure 6.9: (a) Spectrum of light emitted by 3.5 mm bed of 150–212 μm milled AN impacted at $700 \pm 40\,\mathrm{m\,s^{-1}}$. (b) Photodiode output from this bed; shaded region indicates duration for which spectroscope recorded.

$NO(B\,^2\Pi, \nu' = 1 \rightarrow X\,^2\Pi, \nu'' = 12)$ transition. It is interesting that the other peaks in the $\Delta\nu = 12$ and $\nu' = 1$ systems are not observed.

6.2.1.1 Time-dependence of spectra

Only the spectral line at 591 nm was visible in all reaction-like spectra. This line was so persistent that it was visible in some cooling-like spectra, as discussed in section 6.2.2. It was also visible well after the bed had cooled, as shown in figure 6.10. This indicates that the recombination of atomic nitrogen was taking place throughout the experiment. This in turn indicates that this recombination was at least partly independent of whichever reaction led to heating of the bed. The broad 557 nm peak of nitrogen recombination is absent in figure 6.10. This may simply be due to its low intensity, compared with the 591 nm peak.

The spectral lines at 385 and 424 nm varied more with time. Figure 6.11 shows the earliest spectrum obtained, which lacks these lines. This indicates that NO was not formed until later in the experiment. The first occurrence of the NO spectral lines was in spectra taken between 1.1 and 0.6 μs before the peak light output of the bed. This suggests that NO production is associated with a rapid rise in the light output of the bed. The photodiode peak is believed, based on section 6.2.2 and chapter 5, section 5.1.3.2 to be thermal in origin. This suggests that whichever exothermic reaction is heating the bed involves NO.

6.2.2 Cooling-like spectra

Figure 6.12 shows a typical cooling-like spectrum. The uncertainty in the measured spectrum is due to the fibre length and orientation effects discussed in section 6.1.4. The 591 nm peak of N_2 formation is visible in this spectrum. However, the continuum is suitable for temperature measurement.

To measure the temperature of the emitting regions of the bed, they were assumed to emit as black bodies. The spectrum of the light emitted by the bed would then be given by

$$I(\lambda) = A \cdot \frac{2hc^2}{\lambda^5 \left[\exp\left(\frac{hc}{\lambda k_B T}\right) - 1\right]}\ , \tag{6.5}$$

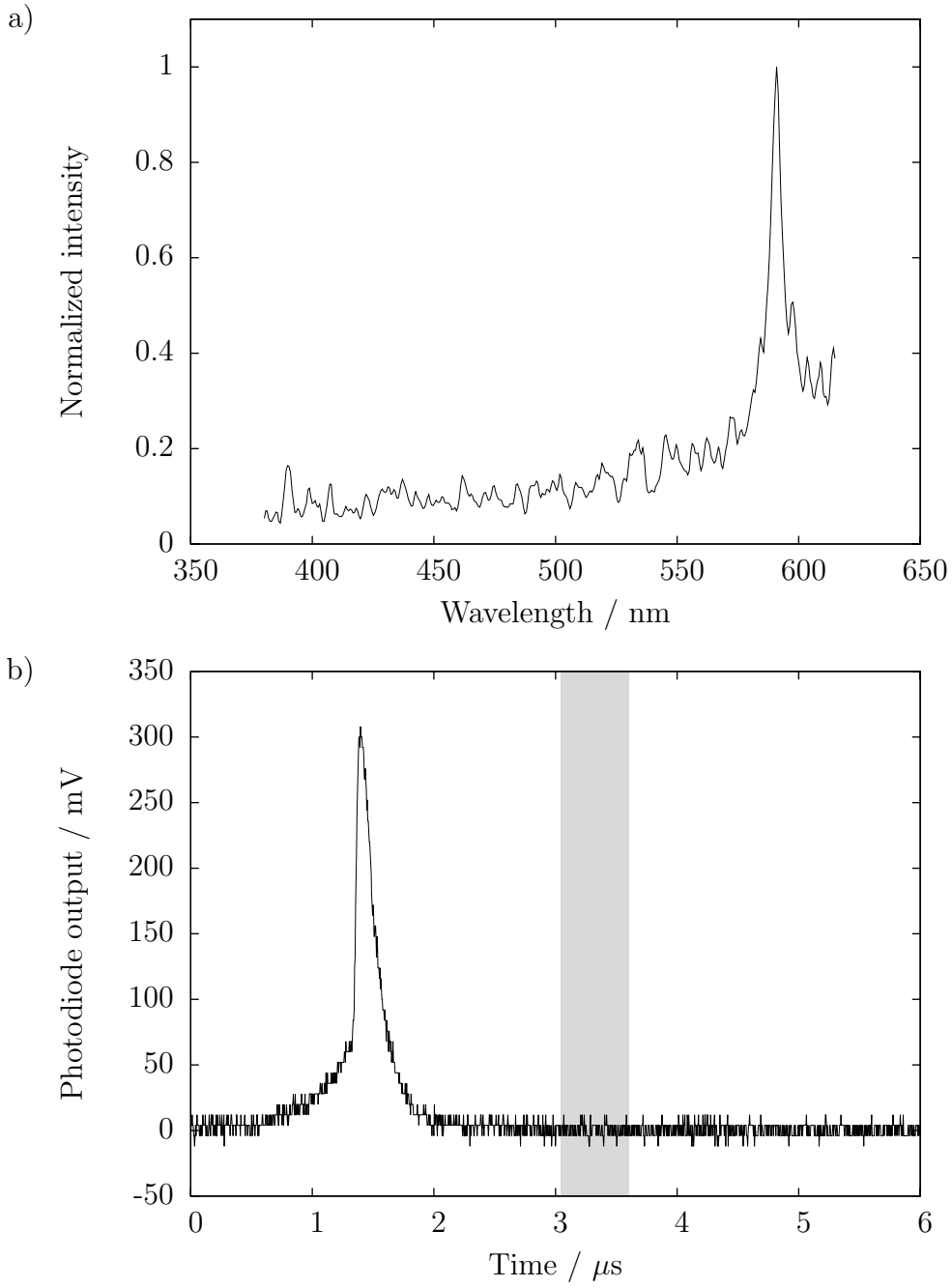

Figure 6.10: (a) Spectrum of light emitted by 3.5 mm bed of 150–212 μm milled AN impacted at $700 \pm 40\,\mathrm{m\,s^{-1}}$. (b) Photodiode output from this bed; shaded region indicates duration for which spectroscope recorded.

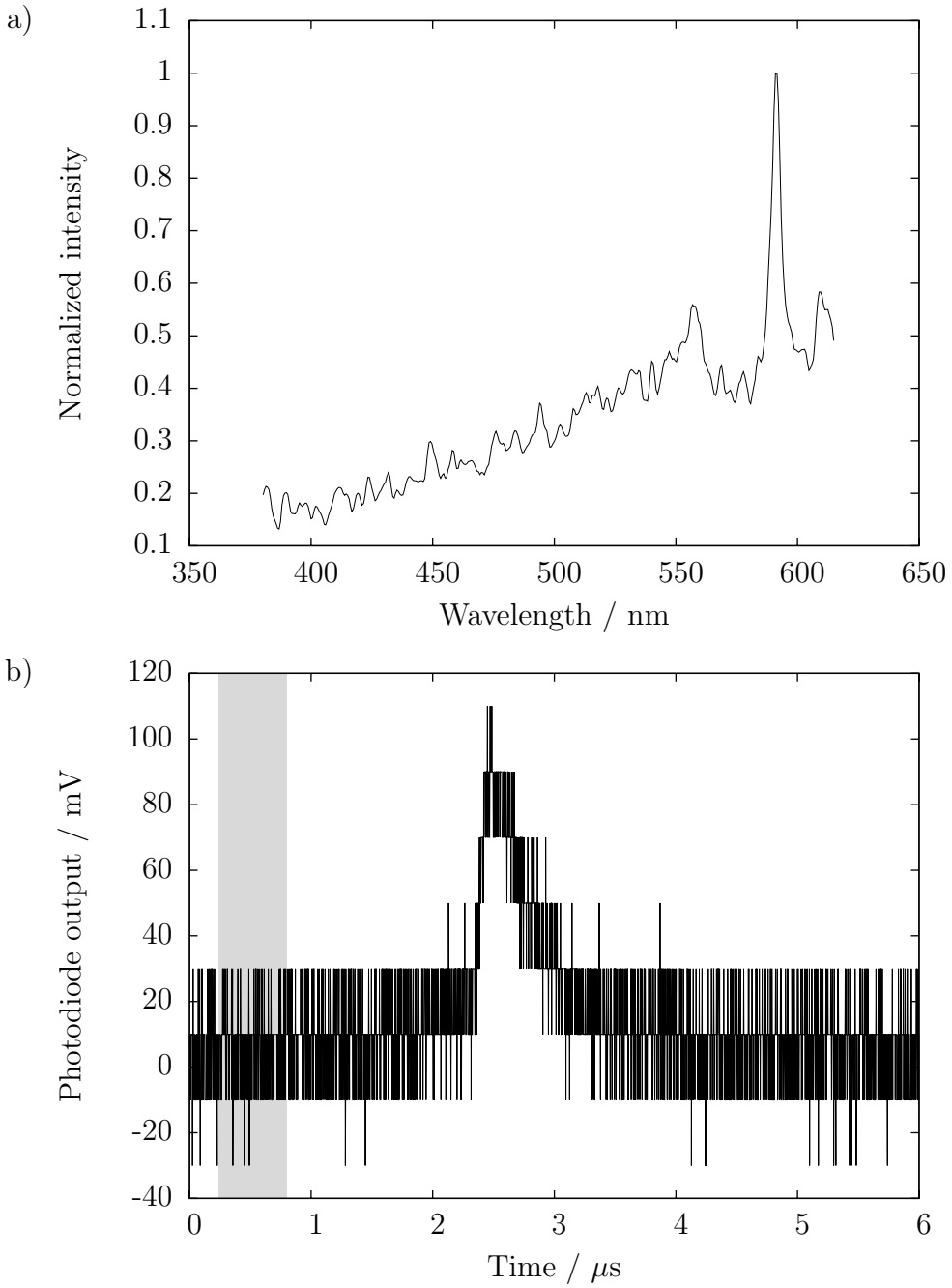

Figure 6.11: (a) Spectrum of light emitted by 3.5 mm bed of 150–212 μm milled AN impacted at $700 \pm 40\,\mathrm{m\,s^{-1}}$. (b) Photodiode output from this bed; shaded region indicates duration for which spectroscope recorded. Digitization indicates inept fibre polishing and oscilloscope configuration, rather than low bed light output.

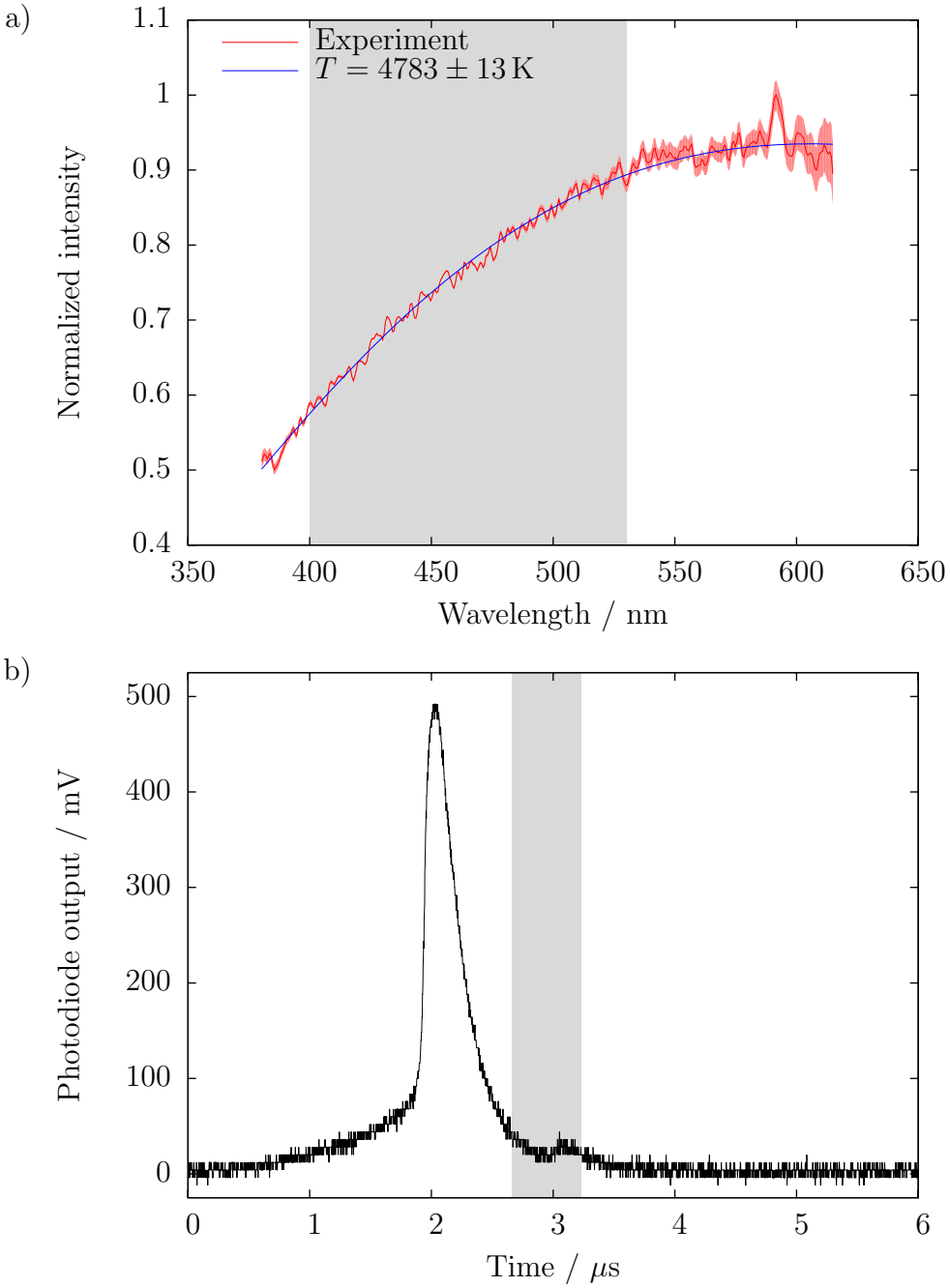

Figure 6.12: (a) Spectrum of light emitted by 3.5 mm bed of 150–212 μm milled AN impacted at $700 \pm 40\,\mathrm{m\,s^{-1}}$. Black body fit to shaded region superimposed. (b) Photodiode output from this bed; shaded region indicates duration for which spectroscope recorded.

where h, k_B and c are Planck's and Boltzmann's constants and the speed of light, respectively, T is the temperature of the emitting regions, and A is the constant multiplier discussed in section 6.1.3. A and T can then be found using a two-parameter Levenberg-Marquardt fit of equation 6.5 to the data, as described in chapter 2, section 2.12. To avoid distortion due to the N_2 recombination spectral lines, the fit considered only wavelengths between 400 and 530 nm. Uncertainty in the fitted parameters was assessed using the bootstrap method, as described in chapter 2, section 2.12.5. The uncertainty in T due to fibre effects was assessed as described in section 6.1.4. These two uncertainties were added in quadrature to give the quoted uncertainty in T.

6.2.2.1 Variation of temperature with time

The spectroscope could only record a single spectrum. Assessing the variation of bed temperature with time therefore required multiple experiments. Between experiments there was some variation in projectile velocity, and thus induction time between the shock entering the bed and the peak of the bed's light output. To reduce the effect of this on these results, the peak of the photodiode output in each experiment was taken as the origin of the time axis. Figure 6.13 shows the results of this series of experiments.

These results are broadly as expected. The temperature falls steadily from the photodiode peak, consistent with the theory that the decaying light output of the bed is thermal in origin. The earliest and highest temperature recorded was 6661 ± 20 K, recorded $0.2 \pm 0.3\,\mu$s after the photodiode peak. However, the temperature fell more slowly than would be expected based on the photodiode data, subject to the assumptions in chapter 5, section 5.1.3.2. It was assumed there that the photodiode captured a constant fraction of the bed's total radiation output over the course of an experiment. Therefore, by rearranging the Stefan-Boltzmann law (chapter 5, equation 5.20) and taking the photodiode output to be proportional to the total power radiated by the bed, we find

$$T \propto \sqrt[4]{V} \,, \tag{6.6}$$

where T is the temperature of the emitting regions and V is the photodiode

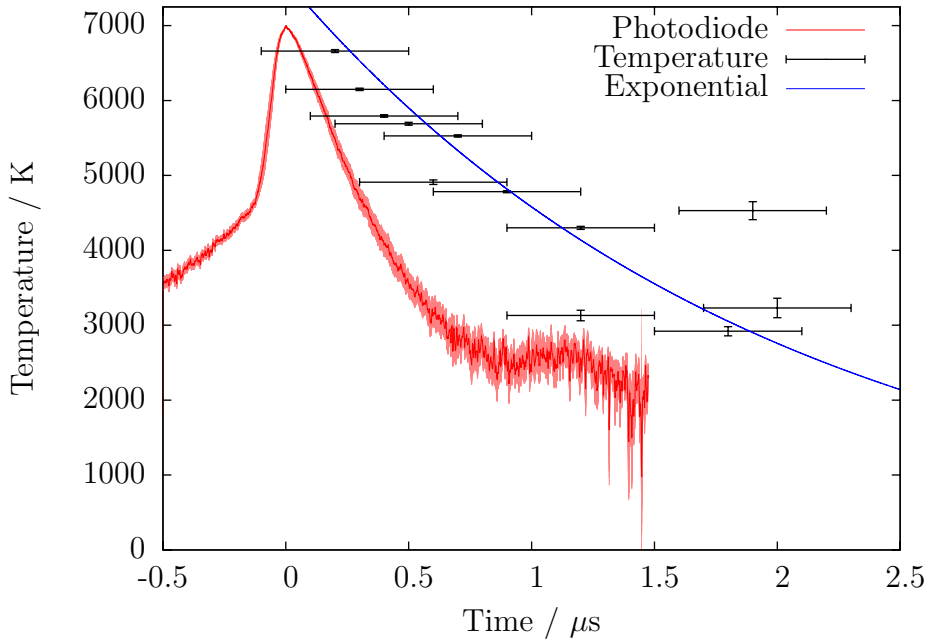

Figure 6.13: Data points show temperature of emitting regions in ammonium nitrate beds impacted at $700 \pm 40\,\mathrm{m\,s^{-1}}$. Origin of time axis taken as peak of photodiode output in each experiment. Horizontal error bars indicate duration over which spectroscope integrated. Blue line is a decaying exponential through these data points to aid comparison. Red line is the fourth root of the normalized average photodiode output for these experiments, multiplied by 7000 to aid comparison. If the photodiode captures a constant fraction of the bed light output, the red line and the blue line should lie near each other. This is clearly not the case.

output. As figure 6.13 shows, $\sqrt[4]{V}$ falls noticeably faster than T.

The most likely explanation for this discrepancy is that it is not safe to neglect the wavelength-dependent sensitivity of the photodiode. As the temperature of the bed changes, both the total radiated energy and the wavelength distribution of that energy change. The output of the photodiode will depend on both of these, rather than only the former as was assumed in chapter 5.

6.2.2.2 Uncertainty in temperature

As figure 6.13 shows, the uncertainty in the fitted temperature of a spectrum is significantly smaller than the vertical scatter of the points at similar times. The most likely explanation is that there is significant shot-to-shot variation in the temperature reached by the reacting regions of the bed. However, it is possible that the probability distribution of T differs markedly from a normal distribution.

The bootstrap method, described in section 2.12.5, generates a probability distribution of the fitted parameters, given the data. Figure 6.14 shows the probability distribution of A and T corresponding to the black body fit shown in figure 6.12, while figure 6.15 shows its projection onto the T axis. A strong negative correlation between T and A is apparent. This is to be expected: if the range of wavelengths used for fitting does not contain the peak of the black-body spectrum, the primary effect of varying T will be to vary the total intensity of the spectrum. This will require an opposing change in A if the fitted and experimental spectra are to agree. The error in T should therefore be reduced when the black body peak is within the fitting region, and this is observed in figure 6.13. Figure 6.15, meanwhile, shows no evidence that the distribution of T differs significantly from a gaussian. It is therefore most likely that the vertical spread of points seen in figure 6.13 is due to shot-to-shot variation. Further experiments would be required to better characterize this effect.

6.2.2.3 Consequences of temperature measurement

These temperature measurements indicate that, in the system studied here, some fraction of the bed reaches a temperature in excess of 6000 K. The chemical energy released by reaction of ammonium nitrate can only heat its products to

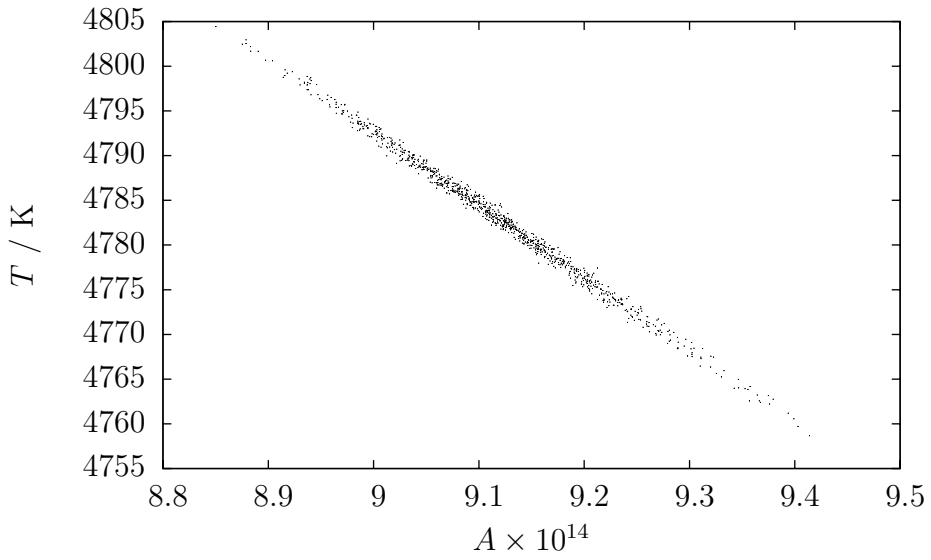

Figure 6.14: Probability distribution of fitted parameters for spectrum of light gathered approximately 1 μs after peak light output from a 3.5 mm bed of 150–212 μm milled AN impacted at 700±40 m s^{-1}. Fit in question shown in figure 6.12.

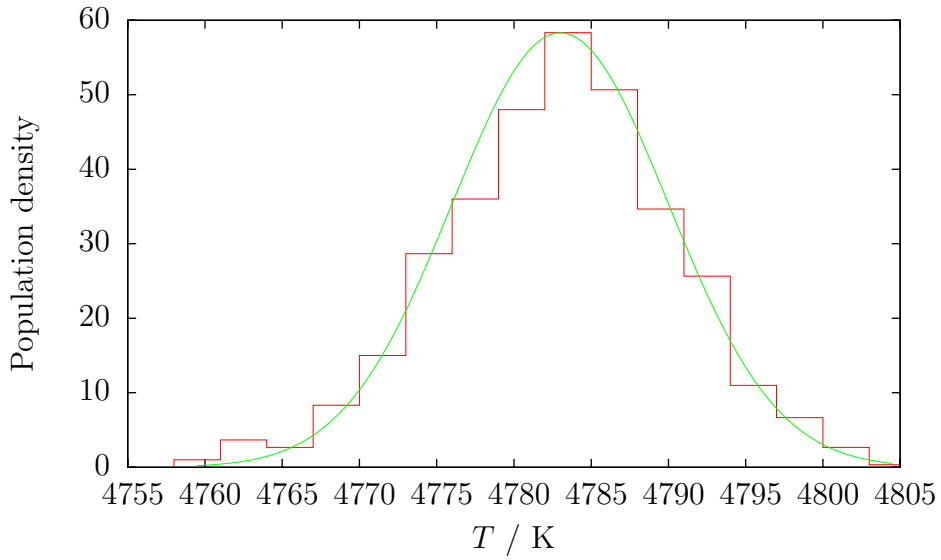

Figure 6.15: Projection of probability distribution of fitted parameters onto T axis for spectrum of light gathered approximately 1 μs after peak light output from a 3.5 mm bed of 150–212 μm milled AN impacted at 700 ± 40 m s^{-1}. Fit in question shown in figure 6.12. Un-projected probability distribution shown in figure 6.14. Gaussian fit to distribution superimposed.

between 1500 K and 2500 K, depending on the model used for the chemistry and for the heat capacity of the products. The discrepancy between the two is interesting, as well as presenting problems for models of AN detonation based entirely on chemical considerations.

The experimental set-up used here simulates detonation in many respects. In detonation, a shock propagates through the material, initiating reaction which then drives the shock. Here, a shock is introduced to the material and initiates reaction; the thin bed avoids the problems of lateral release waves usually encountered in small-scale tests of non-ideal explosives.

One possible explanation for the high temperatures seen in this experiment is that they are purely physical in origin. The various hot spot mechanisms, by definition, convert mechanical energy into local heating. However, subjecting an inert bed of sugar to this experiment resulted in no detectable light emission. This indicates that purely physical heating cannot account for the 4000 K difference between the observed temperature and the temperature due to chemistry. Were hot-spot mechanisms heating the sugar to 4000 K, some light would surely have been visible.

Another possible explanation for these high temperatures is that the heated material's heat capacity diverges drastically from that expected. Were the heat capacity in the emitting material to fall, the same amount of chemical energy from AN decomposition would raise it to a much higher temperature. There are a wide range of effects at work which could conceivably eliminate degrees of freedom from the system, reducing its heat capacity. Probing these quantitatively, however, is challenging.

It is possible that the emissivity of the emitting regions has a strong wavelength dependence. This could cause the colour temperature of these regions to over-estimate their actual temperature. However, the shape of the observed spectra agrees well with that of a black-body spectrum at a range of temperatures. This could not be produced by a wavelength-dependent emissivity: it would also require a very specific (and very unlikely) temperature dependence.

A final possibility is that physical and chemical heating effects couple non-additively. For example, consider the situation where chemistry pre-heats a cavity to 2000K, and this cavity then undergoes adiabatic compression. Under a very

crude treatment, this cavity reaches approximately seven times the temperature of an otherwise identical cavity which was at room temperature before compression. A more rigorous treatment would almost certainly reduce this effect, but it could still be sufficient to explain the apparent discrepancy between chemical energy and the temperature observed in this experiment.

6.3 Conclusions and future work

- The spectroscopic technique described in this chapter is suitable for measuring the temperature of emitting regions in a granular AN bed impacted at $700 \pm 40\,\mathrm{m\,s^{-1}}$ after the peak light output of that bed.

- N_2 formation in such an AN bed begins within 800 ns of impact and continues until at least $3\,\mu$s after impact. The vibrational energy distribution of these N_2 molecules does not appear to be consistent with that observed at room temperature and low pressure.

- Study of the N_2 spectral lines at higher wavelength resolution may allow the vibrational energy distribution of the N_2 molecules to be measured.

- NO formation in such an AN bed begins between 1.1 and $0.6\,\mu$s before the peak light output of the bed, and is associated with an increase in the light output of the bed. It is therefore believed to be involved in the exothermic reactions that heat the bed.

- Study of the emission spectrum of such a bed in the 600–1000 nm range is necessary to determine whether NO_2 is formed during the reaction.

- The fraction of the bed's light output detected by the photodiodes used in chapter 5 is a function of temperature.

- The uncertainty in the temperature found using the spectroscopic technique described in this chapter is significantly smaller than the shot-to-shot variation in this temperature.

- This variation could be ameliorated by reducing the shot-to-shot variation of the impact velocity.
- During this experiment some regions of the bed reach a temperature of 6660 ± 20 K. Chemical decomposition of AN can only reach a temperature of approx. 2000 K. This presents a problem for models of AN detonation that depend solely on chemistry.

References

K. H. Becker, E. H. Fink, W. Groth, W. Jud, and D. Kley. N_2 formation in the Lewis-Rayleigh afterglow. *Faraday Discussions of the Chemical Society*, 53: 35–51, 1972.

V. Guerra, P. A. Sá, and J. Loureiro. Kinetic modeling of low-pressure nitrogen discharges and post-discharges. *European Physical Journal: Applied Physics*, 28:125–152, 2004.

U. H. Kurzweg and H. P. Broida. Vibrational intensity distributions in the nitrogen afterglow. *Journal of Molecular Spectroscopy*, 3:388–404, 1959.

M. Planck. Ueber das Gesetz der Energieverteilung im Normalspectrum. *Annalen der Physik und Chemie*, 4(4):553–563, 1901.

J. Wilson and J. F. B. Hawkes. *Optoelectronics: An Introduction*, chapter 8. Prentice Hall, second edition, 1989.

R. A. Young and R. L. Sharpless. Chemiluminescent reactions involving atomic oxygen and nitrogen. *Journal of Chemical Physics*, 39(4):1071–1102, 1963.

Chapter 7

Conclusions

Both granular ammonium nitrate (AN) and a variety of prill and pellet formulations of AN were studied in this research. Their microstructure and compaction response were investigated, as was the light they produced during shock-induced reactions.

The main technique used for investigating microstructure was environmental scanning electron microscopy (ESEM). X-ray microtomography was also found to be a suitable technique, but was not used extensively in this research. ESEM showed that formulations intended for explosive use contained a network of connected voids with sizes of order tens of microns, while those intended for agricultural use contained very few voids. The void network in explosive formulations would serve two purposes. First, it would allow intimate mixing of fuel and AN. Second, collapse of these voids under shock loading would produce a high density of hot spots. Conversely, the lack of such voids in agricultural formulations would render them less useful as explosives. It would also improve the handling and storage properties of the formulation.

One such low-void-fraction agricultural formulation of AN contained a mixture of AN and dolomite. The dolomite was added to render the formulation harder to detonate. The distribution of the two components was investigated using spatially resolved energy-dispersive X-ray spectroscopy (EDX) in conjunction with ESEM. This indicated that dolomite was present as blocks approximately 50 μm in size.

A prilled fertilizer formulation containing no AN was found which could be used as an inert mechanical mock for the various prill and pellet formulations of

AN studied here. This enabled study of light emission from individual shocked AN prills in later experiments.

The compaction behaviour of beds of various AN formulations was studied at strain rates of $10^{-4}\,\mathrm{s}^{-1}$ and $100\,\mathrm{s}^{-1}$. The former was achieved using an existing screw-driven instrumented press. The latter required the addition of a line laser system to a drop weight. Several results were found. First, the beds were more resistant to compaction at the higher strain rate. Second, dense AN prills intended for agricultural use were more resistant to compaction than low-density AN prills intended for explosive use. This is probably due to the greater distance material must move in the dense prills to fill a void. Mixed AN and dolomite pellets did not follow this trend: despite their dense microstructure, they offered approximately the same resistance to compaction as explosive AN prills. This was probably caused by the pellets' relatively low resistance to disintegration, and lubrication from oil added to the pellets by the manufacturer. Third, the initial porosity, or void fraction, of a bed had little effect on the shape of the pressure-porosity curve found during a compaction experiment. All these phenomena suggest that compaction of ammonium nitrate prill beds is dominated by plastic flow of the prills over length-scales similar to those of prills.

Two simple and popular models, the Heckel and the Kawakita model, were compared with the compaction data. The Heckel model was found to agree very poorly with the data, while the Kawakita model agreed very well.

A copper-fronted flyer was used to introduce a shock to beds of AN, ground and sieved to a particle size of 150–212 μm. This shock induced reaction in the beds, and the light emitted by this reaction was studied using high-speed photography, a photodiode, and gated spectroscopy. It was found that a flyer velocity of $450\,\mathrm{m\,s}^{-1}$ was sufficient to induce reaction, while lower velocities were not. Most investigation took place with a flyer velocity of $700 \pm 40\,\mathrm{m\,s}^{-1}$. There was a delay between the introduction of the shock to the bed and the maximum light output of the bed. This was found to be due to the travel time of the shock through the bed.

The spectrum of light emitted by the shocked bed was studied. A black-body fit to this spectrum found that some regions of the bed reached a peak temperature of 6660 ± 20 K. The energy released by reaction of ammonium nitrate can only

raise its products to a temperature of approximately 2000 K. This discrepancy may prove problematic for purely chemical models of ammonium nitrate detonation. Some possible causes for the difference were suggested, but no definite statements can be made.

This spectroscopic study also found spectral features. These indicate that N_2 formation begins within 800 ns of impact and continues until at least 3 μs after impact. NO formation, meanwhile, begins between 1.1 μs and 0.6 μs before the peak light output of the bed. It therefore seems likely that NO formation is involved in the exothermic reactions which heat the bed. The vibrational energy distribution of the N_2 molecules differs from that observed in low pressure gas-discharge experiments near room temperature, and may merit further study.

The light output of prill and pellet beds during shock-induced reaction was also studied. For low-density prills intended for explosive use, there was evidence that reaction propagated through their porous interior before their dense outer shell failed. For higher-density agricultural prills, there was no such evidence. Photodiode output from these beds showed unexplained features. These features were consistent between reactive prill beds and beds of inert prills with a single reactive prill added. This indicates that effects internal to the prills are dominant in shock-induced reaction. This was supported by drop weight experiments which found no evidence that inter-prill jetting was responsible for reaction of low-density explosive prills. These drop weight experiments also gave some information on the mechanical failure of such prills under uniaxial compression. The fragmentation of the prills suggested that their strength was due to the outer layer of the prill. This layer appeared to fail in a brittle fashion.

There are many possible mechanisms by which hot spots may form in AN prills and granular beds. As these effects are additive rather than competitive, no one effect can be identified as the sole mechanism for initiation in AN: even cosmic rays will have some non-zero (though negligible in practice) contribution. However, the relative importance of these mechanisms can be assessed.

Given that all the prills and beds studied here included cavities, the family of mechanisms related to cavity collapse will clearly be significant. Determining the degree to which each of those mechanisms contributes to reaction is, however, challenging. A wide range of void geometries and sizes is encountered within a

prill. Therefore none of the cavity-collapse mechanisms (jetting, adiabatic compression of gas, viscoplastic work, or evaporation and stagnation) can be ruled out on grounds of geometry or scale.

In common with other secondary explosives, the energy release of fracture in AN is unlikely to be sufficient to cause reaction; crack growth is therefore not a significant hot spot mechanism. Unlike many other secondary explosives, however, AN undergoes some thermal decomposition at its melting point. Frictional heating may therefore contribute to reaction, though it is unlikely to be sufficient to cause detonation alone.

The unusual distribution of vibrational energy levels in N_2 formed during reaction of AN granular beds suggests that some form of vibrational pumping mechanism may be relevant in the initiation of reaction. The simplicity of AN molecules, meanwhile, makes the existence of partially-reacted sensitization centres from previous damage an unlikely contributor to reaction.

Appendix A

Structures of ammonium nitrate

The structures and lattice parameters of the various phases of ammonium nitrate have been known for some time. They are collected here.

A.1 Phase I

This phase has a cubic structure, with space group *Pm3m* and lattice parameter $a = 4.3655(2)$ Å. Diffuse X-ray scattering shows that the nitrate group is in slightly restricted rotation, with either eight or twelve possible orientations (Shinnaka, 1959). In the model with eight orientations, the O−N−O bond angle is exactly 120°. This is not the case in the model with twelve orientations. There is some correlation between the orientations of nearby nitrate groups.

Neutron powder diffraction on deuterated ammonium nitrate was used to find atomic positions, but was unable to determine which model was correct (Ahtee et al., 1979). Multipole analysis of the nuclear smearing functions gave a slight preference for the model with twelve possible orientations. The ammonium group assumes one of two possible orientations with equal probability.

Figure A.1 shows the positions of the nitrogens, which are very similar in each model. Tables A.1 and A.2 show the positions of the atoms in the unit cell. They use, respectively, the models with eight and twelve possible nitrate orientations.

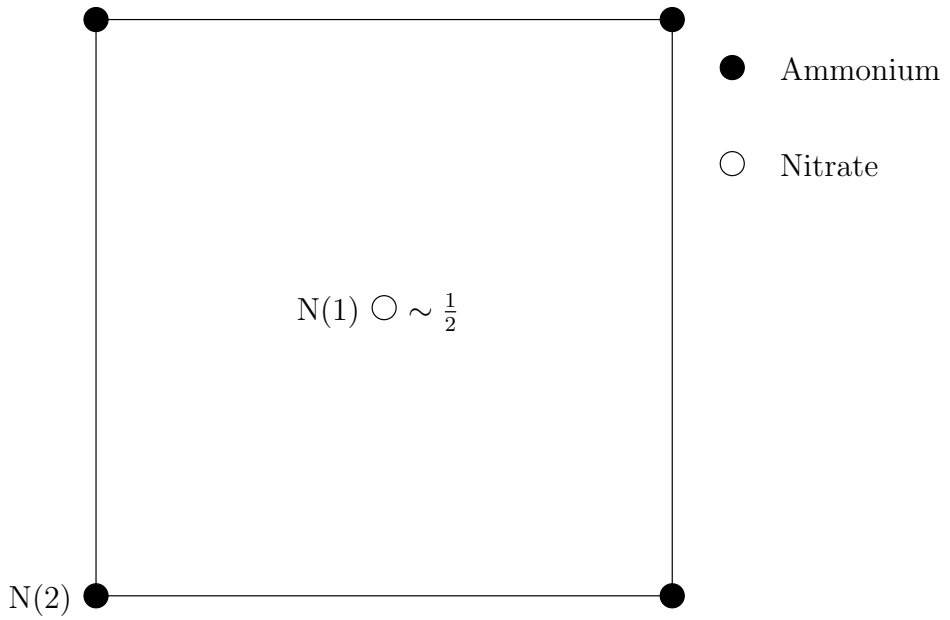

Figure A.1: Centres of molecular groups in ammonium nitrate (I) unit cell, looking down any of the three axes.

	x	y	z
N(1)	0.5179	0.5179	0.5179
O	0.4570(36)	0.4570(36)	0.7936(17)
N(2)	0	0	0
H	0.1265(9)	0.1265(9)	0.1265(9)

Table A.1: Positions of atoms in the ammonium nitrate (I) unit cell, under a model in which there are eight possible nitrate orientations.

	x	y	z
N(1)	$\frac{1}{2}$	$\frac{1}{2}$	0.55
O(1)	$\frac{1}{2}$	$\frac{1}{2}$	0.829
O(2)	$\frac{1}{2}$	0.7725(20)	0.3925
N(2)	0	0	0
H	0.1248(6)	0.1248(6)	0.1248(6)

Table A.2: Positions of atoms in the ammonium nitrate (I) unit cell, under a model in which there are twelve possible nitrate orientations.

	$\boldsymbol{x}$	$\boldsymbol{y}$	$\boldsymbol{z}$
N(1)	0	0	$\frac{1}{2}$
H(1)	0.1404(4)	−0.0171(16)	0.3850(4)
N(2)	0	$\frac{1}{2}$	0.0230(26)
O(1)	0	$\frac{1}{2}$	0.2742(9)
O(2)	0.6287(4)	$\frac{1}{2} + x$	0.1029(10)

Table A.3: Atomic positions in the ammonium nitrate (II) unit cell.

A.2 Phase II

This structure was found by neutron diffraction on powdered, deuterated ammonium nitrate. It is tetragonal, with space group $P\bar{4}2_1m$. Both ammonium and nitrate ions are disordered, each assuming one of two possible orientations. The two nitrate orientations leave the plane of the ion unchanged (Lucas et al., 1979).

$$a = 5.7193(1)\,\text{Å}$$
$$c = 4.9326(1)\,\text{Å}$$
$$Z = 2$$

Figures A.2 and A.3 show the structure with both ammonium and nitrate ions in their first orientation. Figures A.4 and A.5 show the structure with both ions in their alternative orientation. Table A.3 gives the atomic positions.

A.3 Phase III

This structure was found by neutron diffraction on powdered, deuterated ammonium nitrate. It is orthorhombic, with space group *Pnma*. The ammonium ions are disordered, assuming one of two orientations with equal probability (Lucas et al., 1980). This disorder is long-range; the ammonium ions assume a fixed orientation over small regions (Kearley and Kettle, 1982).

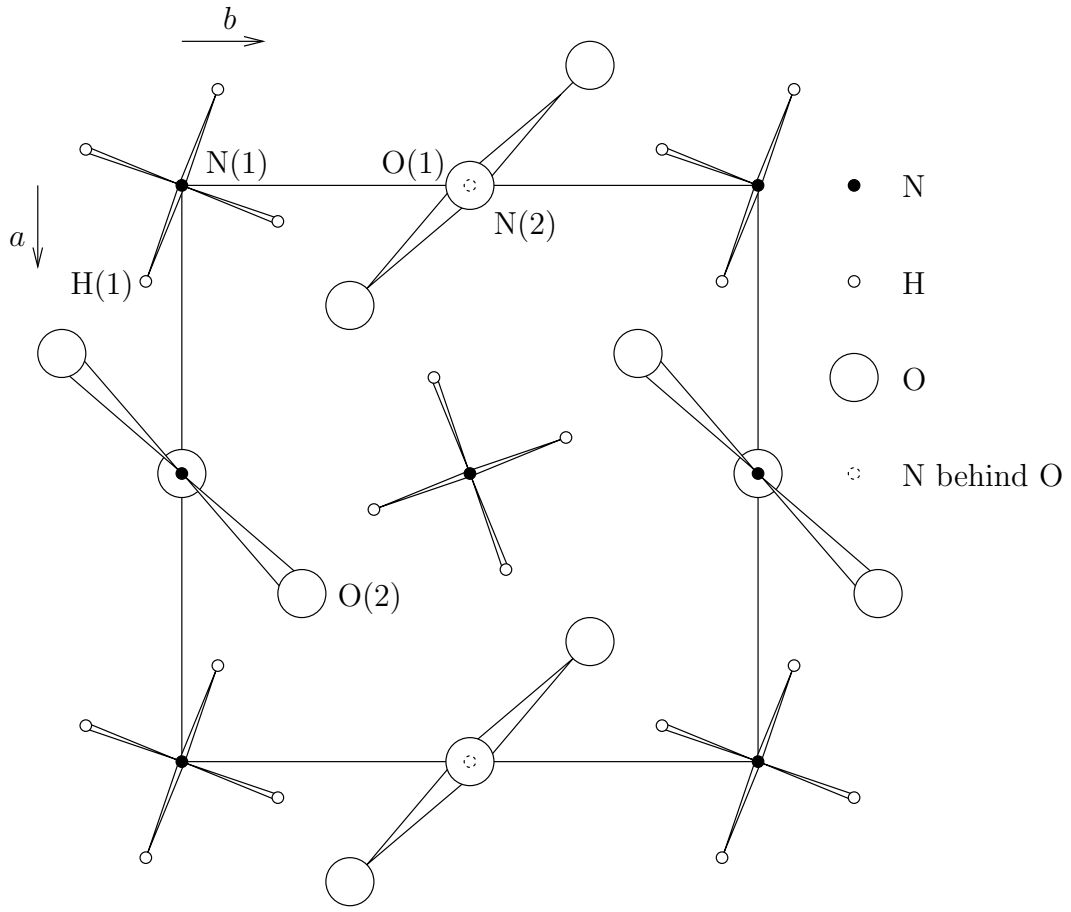

Figure A.2: Structure of ammonium nitrate (II) unit cell, looking down c axis, with ions in first orientation.

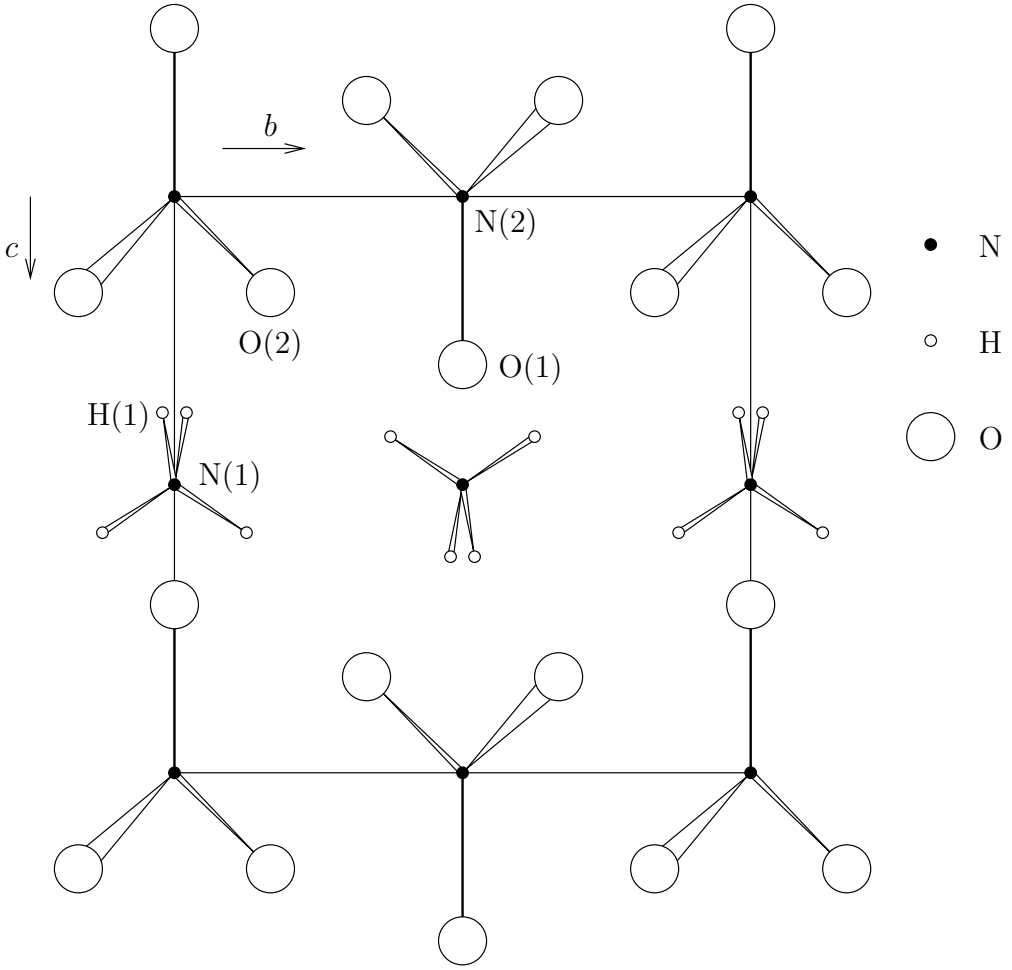

Figure A.3: Structure of ammonium nitrate (II) unit cell, looking down a axis, with ions in first orientation.

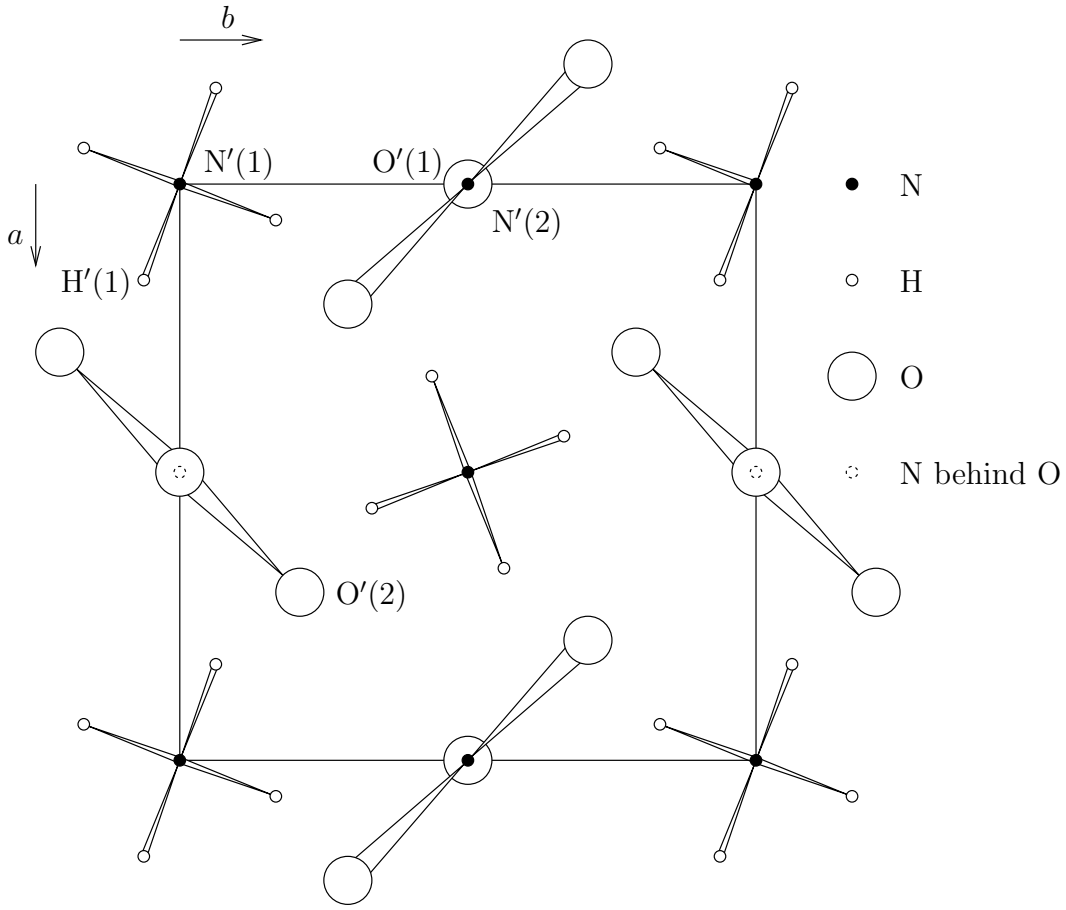

Figure A.4: Structure of ammonium nitrate (II) unit cell, looking down c axis, with ions in second orientation.

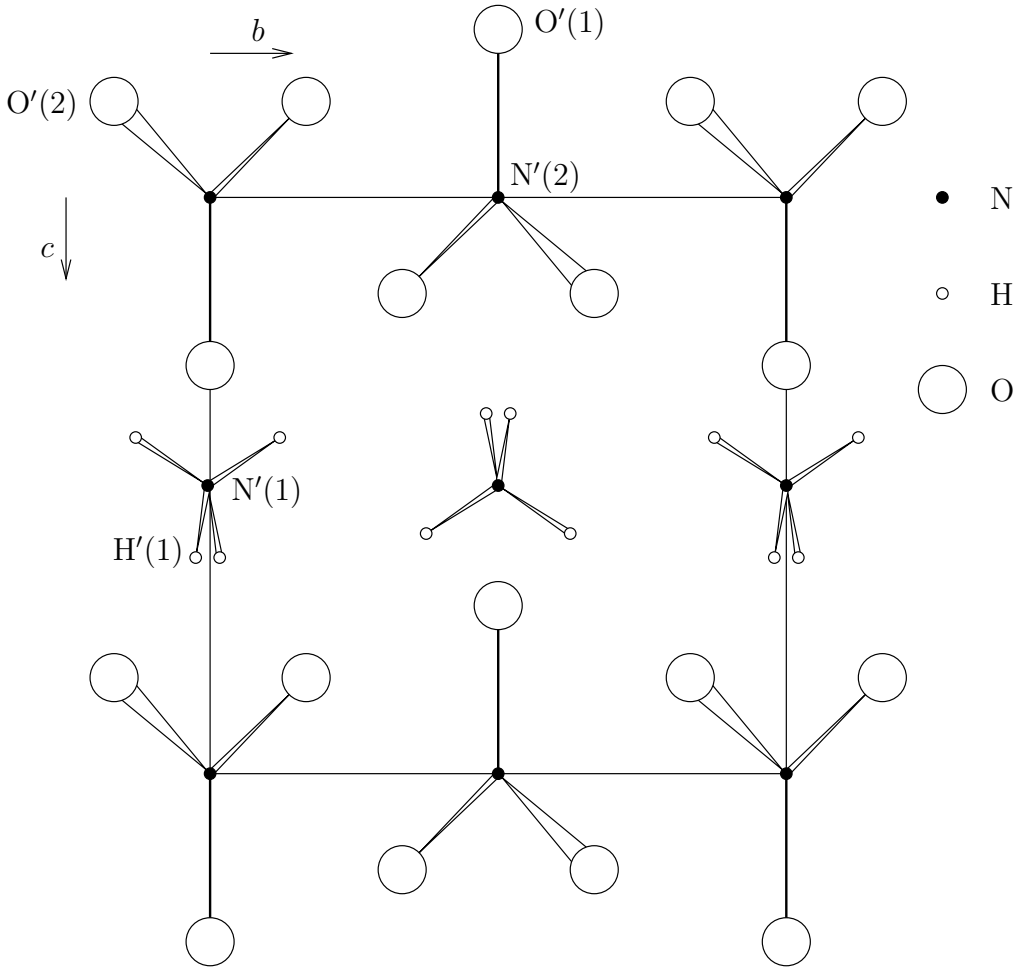

Figure A.5: Structure of ammonium nitrate (II) unit cell, looking down a axis, with ions in second orientation.

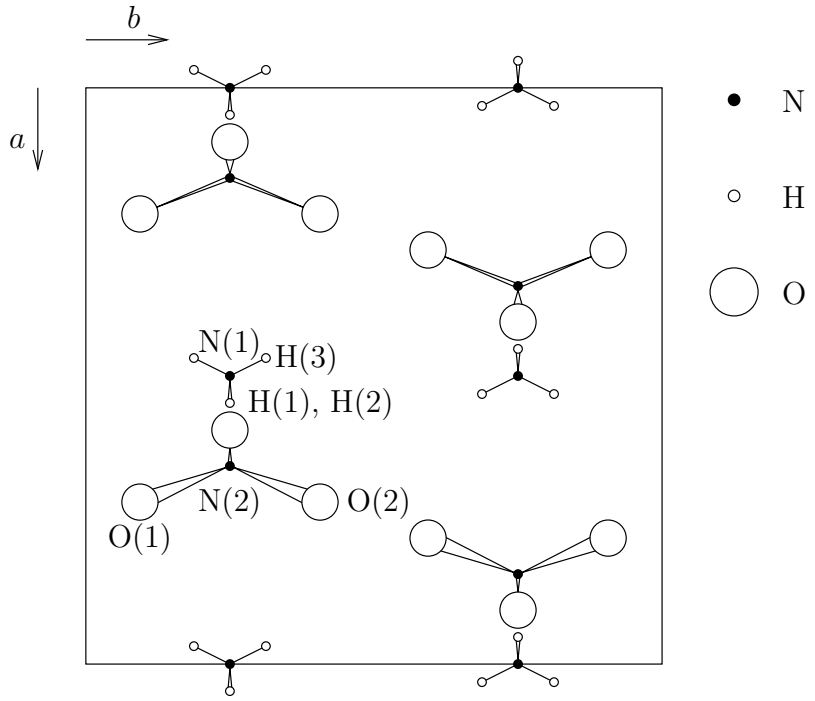

Figure A.6: Structure of ammonium nitrate (III) unit cell, looking down c axis, with ammonium ions in first orientation.

$$a = 7.7184(3)\,\text{Å}$$
$$b = 5.8447(1)\,\text{Å}$$
$$c = 7.1624(2)\,\text{Å}$$
$$Z = 4$$

The structure is shown in figures A.6, A.7, A.8 and A.9. The atomic positions are given in table A.4.

A.4 Phase IV

This structure was found by neutron diffraction on a single crystal. It is orthorhombic, space group *Pmmn*. Hydrogen bonding is significant in this structure. There are hydrogen-bonded sheets parallel to the (001) plane. These sheets

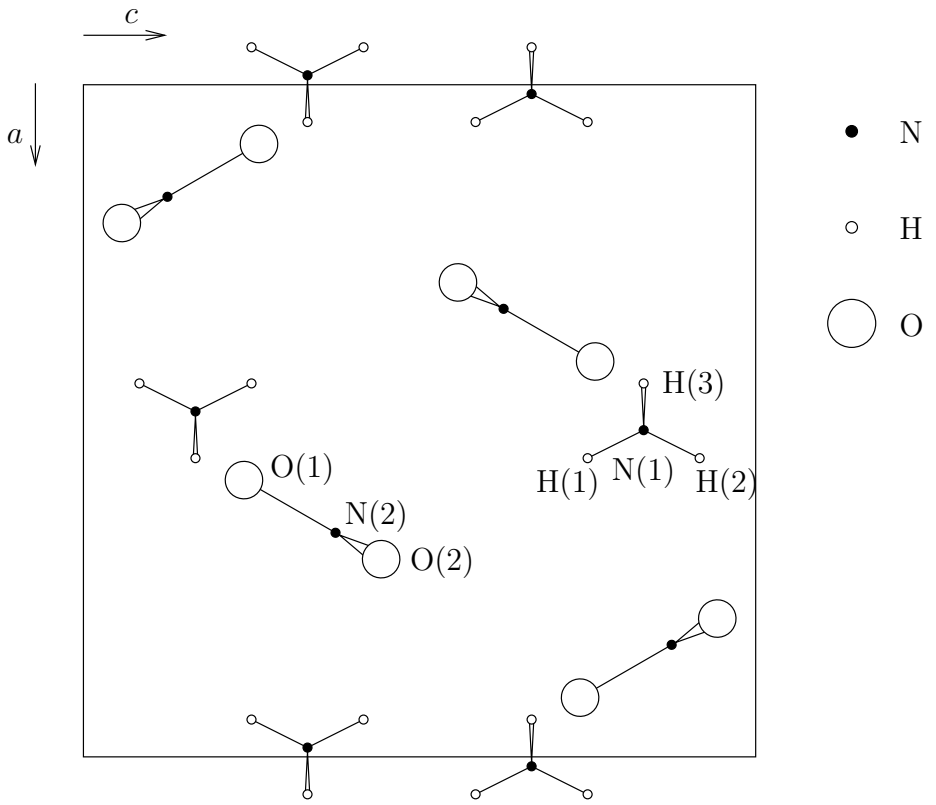

Figure A.7: Structure of ammonium nitrate (III) unit cell, looking down b axis, with ammonium ions in first orientation.

	$\boldsymbol{x}$	$\boldsymbol{y}$	$\boldsymbol{z}$
N(1)	0.5105(3)	$\frac{1}{4}$	0.8177(3)
H(1)	0.5806(4)	$\frac{1}{4}$	0.7282(6)
H(2)	0.5806(4)	$\frac{1}{4}$	0.9118(6)
H(3)	0.4374(4)	0.03624(7)	0.8177(3)
N(2)	0.6557(4)	$\frac{1}{4}$	0.3729(4)
O(1)	0.5662(6)	$\frac{1}{4}$	0.2367(7)
O(2)	0.7004(4)	0.4351(5)	0.4442(5)

$$R = \frac{\sum |sF_0^2 - F_c^2|}{\sum F_0^2} = 0.095$$

Table A.4: Atomic positions in ammonium nitrate (III), from neutron diffraction on powder.

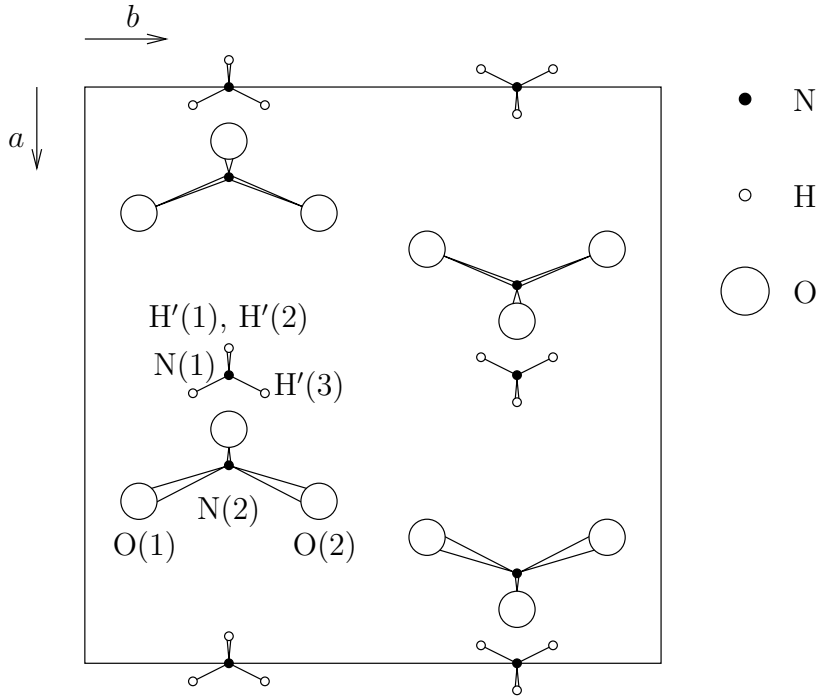

Figure A.8: Structure of ammonium nitrate (III) unit cell, looking down c axis, with ammonium ions in second orientation.

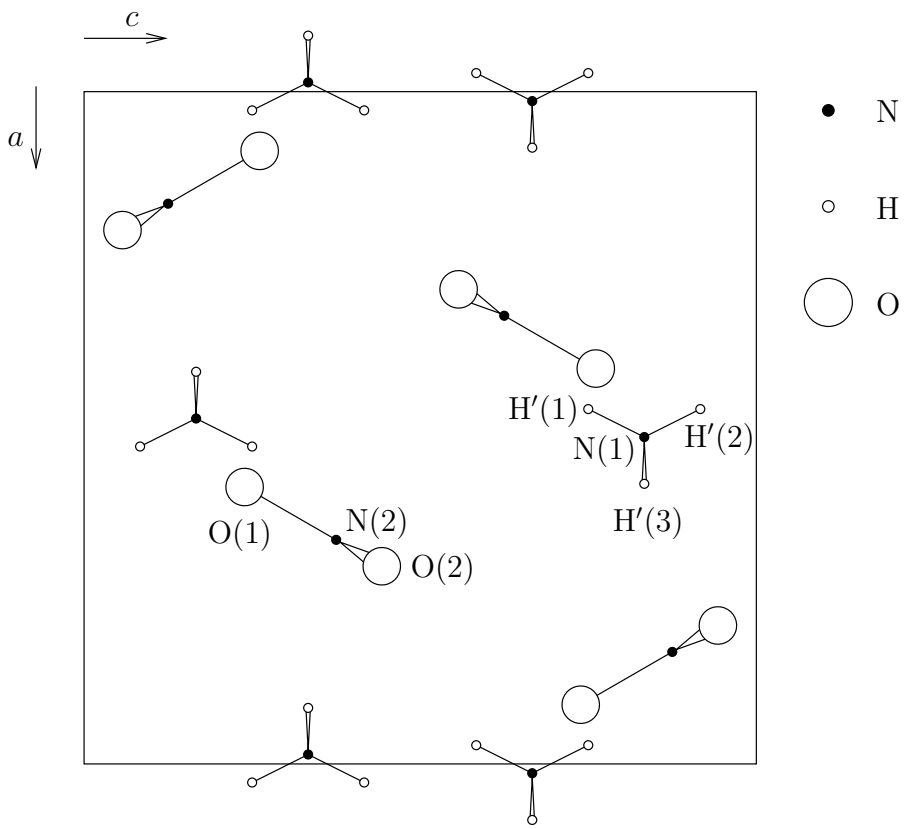

Figure A.9: Structure of ammonium nitrate (III) unit cell, looking down b axis, with ammonium ions in second orientation.

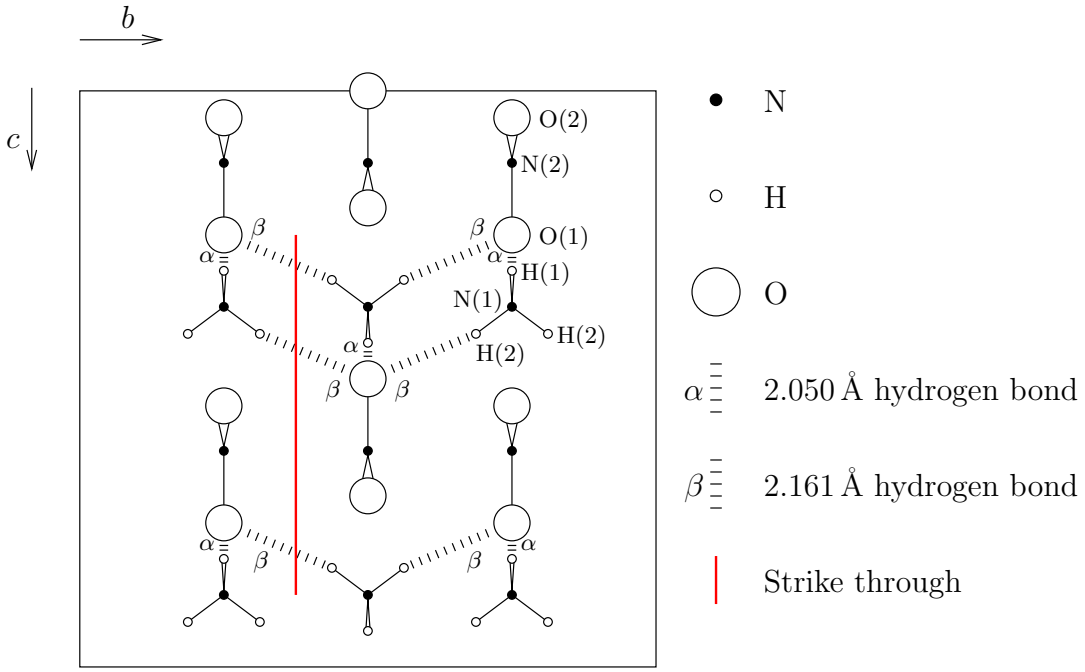

Figure A.10: Structure of ammonium nitrate (IV) unit cell, looking down a axis. The struck through hydrogen bonds must be broken to transform the structure to ammonium nitrate (III).

are held together by van der Waals forces. There is no rotational disorder. In order to transform this structure into phase III, it is necessary to break some of the hydrogen bonds (Choi et al., 1972).

$$a = 5.745\,\text{Å}$$
$$b = 5.438\,\text{Å}$$
$$c = 5.942\,\text{Å}$$
$$Z = 2$$

The structure is shown in figures A.10, A.11 and A.12. The atomic positions are given in table A.5.

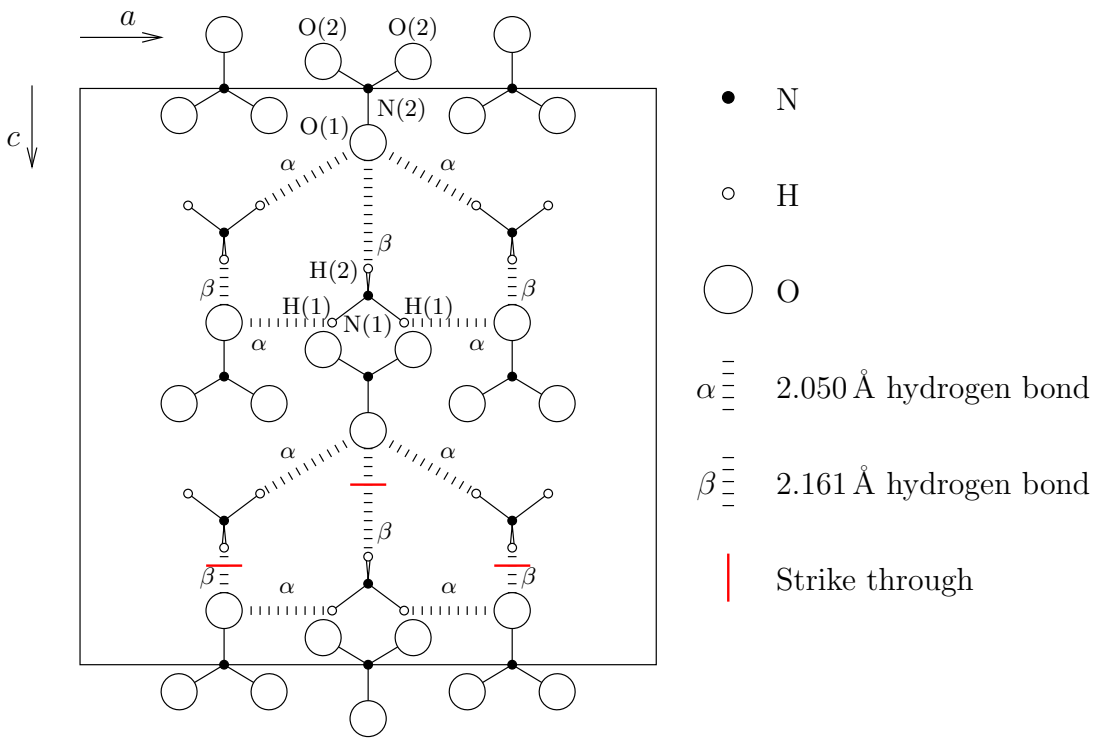

Figure A.11: Structure of ammonium nitrate (IV) unit cell, looking down b axis. The struck through hydrogen bonds must be broken to transform the structure to ammonium nitrate (III).

	$\boldsymbol{x}$	$\boldsymbol{y}$	$\boldsymbol{z}$
N(1)	$\frac{3}{4}$	$\frac{1}{4}$	$-0.0836(4)$
H(1)	0.6045(12)	$\frac{1}{4}$	$-0.1898(17)$
H(2)	$\frac{3}{4}$	0.1011(16)	0.0324(16)
N(2)	$\frac{1}{4}$	$\frac{1}{4}$	0.5067(3)
O(1)	$\frac{1}{4}$	$\frac{1}{4}$	0.7629(6)
O(2)	0.4342(5)	$\frac{1}{4}$	0.3832(5)

Table A.5: Atomic positions in ammonium nitrate (IV), from 1.232 Å neutron diffraction on a single crystal.

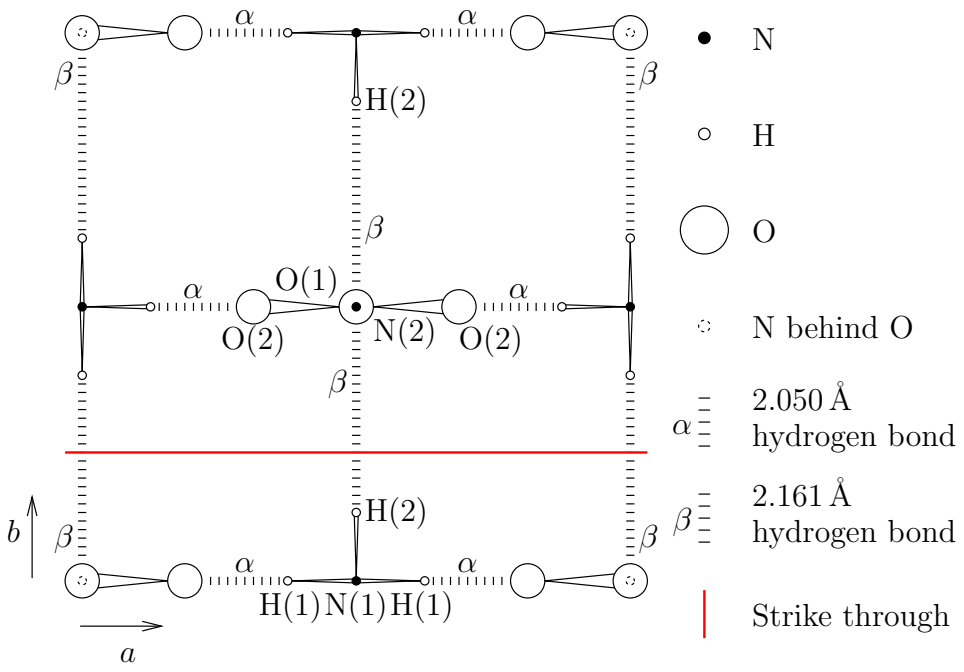

Figure A.12: Structure of ammonium nitrate (IV) unit cell, looking down c axis. The struck through hydrogen bonds must be broken to transform the structure to ammonium nitrate (III).

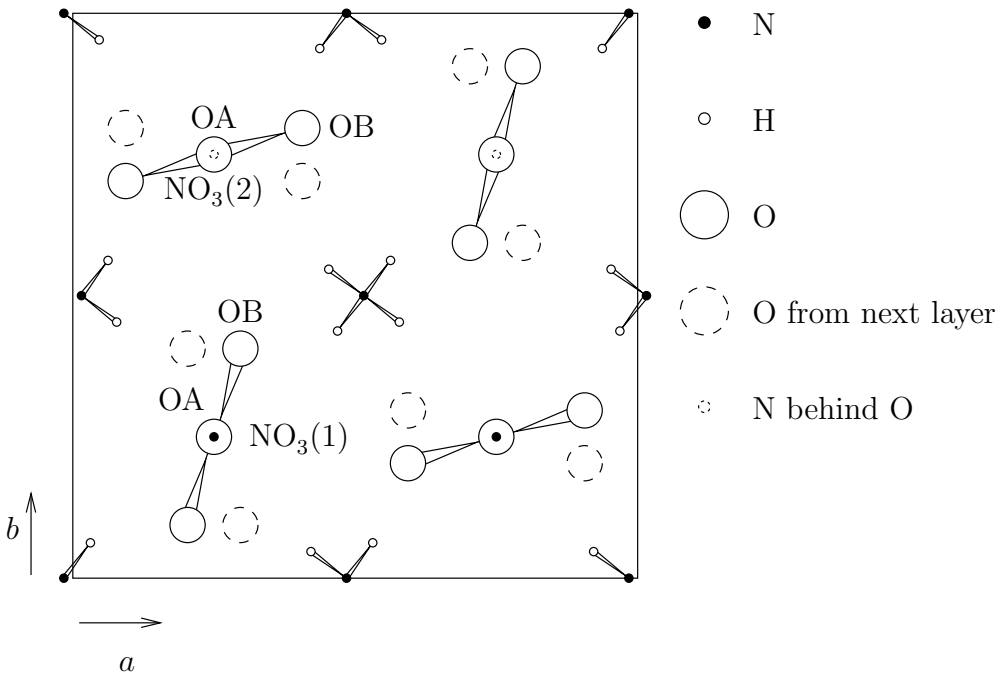

Figure A.13: Structure of ammonium nitrate (V) unit cell, looking down c axis.

A.5 Phase V

This structure was found by neutron diffraction on powdered, deuterated ammonium nitrate. It is orthorhombic, with space group *Pccn* (Ahtee et al., 1983).

$$a = 7.9804(1)\,\text{Å}$$
$$b = 8.0027(1)\,\text{Å}$$
$$c = 9.8099(1)\,\text{Å}$$
$$Z = 8$$

The structure is shown in figures A.13 and A.14. The atomic positions are given in table A.6.

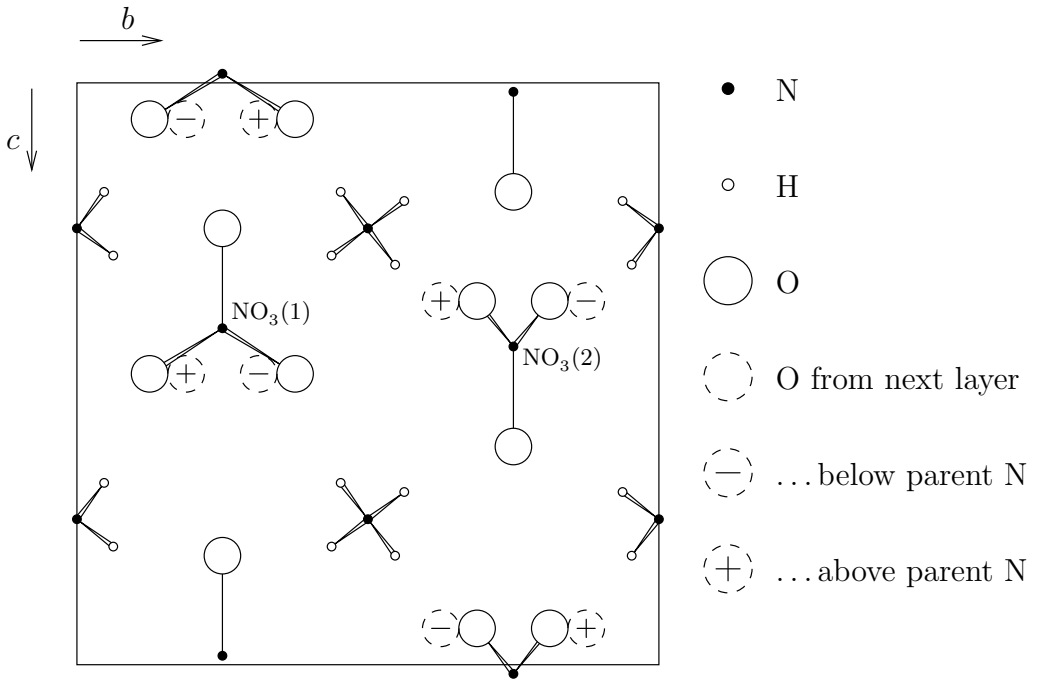

Figure A.14: Structure of ammonium nitrate (V) unit cell, looking down a axis.

	$\boldsymbol{x}$	$\boldsymbol{y}$	$\boldsymbol{z}$	$\boldsymbol{B}$/Å^2
N(1)	$\frac{1}{4}$	$\frac{1}{4}$	−0.0186(5)	0.5(1)
OA(1)	$\frac{1}{4}$	$\frac{1}{4}$	−0.1440(9)	1.1(2)
OB(1)	0.2701	0.3825	0.042(6)	1.9(1)
N(2)	$\frac{1}{4}$	$\frac{3}{4}$	0.0173(6)	1.1(1)
OA(2)	$\frac{1}{4}$	$\frac{3}{4}$	0.1399(10)	2.0(2)
OB(2)	0.3846(6)	0.7774(8)	−0.0405(7)	2.5(1)
N(3)	−0.0177(3)	0.0023(9)	$\frac{1}{4}$	1.6(1)
H(1)	0.0634(10)	0.0535(11)	0.1844(9)	3.4(2)
H(2)	0.0443(9)	−0.0603(11)	0.3246(10)	4.9(2)
H(3)	−0.0917(9)	−0.0772(9)	0.2020(7)	2.2(1)
H(4)	−0.0841(11)	0.1004(12)	0.2890(7)	5.1(2)

Table A.6: Atomic positions in deuterated ammonium nitrate (V), from 1.909 Å neutron diffraction on powder.

References

M. Ahtee, K. Kurki-Suonio, B. W. Lucas, and A. W. Hewat. Determination of molecular orientations in cubic ND_4NO_3. *Acta Crystallographica A*, 35:591–597, 1979.

M. Ahtee, K. J. Smolander, B. W. Lucas, and A. W. Hewat. The structure of the low-temperature phase V of ammonium nitrate, ND_4NO_3. *Acta Crystallographica C*, 39(6):651–655, 1983.

C. S. Choi, J. E. Mapes, and E. Prince. The structure of ammonium nitrate (IV). *Acta Crystallographica B*, 28:1357–1361, 1972.

G. J. Kearley and S. F. A. Kettle. Recent advances in the Raman study of phases II, III and IV of ammonium nitrate. *Journal of Molecular Structure*, 79: 319–321, 1982.

B. W. Lucas, M. Ahtee, and A. W. Hewat. The crystal structure of phase II ammonium nitrate. *Acta Crystallographica B*, 35:1038–1041, 1979.

B. W. Lucas, M. Ahtee, and A. W. Hewat. The structure of phase III ammonium nitrate. *Acta Crystallographica B*, 36:2005–2008, 1980.

Y. Shinnaka. X-ray study on the molecular rotation in cubic ammonium nitrate. *Journal of the Physical Society of Japan*, 14(8):1073–1083, 1959.

Appendix B

Additional photography

The majority of the photography taken in the course of this research was not included in the main body of this document. This was primarily because only a single image was necessary to illustrate most discussions. The remaining images are presented here for completeness. The majority of these images were taken using an Ultranac 501 image conversion camera; see chapter 2, figure 2.19 for the order of frames in those images.

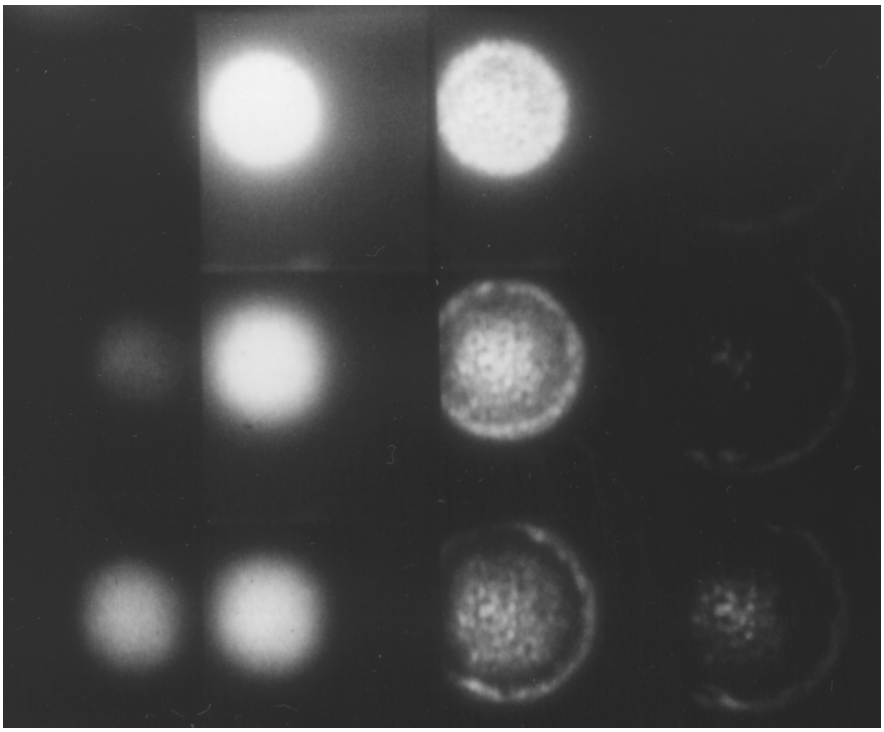

Figure B.1: Framing photography of 150–212 μm ammonium nitrate granular bed. $700 \pm 40\,\mathrm{m\,s^{-1}}$ impact velocity, 460 ns exposure time, 40 ns interframe time. Taken using Ultranac 501 camera; frame order as shown in figure 2.19.

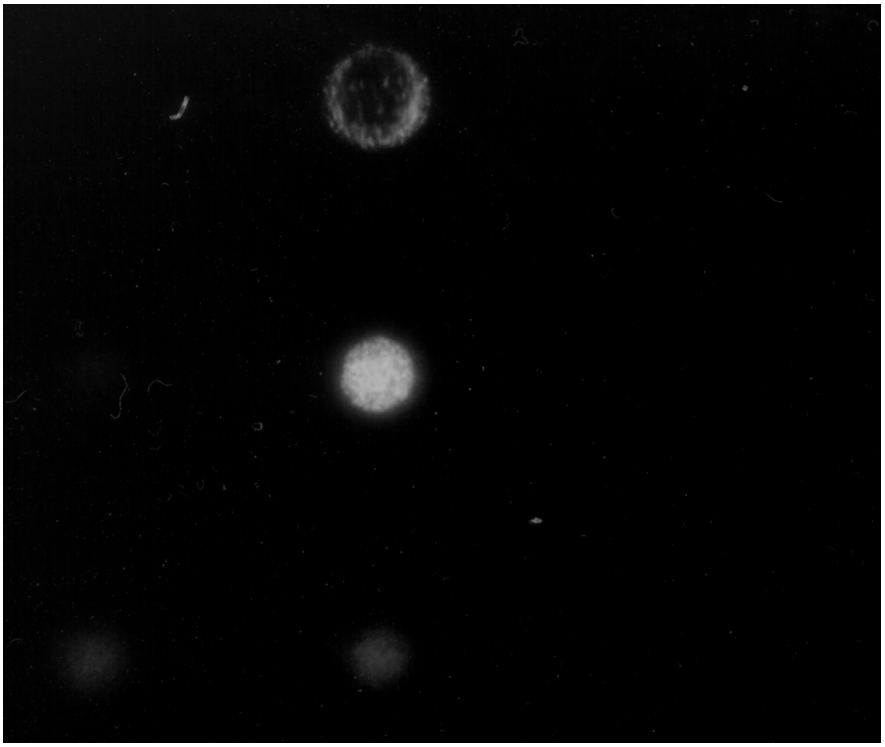

Figure B.2: Framing photography of 150–212 μm ammonium nitrate granular bed. $589 \pm 2\,\mathrm{m\,s^{-1}}$ impact velocity, 460 ns exposure time, 40 ns interframe time. Taken using Ultranac 501 camera; frame order as shown in figure 2.19.

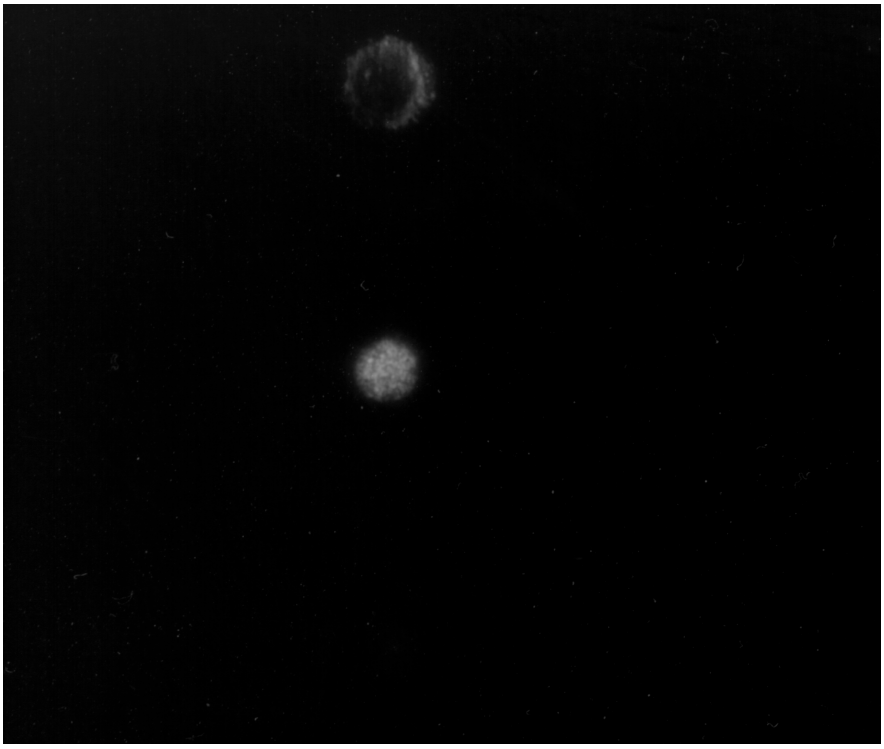

Figure B.3: Framing photography of 150–212 μm ammonium nitrate granular bed. $516 \pm 18\,\mathrm{m\,s^{-1}}$ impact velocity, 460 ns exposure time, 40 ns interframe time. Taken using Ultranac 501 camera; frame order as shown in figure 2.19. Illuminated frames are numbers 5 and 6.

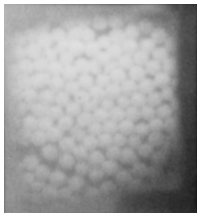

Figure B.4: Static image of the bed of 1.9–2.1 mm Orica prills impacted in figure B.5. To scale with, and taken with the same apparatus as, figure 5.25.

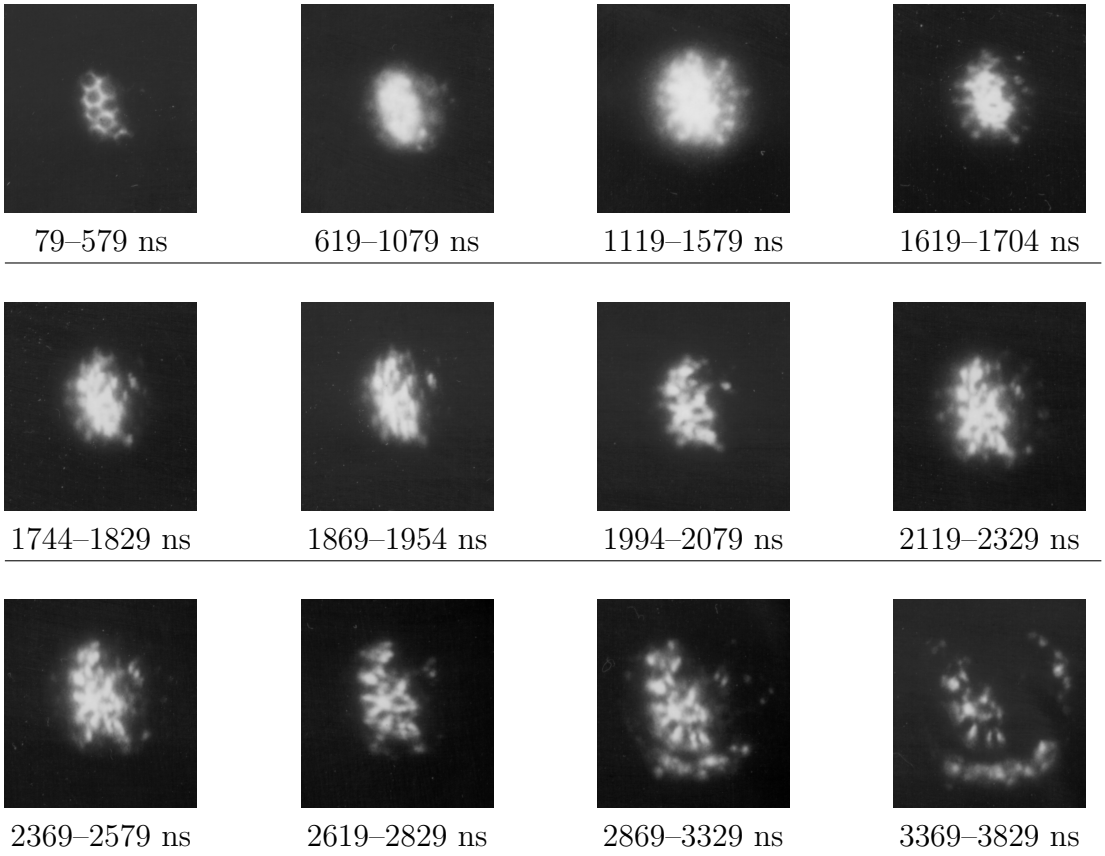

Figure B.5: Framing photography of a bed of 1.9–2.1 mm Orica prills impacted at $700 \pm 40\,\mathrm{m\,s^{-1}}$. Taken using Ultranac 501 camera with variable exposure and interframe time. Times are relative to shock entering bed; all times are subject to the 13 ns uncertainty in shock arrival time.

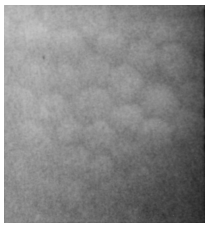

Figure B.6: Static image of the bed of 3.4–3.6 mm agricultural pellets impacted in figure B.7. To scale with, and taken with the same apparatus as, figure B.7.

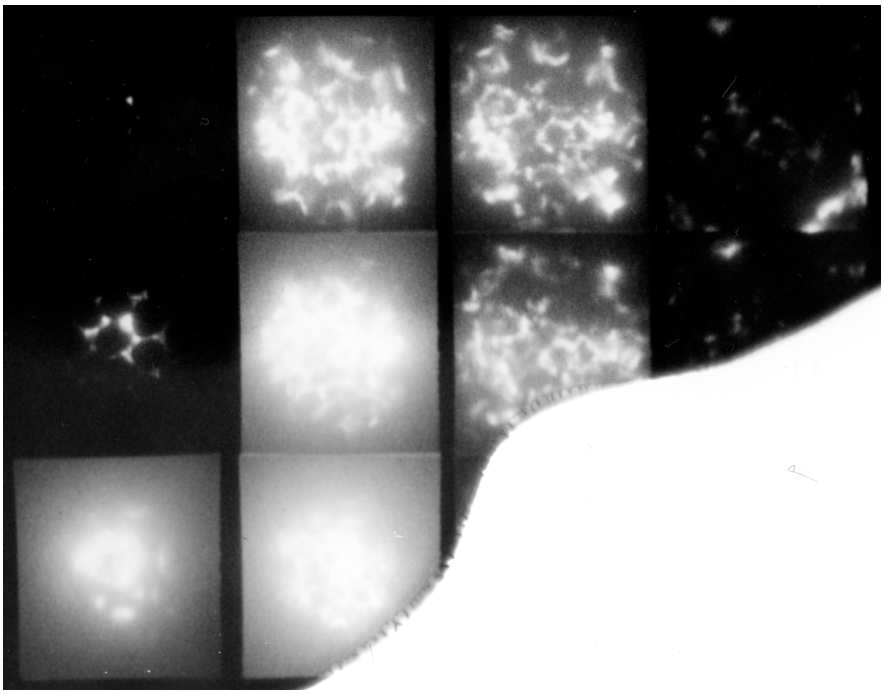

Figure B.7: Framing photography of a bed of 3.4–3.6 mm agricultural pellets impacted at $700 \pm 40\,\mathrm{m\,s^{-1}}$. 460 ns exposure, 40 ns interframe time. Taken using Ultranac 501 camera; frame order as shown in figure 2.19. White region is caused by damage to the photographic film.

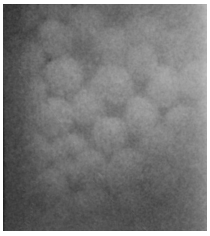

Figure B.8: Static image of the bed of 3.4–3.6 mm Nitram prills impacted in figure B.9. To scale with, and taken with the same apparatus as, figure B.9.

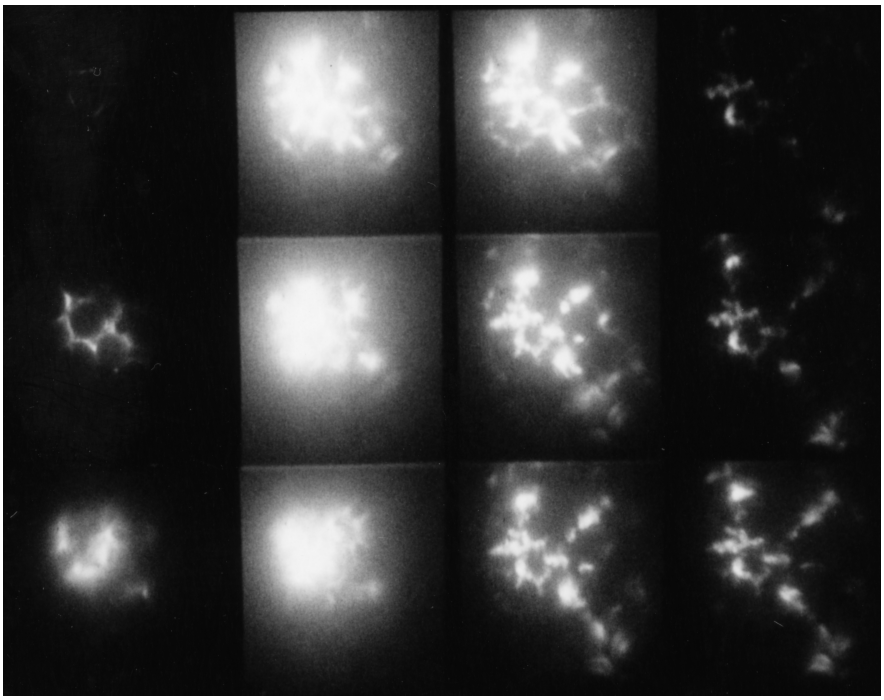

Figure B.9: Framing photography of a bed of 3.4–3.6 mm Nitram prills impacted at $700 \pm 40\,\mathrm{m\,s^{-1}}$. 460 ns exposure, 40 ns interframe time. Taken using Ultranac 501 camera; frame order as shown in figure 2.19.

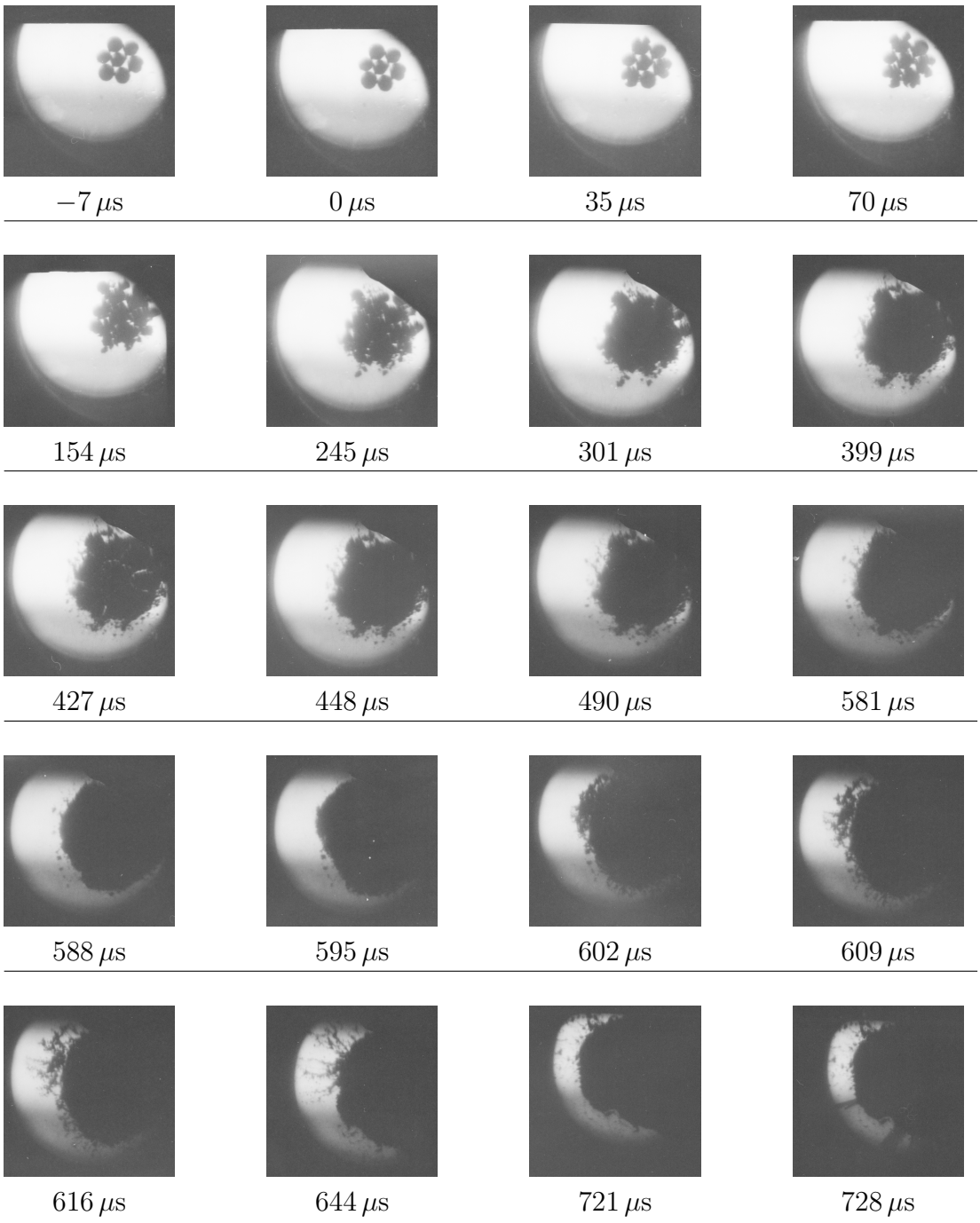

Figure B.10: Photography through sample in drop weight experiment on a hexagonal arrangement of 2 mm ANFO prills taken using C4 camera. Anvils were sapphire rather than the usual float glass. Time is relative to first detectable deformation of prills.

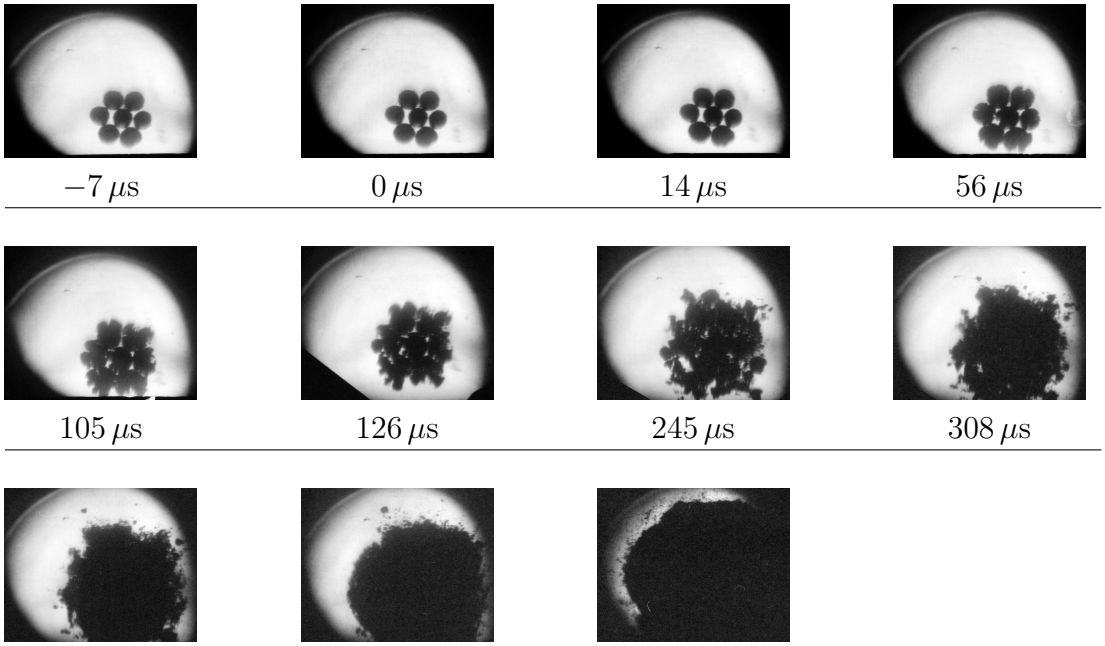

Figure B.11: Photography through sample in drop weight experiment on a hexagonal arrangement of 2 mm ANFO prills taken using C4 camera. Time is relative to first detectable deformation of prills.

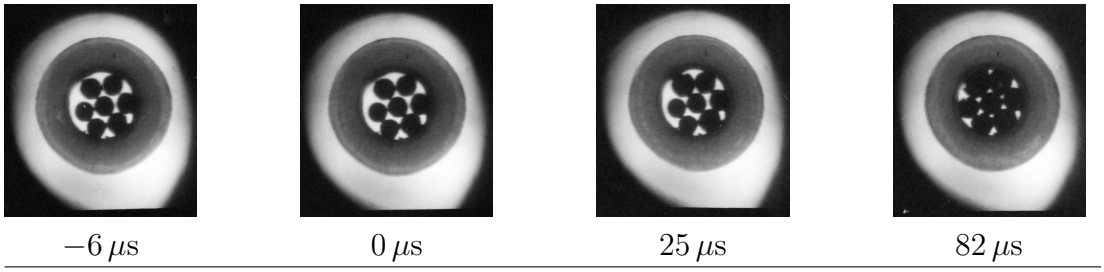

$-6\,\mu$s $0\,\mu$s $25\,\mu$s $82\,\mu$s

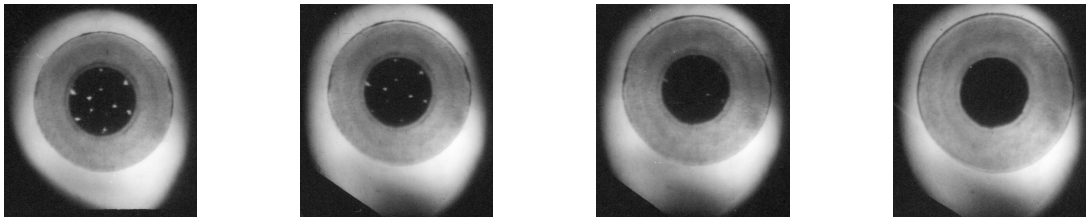

$126\,\mu$s $152\,\mu$s $190\,\mu$s $221\,\mu$s

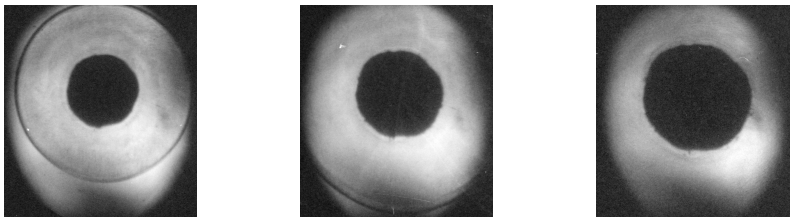

$284\,\mu$s $379\,\mu$s $506\,\mu$s

Figure B.12: Photography through sample in drop weight experiment on a hexagonal arrangement of 2 mm ANFO prills taken using C4 camera. Prills have been surrounded with nylon ring to provide annular confinement. Time is relative to first detectable deformation of prills.

List of corrections

Fig. 1.1, p. 4: AN phase diagram.
p. 2: Discussion of high-pressure AN phases added.
Section 1.1.2.1, p. 6: Short section on AN reaction kinetics added.
Table 1.2, p. 5; fig. 1.2, p. 12; fig. 1.7, p. 15: Citation added to captions.
Fig. 1.3, p. 12; fig. 1.4, p. 13; fig. 1.5, p. 14; fig. 1.6, p. 15; fig. 1.8, p. 16; fig. 1.9, p. 17; fig. 1.10, p. 17; fig. 1.11; p. 18: Captions expanded, citations added.
Fig. 2.1, p. 36; fig. 2.4, p. 43; fig. 2.5, p. 45; fig. 2.6, p. 45; fig. 2.11, p. 54; fig. 2.21, p. 69; fig. 2.22, p. 71; fig. 3.2, p. 87; fig. 3.8, p. 93; fig. 3.10, p. 95; fig. 3.13, p. 97; fig. 3.15, p. 99; fig. 3.16, p. 99; fig. 3.17, p. 100; fig. 3.18, p. 101; fig. 3.19, p. 101; fig. 4.27, p. 126; fig. 4.28, p. 126; fig. 4.4, p. 110; fig. 4.5, p. 110; fig. 4.11, p. 115; fig. 4.14, p. 118; fig. 4.29, p. 127; fig. 4.30, p. 128; fig. 4.31, p. 131; fig. 4.33, p. 134; fig. 5.13, p. 161; fig. 5.3, p. 148; fig. 5.5, p. 149; fig. 5.7, p. 152; fig. 5.8, p. 153; fig. 5.10, p. 158; fig. 5.11, p. 159; fig. 5.16, p. 166; fig. 5.20, p. 172; fig. 5.22, p. 175; fig. 5.23, p. 175; fig. 5.25, p. 177; fig. 5.27, p. 178; fig. 5.30, p. 181; fig. 5.31, p. 182; fig. 5.34, p. 186; fig. 5.36, p. 187; fig. 5.37, p. 188; fig. 5.39, p. 189; fig. 5.40, p. 190; fig. 5.42, p. 192; fig. 5.43, p. 193; fig. 5.45, p. 195; fig. 5.46, p. 196; fig. 5.49, p. 198; fig. 5.50, p. 199; fig. 6.2, p. 205; fig. 6.7, p. 212; fig. 6.14, p. 223; fig. 6.15, p. 223: Captions expanded.
p. 19: Added references for conservation relations.
Section 1.4, pp. 23–25: Short review of compaction work added.
Fig. 2.8, p. 52: Label moved.
p. 75: Added references for Levenberg-Marquardt implementations.
p. 81: Note that bootstrap method needed to be implemented.
p. 105 and 111: Mention length measurements after compaction experiments.
p. 106: Mentioned that bars used were aluminium.

Fig. 4.6, p. 112; fig. 4.7, p. 112; fig. 4.8, p. 113; fig. 4.9, p. 113; fig. 4.17, p. 121; fig. 4.18, p. 121; fig. 4.19, p. 122; fig. 4.20, p. 122; fig. 4.21, p. 123; fig. 4.22, p. 123; fig. 4.23, p. 124; fig. 4.24, p. 124; fig. 4.25, p. 125; fig. 4.26, p. 125: Added length measurements of recovered samples.
Section 4.2.4, p. 120: Removed assertion that coating affects compaction, and associated discussion.
Section 4.2.5.1, p. 128: Evaluated effect of momentum on strain rate dependence of compaction.
Section 4.2.6, p. 130: Moved speculation on implications of initial porosity effects to section 4.2.10, p. 142.
Fig. 4.32, p. 132: Raw, rather than shifted, traces plotted. Caption expanded.
Section 4.2.9, pp. 134–142: Other compaction models considered. ϕ^2 model removed.
Section 4.2.10, p. 142: Added some speculation about mechanisms underlying compaction.
Section 4.3, p. 142: Re-written to agree with corrections.
p. 153: Clarified meaning of "induction time".
p. 153: Clarified explanation of bright ring.
Section 5.1.3.2, pp. 167–169; section 5.3, p. 200; sections 6.2.2.1–6.3, pp. 220–226: Rewritten to incorporate revised heat-conduction model.
Fig. 5.18, p. 170: Original figure replaced with illustration of revised heat-conduction model.
pp. 178, 180, 190, 191, 194, and 197: Removed references to previous heat-conduction model.
pp. 207 and 210, and fig. 6.5 on p. 209: Clarified calibration procedure for spectroscope.
Fig. 6.13, p. 221: Figure re-drawn to account for revised heat-conduction model. Caption expanded.
Section 6.2.2.3, pp. 222–225: Highlighted implications of temperature measurement, and speculated on possible causes.
Fig. 6.14, originally on p. 217; fig. 4.28, originally on p. 118; fig. 4.29, originally on p. 119; fig. 4.34, originally on p. 124: removed.
Chapter 7, p. 227: Re-written to mention revised compaction model, not mention

removed thermal-conduction model, and mention discrepancy between observed temperature and chemistry.
Appendix B, “Monte Carlo simulations”, removed. Appendix C, “Additional photography”, re-labelled Appendix B.